DISSERTATION

ORGANIC-INORGANIC DIPOLAR AND QUADRUPOLAR COUPLING UNDERLIES THE STRUCTURE AND PROPERTIES OF HYBRID PEROVSKITES

Submitted by

Eve M. Mozur

Department of Chemistry

In partial fulfillment of the requirements

For the Degree of Doctor of Philosophy

Colorado State University

Fort Collins, Colorado

Summer 2020

Doctoral Committee:

Advisor: James R. Neilson

Amy Prieto
Amber Krummel
James Sites

ABSTRACT

ORGANIC-INORGANIC DIPOLAR AND QUADRUPOLAR COUPLING UNDERLIES THE STRUCTURE AND PROPERTIES OF HYBRID PEROVSKITES

Hybrid organic-inorganic perovskites are technologically relevant materials with applications in photovoltaics, solid-state lighting, and radiation detection. However, many halide perovskites decompose in the presence of water, oxygen, or radiation. Empirical studies have demonstrated that chemical substitution inhibits the decomposition of hybrid perovskites, but several questions remain about the chemistry and physics underlying the beneficial effects. Here, I show that the organic sub-lattice mediates the phase stability and behavior of hybrid perovskites through dipolar and quadrupolar interactions, which can be tuned with chemical substitution. This work discusses organic-inorganic coupling and the implications of chemical substitution in formamidinium lead bromide ($CH(NH_2)_2PbBr_3$), methylammonium lead bromide ($CH_3NH_3PbBr_3$), formamidinium tin (IV) iodide ($(CH(NH_2)_2)_2PbI_6$), and methylammonium tin bromide ($CH_3NH_3SnBr_3$).

Chapter Two describes how in formamidinium lead bromide the chemical pressure originating from the organic cation modulates the structural and optoelectronic behavior. Formamidinium lead bromide undergoes five distinct, temperature-dependent phase transitions, three of which do not resolve crystallographically and relate primarily to the orientation and dynamics of the formamidinium cation. These crystallographically unresolvable phase transitions resemble ferroelastic transitions with the formation of nanoscale domains, which I demonstrate are mediated by the microstrain exerted from geometric

frustration of formamidinium quadrupoles. Photoconductivity spectra demonstrate that all five phase transitions affect the optoelectronic properties.

Chapter Three demonstrates that cesium substitution in formamidinium lead bromide introduces competing geometric frustration that overpowers the geometric strain from the formamidinium sub-lattice. Nuclear resonance spectroscopies and neutron scattering further elucidate the geometric frustration observed in formamidinium lead bromide and describes the changes in molecular and lattice dynamics with cesium substitution in $(CH(NH_2)_2)_{1-x}Cs_xPbBr_3$ as a function of x. Partial cesium substitution suppresses four of the five phase transitions of $CH(NH_2)_2PbBr_3$. I conclude that cesium suppresses the phase transitions through the relief of geometric frustration associated with the electrostatic quadrupolar interactions between formamidinium molecules, which may in turn explain the greater phase stability of formamidinium perovskites on substitution.

Conversely, crystallography and neutron spectroscopy presented in Chapter Four demonstrate that cesium substitution increases geometric frustration related to the octahedral rotations preferences in methylammonium lead bromide. The geometric frustration manifests as sluggish phase transitions in substituted methylammonium lead bromide, a reentrant phase transition in methylammonium lead bromide with 20% cesium substitution, and inhibited methylammonium dynamics. The inhibited methylammonium reorientational dynamics, which are increasingly slow and glassy as cesium content increases, indicate the formation of an orientational glass. These results suggest that cesium substitution induces geometric frustration within methylammonium lead bromide, most likely originating from the mismatch between methylammonium and cesium bonding preferences.

In three dimensional hybrid perovskites, organic-inorganic coupling must compete with inter-octahedral interactions. To more directly investigate organic-inorganic coupling, we can consider reduced dimensionality perovskite derivatives. Vacancy ordered double perovskites (VODPs) have isolated octahedra, but the structure conserves the close packed halide lattice that provide the advantageous optoelectronic properties of hybrid perovskites. Chapter Five describes how organic-inorganic coupling manifests in the phase behavior of the hybrid VODP formamidinium tin (IV) iodide. Formamidinium undergoes a phase transition to a monoclinic distortion of the high temperature cubic phase that is characterized by broad hysteresis and irreversible particle fracturing. We classify this phase transition as ferroelastic, given that the hysteresis is indicative of domain formation that the presence of spontaneous strain from the alignment of formamidinium cations in the low temperature phase.

The molecular dipoles in methylammonium perovskites can also couple to dipoles related to intra-octahedral distortions, such as the metal off-centering related to stereochemical activation of the s^2 lone pair that occurs in tin and germanium perovskites. Methylammonium tin bromide exhibits crystallographically ordered, static tin off-centering at low temperature indicative of stereochemical activation of lone pairs, while the low temperature phases of cesium tin bromide are characterized by symmetric, undistorted octahedra. Both tin bromide perovskites undergo local, dynamic structural distortions related to stereochemical activation at high temperatures. To understand the driving forces behind this type of organic-inorganic coupling, Chapter Six examines the solid solution series between methylammonium tin bromide and cesium tin bromide. Substitution suppresses the low

temperature phase transition of methylammonium tin bromide, but it does not otherwise change the phase behavior of the solid solution series. Examination of the local structure suggests that all tin bromide perovskites exhibit short range structural distortions related to stereochemical lone pair activation, although cesium rich members and methylammonium rich members exhibit stereochemical activation through different mechanisms.

Chemical substitution moderates the lattice strain of hybrid perovskites in complex, organic-cation dependent pathways. The organic cation identity will drive the phase behavior through dipole or quadrupole interactions with the octahedra. The characterization of these interactions provides a rational approach to substitution in hybrid perovskites that will enable high- performing devices and provide design principles for dynamic semiconductors.

ACKNOWLEDGEMENTS

It is entirely possible that there are too many people to thank for helping me finish this document. I am going to try anyway.

I will always appreciate the institutions that offered the financial support that was instrumental to keeping me in grad school. Thank you to Colorado State University and I would like to acknowledge funding from the U.S. Department of Energy, Office of Science, Basic Energy Sciences, under Award SC0016083.

To the Neilson group - past and present - thank you for creating a safe space for me to learn and grow. Thank you for always having time to proof read and always starting your comments with a “this is good”, even when you proceeded to rip the document to shreds. Thank for you coming along on my various rabbit holes. Thank you especially to Annalise and Andy who spent a lot of my first year telling me to get into lab, to try new things, and to *for the love of all things holy* label my waste correctly and just do the experiment. You have all made me a better scientist.

Thank you to Jamie. You had never ending patience with me, starting from when I walked into your office and declared that I had a passion for solid solutions. You didn’t even chuckle, and encouraged me to indulge that somewhat unusual passion for a good five years. Thank you for your kind words and telling me that it is ok to be frustrated when I needed it. Thank you for being silly for no apparent reason. I will continue to bother you forever, although probably not as often as recently.

Thank you to all my mentors, Mrs. Russo, Prof. Geselbracht, Prof. Fry who showed me that I could be a chemist, and a damn good one at that. Thank you for giving me role models to live up to.

Thank you to Hailey, Kim, Jen, Annalise, Jaz, Chris, Lily, Leslie, Angela. I am overjoyed that I got to spend these years with you to commiserate and support each other. I think back to our laughter filled adventures and grumble filled lunches and I know that I would not have been nearly as happy without you. You all deserve Paul Hollywood handshakes and everything we ate together was definitely worth the calories. I am excited to continue to grumble and laugh together.

To all of my friends who said “of course!” when I told them I wanted a PhD, instead of “why”. You are all the best.

I did not expect to fall in love in grad school, so thank you to Tolby for bringing me that joy. Thank you for supporting me as you learned what a perovskite is and why I felt so strongly about them. Thank you for getting me out of lab when I really needed it. You bring me happiness every day and I’m so excited for our adventures.

To Jesse - always my quietest, steadiest supporter. Your memory keeps reminding me to be a better person.

I don’t know how many times I have thanked my parents, but I know that it will never be enough. Thank you for never questioning my ability to follow my dreams, whether they were be to become a ballerina, an equestrian, a French major, or a chemist. Your unwavering support has gotten me to so many incredible places. I love you so much.

And finally, thank you to myself for committing to this process. Getting here was a ton of hard work and I am proud of it.

TABLE OF CONTENTS

LIST OF FIGURES

1. Introduction

Our society's cutting edge technology, from cell phones and computers, to batteries and solar panels, rely on solid materials. Predicting which materials work best in a given application is a huge challenge for materials chemists, and a large portion of the breakthroughs in materials chemistry have been serendipitous. Developing structure-property relationships enables the rationalization of these breakthroughs.

Most inorganic semiconductors for photovoltaic and lighting applications crystallize in the diamond lattice, characterized by a covalent network of edge-sharing tetrahedra.[1] These materials, such as silicon, gallium arsenide, and cadmium telluride are the basis for most investigations into new inorganic semiconductors. In the late 2000s, however, hybrid perovskites came to prominence as a family of inorganic semiconductors competitive with conventional inorganic semiconductors when incorporated into a solar cell and yet structurally distinct from diamond lattice materials.[1,2] Hybrid halide perovskites are characterized by an ionic, polarizable network of corner-sharing octahedra where a p-block metal occupies the center of the octahedra, a halide ion occupies the vertices, and an organic cation resides in the A-site between octahedra (Figure 1.1). Hybrid perovskites present an exciting opportunity to expand the existing structure-property relationships based on diamond lattice semiconductors.

Hybrid perovskites are ideal materials to build structure-property relationships because they are structurally tunable (Figure 1.2). Early photovoltaic studies focused on three dimensional perovskites, such as methylammonium lead iodide and formamidinium lead

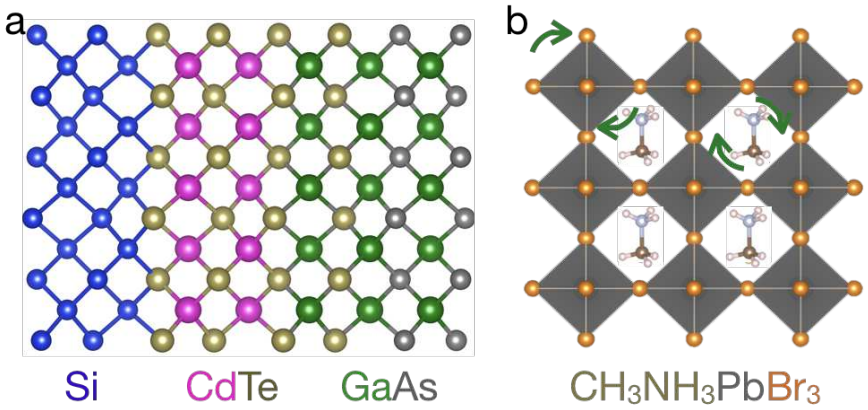

Figure 1.1: The structure of diamond lattice semiconductors silicon, gallium arsenide, and cadmium telluride (a) compared to the structure of the hybrid perovskite methylammonium lead bromide (b). Arrows indicate dynamic degrees of freedom of the octahedra and of the organic cation.

iodide,[1] where dimensionality reflects the connectivity of the octahedral framework. Decreasing the connectivity to two dimensions by incorporating bulky organic cations to separate the octahedral framework into layers increases the exciton binding energy and therefore have increased potential for lighting applications.[3] A subset of these layered materials exhibits broad band white light emission, suitable for single material white light emitting diodes.[4] Vacancy ordered double perovskites (VODPs) are zero dimensional perovskite derivatives, where every other metal site is vacant compared to the three dimensional parent structure. Unlike two and three dimensional perovskites, in which the central metal ion has a formal +2 oxidation state, the metal in VODPs has a formal +4 oxidation state.[5] The preservation of the close packed halide sublattice makes the electronic properties of VODPs closely related to those of the three dimensional perovskites.[6]

In addition to their structural tunability, hybrid perovskites are compositionally distinct from conventional inorganic semiconductors. The bonding in silicon, gallium arsenide and cadmium telluride is covalent and fairly directional. Hybrid perovskites have ionicity stem-

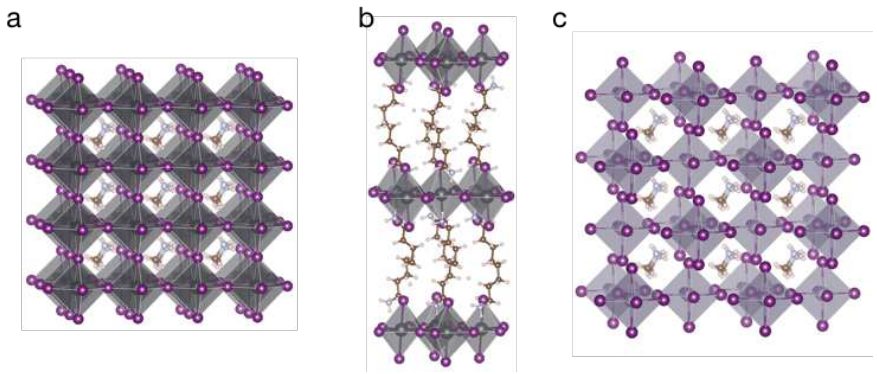

Figure 1.2: The dimensional tunability of hybrid perovskites: (a) the three dimensional perovskite methylammonium lead iodide (b) the two dimensional layered perovskite n-butylammonium lead iodide (c) the zero dimensional vacancy ordered double perovskite methylammonium tin iodide.

ming from the metal-halide bond character and from interactions between the inorganic octahedra and the A-site cation. Rather than one unified lattice, hybrid perovskites can easily be broken into two distinct sub-lattices - the organic and inorganic. In addition, most perovskites implemented in devices are chemically substituted.[7] Unsubstituted hybrid perovskites can decompose rapidly under ambient conditions, which has been attributed to reactivity with water, positive enthalpies of formation relative to their respective binaries, and instability under infrared radiation.[8–10] Chemically substituted perovskites, where the A-site is occupied by a mixture of methylammonium, formamidinium, and cesium and the halide site is occupied by a mixture of bromine, iodine, and chlorine, undergo decomposition or degradation much more slowly.[11,12] Substitution can also tune the optoelectronic properties, which is attractive for tandem solar cell applications.[13,14]

The composition and bonding of hybrid perovskites introduces many dynamic degrees of freedom, which are unusual compared to conventional materials. Hybrid perovskites are known for their cooperative octahedral tilting and rotations, which are dynamic in their high temperature cubic phase and freeze out in their low temperature tetragonal

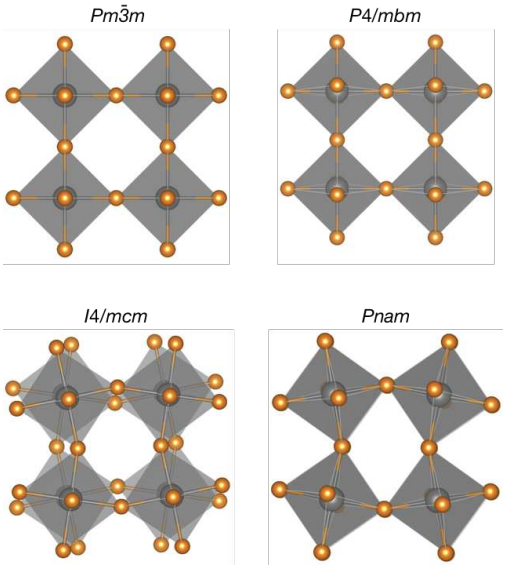

Figure 1.3: The typical phases of hybrid perovskites. The high temperature cubic phase ($Pm\bar{3}m$) transitions to a tetragonal phase ($I4/mcm$ or $P4/mbm$) and then to the orthorhombic phase ($Pnam$) on cooling. A-site cations have been emitted for clarity.

and orthorhombic phases.[15] Symmetry-allowed dynamics include both in-phase rotations (Glazer notation: $a^0a^0c^+$) that are computed to be more favorable in halide perovskites, out-of-phase rotations (Glazer notation: $a^0a^0c^-$) that are computed to be more favorable in oxide perovskites, and tilting perpendicular to the plane of rotation (Glazer notation $a^+b^-b^-$).[16–18] The rotations tend to freeze out first, resulting in a cubic (space group: $Pm\bar{3}m$) to tetragonal (space group: $P4/mcm$, $I4/mcm$) phase transition followed by a tetragonal to orthorhombic phase transition (space group: $Pnam$) as the tilting modes freeze out on cooling (Figure 1.3). In addition, tin and germanium perovskites can undergo dynamic or static metal off-centering due to the stereochemically active lone pair on the metal center.[19–21]

The presence of the organic cation introduces additional dynamic degrees of freedom. Methylammonium and formamidinium vibrate within the A-site similar to the behavior

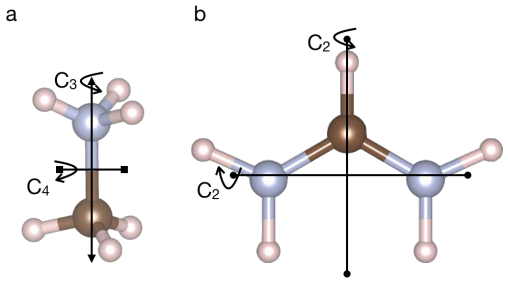

Figure 1.4: Depictions of the symmetry and pseudo-symmetry allowed rotations and reorientations in (a) methylammonium and (b) formamadinium.

of the isolated molecules.[22–25] Additionally, both molecules librate and reorient within the A-site void and the type of reorientation is determined by the symmetry of the molecule and of the unit cell.[26,27] Density functional theory calculations and molecular dynamics simulations predict that in addition to molecular librations, formamidinium will undergo C_2 rotations along the pseudo C_2 axis connecting the two amine groups and along C_2 symmetry axis of the molecule, as depicted in Figure 1.4.[27,28] Experimental identification of the symmetry of formamidinium reorientations remains challenging, but the computational predictions are consistent with transient spectroscopy results that show two molecular motions on femto- and nanosecond time-scales.[29] Dielectric susceptibilities suggest that the formamidinium dynamics change only slightly with temperature.[30,31] Quasielastic neutron scattering experiments have identified that methylammonium undergoes a C_3 rotation parallel to the carbon-nitrogen bond and a C_4, 90° rotation imposed by the C_4 symmetry axes of the unit cell in the high temperature cubic phase of methylammonium lead iodide.[26,32] At the tetragonal to orthorhombic phase transition temperature the C_4 mode completely and abruptly freezes out, in contrast to the more gradual changes in formamidinium perovskites.[26,30,33] The C_3 rotations of methylammonium persist to low temperature.[25,30,33]

As indicated by the simultaneous freezing of the octahedral tilting mode and the methylammonium C_4 rotation at the tetragonal to orthorhombic phase transition of methylammonium lead iodide,[33] hybrid perovskites can exhibit strong organic-inorganic coupling. The large dipole moment of methylammonium allows for hydrogen bonding between the amine and the halides on the vertices of the octahedra.[34–36] These hydrogen bonds are thought to be the reason that methylammonium lead iodide and methylammonium lead bromide crystallize in the $I4/mcm$ tetragonal phase rather than the $P4/mbm$ tetragonal phase preferred by other halide perovskites.[16] High energy resolution inelastic X-ray experiments indicate that, even in the cubic phase, methylammonium librations and reorientations are related to anharmonic octahedral dynamics at the edge of the Brillouin zone.[37] Similar behavior occurs in VODPs, where organic-inorganic interactions lead to anharmonic lattice dynamics manifesting as a random distribution of octahedral tilting angles.[38]

The dynamic degrees of freedom of hybrid perovskites affect many of their optoelectronic properties, such as long excited state charge carrier lifetimes and modest carrier mobilities. The long excited state charge carrier lifetimes of hybrid perovskites are attributed to the formation of large polarons where the lattice locally deforms around an excited charge carrier to stabilize the excited state.[39] Polaron formation also reduces charge carrier mobility relative to an unstabilized charge carrier.[40] Transient spectroscopy demonstrates that the phonons responsible for the structural deformation in methylammonium lead iodide correspond to lead-iodide bond bending and stretching.[41] Similarly, photoemission spectroscopy suggests that hybrid perovskites have Rashba splitting in the frontier energy states,[42] which transforms the relaxation of excited state charge carriers from an

allowed to a spin-forbidden process and increases the excited state lifetime.[43] Rasha splitting results, in part, from non-centrosymmetry in the structure. As perovskites crystallize in centrosymmetric space groups, the non-centrosymmetry most likely comes from transient lattice dynamics.

Organic cation dynamics tend to have a more indirect role on the electronic properties of hybrid perovskites, since the energy states of the organic cation are far from the band gap.[44] Computations predict that local structural distortions of the octahedral framework induced by the organic cation orientation can modify the band gap.[45,46] Optical Kerr spectroscopy and time-resolved photoluminescence data indicate that the liquid-like reorientations of the organic cation correlate to increased hot-carrier excited state lifetimes through a similar mechanism.[47] This could be related to polaron formation, as organic cation dynamics were recently shown to stabilize nascent polarons.[48] The organic cation also modifies the electron-phonon interactions; formamidinium perovskites exhibit temperature dependent charge mobilities indicative of a simple Frolich mechanism, but methylammonium perovskites appear more complex.[49,50] Understanding the organic cation dynamics will lead to insights into the optoelectronic behavior of hybrid perovskites.

In this dissertation, I investigate the organic cation dynamics in pure and in substituted hybrid perovskites. I demonstrate that the dynamics and electrostatics of the organic cation affect the structure and optoelectronic properties through stress-strain relationships. Further, the strain exerted on the inorganic octahedra can be tuned through chemical substitution. By examining the strain exerted by the methylammonium and formamidinium

on hybrid perovskites, I am able to build structure-property relationships that will allow the rational design of the next generation of hybrid perovskite based devices.

Chapters two and three focus on formamidinium perovskites. Chapter two characterizes the temperature dependent photoconductivity, structure, and molecular dynamics of formamidinium lead bromide. The presence of five changes in the photoconductivity of formamidinium lead bromide between room temperature and 100 K are linked to the two known crystallographic phase transitions and three previously uncharacterized crystallographically unresolvable phase transitions. All five phase transitions are characterized by changes in the dynamic degrees of freedom of formamidinium, indicating an important link between formamidinium dynamics and the photoresponse of the perovskite. The phase transitions are attributed to geometric frustration within the formamidinium sublattice. Chapter three discusses the effects of cesium substitution in formamidinium lead bromide. Nuclear magnetic resonance (NMR) spectroscopies, neutron scattering, and crystallography demonstrate that cesium substitution suppresses the four low temperature phase transitions of formamidinium lead bromide and removes the driving force for concerted changes in formamidinium dynamics. Cesium substitution, therefore, relieves strain from formamidinium lead bromide.

Chapter four focuses on the effect of substitution in methylammonium lead bromide. Quasielastic neutron scattering reveals that cesium substitution inhibits methylammonium reorientations with increasing inhibition as more cesium is included. The changes in organic cation dynamics as a function of temperature become more gradual with cesium substitution, and the clear discontinuities at phase transition temperatures become spread

out. Crystallography demonstrates that the phase transitions become glassy, and that 20% cesium substitution results in an unusual cubic-tetragonal-cubic reentrant phase transition. These data indicate the formation of an orientational glass that forms due to increased geometric frustration with cesium substitution. This strain occurs because of the mismatch between coordination preferences of cesium and methylammonium.

Chapter five describes the low temperature structures the VODP formamidinium tin (IV) iodide. Formamidinium tin (IV) iodide transitions into a typical VODP low temperature monoclinic phase, and the hysteresis and crystallographic microstrain evidenced during the phase transition indicate that this material is a ferroelastic. Organic-organic interactions appear to lead to geometric frustration analogous to the three-dimensional perovskite formamidinium lead bromide from chapter 2. These results indicate that the types of organic-inorganic coupling observed in the three dimensional perovskites is exacerbated in VODPs due to the decrease in octahedral connectivity.

Chapter six focuses on a different type of organic-inorganic coupling by investigating how substitution at the A-site of methylammonium tin(II) bromide affects tin off-centering and octahedral deformations related to stereochemical activation of the tin s^2 lone pair. Methylammonium tin bromide undergoes a low temperature phase transition that freezes in tin off-centering. In contrast, cesium tin bromide does not undergo tin off-centering phase transitions, but does exhibit increased dynamic tin off-centering at high temperature. This chapter investigates the structure of cesium substituted methylammonium tin (II) bromide to elucidate the driving interactions between both dynamic and low temperature tin off-centering. Organic-inorganic coupling related to a combination of steric

and hydrogen bonding interactions between methylammonium and the tin-bromide octahedra encourage a polar alignment of the structural distortions related to stereochemical activation, while cesium tin bromide is characterized by greater dynamics at the bromide positions.

The final chapter discusses a unified perspective of the relationship between geometric frustration, organic cation dynamics, and organic-inorganic coupling in hybrid perovskites. The effects of quadrupolar molecules compared to dipolar molecules is discussed, as is the strength of these interactions as a function of dimensionality. I propose that understanding the strain exerted on the octahedral framework by the A-site cation allows a more complete understanding of the structure and properties of hybrid perovskites.

2. Dynamical Phase Transitions and Cation Orientation Dependent Photoconductivity in Formamidinium Lead Bromide †

Summary

The choice of organic cation in hybrid perovskites has large implications for optoelectronic properties, material stability, and crystal structure. In particular, formamidinium ($CH(NH_2)_2^+$) perovskites exhibit unusual temperature-dependent trends in photoluminescence, dielectric constant, and phase behavior that are hypothesized to relate to $CH(NH_2)_2^+$ reorientations. This contribution describes five distinct, temperature-dependent phase transitions in $CH(NH_2)_2PbBr_3$ that produce changes in the steady-state photocurrent. Three of these phase transitions do not resolve crystallographically and relate to the orientation and dynamics of $CH(NH_2)_2^+$. These crystallographically unresolvable phase transitions resemble ferroelastic transitions with the formation of nanoscale domains, which we hypothesize are mediated by the strain exerted from geometric frustration of $CH(NH_2)_2^+$

†Reproduced with permission from Mozur E. M., Trowbridge, J. C., Maughan, A. E., Gorman M. J., Brown C. M., Prisk T. R., Neilson J. R. Dynamical Phase Transitions and Cation Orientation-Dependent Photoconductivity in $CH(NH_2)_2PbBr_3$ *ACS Materials Chemistry Letters* **2019**, 1, 2, 260-264, https://pubs.acs.org/doi/10.1021/acsmaterialslett.9b00209. Copyright 2019 American Chemical Society.
Author contributions: Eve Mozur collected and analyzed the X-ray diffraction, photoconductivity, heat capacity, differential scanning calorimetry data, prepared the manuscript and analyzed the neutron diffraction data. Julia Trowbridge prepared the samples. Annalise Maughan collected the diffraction data. Matthew Gorman. built the photoconductivity instrument and software. Timothy Prisk and Craig Brown collected and analyzed the neutron scattering data. James Neilson built the photoconductivity instrument, edited the manuscript, and oversaw the project.

quadrupoles. This work demonstrates the importance of cation orientation and dynamics, domain behavior, and their interdependence in the steady-state optoelectronic properties of hybrid perovskites.

Introduction

Hybrid perovskites have emerged as high performing semiconductors, with applications in photovoltaics and solid-state lighting.[51,52] Several studies suggest that their transformative optoelectronic properties arise in part from the formation of giant polarons, formed by transient structural fluctuations of the coupled lead-halide octahedral framework and the organic sublattice.[41,48,53] The topologically under-constrained nature of the corner connected octahedral framework and stochastic, liquid-like reorientation of the organic cations methylammonium ($CH_3NH_3^+$) and formamidinium ($CH(NH_2)_2^+$) that occupy the cuboctahedral void render their potential energy landscape highly complex and time-dependent relative to conventional inorganic semiconductors.[53–55] The interplay of the functional properties and structural dynamics motivates investigation into their relationships, such as the role that structural rigidity plays in efficient luminescence.[56]

Formamidinium-based perovskites exhibit complex structural and dynamic behavior when compared to the archetypal methylammonium perovskites. Unlike $CH_3NH_3Pb{X}_3$ perovskites, in which the octahedral tilt patterns couple strongly to $CH_3NH_3^+$ dynamic degrees of freedom to give a unique tilting pattern,[57] changes in $CH(NH_2)_2^+$ molecular dynamics appear gradually over a large temperature range, with little dependence on crys-

tallographic transitions and octahedral tilt patterns.[57–59] The gradual change in molecular dynamics correlates to similar trends in optoelectronic behavior.[49,60]

The differences between the molecular dynamics of $CH_3NH_3^+$ and $CH(NH_2)_2^+$, which could arise from the increased steric bulk of $CH(NH_2)_2^+$, the additional amine capable of hydrogen bonding, the resonant π system, or the weaker dipolar moment and the stronger quadrupolar moment relative to $CH_3NH_3^+$, are associated with differences in the overall structure and phase behavior of formamidinium perovskites. $CH(NH_2)_2^+$ reorientations and the resulting local strain have been implicated in the complex phase behavior of $CH(NH_2)_2PbI_3$. Depending on sample preparation or thermal history, $CH(NH_2)_2PbI_3$ undergoes a reentrant phase transition, a phase transition between a perovskite cubic phase and a non-perovskite hexagonal phase, or retains the cubic phase between 400 K and 8.2 K.[20,57,61,62] While formamidinium perovskites show great promise for photovoltaic applications,[63–65] the implications and driving forces of the unusual phase behavior are not well understood.

Here, we demonstrate that the molecular reorientations of $CH(NH_2)_2^+$ modify the steady-state light-induced charge carrier separation in $CH(NH_2)_2PbBr_3$ by characterizing the temperature-dependent photoconductivity, crystallography, calorimetry, and dynamics of $CH(NH_2)_2PbBr_3$. In addition to the two previously reported crystallographic phase transitions, specific heat and neutron scattering data reveal three phase transitions that are not resolved crystallographically. We demonstrate that the additional three transitions pertain to changes in the molecular reorientations of $CH(NH_2)_2^+$ and also influence the photoconductivity spectrum and intensity. This work indicates that the dynamic degrees of

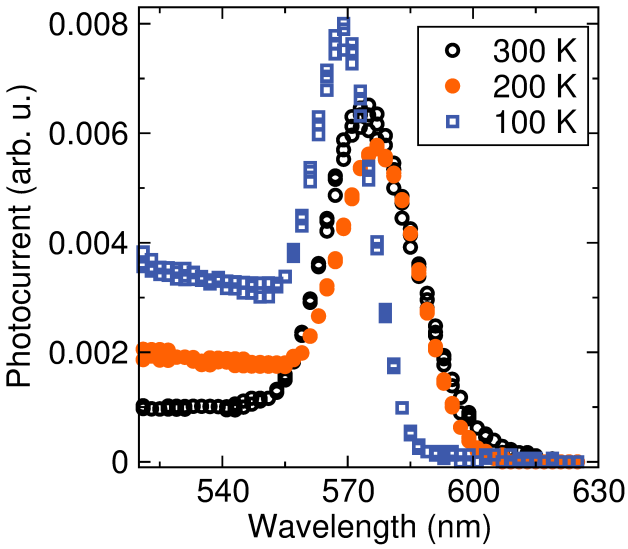

Figure 2.1: Photoconductivity data collected on a single crystal of $CH(NH_2)_2PbBr_3$ at 300 K, 200 K, and 100 K, normalized to the lamp emission profile.

freedom of the organic sublattice influence *steady-state* optoelectronic properties in hybrid perovskites and highlights the importance of studying domain structure in these complex materials.

Results

A typical photoconductivity spectrum collected on a single crystal of $CH(NH_2)_2PbBr_3$ has three regions, which can be seen in Figure 2.1. For excitation energies below the optical gap, there is no observable photocurrent. We attribute to the peak near the optical gap to the generation of excitons as seen in single crystal specimens of related samples.[66] For excitation energies well above the band gap there is a non-zero photocurrent that we attribute primarily to interband transitions.

The temperature dependent photoconductivity data presented on Figure 2.2 exhibit a red-shift in energy of the excitonic peak on cooling between room temperature and

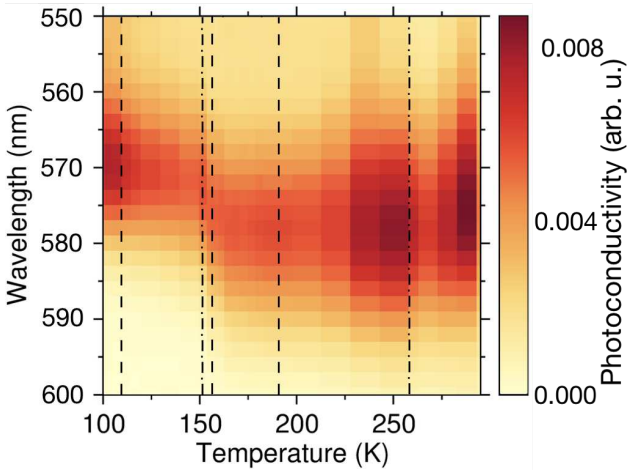

Figure 2.2: False-color representation of the temperature-dependent photoconductivity as a function of excitation wavelength of $CH(NH_2)_2PbBr_3$. Dashed-dotted gray lines indicate crystallographically resolvable phase transition temperatures and dashed gray lines indicate crystallographically unresolvable phase transition temperatures determined from heat capacity and differential scanning calorimetry data. Representative spectra are shown in Figure 2.1.

$T = 180$ K, and a blue-shift on cooling between $T = 180$ K and $T = 100$ K. In general, hybrid perovskites exhibit red-shifting of the optical gap on decreasing temperature.[67,68] This is in contrast to conventional inorganic semiconductors (e.g. Si, GaAs), in which case the band gap energy decreases as temperature increases due both to lattice dilation and electron-phonon coupling.[69] The blue-shift in the band gap on cooling in hybrid perovskites can be explained by considering thermal lattice dilation. As temperature increases the lattice expands, decreasing orbital overlap, which decreases the splitting of the bonding and anti-bonding states. In hybrid perovskites, the top of the valence band is primarily composed of anti-bonding interactions and the bottom of the conduction band is primarily composed of bonding states.[70] Therefore, as the lattice expands the energy between the valence and conduction bands increases as the splitting between anti-bonding and bonding states decreases. We observe this behavior in Figure 2.4a between room temperature

and $T = 180$ K, until orientational phase transitions render electron-phonon coupling more important than lattice dilation, which complicates the optoelectronic response.

By examining the width of the photolumincence (PL) peak as a function of temperature, a previous study determined the primary mode of electron phonon-coupling in formamidinium lead bromide and related hybrid perovskites to involve longitudinal optic (LO) phonons.[68] Therefore, the width of the PL peak follows the relationship: $\Gamma = \Gamma_0 + \gamma_{LO} \times \exp(E_{LO}/kT)$, where Γ is the width of the excitation peak, Γ_0 is the intrinsic peak width, γ_{LO} is the electron-phonon coupling constant, and E_{LO} is the phonon energy. This previous study showed that the temperature-dependent PL data for $CH(NH_2)_2PbBr_3$ yields $\gamma_{LO} = 61 \pm 7$ meV, $E_{LO} = 15.3 \pm 1.4$ meV, and $\Gamma_0 = 20 \pm 1$ meV. The width of the excitonic peak in the photoconductivity spectra presented here (Figure 2.2) closely agrees with the values of γ_{LO} and E_{LO} (Figure 2.3). The photoconductivity data show a larger intrinsic width (70 meV), which suggests that carrier scattering in electrical transport may contribute to additional broadening. This comparison strongly suggests that the electron-phonon coupling probed in PL experiments is comparable to that in charge transport.

Overlaid on these general trends, temperature dependent photoconductivity data, resolve several temperature-dependent transitions. The data exhibit discontinuities in the intensity of the excitonic peak near the energy of the optical gap (λ = 575 nm, $h\nu$ = 2.16 eV), the intensity of the photocurrent at energies above the optical gap, and in the position of the excitonic peak center, as indicated by the vertical lines in Figure 2.2 and Figure 2.4a. These discontinuities in peak intensity, interband intensity, and peak center of the photoconductivity spectra correlate to the five phase transitions observed in the specific heat of

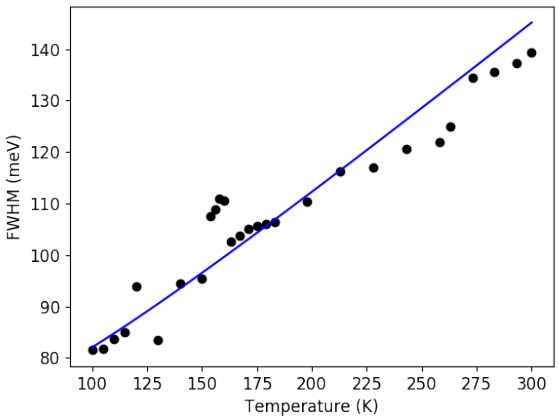

Figure 2.3: Width of the photoconductivity excitonic peak (dots) as a function of temperature, compared to an electron-phonon model[68] described in the text.

$CH(NH_2)_2PbBr_3$, as apparent in Figure 2.4a-b, and agrees with recently reported discontinuities in lattice expansion.[71] Two of the five phase transitions correlate to known crystallographic phase transitions from a high temperature cubic perovskite phase (space group: $Pm\bar{3}m$) to a tetragonal perovskite phase (space group: $P4/mbm$) at $T = 266$ K, and then to a low temperature orthorhombic perovskite phase (space group: $Pnma$) at $T = 153$ K.[72] In both high-resolution neutron diffraction (NPD) and high-resolution synchrotron X-ray diffraction (SXRD) data, these two phase transitions manifest only through the appearance of low intensity Bragg reflections (Figures 2.5, 2.7, 2.11), in contrast to the resolvable peak splitting and discontinuities in lattice parameters observed in $CH_3NH_3PbBr_3$ and $CsPbBr_3$.[73,74] The remaining three phase transitions at $T = 182$ K, 162 K, and 118 K cannot be resolved in either high resolution SXRD or NPD (Figure 2.9).

The phase transitions of $CH(NH_2)_2PbBr_3$ involve subtle changes to powder diffraction and parameters extracted from Rietveld refinements. Figures 2.5 and 2.6 demonstrate that the major reflections in the diffraction data remain extremely similar between $T = 260$ K

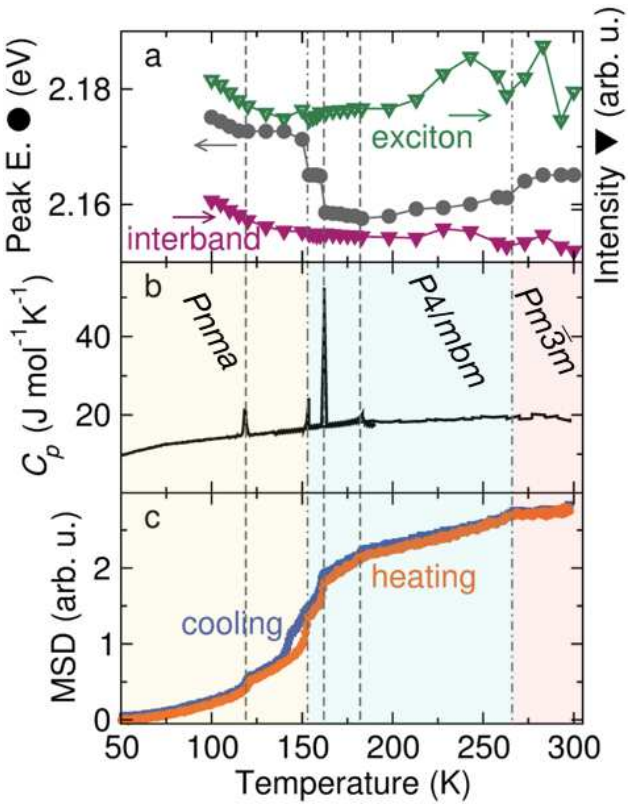

Figure 2.4: (a) Excitonic peak center (left axis, gray circles), excitonic peak intensity (right axis, unfilled green triangles), and interband intensity (right axis, pink triangles) of the photoconductivity data presented in Figure 2.2. (b) Heat capacity data for $CH(NH_2)_2PbBr_3$. The crystallographically-observed phase transitions occur at 266 K and 153 K. While the crystallographically resolvable transition at 266 K is not observed in the heat capacity, it is observed in differential scanning calorimetry (Figure 2.14). (c) Mean squared displacement (MSD) of hydrogen determined from fixed window elastic neutron scattering (collected on HFBS) of $CH(NH_2)_2PbBr_3$ measured on heating (orange circles) and cooling (blue squares). Dashed-dotted gray lines indicate crystallographically resolvable phase transition temperatures and dashed gray lines indicate crystallographically unresolvable phase transition temperatures determined from heat capacity and differential scanning calorimetry data. Estimates of the uncertainties are smaller than the symbols used to represent the data in all subplots.

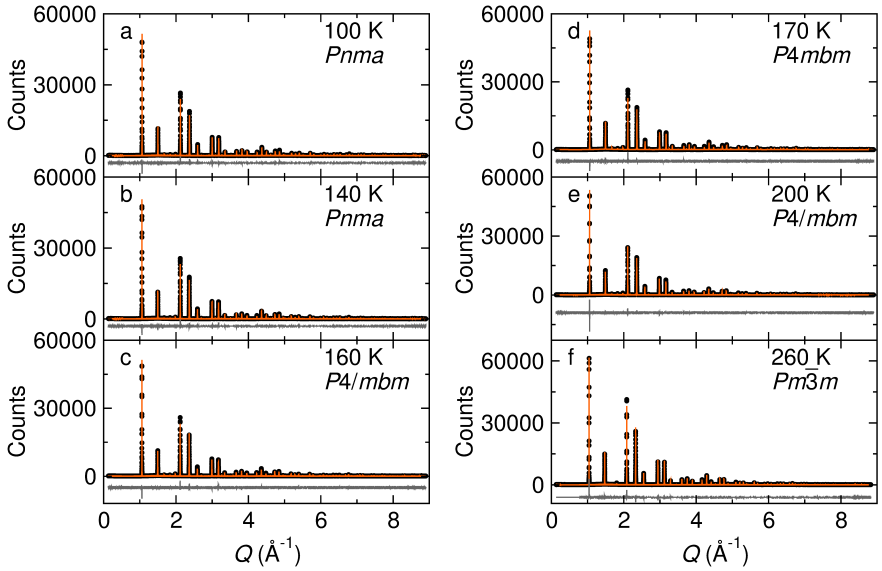

Figure 2.5: High-resolution synchrotron X-ray diffraction patterns collected during a slow cool, resting at each temperature for 30 minutes during data collection. Data are represented as circles, fits from Rietveld refinements are shown as orange lines, and the difference is shown as a gray line beneath the data. Excluding the high temperature $T = 260$ K data, Rietveld refinements were carried out as joint refinements with corresponding neutron diffraction data shown in Figure 2.6. Refinement statistics are provided in Table 2.1.

and $T = 100$ K, although there are some changes in peak intensity. The two crystallographically resolvable phase transitions manifest primarily in the Q region shown in Figure 2.7. Rather than refining atom positions, lattice deformations were modeled using symmetry-mode refinements. Symmetry modes were based on previous symmetry analysis of lead-bromide perovskites and implemented in ISODISTORT.[27,75] The phase behavior is consistent with previous reports.[72] Mode amplitudes were determined and rigid body models organic cations were located using simulated annealing. Refinement statistics from Rietveld refinements of the data are presented in Table S1.

$CH(NH_2)_2PbBr_3$ remains almost metrically cubic through both phase transitions, as evidenced by the close agreement between the pseudocubic lattice parameters a and c determined from Rietveld refinement (Figure 2.8) at all temperatures. The Goldschmidt

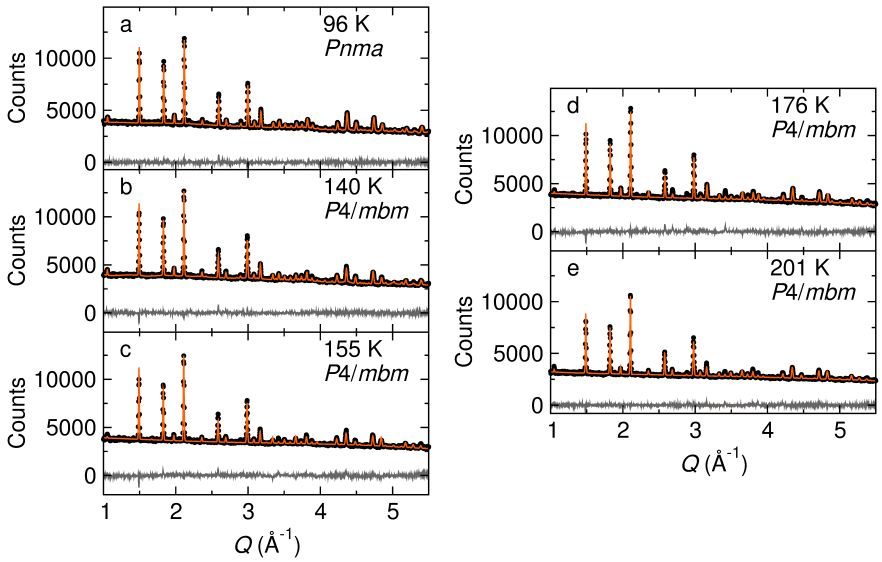

Figure 2.6: High-resolution neutron diffraction patterns collected upon heating from a base temperature of $T = 100$ K. Data are represented as circles, fits from Rietveld refinements are shown as orange lines, and the difference is shown as a gray line beneath the data. Rietveld refinements were carried out as joint refinements with X-ray diffraction data collected within 6 K of the corresponding temperatures shown in Figure 2.5. Refinement statistics are shown in Table 2.1.

Table 2.1: Refinement statistics for joint Rietveld refinements of high resolution XRD and neutron diffraction.

Temperature (K)	Space Group	R_{wp} %
95	$Pnma$	5.890
140	$Pnma$	5.516
160	$P4/mbm$	6.263
175	$P4/mbm$	7.687
200	$P4/mbm$	6.962
260	$Pm\bar{3}m$	9.246

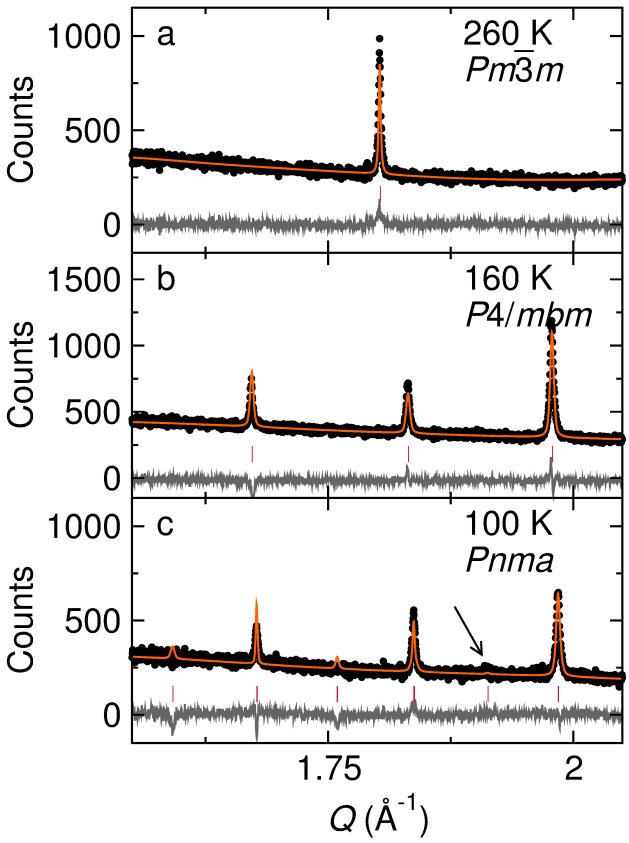

Figure 2.7: Selected Q region showing characteristic Bragg reflections in high-resolution synchrotron X-ray diffraction (SXRD) patterns modeled with the Rietveld method. The arrow indicates a low intensity peak that is not indexed in the $P4/mbm$ space group but is indexed in the $Pnma$ space group to the (113) plane. Data are represented by black circles, fits by orange lines, tick marks as red vertical lines, and the difference curves as gray lines. Refinement statistics can be found in Table 2.1 and full diffraction patterns are shown in Figure 2.5.

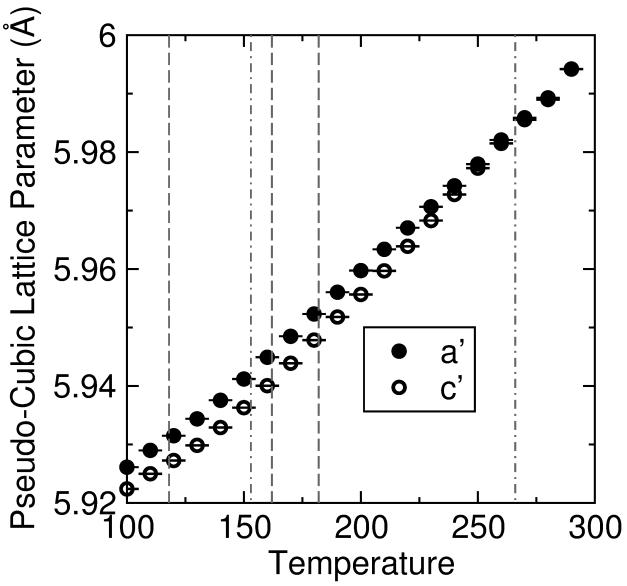

Figure 2.8: Pseudo-cubic lattice parameters extracted from Rietveld refinements of high resolution synchrotron X-ray diffraction. The pseudo-cubic lattice parameter for the a axis is $a' = \sqrt{2a_{tet}}$ or $a' = \sqrt{2a_{orth}}$ and for the c axis is $c' = c_{tet}$ or $c' = c_{orth}/2$. Dashed gray lines indicate crystallographically unresolvable phase transition temperatures and dashed-and-dotted gray lines indicated crystallographically resolvable phase transition temperatures determined from heat capacity and differential scanning calorimetry data.

tolerance factor ($t = 1.008$)[76] suggests that $CH(NH_2)_2PbBr_3$ should in fact remain cubic, with little to no compression of the cuboctahedral void.

Despite the lack of crystallographic features for the three phase transitions at 182 K, 162 K, and 118 K (Figure 2.9), crystal structures obtained by simulated annealing of high-resolution SXRD and NPD data determine the ideal octahedral tilt angle and $CH(NH_2)_2^+$ average position and further demonstrate that the orientation of $CH(NH_2)_2^+$ changes before and after phase transitions. Figure 2.10 shows that at all characterized temperatures, despite the significant positional disorder of $CH(NH_2)_2^+$, the shapes of the nuclear and electronic density are distinct. In the high temperature cubic phase, the overall lattice symmetry dictates the $CH(NH_2)_2^+$ position, which approximates a sphere. After the $T = 260$ K cubic to tetragonal phase transition, the nuclear and electronic density of $CH(NH_2)_2^+$ becomes more anisotropic and consistent with the shape of the deformed A-

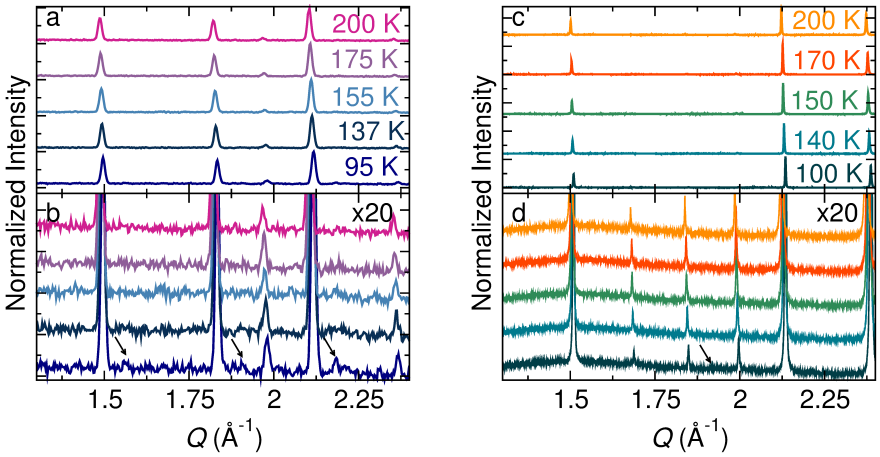

Figure 2.9: Selected Q range of (a, b) neutron diffraction patterns collected as a function of temperature on $CH(NH_2)_2PbBr_3$. (c, d) high-resolution SXRD patterns collected on $CH(NH_2)_2PbBr_3$ as a function of temperature. The arrows in (b) and (d) indicate the low intensity reflections that resolve from the background between $T = 155$ K and $T = 137$ K.

site void. Throughout the $T = 182$ K, 162 K, 153 K, and 118 K phase transitions, the anisotropy of $CH(NH_2)_2^+$ electric and nuclear density exhibits subtle changes. For instance, in the ac plane, the distribution of $CH(NH_2)_2^+$ positions appears ellipsoidal at $T = 200$ K, nearly spherical at $T = 170$ K, and ellipsoidal again at $T = 160$ K. The compression of the cuboctahedral void in the ac plane after the $T = 153$ K tetragonal to orthorhombic phase transition does correlate to a decrease in the anisotropy of $CH(NH_2)_2^+$ positional disorder within the same plane, perhaps indicating organic-inorganic coupling.

The crystallographic resolvability of the low temperature phase transition depends on thermal history. As shown in Figure 2.11, the (113) peak at $Q \approx 1.93$ Å^{-1} appears if diffraction patterns are collected on heating after quenching, but the same peak cannot be resolved if the sample is incrementally cooled from room temperature. The path dependence of the low temperature phase transition resembles the previously observed transition between the cubic α phase and the hexagonal δ phase in $CH(NH_2)_2PbI_3$.[62] In the iodide congener, the path dependence was attributed to a kinetic barrier between the two phases

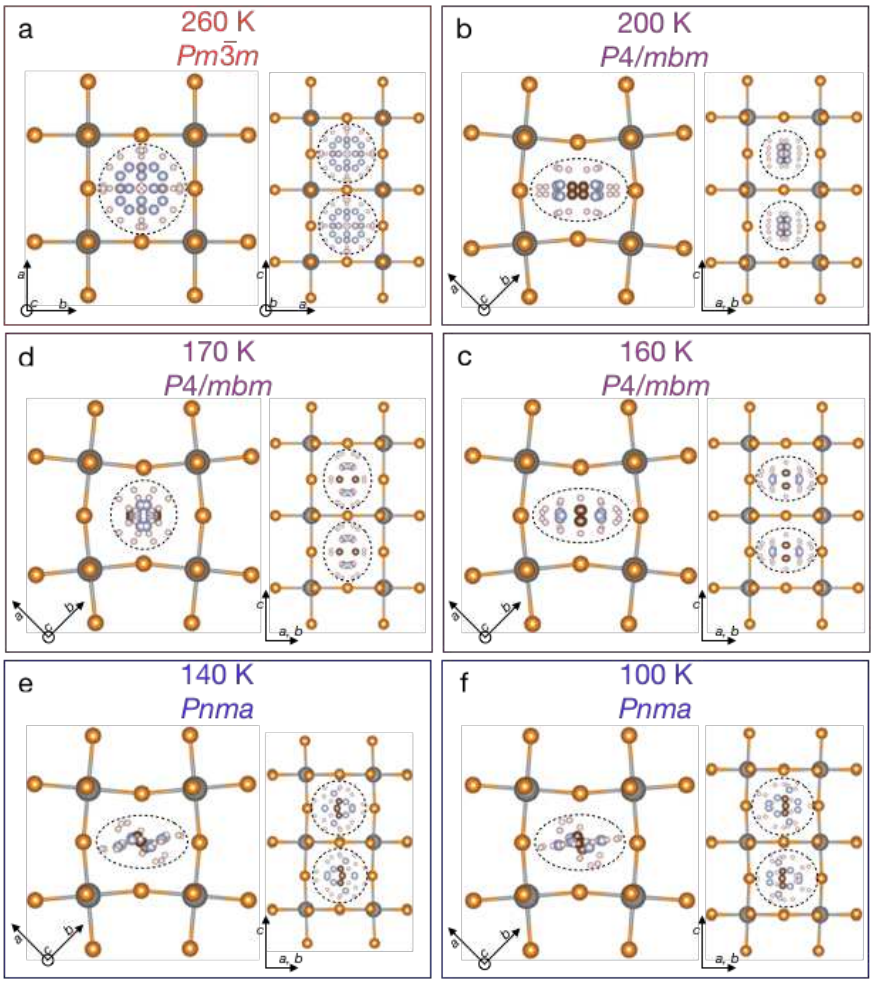

Figure 2.10: Structures generated from simulated annealing of organic cations defined by rigid bodies and of the inorganic framework defined by symmetry-adapted displacement modes. Dashed circles are guides to the eye. The inorganic framework deforms as expected for a halide perovskites as a function of temperature,[77] with in-phase octahedral tilts in the ab plane in the tetragonal $P4/mbm$ phase and additional tilts along the c axis in the orthorhombic $Pnma$ phase. The symmetry of the inorganic framework only changes due to the phase transitions at $T = 260$ K and $T = 153$ K, but the distribution of organic cation positions change before and after all structural phase transitions.

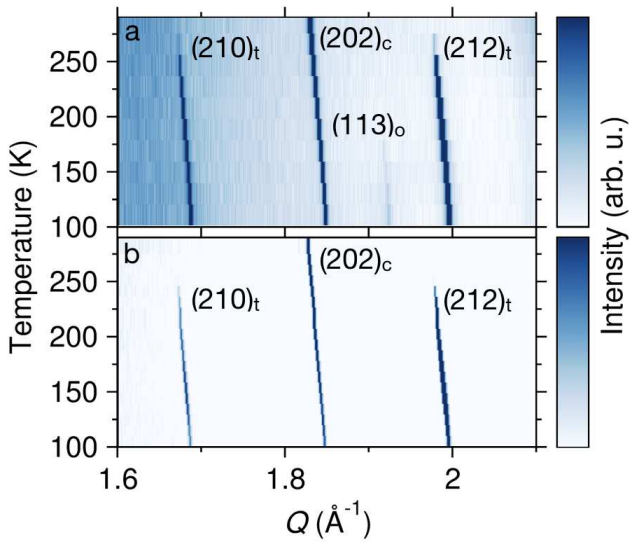

Figure 2.11: False-color representation of a selected region in Q space with temperature-dependent high-resolution synchrotron XRD. Data were collected (a) every 10 K upon heating after quenching from room temperature to $T = 100$ K and (b) upon a slow cool, resting for 30 minutes every 10 K from room temperature to $T = 100$ K. The resolution of the $(210)_t$ and $(212)_t$ peaks from the background indicates the cubic to tetragonal phase transition and the resolution of the $(113)_o$ peak indicates the tetragonal to orthorhombic phase transition.

resulting from the activation energy needed to break and form lead-iodide bonds. As the tetragonal to orthorhombic transition observed here follows a group-subgroup relationship, another phenomenon likely underlies the path dependence.

Neutron scattering confirms the analysis of nuclear and electronic density from neutron and X-ray crystallography. All five phase transitions involve changes in the orientation and dynamics of $CH(NH_2)_2^+$. The mean squared displacements (MSD) of hydrogen determined from temperature-dependent fixed window neutron scattering (Figure 2.4c)[78] show clear discontinuities at all five transitions. Quasielastic neutron scattering (QENS) spectra indicate that all five phase transitions change the relaxation times of $CH(NH_2)_2^+$ reorientations and extent of hydrogen motion (by jump distance or by fraction participating in reorientations), evidenced by changes in peak width in the QENS spectra and the slope of the extracted elastic incoherent structure factors (EISF) (Figures 2.12, 2.13). Therefore, the

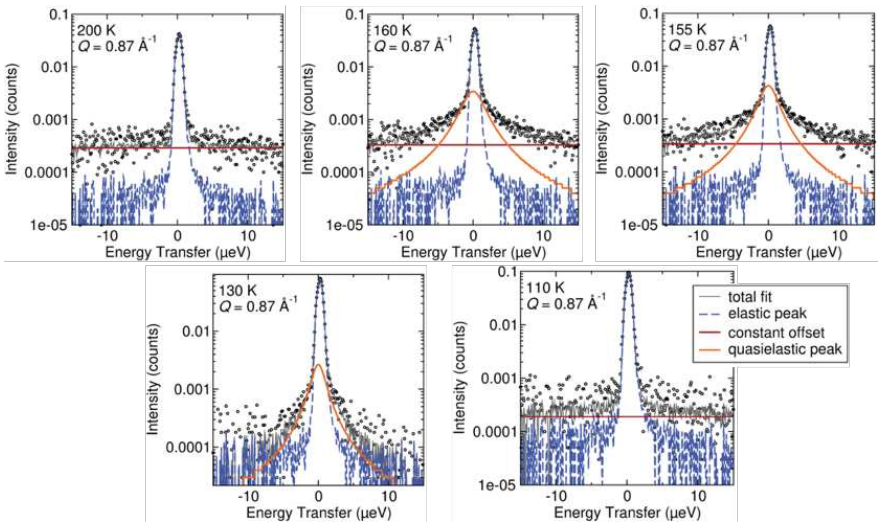

Figure 2.12: Representative quasielastic neutron scattering (QENS) spectra collected above and below phase transition temperatures of $CH(NH_2)_2PbBr_3$. The elastic peak has been modeled as a δ function convolved with the instrument resolution function collected at $T = 20$ K and the quasielastic peak has been modeled as a Lorenztian function. For data collected at $T = 200$ K and $T = 110$ K, visual inspection of the fit with only a background function (a fixed linear offset) and the elastic function suggests no quasielastic component; any dynamics at these temperatures are outside the energy resolution or bandwidth of the spectrometer. The quasielastic component at the other measured temperatures narrows as a temperature decreases, indicative of changes in the molecular dynamics within the energy resolution. Relaxation times are presented for the data with quasielastic components in Table 2.2.

Table 2.2: Residence times calculated from QENS spectra according to the relationship $HWHM = h/(\tau \times 2\pi)$, where $HWHM$ is the half-width-half-maximum of the quasielastic component and τ is the relaxation time.

Temperature (K)	τ (ns)
130	98
155	50
160	43

crystallographically unresolvable phase transitions must relate to cooperative changes in the dynamics of the $CH(NH_2)_2^+$ sublattice.

Neutron scattering data demonstrate that the crystallographically unresolvable phase transitions of $CH(NH_2)_2PbBr_3$ are characterized by changes in the dynamics of $CH(NH_2)_2^+$. As the temperature is reduced, the width of quasielastic neutron scattering (QENS) spectra decreases, for dynamic processes that are within the energy resolution and bandwidth of the spectrometer (Figure 2.12). At $T = 200$ K and $T = 110$ K, the dynamic processes

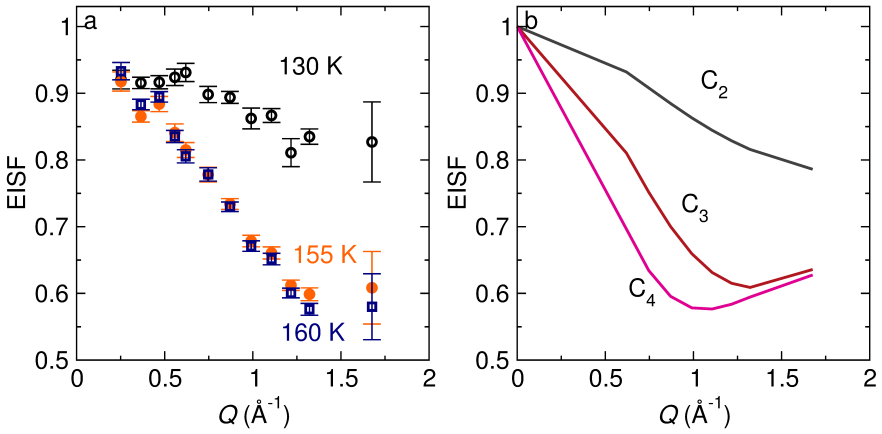

Figure 2.13: (a) Elastic incoherent structure factor (EISF) extracted from models of the QENS spectra at shown in Figure 2.12 at $T = 160$ K, 155 K, and 130 K. Spectra collected at other temperatures exhibited no dynamics within the instrument resolution and so an EISF could not be extracted. The EISF is defined as $I_{elastic}/(I_{elastic} + I_{quasielastic})$, and its slope as a function of Q is indicative of the extent of dynamics within a material. For instance, the smaller slope at $T = 130$ K indicates that the geometry of the motion has changed to encompass a smaller radius in the extent of motion compared to $T = 155$ K. For comparison, models constructed based off of C_2, C_3, and C_4 molecular rotations are shown in (b). Refinements of these models against the data did not yield physically meaningful parameters, suggesting the motion of $CH(NH_2)_2^+$ is complex. Quasielastic neutron scattering measurements were performed on HFBS within a dynamic window of +/- 15 μeV. The resolution function of HFBS at this bandwidth is approximately Gaussian in shape, and it has a full-width at half-maximum of 0.85 μeV.

are outside the bandwidth and energy resolution of the spectrometer, respectively, and no quasielastic component to the QENS spectra is observed (Figure 2.12). These two observations indicate a change in relaxation time of $CH(NH_2)_2^+$ dynamics between each phase transition. Qualitative examination of the elastic incoherent structure factor (EISF) calculated from the QENS spectra as a function of Q also demonstrates changes in $CH(NH_2)_2^+$ dynamics as a function of temperature. The reduced slope of the EISF upon cooling (Figure 2.13a) indicates a smaller fraction of quasielastic events at lower temperatures, which could either be due to a reduction in the percentage of hydrogen atoms participating in molecular reorientations or due to a change in the symmetry and jump distances of the motion. Attempts to fit the data with the models shown in Figure 2.13b did not yield physically meaningful jump distances or fractions of $CH(NH_2)_2^+$ participating, and so de-

convolution of the percentage of $CH(NH_2)_2^+$ and any changes in symmetry remains out of the scope of this work. The motion captured in the QENS spectra is likely quite complex.

In an attempt to determine the processes that underly each phase transition, we calculated the entropy release for each phase transition. The high temperature crystallographically resolvable phase transition does not appear in the heat capacity data, perhaps due to a small entropy release, but can be observed in differential calorimetry data (Figure 2.14). To capture latent heat contributions we conducted long-pulse heat capacity experiments for the remaining four phase transitions; the data are shown in Figure 2.15. To calculate entropy release for each phase transition (at $T = 120$ K, 150 K, 160 K, and 180 K), we calculated a 'background' curve for each lambda anomaly. Background curves (shown in black in Figure 2.15) were calculated by interpolation of the heat capacity on either side of the lambda anomalies, shown in colored circles in Figure 2.15. We attribute the steeply sloped deviations in the background at the beginning and end of each pulse to poor thermal equilibration and radiative thermal losses.[79] The resulting subtracted data are shown in Figure 2.16. Numerical integration of these peaks as c_p/T gave the entropy release values shown in Table 3. We also calculated the corresponding change in degrees of freedom, Ω_f/Ω_i via $\Delta S = Rln(\Omega_f/\Omega_i)$, provided in Table S2. These values do not reflect substantial changes to the degrees of freedom of the system and cannot be used to determine the changes in cation dynamics at the phase transition temperatures.

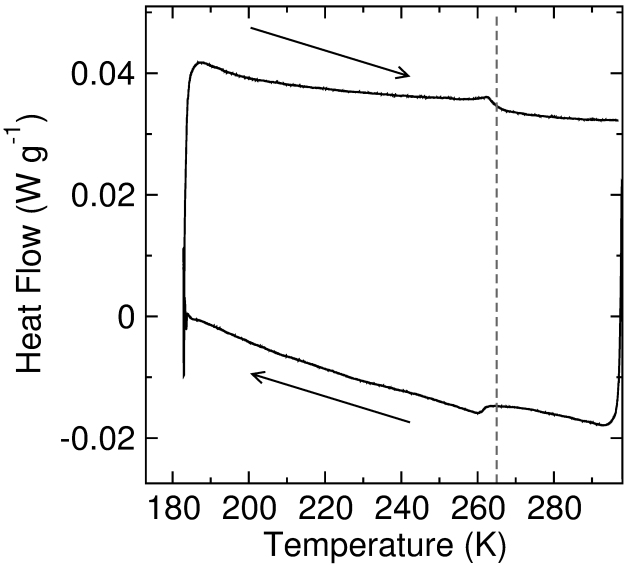

Figure 2.14: Differential scanning calorimetry data of $CH(NH_2)_2PbBr_3$. Arrows indicate the temperature ramp direction. The dashed line is a guide to the eye for the end of the phase transition on heating (T =266 K).

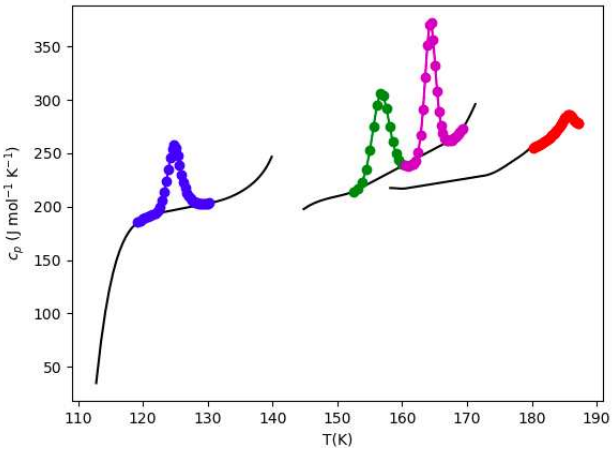

Figure 2.15: Long-pulse heat capacity data for $CH(NH_2)_2PbBr_3$. To calculate entropy release for each phase transition (at T = 120 K, 150 K, 160 K, and 180 K), we calculated a 'background' curve for each lambda anomaly. Background curves (shown in black) were calculated by interpolation of the heat capacity on either side of the lambda anomalies, shown in colored circles.

Table 2.3: Entropy release corresponding to a change in degrees of freedom, according to $\Delta S = Rln(\Omega_f/\Omega_i)$, for each lambda anomaly in Figure 2.16.

T (K)	ΔS (J mol^{-1} K^{-1})	Ω_f/Ω_i
120	1.261	1.16
152	1.679	1.19
164	1.767	1.26
185	0.235	1.03

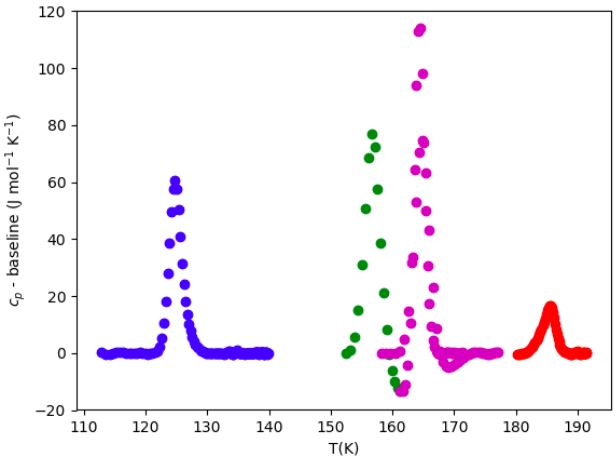

Figure 2.16: Background subtracted heat capacity data for $CH(NH_2)_2PbBr_3$ based on Figure 2.15. Calculated change in entropy values and degrees of freedom are shown in Table S2.

Discussion

Comparison of the MSD and photocurrent data demonstrates that cation dynamics correlate with steady-state optoelectronic properties; this relationship is most obvious around the $T = 182$ K phase transition. At 182 K, the $CH(NH_2)_2^+$ motion changes rapidly, exhibiting an abrupt increase in slope, and the photoconductivity excitonic peak center transitions from red-shifting (> 180 K) to blue-shifting (< 180 K) on cooling. Hybrid perovskites typically exhibit red-shifts on cooling followed by an abrupt blue-shift during structural phase transitions related to octahedral tilt patterns (further discussion in the SI), although the red-shifting on cooling typically resumes after the phase transition.[67,68,70,80,81] As crystal-

lography shows that, on average, the octahedral tilt pattern remains unchanged through the phase transition at $T = 182$ K, $CH(NH_2)_2^+$ dynamics must influence the optoelectronic response. Considering the entire temperature range, $CH(NH_2)_2^+$ dynamics have the greatest impact on the excitonic peak. At high temperature, cation reorientations have a strong influence on the intensity of the excitonic peak and once cation dynamics begin to freeze near $T = 180$ K the intensity of the excitonic peak decreases while the interband photoconductivity continues to increase on cooling, likely due to reduced electron-phonon scattering. These trends further corroborate observations from transient spectroscopy that the cation reorientations stabilize the nascent charge separation state.[48,53] In the data shown here, the suppression of the exciton-derived photocurrent as the organic cations experience hindered motion demonstrates similar phenomena in the steady-state -that is, the transient phenomena manifests in macroscopic, steady-state transport.

The observation of the entropy-releasing phase transitions at 182 K, 162 K, and 118 K in the elastic intensities from QENS measurements, but not in the crystallography, imposes a size restraint on correlation lengths, indicating that these phase transitions order into small (e.g., nanoscale) and potentially dynamic domains. The formation of small domains also explains the low entropy release associated with each phase transition (Table S2), as a significant fraction of the material will remain in disordered domain walls. Imaging of these domains poses a interesting technical challenge, given their size and dynamics, that would shed light onto these conclusions.

The inference of domain behavior here suggests incipient ferroelasticity in the phase transitions of $CH(NH_2)_2PbBr_3$, which aligns with a previous description of an incipient fer-

roelastic transition near the anti-ferrodistortive cubic-tetragonal phase transition in $CH(NH_2)_2PbBr_3$.[82] Such ferroelastic domains have previously been invoked as an alternative explanation to the claims of formation of ferroelectric domains in $CH_3NH_3PbI_3$.[83–85] In a ferroelastic phase transition, the lattice responds to a spontaneous strain by undergoing a reversible phase transition within discrete domains. Discontinuities in the thermal expansion of $CH(NH_2)_2PbBr_3$[71] show the manifestation of spontaneous strain at the phase transition temperatures, which could arise from an incompatibility between the planar shape and large quadrupolar moment of $CH(NH_2)_2^+$ with the A-site void. If one considers only the organic sublattice, the lowest energy local configuration between two neighboring molecules is a "Tee" shape, in which adjacent $CH(NH_2)_2^+$ cations would orient themselves perpendicular to their neighbors.[86] However, as depicted in Figure 2.17 for an organic sub-lattice in a cubic hybrid perovskite, no long range ordered configuration on any Bravais lattice can satisfy this interaction completely. We hypothesize that the formation of ferroelastic domains transition relieves strain from $CH(NH_2)_2^+$ quadrupolar frustration.

In $CH(NH_2)_2PbBr_3$, the orientational dynamics of the organic cations influence steady-state electronic excitation and transport. While organic cation dynamics are known to affect the transient electronic properties, this work demonstrates a similar effect on steady-state properties and implies a larger influence of the organic cation than previously thought. As the frontier energy states of hybrid perovskites are composed of metal and halide electronic states, the relationship between $CH(NH_2)_2^+$ dynamics and optoelectronic properties is likely indirect. The organic orientations can couple to the inorganic framework through quadrupolar interactions, hydrogen bonding, or geometric strain, perhaps resulting in lo-

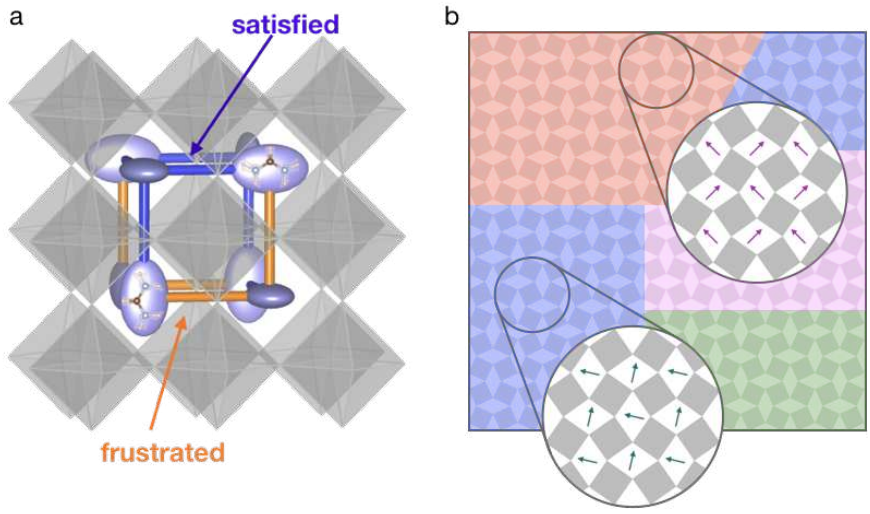

Figure 2.17: (a) Schematic depiction of quadrupolar geometric frustration in the organic sub-lattice in a cubic hybrid perovskite and (b) release of local strain through domain formation. Arrows represent the orientation of the elastic dipole moment of the formamidinium cation, which orients locally 90° from neighboring molecules. Molecules in different domains do not necessarily orient 90° from each other and may not be statically ordered.

cal distortions that contribute to the observed changes in electronic behavior. The presence of local distortions is consistent with the observation of transient polaron formation in ultrafast spectroscopies.[48,53,87] Cation dynamics and related local distortions primarily affect the center and maximum photocurrent of the excitonic peak.

Through these pathways, we propose that orientational strain from the quadrupole moment of $CH(NH_2)_2^+$ provides an origin for incipient ferroelastic behavior that results in nanoscale domains; these collectively correlate to changes in the intensity and energy of the photocurrent. This work suggests that organic cation dynamics and domain behavior are critical for the optoelectronic properties of hybrid perovskites. Furthermore, we suggest that geometric strain arising from the organic sublattice underlies the complex phase behavior and thus the optoelectronic properties of formamidinium perovskites.

Experimental Methods

Certain commercial equipment, instruments, or materials are identified in this document. Such identification does not imply recommendation or endorsement by the National Institute of Standards and Technology nor does it imply that the products identified are necessarily the best available for the purpose.

Sample preparation: $CH(NH_2)_2CH_3COO$ and HBr were obtained from Sigma Aldrich Corporation, $PbBr_2$ and other solvents were obtained from VWR and used without further purification. In a typical preparation of $CH(NH_2)_2PbBr_3$, approximately 0.4 g of $CH(NH_2)_2CH_3COO$ were dissolved in 8 mL of hydrobromic acid (47% v/v) at 80 °C for 15 min. 1.1 g of $PbBr_2$ (1.25:1.0 mole ratio $CH(NH_2)_2CH_3COO$:$PbBr_2$) were added and the solution stirred until all powder had dissolved. $CH(NH_2)_2PbBr_3$ was precipitated using ethanol as an antisolvent and the powder was washed with ethanol.

Single crystals were grown using an anti-solvent method.[88] A small vial containing 0.5 mL of a filtered 1 M solution of $CH(NH_2)_2PbBr_3$ in a 1:1 mixture of dimethylformamide and γ-butyrolactone by volume was placed in a sealed, larger vial containing approximately 5 mL of ethanol. Crystal growth reactions were carried out over three days.

Diffraction: Laboratory powder X-ray diffraction (PXRD) data were collected on a Bruker D8 Discover X-ray diffractometer using a CuK_α radiation source and a Lynxeye XE-T position-sensitive detector to determine phase purity. High-resolution synchrotron powder X-ray diffraction (SXRD) patterns were collected on the diffractometer 11-BM-B at the Advanced Photon Source, Argonne National Laboratory ($\lambda \approx 0.41$ Å) between

$T = 300$ K and $T = 100$ K in intervals of either 10 K or 20 K.[89] Powders were sealed in Kapton® capillaries in ambient atmosphere. Neutron powder diffraction data were collected on a non-deuterated sample with the instrument BT-1 at the NIST Center for Neutron Research, National Institute of Standards and Technology at $T = 95$ K, 140 K, 155 K, 175 K and and 205 K. Powdered samples were loaded into vanadium canisters under helium atmosphere. Data were collected at λ = 2.078 Å, using the Ge311 monochromator with a 60' collimator after the sample.

Data were modeled with the Rietveld method implemented in TOPAS v6. For all refinements, the organics were located through simulated annealing of rigid bodies after initial refinement of parameters related to the background, inorganic framework, and peak profile. We performed joint refinements of neutron and X-ray diffraction for data collected at (+/- 5 K) $T = 200$ K, 175 K, 160 K, 140 K, and 100 K. For the lower symmetry structures, rather than refine atomic positions of the lead-bromide framework, we preformed symmetry mode refinements. To obtain the symmetry adapted modes, the higher symmetry space group was distorted to the lower symmetry space group using ISODISTORT ($Pm\bar{3}m$ to $P4/mbm$ along the M_3^+ representation, $P4/mbm$ to $Pnma$ along the Z_5^+ representation).[17,75] Final values for the mode amplitudes were determined through simulated annealing.

Heat Capacity: Initial heat capacity measurements were performed on single-crystal samples using the quasi-adiabatic heat-pulse technique implemented in the Quantum Design, Inc. PPMS at $T = 2$ - 298 K, equilibrating for four time constants with a 2% temperature rise. To validate the heat pulse measurements, heat capacity measurements were

performed using large heat pulses analyzed using the dual-slope method. Pulse starting temperatures were chosen to best capture the peaks found in the dual time constant quasi-adiabatic heat-pulse experiments and each heat pulse spanned a 30% heat rise. Data were reduced in the Quantum Design software.

Differential Scanning Calorimetry: Data were collected on TA Modulated DSC 2500 with an temperature ramp rate of 20 °C.

Quasielastic Neutron Scattering (QENS): Fixed window elastic scattering and quasielastic spectroscopy experiments were performed on the high flux backscattering spectrometer (HFBS) at the NIST Center for Neutron Research on non-deuterated samples of $CH(NH_2)_2PbBr_3$.[78] The sample environment employed in this experiment is a closed-cycle refrigerator that cools/warms the sample by helium exchange gas. A mass of 3.27 g of $CH(NH_2)_2PbBr_3$ powder was used for this experiment. The cylindrical sample cell has a diameter of approximately 3 cm, and the powder sample was held against the lateral area of the sample can by enclosing it within aluminum foil pouches. The sample cell was loaded within a helium glove box and sealed with an indium o-ring. The enclosed helium ensures good thermal contact between the powder and the rest of the sample environment.

Fixed window scans were performed according to the following protocol. Initially, the sample was quenched by placing it within the well of the closed cycle refrigerator when it was at 60 K. The sample temperature dropped rapidly to approximately 200 K and subsequently took 90 min to reach 6 K. Data was continuously collected upon warming at 0.8 K/min with 60 sec/point. Finally, data was collected upon cooling at the same nominal ramp rate and time per point.

A fixed window scan is a measurement of the elastic intensity $I_{el}(Q,T)$ as a function of Q and temperature. The effective mean-squared displacement of the hydrogen atoms is estimated by assuming that $I_{el}(Q,T)$ is governed by a Debye-Waller factor: $I_{el}(Q,T) = I_{el}(Q,T = 6.0 \text{ K}) \times \exp(-Q^2\langle u^2\rangle/3)$. This calculation was performed using the DAVE software.[90]

Quasi-elastic neutron scattering measurements were performed at $T = 200$ K, 160 K, 155 K, 130 K, and 110 K on cooling. The dynamic structure factor $S(Q,E)$ was determined within an energy range of +/- 15 μeV. The scattering intensity was normalized to both the incident beam monitor and a vanadium standard. This places the measured scattering at all Q upon a common arbitrary intensity scale. The constant instrumental background was subtracted from the scattering. QENS data were reduced and analyzed in DAVE.[90]

Photoconductivity: Photoconductivity data were collected on single crystals of $CH(NH_2)_2PbBr_3$ using a home-built instrument based on prior literature.[91] As the sample is cubic, and remains nearly metrically cubic as a function of temperature *vide infra* choice of the crystal facet was not considered. In short, monochromatic light supplied by a 75 W Xe arc lamp chopped at 82 Hz was fiber guided onto a single crystal with Pt leads fixed onto parallel, opposing facets using colloidal silver paste. A DC voltage of 1 V was applied across the sample using a Keithley source meter (2401) and the photocurrent was detected through lock-in amplification (Stanford Instruments SR5830). Five percent of the incident light is fed into a Si photodiode (Thor Labs PM100) and is used to normalized the observed photoconductivity to account for spectral features of the lamp. Temperature dependent data were collected using the Quantum Design, Inc. PPMS with a fiber optic-guided into

the multi-function probe. Parameters, such as peak centers, full-width-half-maximum, and intensities, were determined by modeling the data as Gaussian functions convolved with a step function.

3. Cesium Substitution Disrupts Concerted Cation Dynamics in Formamidinium Hybrid Perovskites[†]

Summary

Although initial studies on hybrid perovskites for photovoltaic applications focused on simple compositions, the most technologically relevant perovskites are heavily substituted. The influence of chemical substitution on the general phase behavior and specific physical properties remains ambiguous. The hybrid perovskite formamidinium lead bromide, $CH(NH_2)_2PbBr_3$, exhibits complex phase behavior manifesting in a series of crystallographically-unresolvable phase transitions. Here, we characterize the molecular and lattice dynamics of $CH(NH_2)_2PbBr_3$ as a function of temperature, and their evolution upon chemical substitution of $CH(NH_2)_2^+$ for cesium (Cs^+) with crystallography, neutron scattering, ^1H and ^{14}N nuclear magnetic resonance spectroscopy, and ^{79}Br nuclear quadrupolar spectroscopy. Cs^+ substitution suppresses the four low-temperature phase

[†]Reproduced with permission from Mozur E. M., Hope M. A., Trowbridge J. C., Halat, D. M., Daemen L. D., Maughan A. E., Prisk T. R., Grey C. P., Neilson J. R. Cesium Substitution Relieves Geometric Frustration in Formamidinium Hybrid Perovskites. *Chem Mater.* **2020** *accepted*. Copyright 2020 American Chemical Society.
Author Contributions: Eve Mozur collected and analyzed the X-ray diffraction data and prepared the manuscript. Michael Hope collected and analyzed the NMR and NQR data and prepared the manuscript. Julia Trowbridge prepared the samples. David Halat collected and analyzed the NMR and NQR data. Luke Daemen collected and reduced the INS data and performed the phonon calculations. Timothy Prisk collected and analyzed the neutron scattering data. Annalise Maughan collected the X-ray diffraction data. Clare Grey oversaw the NMR experiments. James Neilson. edited the manuscript and oversaw the project.

transitions of $CH(NH_2)_2PbBr_3$, which propagate through concerted changes in the dynamic degrees of freedom of the organic sub-lattice and local or long-range distortions of the octahedral framework. We propose that cesium substitution suppress the phase transitions through the relief of geometric frustration associated with the orientations of $CH(NH_2)_2{}^+$ molecules, which retain their local dynamical degrees of freedom.

Introduction

Hybrid halide perovskites tend to be more compositionally complex than compound inorganic semiconductors, especially as most hybrid perovskites in devices are highly substituted. For example, the unsubstituted hybrid perovskites $CH_3NH_3PbX_3$ and $CH(NH_2)_2PbX_3$ (X = I, Br, Cl), are not stable under ambient conditions, which has been attributed to their positive enthalpies of formation.[9,92] Recent calculations suggest that A-site mixing can decrease the Gibbs free energy of a given hybrid perovskite,[93] which aligns with studies showing that chemical substitution at the A and X sites prevents decomposition to the binaries or competing non-perovskite phases.[7,94–96] While unsubstituted $CH_3NH_3PbI_3$ decomposes into the binaries in 20 hours under 85% relative humidity, partial substitution of $CH_3NH_3{}^+$ with $CH(NH_2)_2{}^+$ prevents decomposition under the same conditions.[97] The highly-substituted hybrid perovskite $(CH(NH_2)_2)_{0.79}(CH_3NH_3)_{0.16}Cs_{0.05}Pb\text{-}(I_{0.83}Br_{0.17})_{2.97}$ maintains the perovskite structure after >250 hours under operating conditions, and similar substituted perovskites remain stable in devices for >1,000 hours.[7,98] These studies further demonstrate that chemical substitution preserves the advantageous optoelectronic properties of hybrid perovskites, while also allowing tunability of parameters like the band

gap and phase stability.[13] Chemical substitution is a powerful tool to improve the phase stability of hybrid perovskites, but the fundamental chemistry and physics describing how the substitution prevents decomposition remains underexplored.

Recent studies show that substitution at either the halide or *A*-site leads to inhibition of organic cation reorientations. Comparison of two-dimensional infrared spectroscopy data of the unsubstituted perovskites $CH_3NH_3PbX_3$ (X = I, Br, Cl) with mixed halide perovskites demonstrated that the organic cations become partially immobilized upon halide substitution.[99] Furthermore, our previous characterization of the series $(CH_3NH_3)_xCs_xPbBr3_3$ elucidated similar trends in *A*-site substituted methylammonium perovskites.[100] In both cases, the breaking of local symmetry was implicated in reducing the organic dynamic degrees of freedom relative to the unsubstituted materials. *A*-site substituted materials also have higher activation energies for halide migration, which suggests a possible relationship between decomposition from ion migration and the organic cation dynamics.[101]

Organic cation dynamics are known to be linked to device performance and behavior, as they affect the optoelectronic properties of hybrid perovskites.[102] Computational studies suggest that the orientation of the organic cation influences the character of the band edges through organic-inorganic coupling.[45,103] The liquid-like reorientations of these cations also affect the electronic excited state lifetimes of hot carriers; charge carriers excited far above the band gap relax more slowly in the hybrid perovskites $CH(NH_2)_2PbBr_3$ and $CH_3NH_3PbBr_3$ than in their inorganic counterpart $CsPbBr_3$, and cation reorientations are thought to stabilize nascent polarons.[47,104] The presence of a dynamic organic cation changes the relationship between the carrier density and the hot carrier cooling rates,

which was attributed to changes in the phonon density between hybrid and fully organic perovskites.[105] The reorientations of the organic cation are also likely to participate in dynamic, local symmetry breaking that increases the electronic excited state lifetimes through Rashba splitting of the frontier energy states.[106,107] Rashba splitting may be enhanced in substituted perovskites.[108]

These links between phase stability, cation dynamics, and optoelectronic properties align with studies showing that the reorientations of the organic cations inform the structure and phase behavior of hybrid perovskites. In methylammonium perovskites, reductions in the dynamic degrees of freedom of methylammonium occur concurrently with decreases in symmetry within the octahedral framework.[35,109] In formamidinium perovskites, the organic-inorganic coupling manifests through more incremental, complex pathways.[110,111] The reorientation of formamidinium in formamidinium lead iodide ($CH(NH_2)_2PbI_3$) participates in the path-dependent phase transitions, for which the cooling rate determines whether the lattice remains in the cubic perovskite phase down to T = 8.2 K, decomposes to a non-perovskite phase, or undergoes a reentrant phase transition.[112,113] The bromide analogue also undergoes complex structural changes, manifesting through five calorimetrically-observed phase transitions.[114,115]

We have previously described the contributions of the organic sub-lattice to the phase transitions of $CH(NH_2)_2PbBr_3$.[115] $CH(NH_2)_2PbBr_3$ undergoes two crystallographic phase transitions upon cooling from room temperature. At T = 265 K, the lattice transitions from the high-temperature cubic phase to a tetragonal phase characterized by in-phase octahedral rotations perpendicular to the c axis. Upon cooling to T = 153 K, the tetrag-

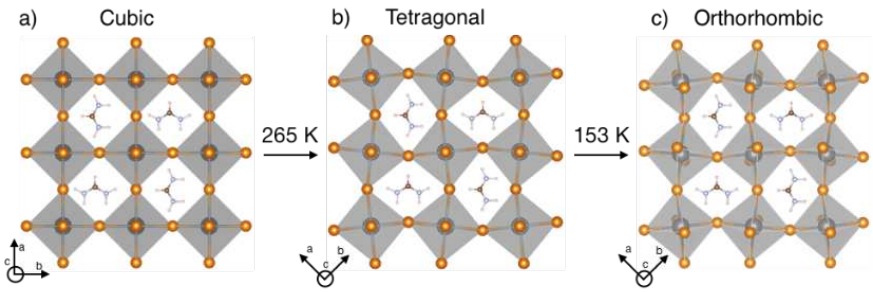

Figure 3.1: Octahedral tilt patterns of formamidinium lead bromide ($CH(NH_2)_2PbBr_3$) in (a) the high-temperature cubic phase (Glazer tilt: $a^0a^0a^0$), (b) the tetragonal phase (Glazer tilt: $a^0a^0c^+$), and (c) the low-temperature orthorhombic phase (Glazer tilt: $a^-b^-c^-$). Lead resides at the center of each octahedron, coordinated by six bromide ions. Formamidinium cations, which are shown in idealized positions, reside in the *A*-site void between octahedra. Transition temperatures are written above the arrows.

onal phase transitions to a low-temperature orthorhombic phase characterized by additional octahedral titling along the *c* axis (Figure 3.1).[115,116] The dynamic degrees of freedom of $CH(NH)_2^+$ change at both crystallographic phase transitions.[115] Three additional phase transitions have been observed through dilatomatry[114] and heat capacity measurements,[115] which neutron scattering data show are also related to the dynamic degrees of freedom of $CH(NH)_2^+$.[115] Furthermore, all five transitions influence the electronic transport under steady-state light illumination.[115] Therefore, $CH(NH_2)_2PbBr_3$ provides an excellent case study to probe how chemical substitution modifies the organic sub-lattice and how organic cation dynamics inform the overall structure.

Nuclear magnetic resonance (NMR), nuclear quadrupole resonance (NQR), and neutron scattering spectroscopies are ideal probes to investigate the relationships between organic cation dynamics, phase transitions, and chemical substitution, as they are element-sensitive probes of local structure and dynamics.[8,117–119] Specifically in NMR, the spin-lattice relaxation constant (T_1), which measures the return of nuclear magnetization to equilibrium following a perturbation, is sensitive to motion on a similar timescale to the

nuclear Larmor frequency and depends on both the correlation time of the motion and its nature.Nuclear resonance studies also enable elucidation of the nuclear quadrupolar coupling tensor, characterized by a magnitude C_Q and an asymmetry η_Q , which measures the coupling between the nuclear quadrupole moment and any electric field gradient present at the nucleus. Therefore, the nuclear quadrupolar coupling tensor is extremely sensitive to the symmetry of the nuclear environment (or the motionally averaged environment). The nuclear quadrupolar coupling tensor can be determined from the NMR spectrum in the case of small C_Q constants (e.g., ^{2}H and ^{14}N) or from the NQR spectrum for large C_Q constants (e.g., $^{79/81}$Br and ^{127}I),[120–125] although even nuclei with large C_Q constants are also becoming accessible by NMR in some cases, with sufficiently high-field magnets.[126,127] Neutron scattering is a complementary technique to characterize dynamics of the organic sub-lattice, as neutrons interact strongly with hydrogen. Furthermore, the tunable energies of incident neutrons allow access to low-energy modes that are difficult to probe with optical spectroscopies. Neutron scattering has previously been used to characterize the reorientation rate and nature of the organic cation dynamics in hybrid perovskites, as well as organic-inorganic coupling.[100,128–130]

In the present work, we have incrementally substituted cesium for formamidinium in formamidinium lead bromide to prepare the series $(CH(NH_2)_2)_{1-x}Cs_xPbBr3_3$ to elucidate the influence of chemical substitution on the temperature-dependent structure and dynamics. We confirm that in unsubstituted $CH(NH_2)_2PbBr_3$, cation dynamics participate in the previously observed crystallographically unresolvable phase transitions[114,115] and nuclear resonance spectroscopies show that these dynamics correlate with local distor-

tions in the octahedral framework at low temperatures. Cesium substitution suppresses these phase transitions, while preserving the short-range organic-organic interactions. We propose that chemical substitution disrupts the long-range order of the organic-organic interactions by introducing compressive microstrain, thus removing the driving force for the low-temperature phase transitions.

Results

Cation dynamics of $CH(NH_2)_2PbBr_3$

In $CH(NH_2)_2PbBr_3$, neutron scattering and nuclear magnetic resonance spectroscopy (NMR) demonstrate that overall $CH(NH_2)_2^+$ dynamics become inhibited and slow upon cooling (Figure 3.2). Mean squared displacement (MSD) values from fixed window elastic neutron scattering data decrease as a function of temperature (Figure 3.2a), indicating inhibited motions of the hydrogen atoms, and thus the organic cations, as the sample is cooled. Figure 3.2b shows the ^{1}H spin-lattice relaxation constant (T_1) as a function of temperature. Assuming idealized reorientations according to Bloembergen-Purcell-Pound (BPP) theory,[131] the T_1 relates to the correlation time of motion through the spectral density as:

$$\frac{1}{T_1} = A(J(\omega_0) + 4J(2\omega_0))) \tag{3.1}$$

$$(J(\omega) = \frac{\tau_c}{1 + \omega^2\tau_c^2}) \tag{3.2}$$

where $J(\omega)$ is the spectral density, ω_0 is the Larmor frequency, τ_c is the correlation time of the motion, and the pre-factor *A* is given by the magnitude of the oscillations in the local field and depends on the nature of the motion. The Lorentzian form of the spectral density predicted by BPP theory explains the overall trends in the data: rom room temperature, the T_1 decreases with decreasing temperature since the cation rotation is in the fast-motion regime ($\omega_0\tau_c \ll 1$ and $T_1 \propto 1/\tau_c$,). This trend continues until at $\sim$ 150 K the T_1 exhibits a minimum as the motion rate approaches the Larmor frequency ($\tau_c \sim 1$ ns). Below $\sim$ 150 K the T_1 then increases with decreasing temperature since the rotation is in the slow-motion regime ($\omega_0\tau_c \gg 1$ and $T_1 \propto \tau_c$).

Overlaid on these general trends, anomalies in the MSD and ^{1}H T_1 data at T = 265 K, 182 K, 162 K, 153 K and T = 118 K correlate with previously reported thermodynamic phase transitions.[114–116] At T = 265 K, $CH(NH_2)_2PbBr_3$ transitions from the cubic perovskite phase to a tetragonal perovskite phase,[114,116] which appears as an anomaly in the MSD data in Figure 3.2b, and as a dip in the ^{1}H T_1. This dip is ascribed to a convolution of the discontinuity caused by a first order transition[132] with magic angle spinning (MAS) induced temperature gradients. The MSD and ^{1}H T_1 exhibit similar features at the T = 153 K tetragonal to orthorhombic phase transition. This transition also exhibits hysteresis that is indicative of a sluggish first order phase transition. While they do not manifest crystallographically, the three additional phase transitions display anomalies in the MSD, indicating that they relate to the dynamic degrees of freedom of $CH(NH_2)_2{}^+$. The kink in the ^{1}H T_1 at the T = 182 K phase transition suggests second order character.[132] Any features associated with the T = 162 K and 118 K phase transitions in the ^{1}H T_1 are too subtle to resolve. The

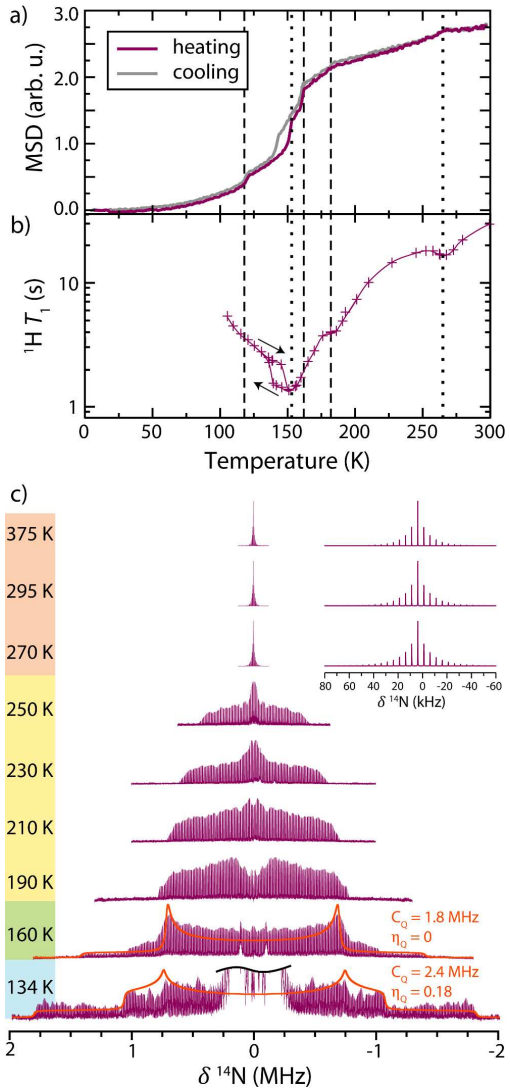

Figure 3.2: (a) Mean squared displacement (MSD) from fixed window elastic neutron scattering spectra for $CH(NH_2)_2PbBr_3$. (b) ^{1}H NMR T_1 values as a function of temperature for $CH(NH_2)_2PbBr_3$, recorded at 12.5 kHz MAS and 14.1 T (T ¡ 200 K) or 16.4 T (T ¿ 200 K); the largest measured spread of sample temperatures for these measurements was 6 K at 200 K. In (a) and (b) dotted lines indicate known crystallographic transitions and dashed lines indicate crystallographically-unresolvable phase transitions. Measurement errors are smaller than the symbols. (c) ^{14}N NMR spectra of $CH(NH_2)_2PbBr_3$, collected as a function of temperature. Colors on the temperature scale indicate phase transitions.[114,115] Spectra at T = 270 K and above were recorded at 5 kHz MAS using a Hahn echo pulse sequence, while those at and below 250 K were recorded under static conditions using a WURST CPMG pulse sequence with VOCS acquisition. The truncated signals in the T = 134 K spectrum are due to probe ringing; this was removed from the other WURST CPMG spectra by not recording the first two echoes. However, the short spin-spin relaxation (T_2) constant made similar modifications impossible for the 134 K spectrum due to insufficient signal-to-noise if the first two echoes were removed.

^{1}H T_1 and neutron MSD data demonstrate that the phase transitions of $CH(NH_2)_2PbBr_3$ correlate to modulation of the dynamic degrees of freedom of $CH(NH_2)_2^+$.

Further details about the changes to $CH(NH_2)_2^+$ dynamic degrees of freedom are evident in the nuclear quadrupolar coupling observed in the ^{14}N NMR spectra. In the absence of any rotation, the calculated C_Q of a formamidinium ^{14}N is 2.8 MHz (further details in Methods). In the high-temperature cubic phase, the ^{14}N NMR spectra exhibit nearly isotropic tumbling, with a spectral width corresponding to effective C_Q constants less than 50 kHz. The lack of a single $I = 1$ nuclear quadrupolar line-shape indicates a distribution of cation motions with different anisotropies. This line-shape is conserved at higher temperatures, signifying that the nature of the motion remains unchanged, despite the changes in reorientation rate apparent in the ^{1}H T_1. Upon cooling, the cubic to tetragonal phase transition at $T = 265$ K results in a greater anisotropy of tumbling and C_Q constants are observed of up to $\sim$ 600 kHz, with increasing anisotropy as the temperature decreases. The lack of a single nuclear quadrupolar line-shape still indicates a distribution of motions. In contrast, below the crystallographically-unresolvable $T = 182$ K phase transition, a subset of signals can be distinguished with a well-defined nuclear quadrupolar line-shape (C_Q = 1.8 MHz, $\eta_Q = 0$), in addition to a signal with a distribution of C_Q constants, akin to the higher temperature spectra. Therefore, by this temperature, a component of the reorientational dynamics has been frozen out for a population of $CH(NH_2)_2^+$. The ^{14}N NMR spectrum collected at $T = 134$ K, below the tetragonal to orthorhombic phase transition and above the $T = 118$ K phase transition is characterized by only one nuclear quadrupolar tensor, indicating that all the cations are now undergoing the same type of motion.

The increase in the C_Q to 2.4 MHz with $\eta_Q = 0.18$, close to the calculated values for static formamidinium, indicates that overall reorientations have been frozen out, leaving only libration. Constricted or slow molecular motions are consistent with the quasielastic neutron scattering spectra; between $T = 130$ K and 110 K any organic cation reorientations or librations become slower than the resolution of the instrument ($\pm$ 1 μ eV, or a residence time $\gtrsim$ 4 ns; Figure 3.3), consistent with observations of the ^{1}H T_1 (Figure refFig2b).

Bromine nuclear quadrupolar resonance (NQR) spectra (Figure 3.4a) suggest that the organic dynamic degrees of freedom couple to local distortions of the octahedral framework during the crystallographically-unresolvable phase transitions of $CH(NH_2)_2PbBr_3$. Previous total scattering measurements of methylammonium lead bromide have suggested that the orthorhombic distortion is still present in the higher symmetry phases, but is dynamically or configurationally averaged.[133] However, the single resonance observed at temperatures above the cubic to tetragonal phase transition indicates that all bromine environments are equivalent; therefore, any dynamic distortion is faster than the resultant separation of the NQR signals (at least 100 kHz). The general trend of decreasing quadrupolar frequency (ν_Q given by $C_Q/2$ in axial environments) on cooling occurs because the anisotropy of the bromine environment is reduced by lattice contraction. At the cubic to tetragonal phase transition at $T = 265$ K, the NQR signal splits into two distinct bromine environments, consistent with the reduction in crystallographic symmetry. Above the $T = 182$ K crystallographically-unresolvable phase transition, the ratio of ν_Q for the two signals depends linearly on the magnitude of the crystallographic tetragonal compression, quantified as the ratio of the lattice parameters $\sqrt{2}\ c_{tet}\ /\ a_{tet}$ (Figure 3.4b). We note

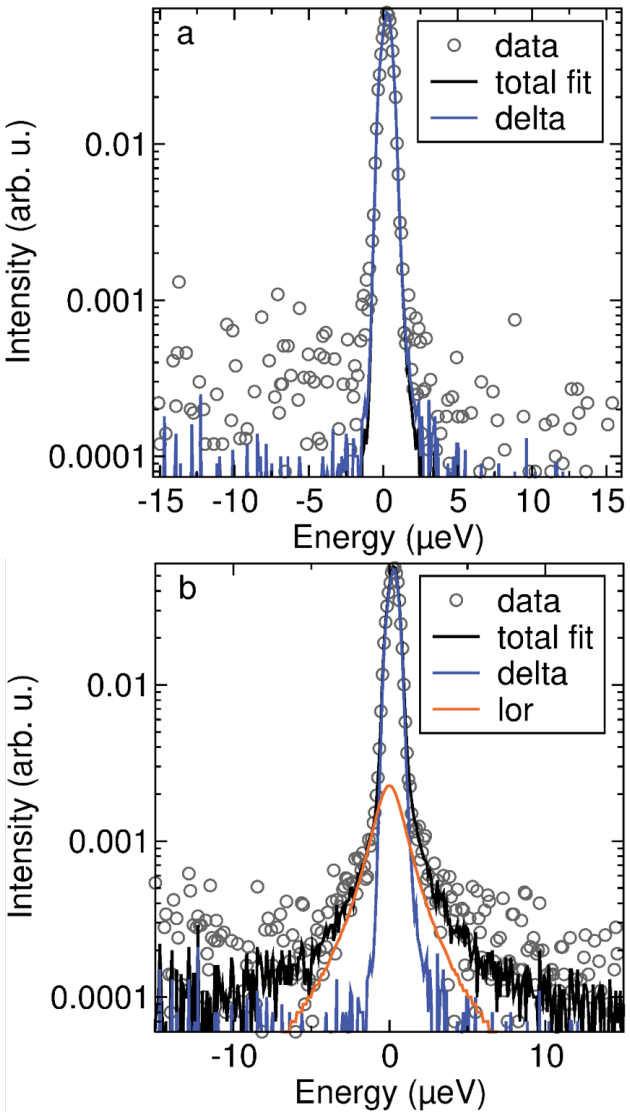

Figure 3.3: Quasielastic neutron scattering spectra collected at (a) 110 K and (b) 130 K. At 110 K, only a resolution-limited, elastic signal is observed. This implies the motion of hydrogen atoms occurs on time-scales that are too long to fall into the experimental time window of HFBS (approximately 100 ps to 5 ns). At 130 K, quasi-elastic broadening is observed. In (b), the intrinsic Lorentzian lineshape is shown as a solid orange curve. When fitting the scattering, we have folded the model dynamic structure factor with the instrumental resolution function, resulting in the solid black curve.

that the tetragonal compression of the unit cell ($c/a < 1$) necessitates a large compression of the apical lead-bromide bonds relative to the shrinking of $a_{tet}/\sqrt{2}$ due to the octahedral tilting, akin to the *P4/mbm* phase of $AgTaO_3$ and the pseudo-tetragonal *Imma* phase of $SrZrO_3$.[134,135] Below 182 K the higher frequency peak assigned to the *c* axis bromide in the NQR spectra begins to decrease in frequency. As the ratio of the nuclear quadrupolar frequencies deviates from a linear relationship with the $\sqrt{2}\ c_{tet}\ /\ a_{tet}$ ratio, contraction of the inorganic framework is insufficient to explain the data. Below the phase transition at *T* = 162 K no NQR signal could be determined between 60 and 80 MHz, which indicates a significant change in the bromine environment. The disappearance of the NQR signal could be due to rapid relaxation induced by the cation motion, the timescale of which is approaching the NQR frequency as the temperature decreases (*vide infra*), or to a wide distribution of environments leading to signals that lie below the signal-to-noise ratio; if not motionally averaged, the $CH(NH_2)_2{}^+$ cation can induce large changes to the local bromine environment (Figure 3.16), which could be exacerbated by the geometric frustration of the $CH(NH_2)_2{}^+$ cations. As the MSD and ^1H T_1 data demonstrate a change in the organic cation dynamics at 182 K and 162 K, the changes in the bromine environments exhibited in the NQR spectra likely arise from bromine-$CH(NH_2)_2{}^+$ interactions.

Effect of Cesium Substitution

The phase behavior of the series $(CH(NH_2)_2)_{1-x}Cs_xPbBr3_3$ also suggests that the *A*-site cation actively participates in the phase transitions of $CH(NH_2)_2PbBr_3$, as partial cesium substitution suppresses the low-temperature phase transitions. All members of the series

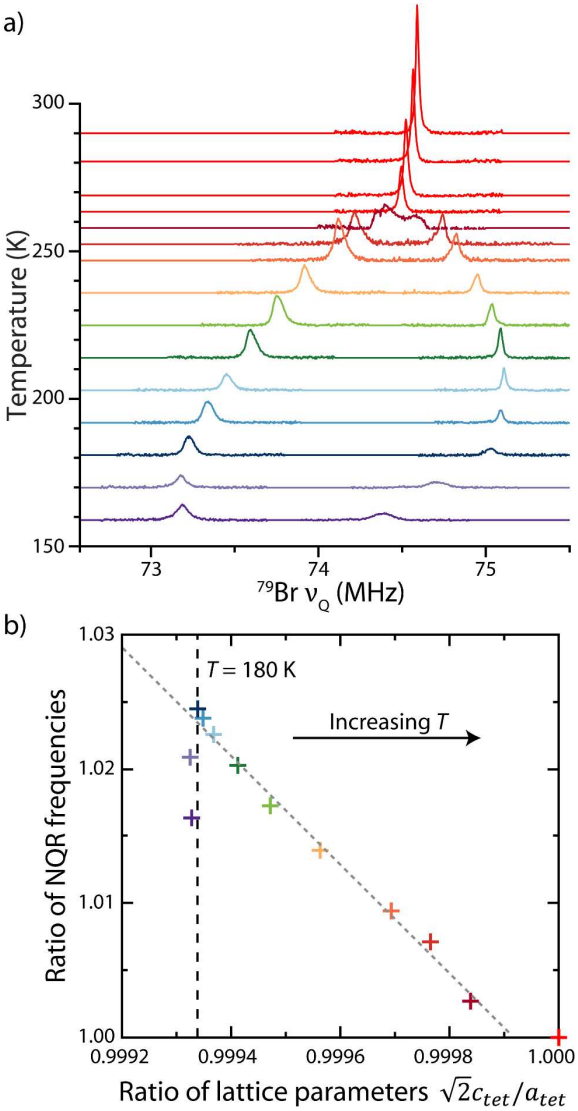

Figure 3.4: (a) ^{79}Br NQR spectra collected on $CH(NH_2)_2PbBr_3$. The T = 265 K phase transition results in peak splitting. The relative intensities of each resonance indicate that the higher frequency (lower intensity) signal relates to the bromine site on the unique c axis. (b) Ratio of the frequency of the NQR signals compared to the degree of tetragonal compression given by the ratio of the pseudocubic lattice parameters, $\sqrt{2}c_{tet}/a_{tet}$ according to the relationships $\sqrt{2}a_{cub} = a_{tet}$ and $a_{cub} = c_{tet}$. The dashed grey line represents a linear relationship. The vertical dashed line indicates the phase transition temperature. Measurement errors are smaller than the symbols.

with x ¡ 0.4 crystallize in the high-temperature cubic phase. Any substituted sample with x ¿ 0.4 is phase separated between a substituted cubic perovskite phase and an orthorhombic $CsPbBr_3$ phase. Phase separated materials were not investigated further. On cooling, all single-phase materials undergo the cubic to tetragonal phase transition, which is observed in the high-resolution synchrotron X-ray diffraction (SXRD) data (Figure 3.5, 3.6). In contrast, SXRD data do not show any change in the characteristic region between Q = 1.5 $Å^{-1}$ and 2.1 $Å^{-1}$ to indicate a tetragonal to orthorhombic phase transition between room temperature and T = 100 K (Figure 3.5) for the substituted samples. However, the characteristic features of the orthorhombic phase in $CH(NH_2)_2PbBr_3$ have low, path-dependent intensities, so it may simply not be possible to resolve them.[115]

Characterization of the organic cation dynamics reveals an absence of any signatures of the four low-temperature phase transitions in $(CH(NH_2)_2)_{1-x}Cs_xPbBr3_3$ with x ¿ 0. The cubic to tetragonal phase transition manifests with features in the MSD, ^{1}H T_1 values, and ^{14}N NMR spectra; aside from these features, however, there is no indication of further phase transitions (Figure 3.7).

For $(CH(NH_2)_2)_{1-x}Cs_xPbBr3_3$ with x = 0.1 and 0.2, the MSD decreases smoothly with temperature below the cubic to tetragonal phase transition. Similarly, with as little as 5% Cs^+ substitution, the features in the ^{1}H T_1 that correlate to the low-temperature ($T \leq$ 182 K) phase transitions do not appear. ^{14}N NMR spectra for $(CH(NH_2)_2)_{0.95}Cs_{0.05}PbBr_3$ preserve the general trend of increasing anisotropy (C_Q) with decreasing temperature in $CH(NH_2)_2PbBr_3$, but the component with a distinct nuclear quadrupolar line-shape observed for $CH(NH_2)_2PbBr_3$ below T = 182 K is not observed in the 170 K spectrum. There

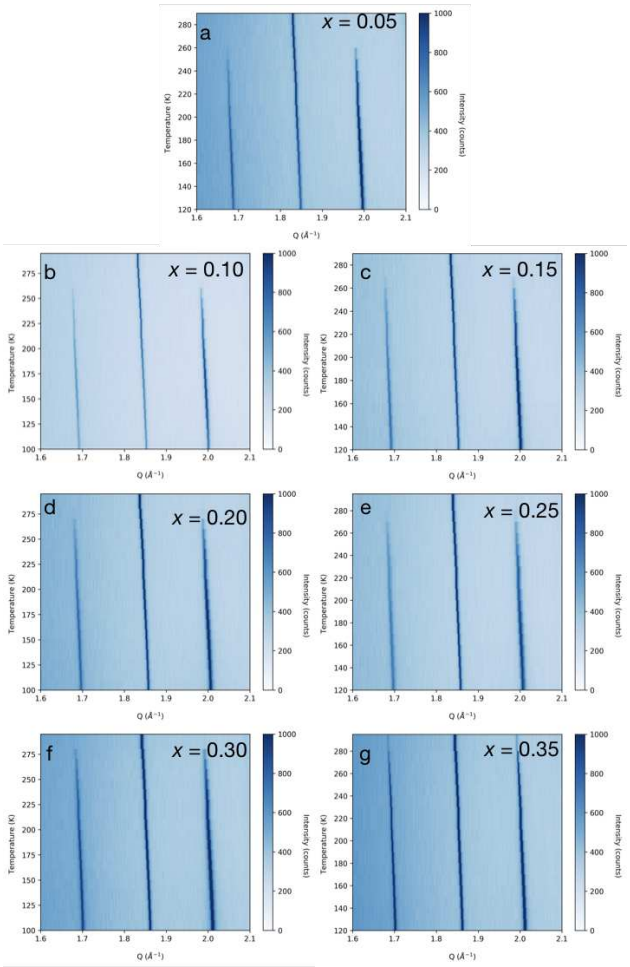

Figure 3.5: False color representation of selected Q region of normalized high-resolution synchrotron X-ray diffraction patterns of $(CH(NH_2)_2)_{1-x}Cs_xPbBr_3$, collected between 300 K and 100 K.

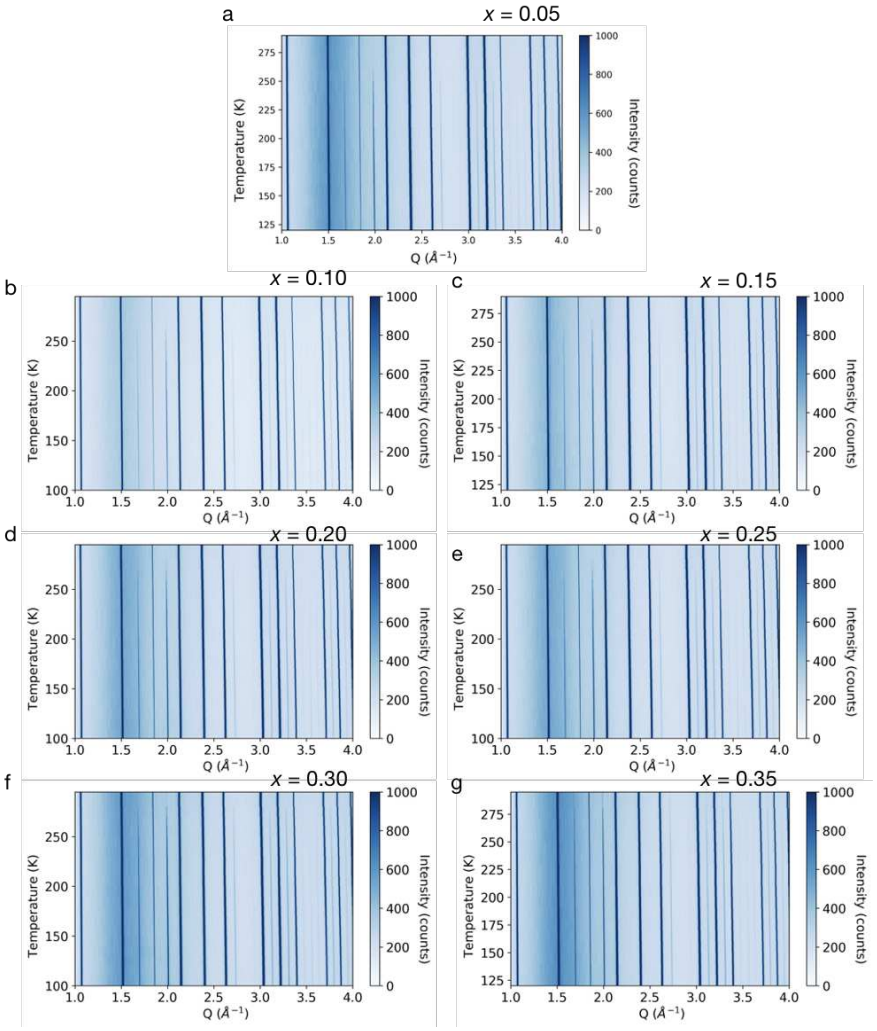

Figure 3.6: False color representation of selected Q region of normalized high-resolution synchrotron X-ray diffraction patterns of $CH(NH_2)_2)_{1-x}Cs_xPbBr_3$, collected between 300 K and 100 K.

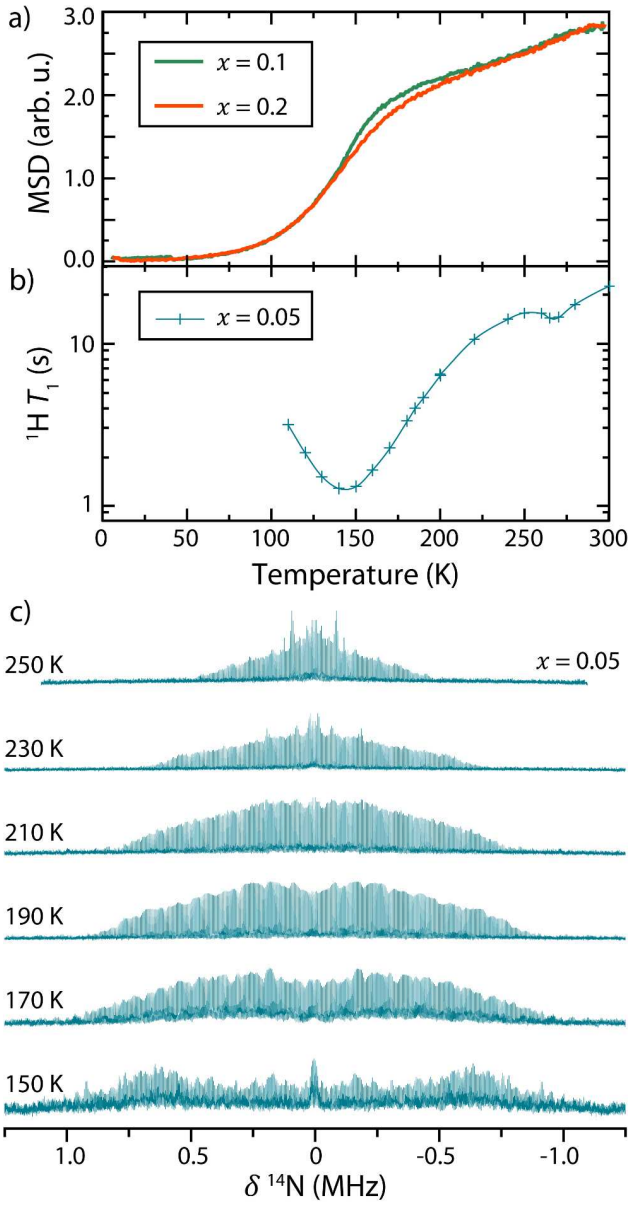

Figure 3.7: (a) Mean squared displacement (MSD) extracted from fixed window elastic neutron scattering spectra for $(CH(NH_2)_2)_{1-x}Cs_xPbBr3_3$, where x = 0.1 and 0.2. (b) ^{1}H NMR T_1 values for $(CH(NH_2)_2)_{0.95}Cs_{0.05}PbBr_3$ as a function of temperature. (c) ^{14}N NMR spectra of $(CH(NH_2)_2)_{0.95}Cs_{0.05}PbBr_3$ as a function of temperature.

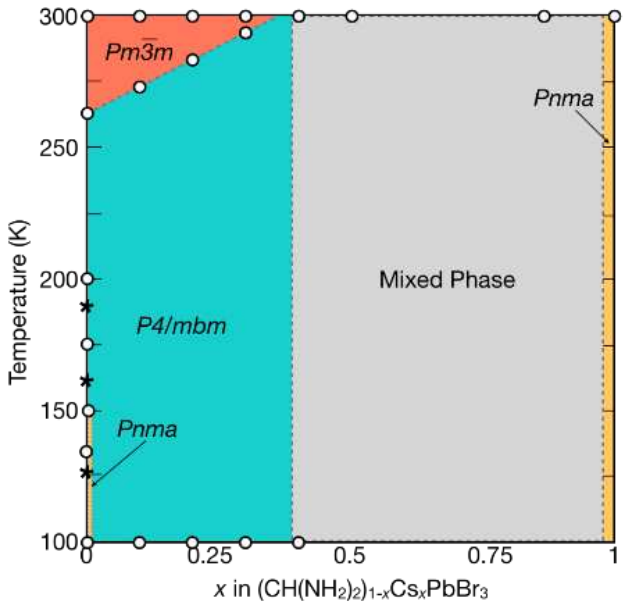

Figure 3.8: The phase behavior of the series $(CH(NH_2)_2)_{1-x}Cs_xPbBr3_3$, constructed from crystallography, neutron spectroscopy, and solid-state NMR spectroscopy. Black asterisks indicate dynamically driven phase transitions that do not result in a change in space group and open white circles indicate data collection temperatures near phase transition temperatures. The increase in cubic-tetragonal phase transition temperature as a function of x results from the substitution of a smaller cation in the *A*-site void.

is some evidence of a more defined environment near $T = 150$ K with $C_Q \approx 1.8$ MHz, but the features are approximately 100 kHz broader than for the unsubstituted perovskite. Together, these data demonstrate that Cs^+ substitution suppresses the low-temperature phase transitions of $CH(NH_2)_2PbBr_3$. A summary phase diagram is presented in Figure 3.8.

Cesium substitution increases the number of distinct local environments in $(CH(NH_2)_2)_{1-x}Cs_xPbBr3_3$, evidenced by ^{14}N NMR spectra (Figure 3.9a) and ^{79}Br NQR spectra (Figure 3.9b) collected for all samples in the high-temperature cubic phase. The ^{14}N NMR spectra broaden with increasing substitution due to components with larger C_Q values. The broad features indicate increasing anisotropy of cation rotations with x, likely due to the introduction of local distortions from Cs^+ substitution. This anisotropy extends

to the inorganic framework. With just 5% Cs^+ substitution, the sharp peak observed in the ^{79}Br NQR data of $CH(NH_2)_2PbBr_3$ broadens and splits into multiple signals, corresponding to different local environments throughout the bulk of the sample. Specifically, the broad signals at $\sim$ 74.4, 73.6 and 72.8 MHz are ascribed to ^{79}Br environments with zero, one and two Cs^+ nearest neighbors, respectively. Increasing the level of substitution leads to a corresponding increase of the lower-frequency signals, as the probability of having Cs^+ in the immediate coordination shells increases. By $x = 0.35$ only a broad featureless resonance is observed, corresponding to an effectively continuous distribution of possible local environments due to the different possible configurations of Cs^+ substitution in the immediate and extended coordination shells. This NQR broadening is consistent with the microstrain detected from XRD peak broadening with increasing substitution, x. The microstrain terms in the substituted samples are larger than in unsubstituted $CH(NH_2)_2PbBr_3$ (Figure 3.10).

Although Cs^+ substitution increases the disorder within the inorganic framework, the local behavior of $CH(NH_2)_2{}^+$ appears to be preserved. Spectroscopic characterization of the vibrational modes of $(CH(NH_2)_2)_{1-x}Cs_xPbBr3_3$ with inelastic neutron scattering (INS) demonstrates that the vibrational landscape around $CH(NH_2)_2{}^+$ is similar across the series of $(CH(NH_2)_2)_{1-x}Cs_xPbBr3_3$ compounds, as the major features in the INS spectra are conserved (Figure 3.11). Several features are damped upon substitution, primarily the features near 15 meV that broaden with increasing x and near 45 meV that cannot be resolved for $x > 0.1$ (Figure 3.13). These modes correspond to coupled lead$-$ bromide bending and formamidinium librations, similar to those in related perovskites,[136–138] as confirmed by the calculated phonon spectrum (Figure 3.17). Relative to the series of

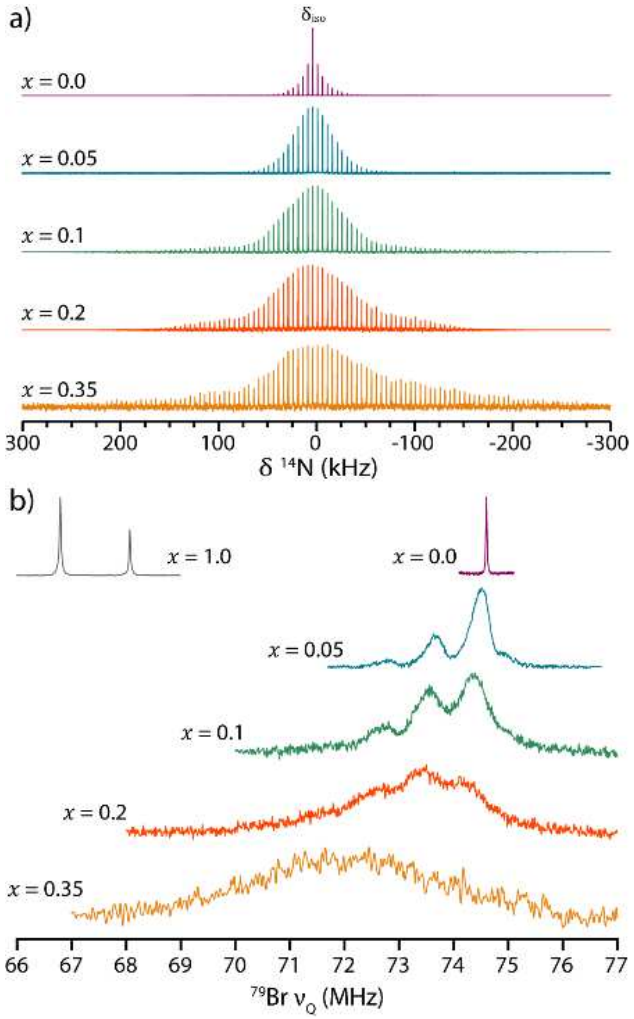

Figure 3.9: (a) Room-temperature ^{14}N NMR spectra of $(CH(NH_2)_2)_{1-x}Cs_xPbBr3_3$, where x = 0 to 0.35, recorded at 16.4 T and 5 kHz MAS using a Hahn echo pulse sequence. (b) Room-temperature ^{79}Br NQR spectra collected with VOCS acquisition in steps of 200 kHz on $(CH(NH_2)_2)_{1-x}Cs_xPbBr3_3$. Data for $CsPbBr_3$ are presented in the top left corner.

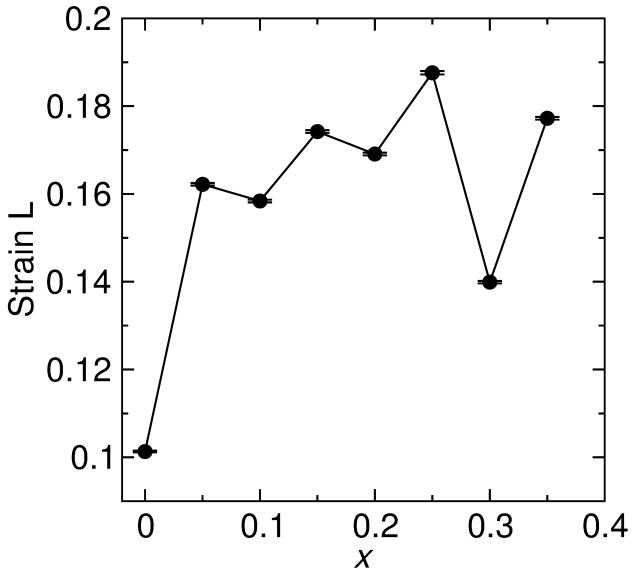

Figure 3.10: Strain from LeBail refinements of room temperature high resolution synchrotron x-ray diffraction as a function of x in $(CH(NH_2)_2)_{1-x}Cs_xPbBr3_3$.

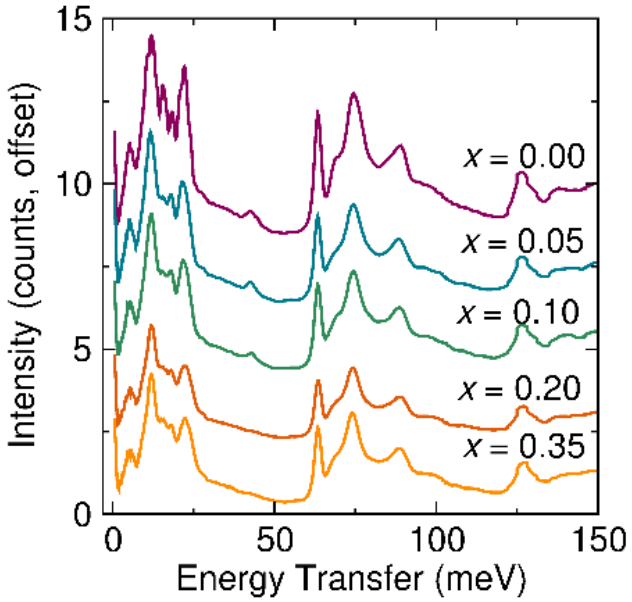

Figure 3.11: Inelastic Neutron Scattering data for $(CH(NH_2)_2)_{1-x}Cs_xPbBr3_3$, collected at $T = 5$ K showing that chemical substitution has a minimal influence on the internal vibrational modes of formamidinium. Phonon calculations indicate that the low-energy modes (¡30 meV) correspond to coupled organic cation librations and octahedral tilting, and high-energy modes (¿50 meV) correspond to internal organic cation vibrations.

compounds $(CH_3NH_3)_{1-x}Cs_xPbBr3_3$, which form an orientational glass on substitution,[100] these changes are minor and correlate to the changes in organic-inorganic coupling also revealed by the ^{79}Br NQR. The rates of cation reorientations also remain similar as a function of x (Figure 3.12), where the correlation times from the ^{1}H T_1 values have been predicted using BPP theory (details in SI). Furthermore, the apparent activation energies for cation motion extracted from Arrhenius plots of the correlation times change by less than 0.02 eV as a function of x (Figure 3.11). Above 140 K, the activation energy of cation motions (E_a) for $(CH(NH_2)_2)_{1-x}Cs_xPbBr3_3$ with x = 0.00, 0.05 and 0.35 is close to 0.10 eV; below $\sim$ 140 K E_a decreases to 0.05 eV. The reduction in activation energy at lower temperature may be associated with the freezing out of overall rotation observed by ^{14}N NMR at the T = 153 K transition. The preservation of this reduction in activation energy with chemical substitution implies that the same freezing still occurs in the substituted materials, but not cooperatively and perhaps over a range of temperatures rather than as a sharp transition, due to the heterogeneity in the local environment. The change in apparent activation energy occurs at approximately the minimum in the ^{1}H T_1 (Figure 3.4b), and as such the T_1 minimum is asymmetric (Figure 3.5).

An alternative explanation for the change in gradient is therefore non-BPP behavior, rather than a change in the true activation energy.[139,140] An Arrhenius plot of the ^{1}H T_1 exhibits an asymmetric T_1 minimum, as shown in Figure 3.14 for x = 0.05. This could be due to a coincidental change in the activation energy for the motion around the temperature of the T_1 minimum, as discussed in the main text, but could also be caused by non-BPP behavior. A symmetric T_1 minimum, as predicted by BPP theory, arises from the assump-

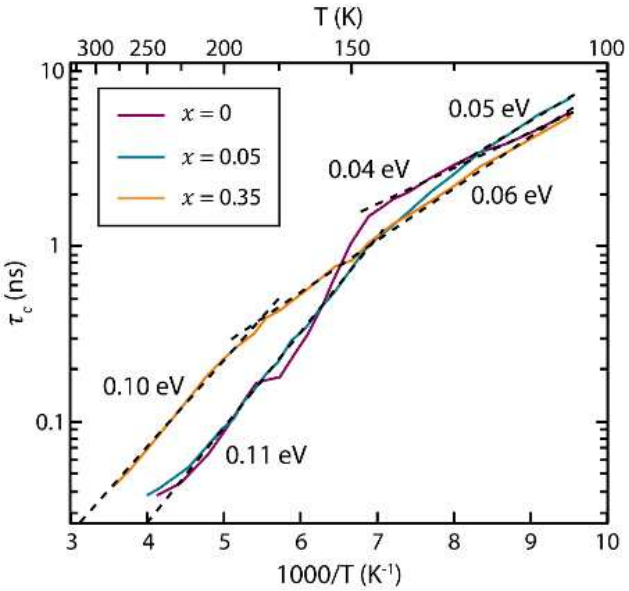

Figure 3.12: (a) Correlation times extracted from the ^{1}H NMR T_1 collected as a function of temperature for $(CH(NH_2)_2)_{1-x}Cs_xPbBr3_3$, where x = 0.00, 0.05, and 0.35. Details about the derivation of the correlation times are presented in the experimental. The dashed lines represent linear fits.

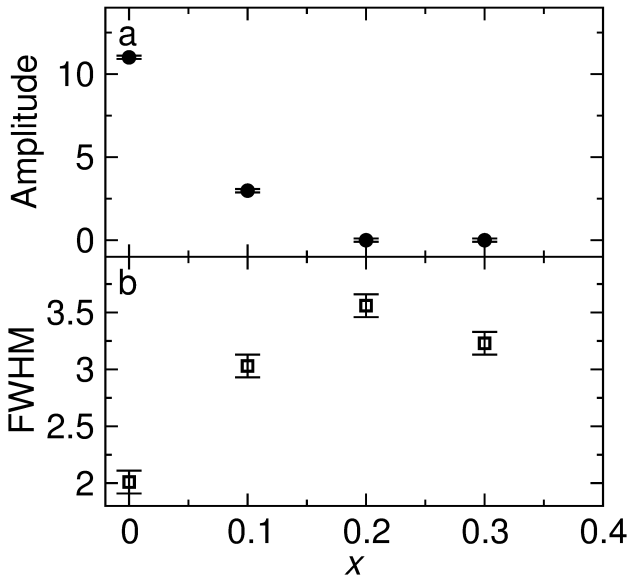

Figure 3.13: (a) The amplitude of the mode centered at 45 meV and (b) the full-width-half-maximum of the mode centered at 15 meV in the INS as a function of x in $(CH(NH_2)_2)_{1-x}Cs_xPbBr3_3$.

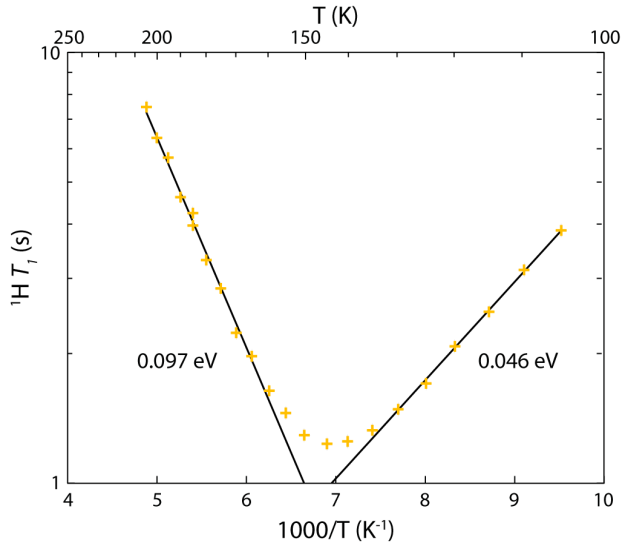

Figure 3.14: Arrhenius plot of the ^{1}H T_1 of $(CH(NH_2)_2)_{1-x}Cs_xPbBr_3$, where $x = 0.05$. Straight lines are linear fits.

tion of an exponentially decaying autocorrelation function, which results in a Lorentzian spectral density function (see above). If the autocorrelation function is not an exponential decay, the slope of the T_1 is no longer simply given by the activation energy as predicted by BPP theory.[139,140] A non-exponentially decaying autocorrelation function could occur if there is an energetic preference for a cation remaining in a locally favorable orientation, for instance due to the arrangement of adjacent cations. These results could therefore suggest correlations between the cations; however, to unambiguously determine the cause of the change in gradient, a significantly higher or lower magnetic field would be required in order to shift the temperature of the T_1 minimum.

Discussion

We propose that organic cation dynamics actively participate in the four low-temperature phase transitions of $CH(NH_2)_2PbBr_3$, and that organic−organic interactions underlie the

three

crystallographically-unresolvable phase transitions. At each phase transition temperature the MSD, ^{1}H T_1, and ^{14}N NMR data demonstrate a change in the dynamic degrees of freedom of $CH(NH_2)_2^+$ and the anisotropy of the *A*-site void. This does not necessarily indicate positional long-range ordering of the organic sub-lattice; rather, these transitions are characterized by a cooperative change in cation dynamics. While ^{79}Br NQR data demonstrate that the octahedra also experience changes in their local environment at these temperatures, inter-octahedral interactions are unlikely to drive the phase transitions at $T = 182$ K, 162 K, and 118 K, as no analogous transitions occur in related hybrid perovskites.[100,129] The changes observed in the NQR are likely a response of the lead-bromide octahedra to $CH(NH_2)_2^+$ dynamics. The frequency ratio between the two NQR signals in the tetragonal phase correlates closely with the ratio of lattice parameters ($\sqrt{2}\ c_{tet}/a_{tet}$) until below the $T = 182$ K phase transition, at which point the two ratios deviate dramatically (Figure 3.4b). Therefore, while lattice compression accounts for the changes in local bromide environment initially, below 182 K another interaction must lead to the observed peak shift. As this transition occurs concurrently with a reduction in the dynamic degrees of freedom of $CH(NH_2)_2^+$, organic-inorganic coupling most likely leads to a change in the local bromide environment. A similar argument can be made for the signal change at $T = 162$ K and emphasizes the role of the organic cation in the low-temperature phase transitions. These changes in the bromine environment also explain why transitions are observed in the photoconductivity at the crystallographically-unresolvable phase transitions.[115]

Organic interactions appear quite sensitive to disruption from Cs^+ substitution. As little as 5% Cs^+ substitution suppresses any signature of the four low temperature phase transitions in the crystallography, MSD, ^{1}H T_1, and ^{14}N NMR. We cannot rule out the presence of sluggish phase transitions that have obscured signatures outside the sensitivity of our techniques; however, we do not observe features characteristic of glassy dynamics or other short-range ordered phenomena, which we and others have previously observed in related systems.[100,141] Therefore, we conclude that the phase transitions are suppressed in the cesium substituted samples below the cubic to tetragonal phase transition. While these data indicate a lack of cooperative changes in the dynamic degrees of freedom in substituted samples, $CH(NH_2)_2^+$ molecules exhibit similar local behavior across the series $(CH(NH_2)_2)_{1-x}Cs_xPbBr3_3$, with similar temperature dependent reorientation rates and internal vibration energies.

Describing these interactions necessitates an understanding of the driving forces behind perovskite phase transitions. Oxide and halide perovskite phase transitions generally occur to maximize coordination of the *A*-site cation by the octahedral framework.[16] In hybrid perovskites, the organic cations can coordinate the octahedral units through hydrogen bonds,[110,142] but unlike $CH_3NH_3^+$ perovskites, the geometry and coordination of the lead-bromide octahedra conflict with the geometry and electrostatic interactions of $CH(NH_2)_2^+$. The hydrogen-bonding pattern of $CH(NH_2)_2^+$ is not compatible with the geometry of the bromide hydrogen bonding acceptors and appears to have more complex molecule-cage interactions than for $CH_3NH_3^+$ counterparts.[141] Furthermore, $CH(NH_2)_2^+$ has a weak electrostatic dipole (p = 0.35 D) but a strong molecular electrostatic quadrupole ($|Q_{11}| =$

$18.3\ D \circ \mathring{A}$) due to the cancellation of the strong bond dipoles between carbon and each nitrogen (cf., $CH_3NH_3^+$, p = 2.3 D, $|Q_{11}| = 3.6\ D \circ \mathring{A}$).[143] The quadrupolar moments of formamidinium cations yield a strain field due to electrostatic interactions with the inorganic lattice (Figure 3.15a,b), where positive charge attracts the anionic sublattice and negative charge repulses the anionic sublattice. These strain fields are analogous to chemical pressure, as has been visualized in intermetallic compounds,[144] and are mathematically equivalent to elastic dipoles (a second rank tensor).[145] Pairs of axially-symmetric electrostatic quadrupoles (and elastic dipole tensors in a homogeneous dielectric) have a preference to order in a "T" shape due to their compatible compressive and expansive strain fields (Figure 3.15c); this "T" -shape ordering can tile in two dimensions (Figure 3.15d), however such local ordering cannot geometrically tile space in three dimensions.[115,145] The electrostatic quadrupole of formamidinium is not axially symmetric, but there are nevertheless many possible low-energy 3D orientational arrangements, and we previously showed that the resulting geometric frustration leads to the cation-orientation mediated phase transitions.[115,145] This aligns with the recent description of $CH(NH_2)_2PbBr_3$ as an incipient ferroelastic,[146] as a uniform strain field causes elastic dipoles to spontaneously align.[145] Cesium substitution introduces a compressive microstrain in the lattice from size mismatch ($r_{Cs} = 1.88\mathring{A}$, $r_{CH(NH_2)_2^+} = 2.53\mathring{A}$) that induces a local alignment of neighboring quadrupole moments, disrupting the "T" shape ordering and relieving geometric frustration (Figure 3.15e).[147,148] Cesium substitution produces short-range ordered regions that interrupt the long-range coherent, orientational phase transitions.

The relief of geometric frustration upon substitution contrasts with the behavior of $CH_3NH_3^+$ perovskites. In $CH_3NH_3^+$ perovskites, Cs^+ substitution leads to the formation of an orientational glass in the methylammonium sub-lattice with reduced $CH_3NH_3^+$ dynamics, which derives from the conflicting inorganic octahedral tilting preferences imparted by $CH_3NH_3^+$ *vs* Cs^+.[100] This contrasts with $CH(NH_2)_2PbBr_3$ and $CsPbBr_3$ which both display the same octahedral tilting distortions upon cooling.[116,149] In the case of $(CH(NH_2)_2)_{1-x}Cs_xPbBr3_3$, the retained local dynamics of the organic molecules prevents glass formation, but cesiation disrupts long-range ordered phase transitions. The INS data in particular demonstrate the presence of *local* microstrain-induced broadening upon substitution in $(CH(NH_2)_2)_{1-x}Cs_xPbBr3_3$ and the comparative lack of *local* microstrain in $(CH(NH_2)_2)_{1-x}Cs_xPbBr3_3$ (Figure 3.11), consistent with peak broadening observed in PXRD (Figure 3.10). The lack of disrupted vibrational modes at $T = 5$ K in $(CH(NH_2)_2)_{1-x}Cs_xPbBr3_3$ with increasing cesium content emphasizes the high tolerance of hybrid perovskites towards substitution, as Cs^+ is nearly 70 pm smaller than $CH(NH_2)_2^+$. Each organic cation has markedly different responses upon substitution, which highlights the complexity of the potential energy landscape within mixed-cation perovskites commonly used in photovoltaic devices.[7] The increased chemical stability of substituted formamidinium perovskite solar cells relative to unsubstituted solar cells[150] could arise from the relief of geometric frustration from long-range elastic dipolar interactions upon Cs^+ substitution.

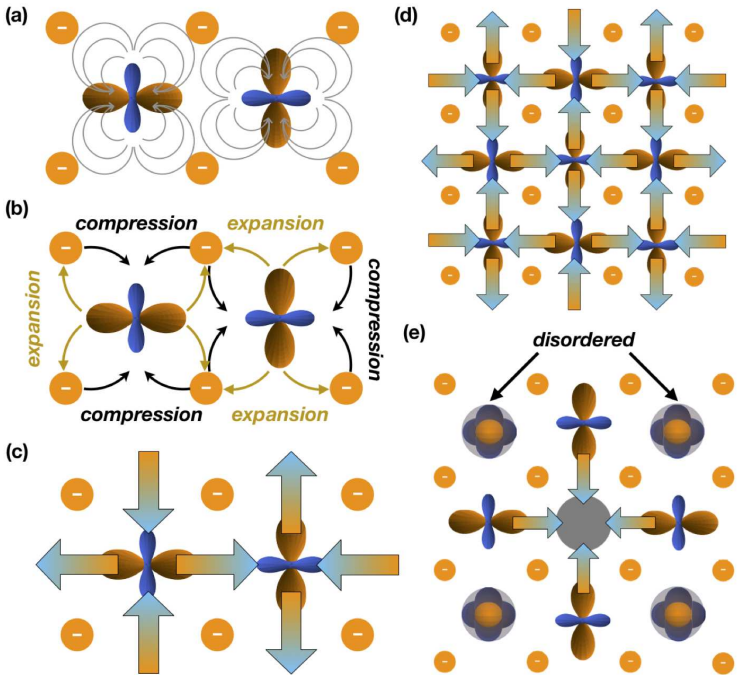

Figure 3.15: Schematic cartoon illustrating the role of quadrupolar and elastic interactions. (a) Electrostatic potential field lines emanating from the geometric representation of the quadrupolar moment tensor of formamidinium[143] (orange density denotes negative; blue is positive) provide attractive or repulsive interactions to the anionic lattice framework, as depicted in (b). (c) The resulting expansive and compressive strain fields map onto an elastic dipole tensor model, depicted by the pairs of large arrows. (d) In a hypothetical two-dimensional plane, the elastic dipoles have a stable long-range ordered configuration that minimizes the elastic energy; however, a favorable three-dimensional configuration cannot be tiled. (e) Introduction of a smaller Cs^+ cation results in a neighboring compressive microstrain, thus causing a preferred orientation of quadrupolar cations around the Cs^+ and frustrated orientations of the next-nearest neighboring quadrupoles.

Conclusions

Chemical substitution in the hybrid perovskite $CH(NH_2)_2PbBr_3$ leads to the release of geometric frustration of $CH(NH_2)_2{}^+$ interactions, while retaining the local dynamic degrees of freedom. From ^{1}H NMR, ^{14}N NMR, ^{79}Br NQR, and neutron scattering we confirm that the five phase transitions of $CH(NH_2)_2PbBr_3$ are characterized by changes to the dynamic degrees of freedom of $CH(NH_2)_2{}^+$, further corroborating previous studies. Additionally, these changes couple to the inorganic octahedral framework through either long-range cooperative tilting or local distortions. Cesium substitution interrupts organic-organic interactions and leads to the suppression of the four low-temperature phase transitions, which we have demonstrated through dynamic and crystallographic characterization of the series $(CH(NH_2)_2)_{1-}Cs_xPbBr3_3$. This work provides insight into the sensitivity of the organic-organic interactions in $CH(NH_2)_2PbBr_3$ and demonstrates that Cs^+ substitution has important implications for the structure of hybrid perovskites that could explain the increased phase stability of chemically substituted hybrid perovskites that retain advantageous electronic properties.

Experimental Methods

Sample preparation: $CH(NH_2)_2PbBr_3$ was prepared as previously described.[115] In brief, $CH(NH_2)_2CH_3COOH$ (VWR, 98%) was dissolved in hydrobromic acid (Sigma Aldrich, 48%) and reacted with $PbBr_2$ (Sigma Aldrich, 99.99%) at 80 $^\circ$ C. $CH(NH_2)_2PbBr_3$ was precipitated with ethanol as an antisolvent and washed with ethanol. $CsPbBr_3$ was prepared via

a solid-state reaction from the binaries CsBr (VWR, 99.9%) and $PbBr_2$, carried out at 600 ° C for six hours. The solid solutions were prepared by grinding molar quantities of the end members, sealing in an evacuated silica ampoule and gently heating at 150 ° C for between one and three weeks.

Diffraction: Laboratory powder X-ray diffraction (PXRD) data were collected on a Bruker D8 Discover X-ray diffractometer using a Cu K_α radiation source and a Lynxeye XE-T position-sensitive detector to check phase purity. Accurate lattice parameters were obtained using an internal silicon standard intimately mixed with each sample. High-resolution synchrotron powder X-ray diffraction (SXRD) patterns were collected on the diffractometer 11-BM-B at the Advanced Photon Source, Argonne National Laboratory ($\lambda \approx 0.41$ Å) between $T = 300$ K and $T = 100$ K in intervals of Δ T = 10 K.[151] Powders were flame sealed in glass capillaries under vacuum.

NMR and NQR: Low-temperature ^{1}H T_1 measurements (i 200 K) were performed using the low-temperature magic angle spinning (MAS) capabilities at the UK DNP MAS NMR Facility at the University of Nottingham, on a 14.1 T AVANCE III HD spectrometer corresponding to a ^{1}H Larmor frequency of 600 MHz, with a 3.2 mm probe. All other NMR experiments were performed on a 16.4 T AVANCE III spectrometer (University of Cambridge) corresponding to a ^{1}H Larmor frequency of 700 MHz using a 4 mm MAS probe. The NQR experiments were performed on an AVANCE spectrometer (University of Cambridge) using a 4 mm MAS probe designed for use with a 9.40 T (400 MHz) magnet.

The ^{1}H T_1 constants were measured using a saturation recovery experiment with an appended Hahn echo, without (or with truncated) phase cycling to reduce the experimental time in the case of long T_1 constants.

^{14}N NMR spectra in the cubic phase were measured at 5 kHz MAS using a Hahn echo pulse sequence, a radiofrequency (rf) power of 41 kHz and a recycle delay of 5 ms; where the spectra were broader than could be excited in a single spectrum, variable offset cumulative spectroscopy (VOCS) acquisition was used in steps of 40 kHz. Below the cubic-tetragonal phase transition, ^{14}N NMR spectra were recorded under static conditions with a WURST CPMG pulse sequence[152–154] and an echo length of 200 μ s yielding a spikelet separation of 5 kHz. Between 6 and 60 echoes were recorded depending on the T_2 constant, using 50 μ s WURST-80 pulses with a 500 kHz excitation width and a rf power of 22 kHz; recycle delays of 5 - 50 ms were used, and continuous wave ^{1}H decoupling of 50 kHz was applied. Probe ringing was removed by not recording the first two echoes, where the T_2 constant was sufficiently long to permit this. These ultra-wideline spectra were recorded using VOCS acquisition in steps of 100 kHz, with retuning achieved by an external automatic tuning and matching (eATM) robot,[155] before being recombined by taking the magnitude data for each spectrum and performing a skyline projection.[154] The symmetric $I = 1$ quadrupolar interaction is expected to dominate the ^{14}N spectrum, and so only the low-frequency half of the spectrum was recorded and then reflected to reproduce the complete spectrum.

DFT Calculation of ^{14}N, ^{79}Br Quadrupolar Parameters

Calculations of nuclear quadrupolar parameters were performed using the CASTEP plane wave density functional theory (DFT) code,[156,157] the PBE exchange-correlation functional,[158] treating relativistic effects with ZORA and applying the G06 semi-empirical dispersion correction.[159] To avoid interactions between adjacent formamidinium cations and the need to consider different orderings, a $2\times\ 2\times\ 2$ $PbBr_3^-$ supercell was constructed with 7 Cs^+ cations and a single formamidinium cation, so that there were no nearest-neighbour or next-nearest-neighbour FA-FA interactions. A plane wave cut-off energy was used of 800 eV and a $2\times\ 2\times\ 2$ Monkhorst$-$ Pack k-point mesh. The structure was geometry optimized to within 10^{-5} eV/ion and allowing an orthorhombic distortion of the unit cell. The optimized pseudo-cubic unit cell parameters were $a = 5.929$ Å, $b = 5.904$ Å, $c = 5.907$ Å. The ^{14}N quadrupolar coupling parameters were calculated to be $C_Q = 2.83$ MHz and $\eta_Q = 0.23$.

The calculated ^{79}Br quadrupolar frequencies are shown in Figure 3.16. The presence of the formamidinium cation causes a significant change to the local environments of the adjacent bromide ions: the ions in the plane of the cation, colored blue, have lower quadrupolar frequencies (71 and 74 MHz), while the remaining adjacent ions have higher frequencies (81 - 82 MHz), compared to the average $CsPbBr_3$-like environment of $\sim$ 78 MHz (colored green). The calculated quadrupolar frequencies are not expected to be quantitatively accurate since the experimental ^{79}Br ν_Q values for $CsPbBr_3$ are 67 and 68 MHz (Figure 3.9), compared to the calculated value of $\sim$ 78 MHz for the $CsPbBr_3$-like environments, suggesting that the calculations overestimate the quadrupolar frequency. Nevertheless, it can be seen that a single static formamidinium cation significantly affects

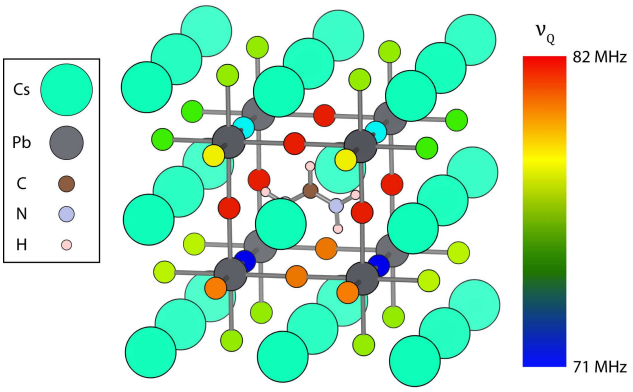

Figure 3.16: Colormap of calculated ^{79}Br NQR frequencies, ν_Q , for a 2× 2× 2 supercell comprising 7 Cs^+ cations and a single formamidinium cation.

the local environment of the bromide ions, which further depends on the orientation of the cation.

Calculation of correlation times

The ^{1}H longitudinal (T_1) relaxation for $(CH(NH_2)_2)_{1-x}Cs_xPbBr_3$ is dominated by dipole-dipole coupling over the temperature range studied here,[160] so that the relaxation rate is given by

$$\frac{1}{T_1} = A(J(\omega_0) + 4J(2\omega_0)) \tag{3.3}$$

where ω_0 is the Larmor frequency, $J(\omega)$ is the spectral density at a frequency ω and the pre-factor A is determined by the magnitude of the oscillations in the dipole-dipole coupling due to the motion (and hence is determined by the nature of the motion).

In order to continue the analysis of the relaxation data, a functional form for the spectral density is required. For this we resort to BPP theory,[130] which assumes that the autocorrelation function takes the form of a single exponential decay, characterized by a correlation time τ_c :

$$G(t) = \exp(-\frac{t}{\tau_c}). \tag{3.4}$$

Fourier transformation of $G\,(t)$ yields a Lorentzian spectral density function:

$$J(\omega) = \frac{\tau_c}{1 + \omega^2 \tau_c^2}. \tag{3.5}$$

Substituting the above expression for T_1 into this expression for $J(\omega)$ and differentiating yields the expected T_1 minimum at

$$\tau_c = \frac{0.616}{\omega_0}. \tag{4}$$

In the limits of fast or slow motion, the numerator or the denominator of [3] dominate, respectively, resulting in the following limits for the relaxation rate: Fast:

$$\tau_c \omega_0 \ll 1,\ \frac{1}{T_1} = 5A - \tau_c \tag{3.6}$$

Slow:

$$\tau_c \omega_0 \gg 1,\ \frac{1}{T_1} = \frac{2A}{\omega_0^2} - \frac{1}{\tau_c} \tag{3.7}$$

Furthermore, if one assumes an Arrhenius form of the correlation time

$$\tau_c = \tau_0 \exp\left(\frac{E_a}{RT}\right), \tag{3.8}$$

with activation energy E_a, we find that the T_1 constant also follows an Arrhenius dependence in these limits, with at most a change of sign,

$$T_1 \propto \exp\left(\pm\frac{E_a}{RT}\right), \tag{3.9}$$

so that an Arrhenius plot of ln T_1 against $1/T$ should result in symmetric straight lines of gradient $\pm E_a$ in the high- and low-temperature limits.

Although the BPP approximation makes several assumptions, it can be used to extract estimations of the correlation time τ_c as a function of temperature. As a starting point, we use the fact that at the T_1 minimum the correlation time is known, since $\tau_c\omega_0 \approx 1$ (which remains true despite correlated motional effects, although the exact numerical relation in [4] may change). From this we use the BPP spectral density, again substituting [3] into [1], and, using the experimental T_1 constant at the T_1 minimum, calculate the pre-factor A . With this value for A , the correlation time τ_c can be calculated from the experimental T_1 constant at every other temperature (main text, Figure 3.12). This is effectively an extrapolation of τ_c away from the T_1 minimum using BPP theory; the further from the T_1 minimum, the greater the error in the estimated value of τ_c which will have been introduced by non-BPP behavior.

It is also possible to calculate the pre-factor A from first principles, as previously used to interpret the T_1 constants in hybrid perovskites by Fabini et al.[110] Assuming isotropic reorientation of the internuclear vector and no vibrational motion,[7]

$$A = \frac{3\mu_0^2\hbar^2\gamma^4}{160\pi^2 r^6}, \tag{3.10}$$

where μ_0 is the permeability of free space, γ is the gyromagnetic ratio, in this case of the ^{1}H nuclei, and r is the separation of the two nuclei, in this case of the two ^{1}H nuclei in each formamidinium NH_2 group. Taking $r = 1.56$ $\mathring{A}$, this yields $A = 1.19 \times 10^{10}$ s^{-2}, which predicts a T_1 constant at the T_1 minimum of 0.04 s, compared to an experimental minimum of 1.2 s for 5% cesium substitution. This discrepancy is ascribed to vibration of the N-H bonds and anisotropic motion of the cation, both of which act to reduce A and hence to increase T_1; non-BPP behavior may also affect the effective pre-factor. For these reasons, the pre-factor determined from the experimental T_1 minimum was used to calculate the correlation times rather than the theoretical value.

^{79}Br NQR spectra were recorded with a Hahn echo pulse sequence, a rf power of 200 kHz, a recycle delay of 25 ms and VOCS acquisition in steps of 200 kHz, again with retuning by an eATM robot.

The sample temperature for all experiments was determined with an *ex situ* temperature calibration using the temperature-dependent ^{207}Pb chemical shift of $Pb(NO_3)_2$,[161] except for the low-temperature ^{1}H T_1 experiments (¡ 200 K), for which the sample temperature was determined from an *ex situ* temperature calibration using the temperature-dependent ^{79}Br T_1 constant of KBr.[140] ^{14}N NMR spectra were referenced to NH_4Cl at 0 ppm.

Inelastic Neutron Scattering (INS): Data were collected using the indirect-geometry spectrometer VISION at the Spallation Neutron Source, Oak Ridge National Laboratory. The instrument measures neutron energy transfer in the range of $-$ 2 to 1000 meV, with a resolution of dE/E = 1.5% . Powders were packed into aluminum canisters under a helium

atmosphere. Data were collected between $T = 5$ K and $T = 275$ K in 25 K intervals, with data collection times up to 1.5 hours. Time-of-flight data were reduced in MANTID.[162] Reduced data were modeled as damped harmonic oscillators in DAVE.[163] To lend assistance to interpretation of the INS spectra, phonon calculations were performed.

Phonon Calculations:

The calculated phonon spectrum is shown in Figure 3.17. DFT calculations were performed using CASTEP.[164] The Generalized Gradient Approximation (GGA), as implemented by the Perdew-Burke-Ernzerhof (PBE) functional, was used to describe the exchange-correlation interactions. Ultra-soft pseudopotentials were employed to account for the effects of core electrons. Tkatchenko-Scheffler dispersion correction[94] was used for van der Waals interactions. The energy cutoff for plane-wave basis was 310 eV. The unit cell configuration determined by powder x-ray diffraction was used as the initial structure for the simulations. The atomic coordinates were relaxed to allow minimization of the potential energy and the interatomic forces. The energy tolerance for the electronic structure calculations was 5×10^{-10} eV, and the energy tolerance for ionic relaxation was 5×10^{-9} eV. The tolerance for the interatomic forces was 1 meV/$\mathring{A}$. After convergence was reached, the dynamical matrix was obtained using the finite displacement method, from which the phonon frequencies and vibrational modes were calculated. The supercell use for phonon calculation was $2\times\ 2\times\ 1$ of the unit cell. The electronic structure calculations were performed on an $8\times\ 7\times\ 5$ Monkhorst-Pack mesh for the unit cell, and $3\times\ 3\times\ 5$ Monkhorst-Pack mesh for the supercell. Phonon sampling in the Brillouin zone was performed on a $9\times\ 7\times\ 5\ \Gamma$

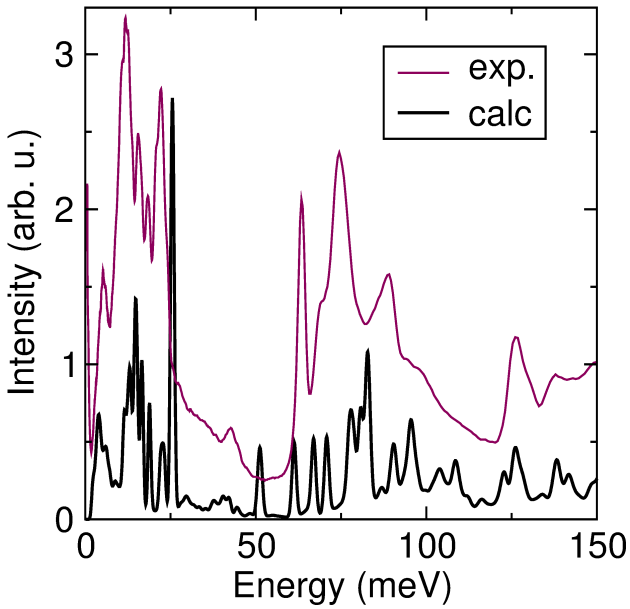

Figure 3.17: Comparison of experimental INS data and calculated phonon density of states.

-centered mesh. The OClimax software[99] was used to convert the DFT-calculated phonon results to the simulated INS spectra.

Quasielastic Neutron Scattering (QENS):

Fixed window elastic scattering and quasielastic spectroscopy experiments were performed on the high flux backscattering spectrometer (HFBS) at the NIST Center for Neutron Research on non-deuterated samples of $CH(NH_2)_2PbBr_3$.[165] The sample environment employed in this experiment is a closed-cycle refrigerator that cools/warms the sample by helium exchange gas. A mass of 3.27 g of $CH(NH_2)_2PbBr_3$ powder was used for this experiment. The cylindrical sample cell has a diameter of approximately 3 cm, and the powder sample was held against the lateral area of the sample can by enclosing it within aluminum foil pouches. The sample cell was loaded within a helium glove box and sealed with an indium gasket. The enclosed helium ensures good thermal contact between the powder and the rest of the sample environment.

Fixed window scans were performed according to the following protocol. Initially, the sample was quenched by placing it within the well of the closed cycle refrigerator when it was at 60 K. The sample temperature dropped rapidly to approximately 200 K and subsequently took 90 min to reach 6 K. Data was continuously collected upon warming at 0.8 K/min with 60 sec/point. Finally, data was collected upon cooling at the same nominal ramp rate and time per point.

A fixed window scan is a measurement of the elastic intensity I_{el} (Q, T) as a function of Q and temperature. The effective mean-squared displacement of the hydrogen atoms is estimated by assuming that $I_{el}(Q,T)$ is governed by a Debye-Waller factor:

$$I_{el}(Q,T) = I_{el}(Q, T = 6.0\ \mathrm{K}) \times \exp(-Q^2\langle u^2\rangle/3) \tag{3.11}$$

This calculation was performed using the DAVE software.[163]

4. Orientational Glass Formation in Methylammonium Hybrid Perovskites[†]

Summary

Hybrid organic-inorganic perovskites have gained notoriety in the photovoltaic community for their composition-tunable band gaps and long lived electronic excited states, which are known to be related to the crystalline phase. While indirect evidence suggests that coupling between polar organic cations affects the phase behavior, it remains unclear how the coupling manifests in hybrid perovskites such as methylammonium lead halides ($CH_3NH_3PbX_3$). Here, we present crystallographic and spectroscopic data for the series $(CH_3NH_3)_{1-x}Cs_xPbBr_3$. $CH_3NH_3PbBr_3$ behaves as a plastic crystal in the high temperature cubic phase, and substitution of $CH_3NH_3^+$ with Cs^+ leads to the formation of an orientational glass. While the organic molecule exhibits slow, glassy reorientational dynamics, the inorganic framework continues to undergo crystallographic phase transitions. These crystallographic transitions occur in the absence of thermodynamic signatures in the specific heat, which suggests that the phase transitions result from underlying instabilities

[†]Reproduced with permission from Mozur E. M., Maughan A. E., Cheng Y., Huq A., Jalarvo N., Daemen L. D., Neilson J. R. Orientational Glass Formation in Substituted Hybrid Perovskites. *Chemistry of Materials* **2017**, 29, 23, 10168-10177, https://pubs.acs.org/doi/10.1021/acs.chemmater.7b04017. Copyright 2017 American Chemical Society.
Author Contributions: Eve Mozur prepared the samples, collected and analyzed the diffraction data, heat capacity data, neutron scattering data and prepared the manuscript. Annalise Maughan collected the X-ray diffraction data and neutron scattering data. Luke Daemon collected and reduced the INS data. YQ Cheng performed the phonon calculations. Ashfia Huq collected the neutron scattering data. Niina Jalarvo collected and analyzed portions of the quasielastic neutron scattering data. James Neilson collected the inelastic neutron scattering data, edited the manuscript, and oversaw the project.

intrinsic to the inorganic lattice . However, these transitions are not decoupled from the reorientations of the organic molecule, as indicated by inelastic and quasielastic neutron scattering. Observation of a reentrant phase transition in $(CH_3NH_3)_{0.8}Cs_{0.2}PbBr_3$ permits the resolution of these complex behaviors within the context of strain mediated interactions. Together, these results provide critical insight to the coupled phase behavior and dynamics in hybrid perovskites.

Introduction

Hybrid organic-inorganic perovskites, characterized by an inorganic framework of corner-connected octahedra with an organic cation occupying the cuboctahedral void, are technologically relevant materials, with promise for use in photovoltaics,[166] solid state lighting,[167] and radiation detection.[168] The electronic and optical properties are heavily influenced by the structure of the octahedral framework as cooperative octahedral tilting affects the degree of orbital overlap.[77,169–173] Halide perovskites exhibit three major octahedral tilting patterns, a cubic perovskite phase (space group $Pm\bar{3}m$, Glazer tilt notation: $a^0a^0a^0$), a tetragonal perovskite phase (space group $I4/mcm$, Glazer tilt notation: $a^0a^0c^-$), and an orthorhombic perovskite phase (space group $Pbnm$, Glazer tilt notation: $a^+b^-b^-$) as depicted in Figure 4.1.[59,77,174–176] The room temperature octahedral tilting pattern of halide perovskites can be predicted with the Goldshmidt tolerance factor, a geometric argument that relies on the ionic radii of the constituent ions.[76,177,178] Halide perovskites undergo well-known symmetry lowering phase transitions upon cooling, from a high temperature cubic perovskite phase to a tetragonal perovskite phase to an orthorhombic perovskite

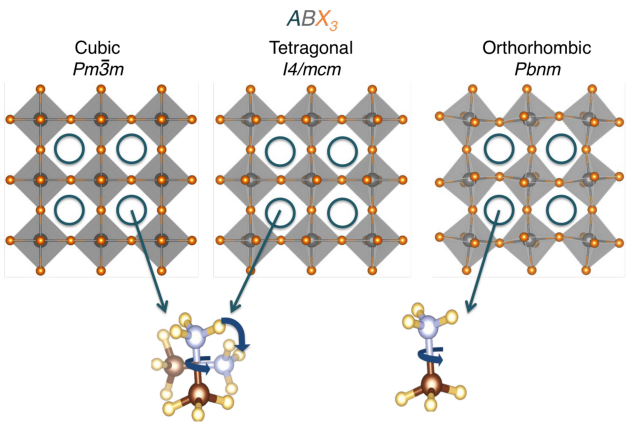

Figure 4.1: Possible crystalline phases for a generic halide perovskite ABX_3. At room temperature, $CH_3NH_3PbBr_3$ crystallizes in the cubic $Pm\bar{3}m$ structure and $CsPbBr_3$ crystallizes in the orthorhombic $Pbnm$ structure. Both materials undergo the same phase transitions, from cubic at elevated temperature, to tetragonal at moderate temperature, to orthorhombic at low temperature.[174,184,185] In $CH_3NH_3PbBr_3$ the phase transitions have been correlated with the freezing of $CH_3NH_3^+$ dynamics, particularly molecular reorientations in the cuboctahedral void as shown at the bottom.[26,186]

phase.[174,175] Compositional substitution, as in $(CH_3NH_3)_{1-x}Cs_xPbX_3$, where $X = Br$[169] and $X = I$,[179] has been shown to modulate the magnitude of octahedral tilting. Temperature dependent studies demonstrate that the changes in octahedral tilting correlate with substantial changes in optical,[50,169,180] thermal,[181] dielectric,[182] and photovoltaic[183] properties.

Hybrid organic-inorganic perovskites have additional structural and dynamic degrees of freedom relative to all-inorganic perovskites. Cations like $CH_3NH_3^+$ hydrogen bond with the halide anions at the X-site, which can distort the octahedral framework.[20,187–190] In the cubic and tetragonal phases, $CH_3NH_3^+$ dynamically rotates in the cuboctahedral void (Figure 4.1).[26,175,191–193] Single crystal neutron diffraction has been used to show that in $CH_3NH_3PbI_3$, $CH_3NH_3^+$ jumps between eight equivalent positions in the cubic phase and four equivalent positions in the tetragonal phase, as predicted computationally.[186,194] After the material transitions to the orthorhombic phase, the molecular orientations of

$CH_3NH_3^+$ freeze into a single antiferroelectric configuration, while the molecule continues to hop around its C_3 axis (Figure 4.1).[25,26,191] In $CH_3NH_3PbBr_3$, this transition manifests with an intermediate incommensurate phase, in which $CH_3NH_3^+$ dipoles begin to order.[195] The freezing of $CH_3NH_3^+$ molecular dynamics is correlated to the tetragonal to orthorhombic phase transition and thereby any changes in optical, electronic, thermal, dielectric, and photovoltaic properties discussed above.[50,169,180–183] In addition, molecular dynamics associated with phase transitions are thought to participate in electron-phonon coupling, which affects the band gap and electronic excited state lifetimes in $CH_3NH_3Pb\mathit{X}_3$.[42,53,196–199] Distortions to the octahedral framework from interactions with an organic cation can then alter the electronic structure of the perovskite.[187,200,201]

Recently, hybrid perovskites with mixed halide and mixed A-site occupancies have been shown to improve photovoltaic device efficiencies.[202,203] Substitutions at the A-site have been shown to reduce the propensity for hybrid perovskites to decompose into the binaries $Pb\mathit{X}_2$ and $A\mathit{X}$[204–206] as is enthalpically favored.[207] Ion migration is often implicated in the decomposition pathway of hybrid perovskites, which suggests that substitution inhibits ion dynamics.[12,208,209] Halide substitution in $CH_3NH_3PbI_3$ has been shown both to inhibit lattice dynamics and to decrease the electronic excited state lifetime.[210–212] However, it remains unclear how these complex substitutions affect the phase behavior and how substitution at the A-site changes the lattice dynamics.

We have prepared the series $(CH_3NH_3)_{1-x}Cs_xPbBr_3$, where $x = 0.0, 0.1, 0.2, 0.3,$ and 0.4 and have characterized the crystallographic phase behavior and dynamic behavior as a function of x with diffraction, heat capacity, and time-of-flight neutron diffraction and

spectroscopy. We show that cesium substitution leads to orientational glass behavior and can produce materials with reentrant phase transitions. These data demonstrate that the organic cation actively participates in the phase transitions of hybrid perovskites, as introducing geometric strain from Cs^+ substitution changes the phase behavior. These results provide atomistic insight into the complex energy landscape and dynamics of $CH_3NH_3PbBr_3$ and related hybrid perovskites.

Results

At room temperature, all members of the series $(CH_3NH_3)_{1-x}Cs_xPbBr_3$, where $0 \leq x \leq 0.4$ crystallize in the cubic perovskite structure (space group $Pm\bar{3}m$). High resolution

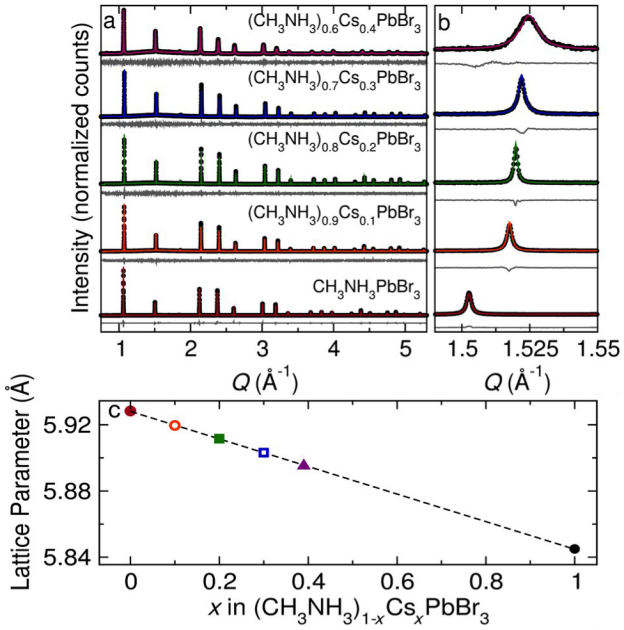

Figure 4.2: (a) High resolution synchrotron XRD patterns of $(CH_3NH_3)_{1-x}Cs_xPbBr_3$ collected at room temperature. Data are shown as black circles and fits from Rietveld refinements of the cubic perovskite structure (space group $Pm\bar{3}m$) are shown as colored lines. Difference curves are shown in gray beneath each data set. (b) Narrower Q range of the high resolution synchrotron XRD patterns illustrating the peak shift in the diffraction pattern as a function of x. (c) Cubic lattice parameter of $(CH_3NH_3)_{1-x}Cs_xPbBr_3$ as a function of x determined from PXRD with an internal silicon standard demonstrating that the series follows Vegard's law for solid solution behavior.

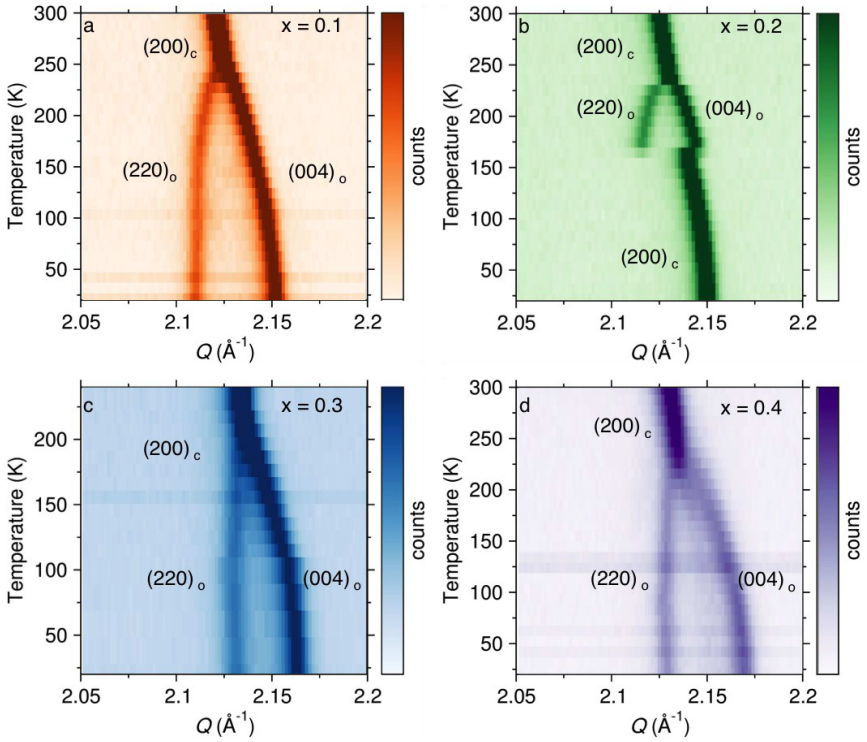

Figure 4.3: Representative temperature-dependent NPD of $(CH_3NH_3)_{1-x}Cs_xPbBr_3$ where (a) $x = 0.1$ (b) $x = 0.2$, (c) $x = 0.3$, (d) $x = 0.4$. Shown here is the $(200)_c$ peak in the cubic phase, which splits into the $(220)_o$ and $(004)_o$ peaks indexed to the tetragonal and orthorhombic phases.

synchrotron XRD patterns of the series $(CH_3NH_3)_{1-x}Cs_xPbBr_3$ are presented in Figure 4.2a. For all x the data have been modeled with the cubic perovskite structure and the series follows Vegard's Law for $x \leq 0.4$ (Figure 4.2b,c). For $x = 0.4$, a small fraction of a second perovskite phase (approximately 3 mol% from Rietveld Refinement) is present, demonstrated by the appearance of small shoulders on all peaks as described in Figure 4.4. This suggests that the solubility limit of Cs^+ into $CH_3NH_3PbBr_3$ is at or near $x = 0.4$. Attempts to prepare $(CH_3NH_3)_{1-x}Cs_xPbBr_3$ with $x > 0.4$ leads to diffraction patterns with dramatically split peaks indicative of phase separation.

All members of the series undergo temperature dependent changes of the lattice symmetry. Plots of temperature-dependent NPD data for the cubic (200) peak, which splits

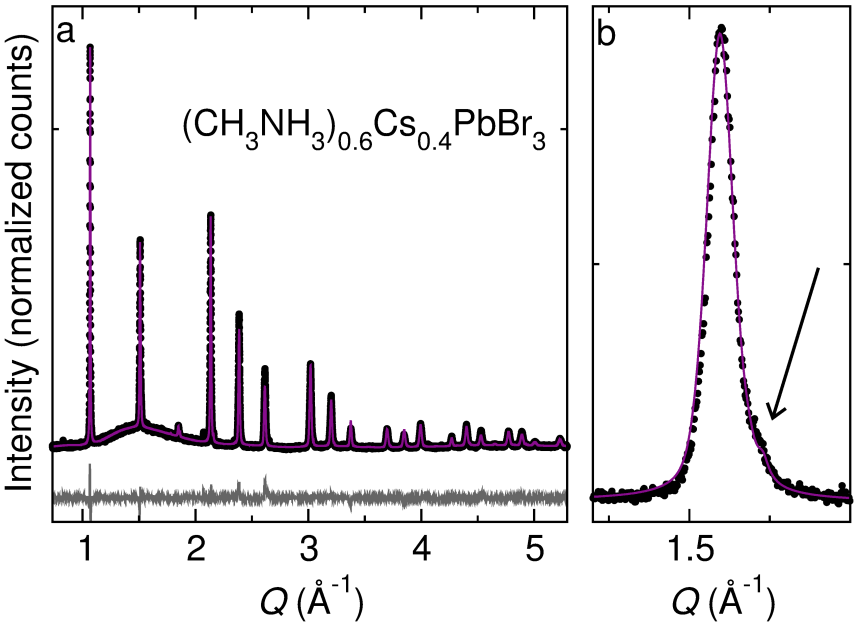

Figure 4.4: High-resolution synchrotron X-ray diffraction data for $(CH_3NH_3)_{0.6}Cs_{0.4}PbBr_3$ with data as black dots, the Rietveld fit as a purple line, and the difference in gray. (a) The major phase is a cubic perovskite, but (b) close inspection of the peaks shows a shoulder that indicates the presence of a second perovskite phase. Rietveld refinement demonstrates that the minor phase is present in very small amounts, approximately 3 mol%.

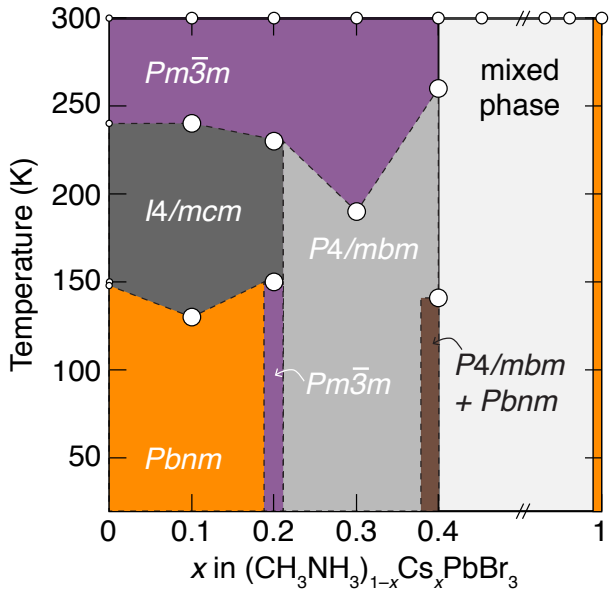

Figure 4.5: Schematic phase diagram of the series $(CH_3NH_3)_{1-x}Cs_xPbBr_3$. Circles correspond to experimentally determined features and are scaled to represent the uncertainty in the temperature based on the temperature ramp rate.

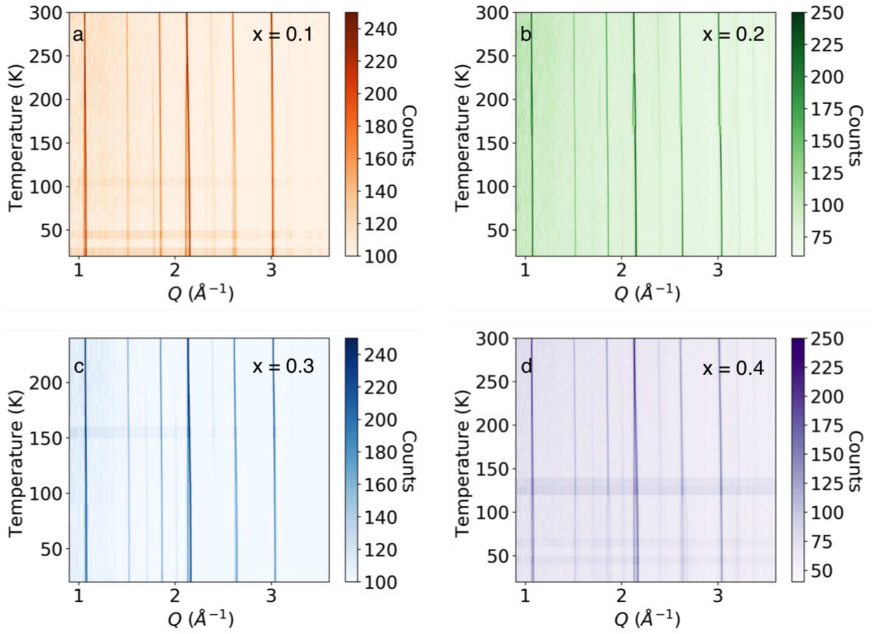

Figure 4.6: Neutron diffraction patterns of $(CH_3NH_3)_{1-x}Cs_xPbBr_3$ as a function of temperature, where x = (a) 0.1, (b) 0.2, (c) 0.3, and (d) 0.4. These data were collected on the neutron diffractometer, POWGEN, at the Spallation Neutron Source, Oak Ridge National Laboratory.

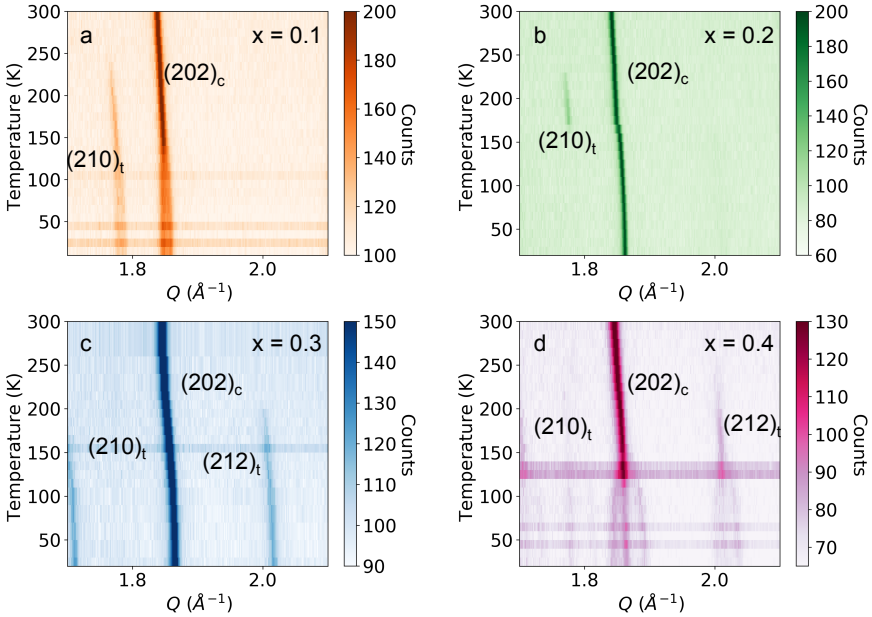

Figure 4.7: Selected region of high resolution neutron diffraction patterns as a function of temperature for $(CH_3NH_3)_{1-x}Cs_xPbBr_3$ where (a) $x = 0.1$, (b) $x = 0.2$, (c) $x = 0.3$, and (d) $x = 0.4$. Shown here are three peaks: a peak at $Q = 1.7$ Å describes the $(210)_{tetragonal}$, a peak at $Q = 1.85$ Å describes the $(202)_{cubic}$, a peak at $Q = 2.0$ Å describes the $(212)_{tetragonal}$.

during symmetry lowering phase transitions, are presented in Figure 4.3. Full diffraction patterns are presented in Figure 4.6. The crystallographic phase behavior determined from Pawley refinements is summarized in Figure 4.5. As the orientational disorder of $CH_3NH_3^+$ prevents the determination of accurate atomic positions, Pawley refinements were preformed to assign space groups and obtain lattice parameters. While no incommensurate phases were detected, we cannot rule out their presence given the temperature steps used in this experiment.[192,195] Initial space groups assignments were chosen based on those of the end members $CsPbBr_3$ and $CH_3NH_3PbBr_3$ and were found to be consistent with the collected neutron and X-ray diffraction patterns. Qualitatively, the cubic phase (space group $Pm\bar{3}m$) is characterized by a lack of peak splitting in the $(200)_{cubic}$ peak (Figure 4.3). Splitting of this peak as well as the appearance of the $(210)_{tetragonal}$ peak at $Q = 1.7$ Å (Figure 4.7) indicates a decrease in symmetry to either of two tetragonal perovskite lattices (space groups $I4/mcm$ and $P4/mbm$) or the orthorhombic perovskite lattice (space group $Pbnm$). Both the $Pbnm$ and $P4/mbm$ lattices are characterized by the presence of a peak at $Q = 2$ Å , while this peak is systematically absent in the $I4/mcm$ lattice (Figure 4.7). The $Pbnm$ and $P4/mbm$ lattices can be differentiated by the peaks shown in Figure 4.8; in the $P4/mbm$ lattice these peaks describe the $(204)_{tetragonal}$ and the $(312)_{tetragonal}$, while in the $Pbnm$ lattice these peaks split further into the $(024)_{orthorhombic}$, $(204)_{orthorhombic}$, $(312)_{orthorhombic}$, and $(132)_{orthorhombic}$. These descriptors were validated with Pawley and Rietveld refinements (Figures 4.9, 4.10, 4.11, and 4.12).

$CH_3NH_{3\,0.9}Cs_{0.1}PbBr_3$ undergoes similar phase transitions as $CH_3NH_3PbBr_3$, from a cubic perovskite lattice ($Pm\bar{3}m$) at room temperature, to a tetragonal perovskite lattice

($I4/mcm$) at $T = 240$ K, and finally to an orthorhombic perovskite lattice ($Pbnm$) at $T = 130$ K. $(CH_3NH_3)_{0.7}Cs_{0.7}PbBr_3$ transitions from the cubic $Pm\bar{3}m$ lattice to the tetragonal $P4/mbm$ lattice at $T = 190$ K. There is a subtle deviation in the c lattice parameter extracted from Pawley refinements that could indicate a second phase transition close to $T = 100$ K (Figure 4.13). However, based on the lack of peak splitting or appearance of new peaks in the diffraction data within our resolution and signal to noise ratio (Figure 4.11) we do not assign a different low temperature crystal structure. $(CH_3NH_3)_{0.6}Cs_{0.4}PbBr_3$ also transitions from the cubic $Pm\bar{3}m$ lattice to the tetragonal $P4/mbm$ lattice at $T = 260$ K. A small $CsPbBr_3$ impurity is also present (Figure 4.14), although the difficulty in describing the atomic positions of the organic cation in the major phase means the intensities are not well described in a Rietveld refinement, making accurate determinations of the mole percent of the impurity challenging. $(CH_3NH_3)_{0.6}Cs_{0.4}PbBr_3$ undergoes a second phase transition to the tetragonal $Pbnm$ lattice at $T = 140$ K. However, the complex splitting pattern near $Q = 1.8$ Å cannot be described by the major $Pbnm$ phase and the $CsPbBr_3$ impurity (Figure 4.14). To accurately index the peaks, three phases must be included: the major $Pbnm$ phase, a $P4/mbm$ phase, and an orthorhombic $CsPbBr_3$ impurity. This suggests that the phase transition to the low temperature orthorhombic phase is not complete, and the tetragonal phase persists to room temperature, as is consistent with the behavior of $(CH_3NH_3)_{0.7}Cs_{0.3}PbBr_3$.

Notably, $(CH_3NH_3)_{0.8}Cs_{0.2}PbBr_3$ undergoes a reentrant phase transition, transitioning from the cubic perovskite lattice ($Pm\bar{3}m$) at room temperature to the tetragonal perovskite lattice ($I4/mcm$) at $T = 240$ K, before returning to the cubic perovskite lattice

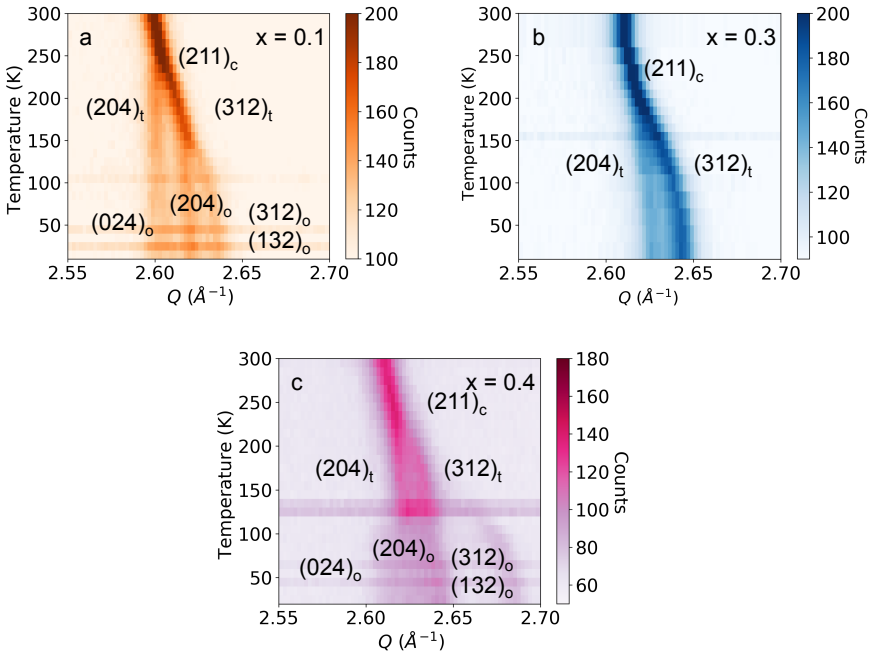

Figure 4.8: Selected region of high resolution neutron diffraction patterns as a function of temperature for $(CH_3NH_3)_{1-x}Cs_xPbBr_3$ where (a) $x = 0.1$, (b) $x = 0.3$, and (c) $x = 0.4$. Shown here is the (211) peak in the cubic phase, which splits into the (204) and (312) peaks in either tetragonal phase, and splits further into the (024), (204), (312), and (132) when referenced to the orthorhombic phase.

at $T = 150$ K. The increase in lattice symmetry upon cooling is apparent from the peak splitting and rejoining in Figure 4.3b and is confirmed by low temperature high resolution synchrotron XRD (Figure 4.15). Reentrant phase transitions have been previously observed in hybrid perovskites; $CH(NH_2)_2PbI_3$ undergoes a reentrant phase transition on cooling from a cubic lattice, to a tetragonal lattice, to a higher symmetry tetragonal lattice.[20,59] However, at $T = 150$ K $(CH_3NH_3)_{0.8}Cs_{0.2}PbBr_3$ reverts to the same cubic structure as at high temperature (Figure 4.15); this ignores the $CH_3NH_3^+$ positions, which are disordered in both phases. While the unit cell volume decreases monotonically in $CH(NH_2)_2PbI_3$, in $(CH_3NH_3)_{0.8}Cs_{0.2}PbBr_3$ there is a slight expansion of the unit cell volume at $T = 150$ K during the low temperature phase transition (Figure 4.16).

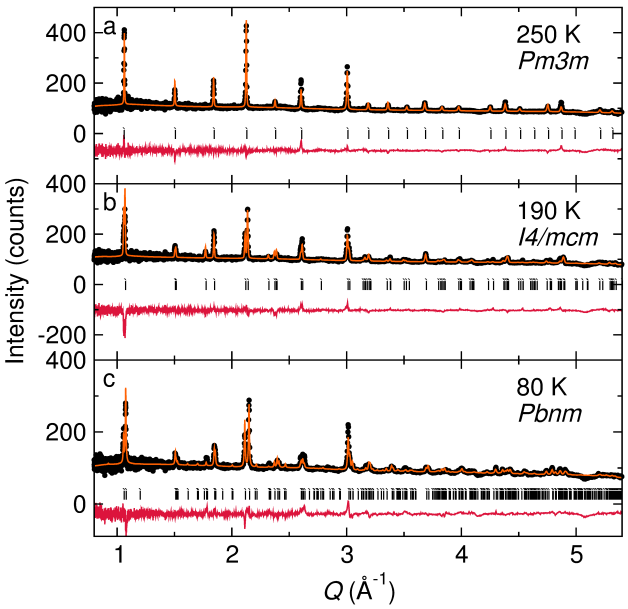

Figure 4.9: High resolution neutron diffraction data of $(CH_3NH_3)_{0.9}Cs_{0.1}PbBr_3$ at (a) $T = 250$ K (b) $T = 190$ K and (c) $T = 80$ K. Data are represented as black circles, models from Rietveld refinements as solid orange lines, peak indexes as vertical black lines, and the difference between the model and the data as a red line.

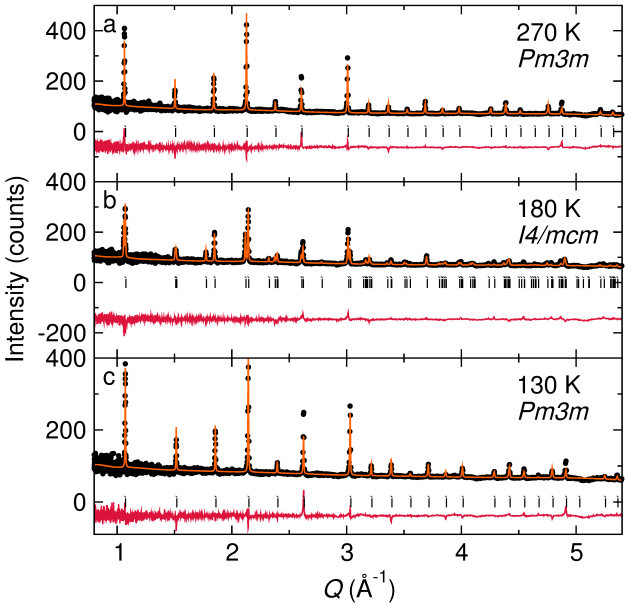

Figure 4.10: High resolution neutron diffraction data of $(CH_3NH_3)_{0.8}Cs_{0.2}PbBr_3$ at (a) $T = 270$ K (b) $T = 180$ K and (c) $T = 130$ K. Data are represented as black circles, models from Rietveld refinements as solid orange lines, peak indexes as vertical black lines, and the difference between the model and the data as a red line.

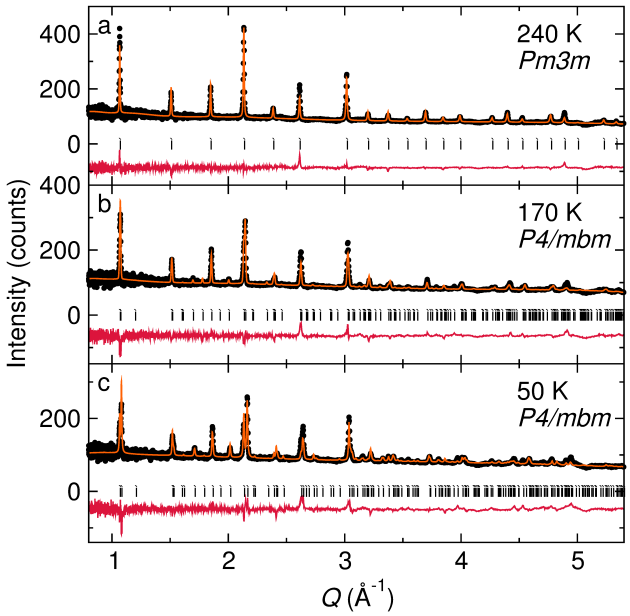

Figure 4.11: High resolution neutron diffraction data of $(CH_3NH_3)_{0.7}Cs_{0.3}PbBr_3$ at (a) $T = 240$ K (b) $T = 170$ K and (c) $T = 50$ K. Data are represented as black circles, models from Rietveld refinements as solid orange lines, peak indexes as vertical black lines, and the difference between the model and the data as a red line.

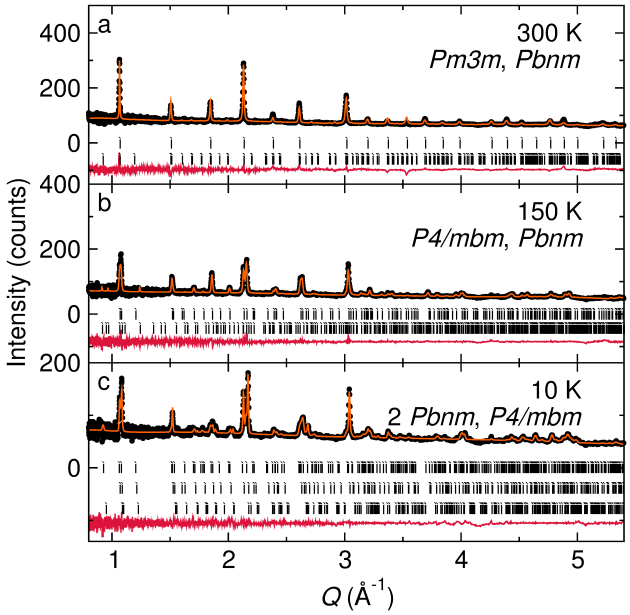

Figure 4.12: High resolution neutron diffraction data of $(CH_3NH_3)_{0.6}Cs_{0.4}PbBr_3$ at (a) $T = 300$ K (b) $T = 150$ K and (c) $T = 10$ K. Data are represented as black circles, models from Pawley refinements as solid orange lines, peak indexes as vertical black lines, and the difference between the model and the data as a red line.

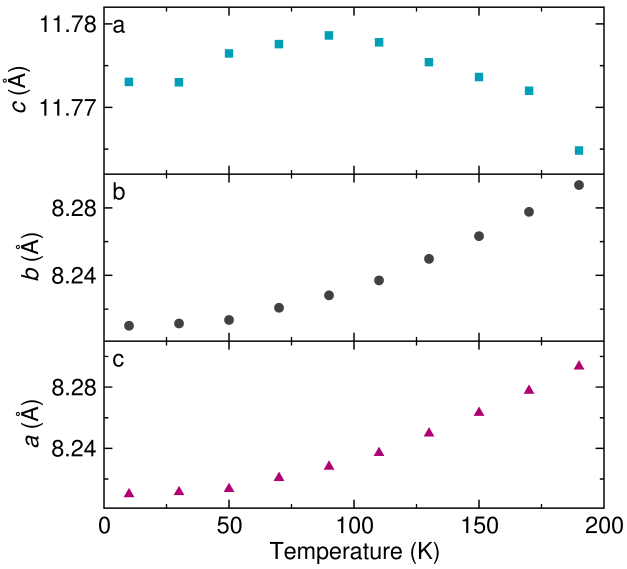

Figure 4.13: Temperature dependence of the lattice parameters of $(CH_3NH_3)_{0.7}Cs_{0.3}PbBr_3$ from Pawley refinments of high resolution neutron diffraction data.

The NPD data collected of $(CH_3NH_3)_{1-x}Cs_xPbBr_3$, where $x = 0.1, 0.2, 0.3,$ and 0.4 at $T = 300$ K, 100 K, and 10 K were analyzed using the Rietveld method to determine if there is preferred orientation of $CH_3NH_3^+$ in the cuboctahedral void. Residual nuclear density maps generated from Rietveld refinements of only the inorganic framework, shown in Figures 4.17, demonstrate that there is no preferred $CH_3NH_3^+$ orientation in $(CH_3NH_3)_{1-x}Cs_xPbBr_3$, where $x = 0.1, 0.2, 0.3,$ and 0.4 in either the high temperature or low temperature phases.

Heat capacity data indicate that cesium substitution changes the nature of the phase transitions of the substituted materials relative to $CH_3NH_3PbBr_3$ (Figure 4.18). In the end member $CH_3NH_3PbBr_3$, all expected peaks appear in the heat capacity data (Figure 4.18a) that correlate with the three previously known phase transitions ($T = 240$ K, $T = 154$ K, $T = 148$K).[175] These peaks are narrow and well resolved. As cesium is added to the lattice, these peaks broaden such that the curve shows no features when $x \geq 0.2$ (Figure

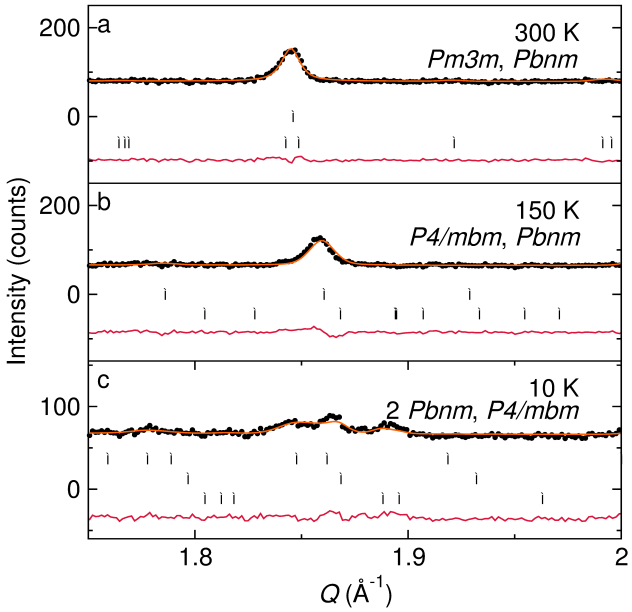

Figure 4.14: Selection of high resolution neutron diffraction data of $(CH_3NH_3)_{0.6}Cs_{0.4}PbBr_3$ at (a) $T = 300$ K (b) $T = 150$ K and (c) $T = 10$ K. Data are represented as black circles, models from Pawley refinements as solid orange lines, peak indexes as vertical black lines, and the difference between the model and the data as a red line.

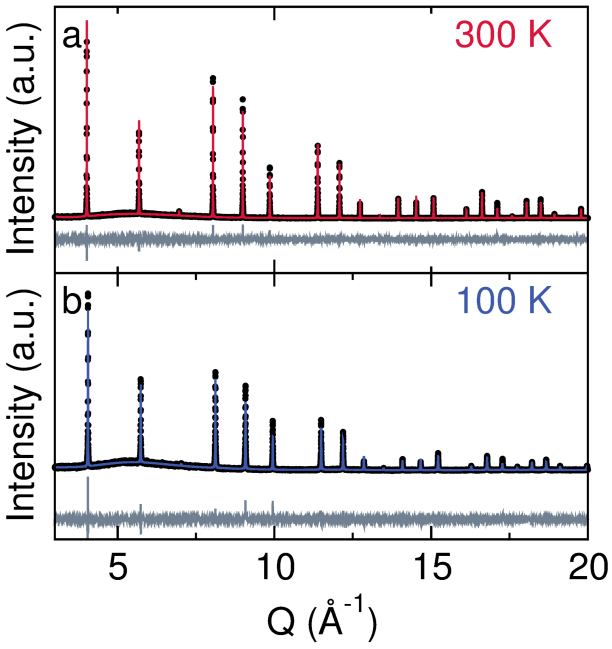

Figure 4.15: High resolution synchrotron X-ray diffraction of $(CH_3NH_3)_{0.8}Cs_{0.2}PbBr_3$ at (a) 300 K and (b) 100 K. Data are shown as dots, fits as lines and the difference is shown in gray. At both temperatures the data are consistent with a cubic perovskite lattice.

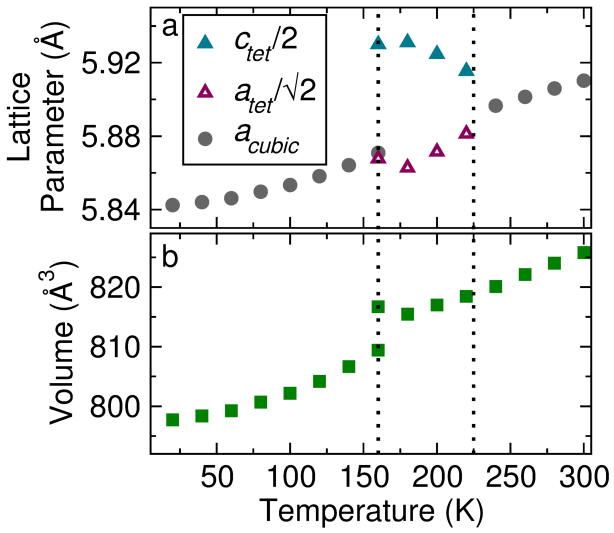

Figure 4.16: (a) The pseudocubic lattice parameters of $(CH_3NH_3)_{0.8}Cs_{0.2}PbBr_3$ extracted from Pawley refinements as a function of temperature. (b) Volume of a formula unit of $(CH_3NH_3)_{0.8}Cs_{0.2}PbBr_3$ calculated from lattice parameters extracted from Pawley refinements. Crystallographic transition temperatures are indicated with vertical dashed lines.

4.18b). When the heat capacity is normalized to T^3 (based on the Deybe model of acoustic phonons), the heat capacity at low temperature increases as x increases (Figure 4.18c), suggestive of an excess of low energy modes from increased disorder.[213]

Inelastic neutron scattering (INS) spectra show that the vibrational modes thought to be indicators of the phase transitions in $CH_3NH_3PbBr_3$ become disordered as Cs^+ concentration increases. In particular, the phase transitions of hybrid perovskites manifest crystallographically through tilting of the inorganic octahedra;[174,175] the phonons related to octahedral tilting can be tracked through INS.[25,192] Calculations allow the assignment of the peak at 4-5 meV to octahedral dynamics and the peak at 33-37 meV to $CH_3NH_3^+$ torsion (additional details about the assignments can be found in Figures 4.20 and 4.21 and the discussion within). Both the peaks describing the octahedral dynamics and $CH_3NH_3^+$ torsion (Figure 4.19a) broaden as Cs^+ is added to the lattice, indicative of heterogenous envi-

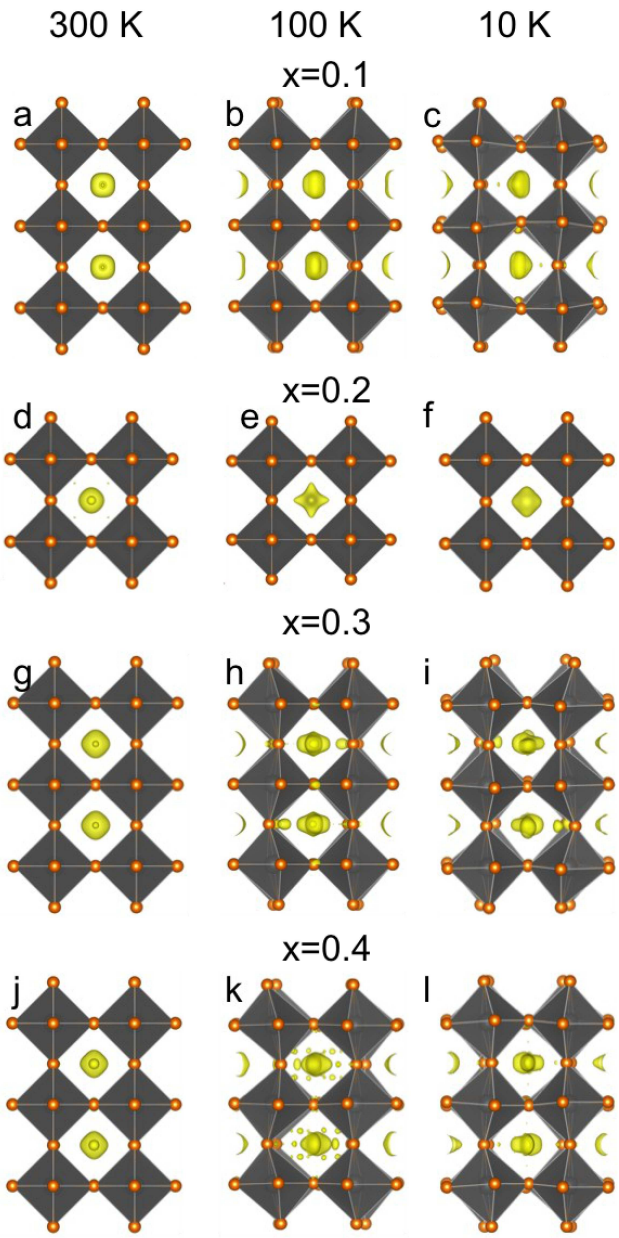

Figure 4.17: Visualization of the residual nuclear density in $(CH_3NH_3)_{1-x}Cs_xPbBr_3$ based off a Rietveld refinement of high resolution neutron diffraction patterns with the A-site cation omitted for $x = 0.1$ at (a) $T = 300$ K and (b) $T = 100$ K, and (c) $T = 10$ K, $x = 0.2$ at (d) $T = 300$ K and (e) $T = 100$ K, and (f) $T = 10$ K, $x = 0.3$ at (g) $T = 240$ K and (h) $T = 100$ K, and (i) $T = 10$ K, $x = 0.4$ at (j) $T = 300$ K and (k) $T = 100$ K, and (l) $T = 10$ K. Residual nuclear density maps were extracted at an isosurface level of 0.19.

ronments of both the inorganic octahedra and $CH_3NH_3^+$. The average energy of the modes as described in Figures 4.19b and 4.19c were extracted by fitting the peaks to a Gaussian distribution and extracting the center of the peak (Figure 4.21a,b). In $CH_3NH_3PbBr_3$ mul-

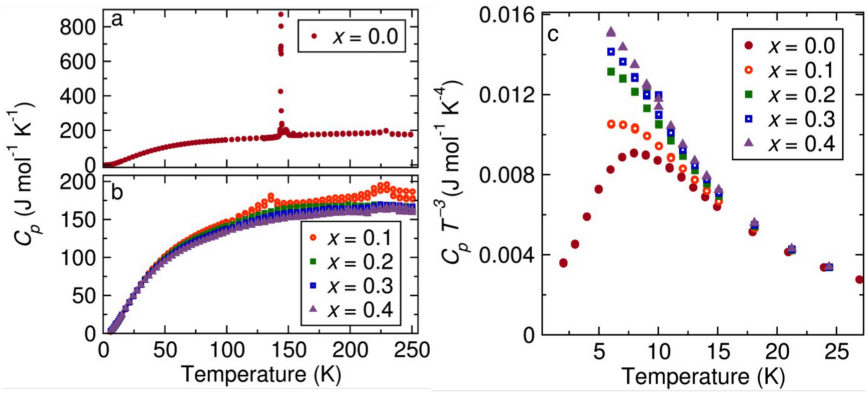

Figure 4.18: Heat capacity data for (a) $CH_3NH_3PbBr_3$, (b) $(CH_3NH_3)_{1-x}Cs_xPbBr_3$, where x = 0.1, 0.2, 0.3, and 0.4; (c) the low temperature heat capacity normalized by the T^3 Debye model for $(CH_3NH_3)_{1-x}Cs_xPbBr_3$, where x = 0.1, 0.2, 0.3, and 0.4.

tiple optical phonons can be resolved; however, this resolution disappears with Cs^+ substitution. This analysis shows that the disorder at inorganic and organic sites are correlated to a softening of octahedral dynamics and $CH_3NH_3^+$ torsion as Cs^+ is added to the lattice.

To further elucidate the dynamics of $CH_3NH_3^+$, particularly those that change the intermolecular interactions between $CH_3NH_3^+$ and the inorganic framework, we collected quasielastic neutron scattering (QENS) spectra of $(CH_3NH_3)_{1-x}Cs_xPbBr_3$ for x = 0.0, 0.1, 0.2, 0.3, and 0.4. Representative QENS spectra are shown in Figures 4.24 and 4.25. From QENS spectra, we extracted a mean squared displacement (MSD, $\langle u^2 \rangle$ as described in the SI) which are plotted in Figure 4.23. The MSD are most representative of hydrogen motion, as the neutron scattering cross section of hydrogen is nearly an order of magnitude greater than the neutron cross section of the other constituent elements. The data for $CH_3NH_3PbBr_3$ are consistent with previous experiments, showing a monotonic decrease in MSD as temperature is reduced, until $T = 150$ K at which point the MSD dramatically decreases in magnitude.[192] The change in slope of the MSD correlates with the tetragonal to orthorhombic phase transition, as illustrated by the bars describing the phase behavior in

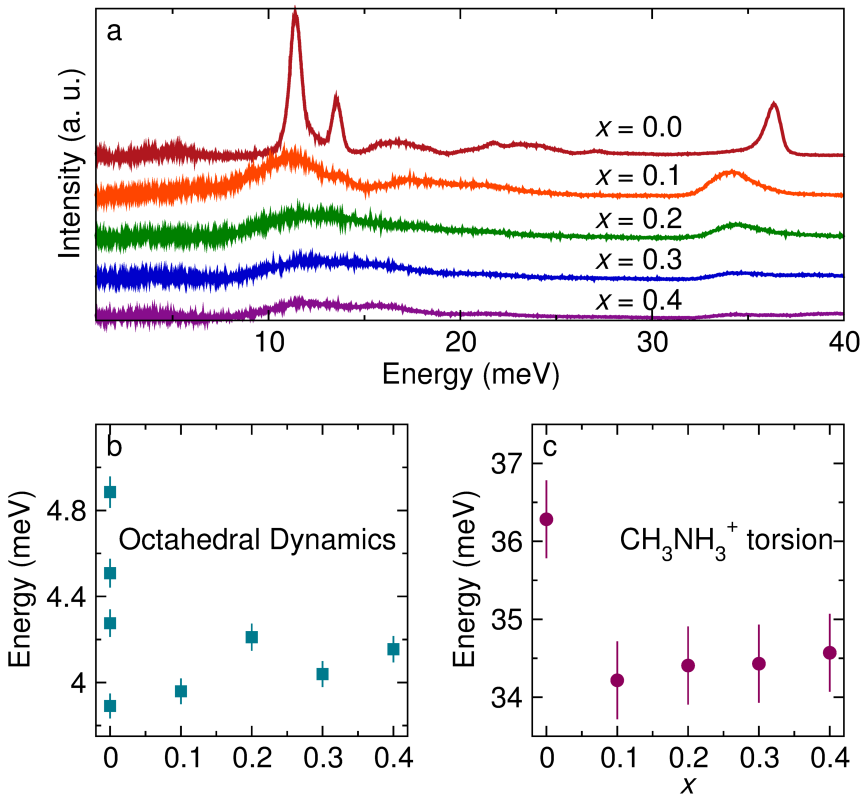

Figure 4.19: (a) INS spectra collected at $T = 5$ K of $(CH_3NH_3)_{1-x}Cs_xPbBr_3$ over the energy range 2-40 meV. (b) The centroid of the low-lying optic phonons (4-5 meV) as a function of x. (c) The average energy of the $CH_3NH_3^+$ torsion (33-37 meV) as a function of x. Error bars in (b) and (c) are taken from the instrument resolution, respectively. The centroid of the peaks were determined by fitting the peak in the INS spectra to a Gaussian function and extracting the center (Figure 4.22).

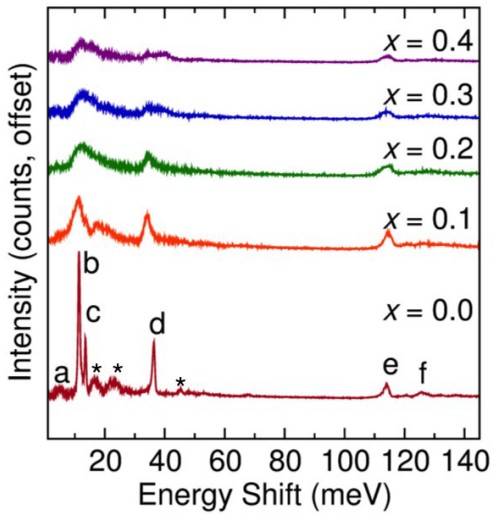

Figure 4.20: INS spectra of $(CH_3NH_3)_{1-x}Cs_xPbBr_3$ collected at $T = 5$ K. The modes of $CH_3NH_3PbBr_3$ are labeled to correspond to modes calculated using phonopy as described in the Experimental Methods section: a indicates an octahedral rotation, b and c indicate coupled octahedral rotations and $CH_3NH_3^+$ librations, d indicates $CH_3NH_3^+$ torsion, e and f indicate internal methylammonium vibrations. Asterisks indicate second overtones.

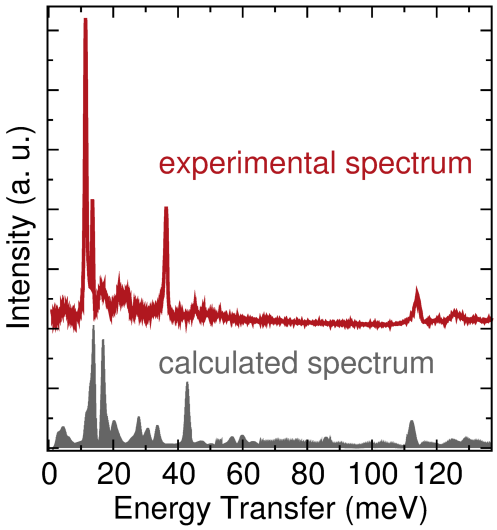

Figure 4.21: Experimental INS spectrum of octahedral $CH_3NH_3PbBr_3$ collected at $T = 5$ K compared to the calculated spectrum. More details about the calculation can be found in the Experimental Methods section.

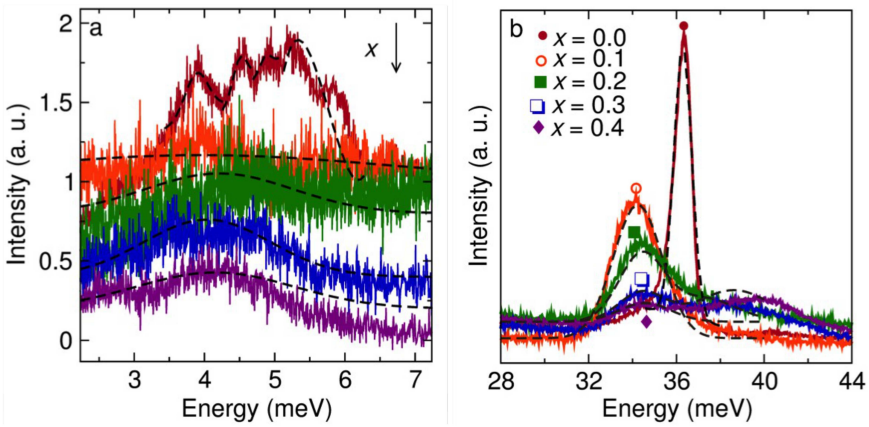

Figure 4.22: Gaussian fits to the INS spectra of $(CH_3NH_3)_{1-x}Cs_xPbBr_3$ collected at $T = 5$ K for energy ranges between (a) 4-5 meV and (b) 32-38 meV, which correspond to octahedral dynamics and $CH_3NH_3^+$ torsion respectively.

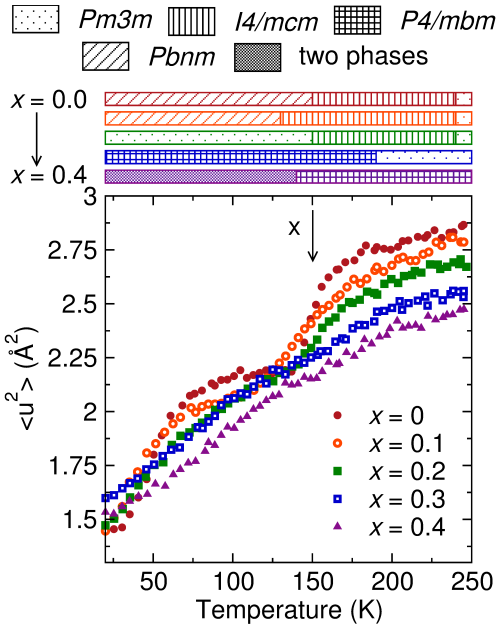

Figure 4.23: Mean squared displacement ($\langle u^2 \rangle$) of hydrogen as a function of temperature extracted from QENS spectra of $(CH_3NH_3)_{1-x}Cs_xPbBr_3$ illustrating a smearing of transitions and decreased MSD amplitude with increasing x. The bars at the top illustrate the observed lattice symmetry of $(CH_3NH_3)_{1-x}Cs_xPbBr_3$ for $x = 0.0, 0.1, 0.2, 0.3$, and 0.4. Dotted fill indicates a cubic perovskite lattice, striped fill indicates a tetragonal perovskite lattice, diagonal striped fill indicates an orthorhombic perovskite lattice, and hatched fill indicates a two-phase region.

Figure 4.23. Two significant changes occur as cesium content increases. First, the overall magnitude of the MSD decreases as x increases, as is especially clear at high temperatures. Second, at low values of x the slope of the MSD still changes as the lattice symmetry

changes, for $x \geq 0.3$, the MSD decreases continuously over all measured temperatures. This is consistent with the smeared out features in the heat capacity data in Figure 4.18.

Table 4.1: Activation Energies extracted from the slopes of the fit lines in Figure 4.29.

x	**Activation Energy**
0.0	22 meV
0.1	6.9 meV
0.2	4.5 meV
0.3	10. meV
0.4	9.6 meV

Further information about the inhibited molecular motion was obtained through analysis of the Q-dependence of the QENS spectra in the form of the elastic incoherent structure factor (EISF) extracted from the QENS spectra. The EISF is defined as the fraction of elastic scattering out of total scattering, and the slope and shape of the EISF as a function of Q gives additional information about the types of dynamics present in the material , as shown in Figure 4.27.[26,214] Previously, QENS has been used to identify two types of methylammonium molecular dynamics in methylammonium lead halide perovskites: a rotation along the C_3 symmetry axis parallel to the C–N bond that dominates at low temperatures (here denoted as a C_3 rotation) and a $C_3 \otimes C_4$ rotation in which rotation about the C_3 axis occurs concurrently with a molecular reorientation around the C_4 axis of the unit cell that dominates at higher temperatures.[26,191] The EISF curves are well modeled using zeroth-order Bessel functions that describe these rotations with parameters derived from Group Theory.[26] These models assume that if a molecule is not participating in a given motion, such as the $C_3 \otimes C_4$ rotation, the molecule is frozen on the timescale that falls within the instrument resolution. The decrease in MSD with increasing x and decreasing T (Figure

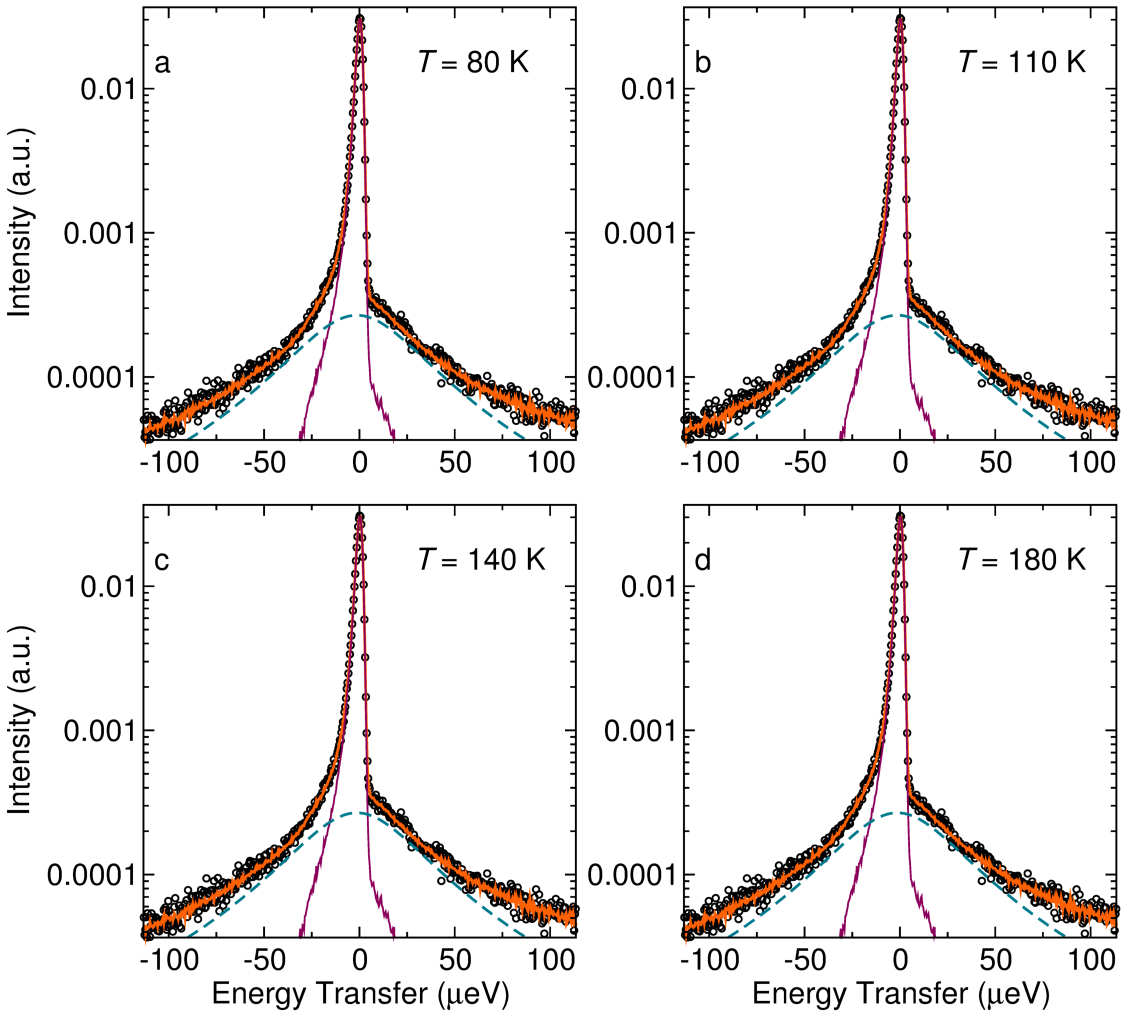

Figure 4.24: Representative QENS spectra of $CH_3NH_3PbBr_3$ at $T =$ (a) 80 K, (b) 110 K, (c) 140 K, and (d) 180 K for $Q = 0.9$. The spectra are shown as black circles, with the overall fit shown as a thick orange line. The data are modeled with a delta function convolved with an instrument resolution function collected for each sample at $T = 20$ K to account for elastic scattering, shown here as a thin pink line. The broadening from quasielastic scattering fit is with a Lorenztian, shown as a dashed green line. See Eqn. 4.3.

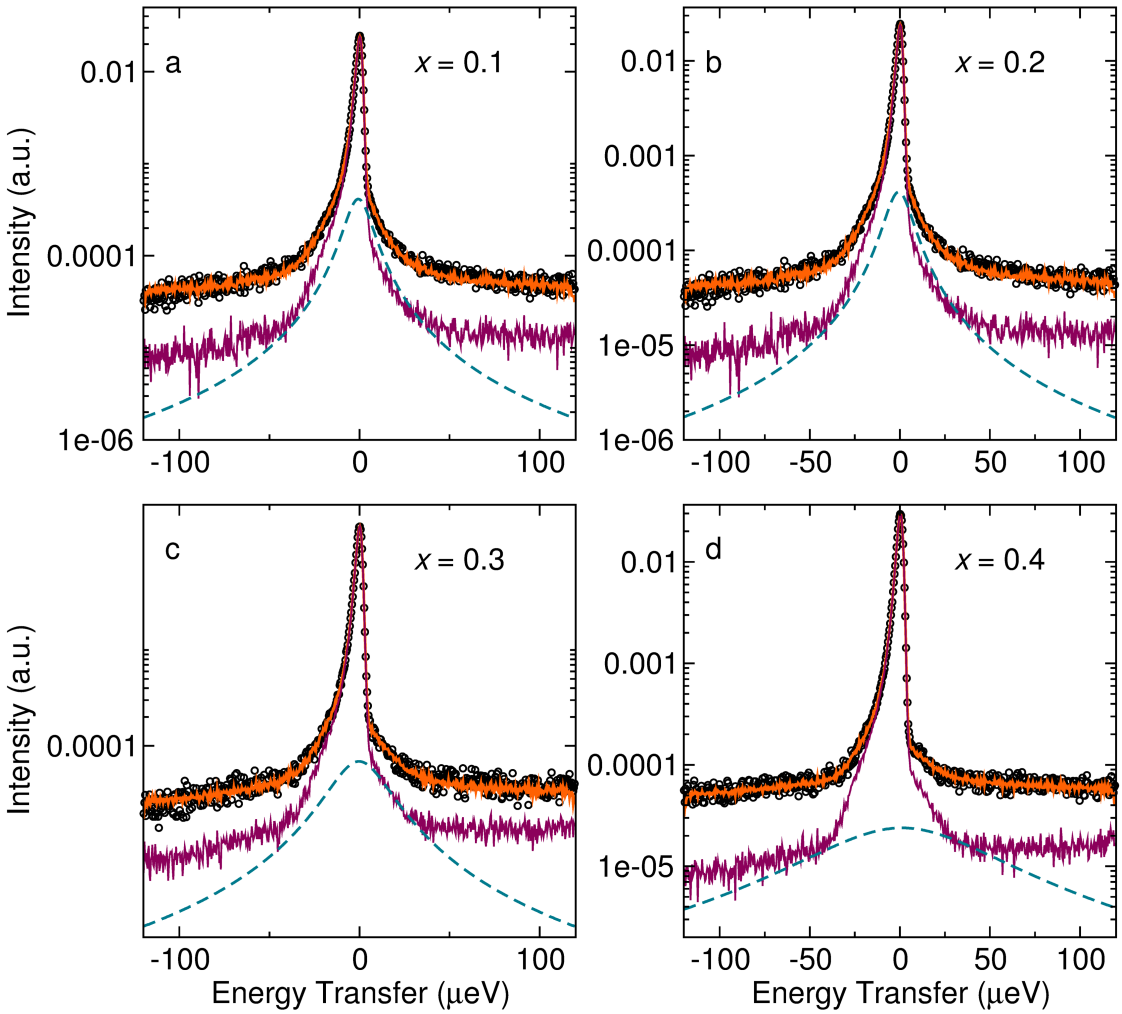

Figure 4.25: Representative QENS spectra of $(CH_3NH_3)_{1-x}Cs_xPbBr_3$ at $T = 140$ K at $Q = 0.9$. The spectra are shown as black circles, with the overall fit shown as a thick orange line. The data are modeled with a delta function convolved with an instrument resolution function collected for each sample at $T = 20$ K to account for elastic scattering, shown here as a thin pink line. The broadening from quasielastic scattering is fit with a Lorentzian, shown as a dashed green line. See Eqn. 4.3.

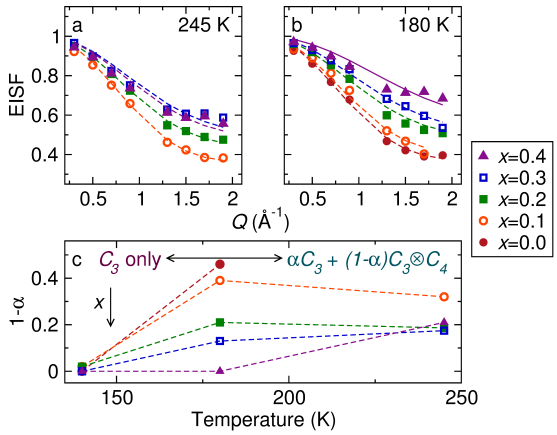

Figure 4.26: Selected EISF values for $(CH_3NH_3)_{1-x}Cs_xPbBr_3$ extracted from QENS spectra collected at (a) $T = 245$ K and (b) $T = 180$ K. Dashed lines are fits to the $(\alpha C_3 + (1-\alpha)(C_3 \otimes C_4))$ model, while solid lines are fits to the C_3 model. (c) The fraction of $CH_3NH_3^+$ participating in a $C_3 \otimes C_4$ rotation $(1-\alpha)$ as extracted from the EISF modeling. Dashed lines are guides to the eye.

4.23) is consistent with the freezing out of the $C_3 \otimes C_4$ rotation; however, at elevated temperatures $CH_3NH_3^+$ may still reorient about its C_3 axis. Above the $C_3 \otimes C_4$ freezing temperature the EISF curves are best described as a linear combination of the C_3 and $C_3 \otimes C_4$ rotational models, such that a given molecule is either participating in the $C_3 \otimes C_4$ rotation or only the C_3 rotation. The linear combination is denoted $(\alpha C_3 + (1-\alpha)(C_3 \otimes C_4))$, where α is a refineable scale factor. Fits of the extracted EISF values to both models (C_3 and $(\alpha C_3 + (1-\alpha)(C_3 \otimes C_4))$) are plotted in Figure 4.27 for all compositions and temperatures.

From inspection of the EISF curves (Figure 4.26), as the concentration of cesium increases, the fraction of elastic scattering increases at a given temperature, which is consistent with the MSD (Figure 4.23). The fits of the models to the data demonstrate that this decrease in dynamics corresponds to an inhibition of the $C_3 \otimes C_4$ rotation. Inspection of the refining parameters (Figure 4.26c) show that the fraction of molecules participating in the $C_3 \otimes C_4$ rotation decreases as x increases at all measured temperatures. This is especially notable at $T = 180$ K, where the $C_3 \otimes C_4$ rotation is accessible in the samples

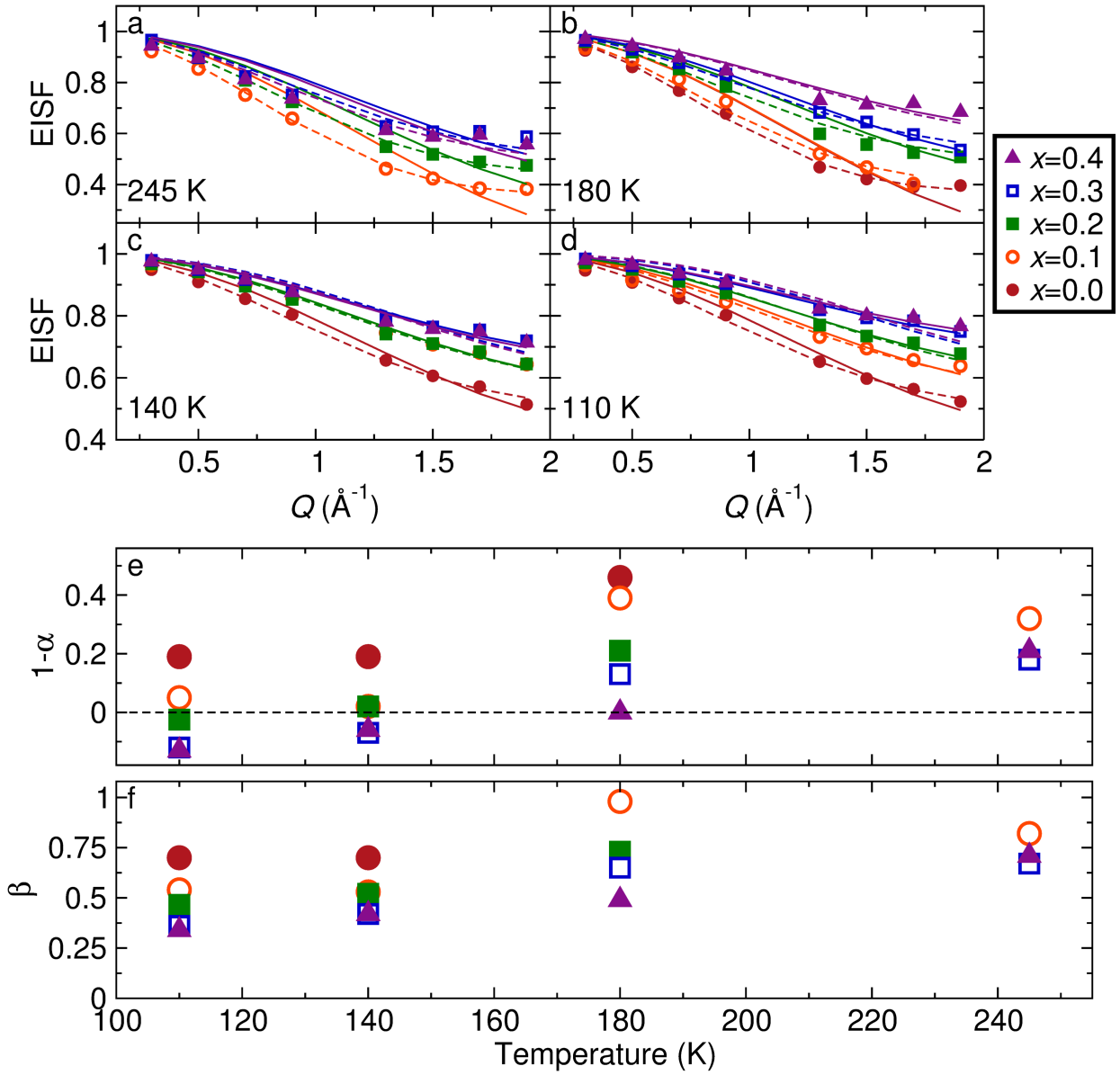

Figure 4.27: EISF as a function of Q from QENS spectra of $(CH_3NH_3)_{1-x}Cs_xPbBr_3$ collected at T = (a) 245 K, (b) 180 K, (c) 140 K, (d) 110 K. Extracted EISF values are shown as data points, while the fit to either the $(\alpha \times C_3 + (1-\alpha) \times (C_3 \otimes C_4))$ or C_3 rotational model is shown as a dashed or solid line, respectively. (d) The scale factor $(1-\alpha)$ for the $(\alpha \times C_3 + (1-\alpha) \times (C_3 \otimes C_4))$ model as a function of temperature for several values of x. When $(1-\alpha) \leq 0$, shown by the dashed line, the model is no longer physically meaningful, and the C_3 model is used, which corresponds to a better or equivalent visual fit. (e) The fraction of hydrogen atoms on methylammonium participating in the C_3 rotation as a function of temperature for several values of x. Assuming the ammonium hydrogen atoms hydrogen bond to bromide, an initial value of 0.5 is reasonable. This model is used for temperatures where $\alpha \leq 0$.

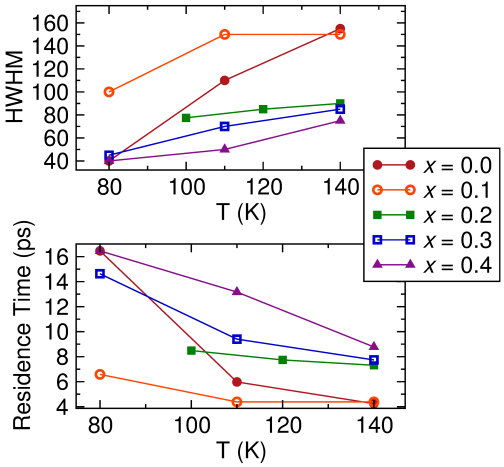

Figure 4.28: Residence times (τ) extracted from QENS spectra according to the formula $HWHM_{Lorentzian} = \frac{h}{2\pi\tau}$.

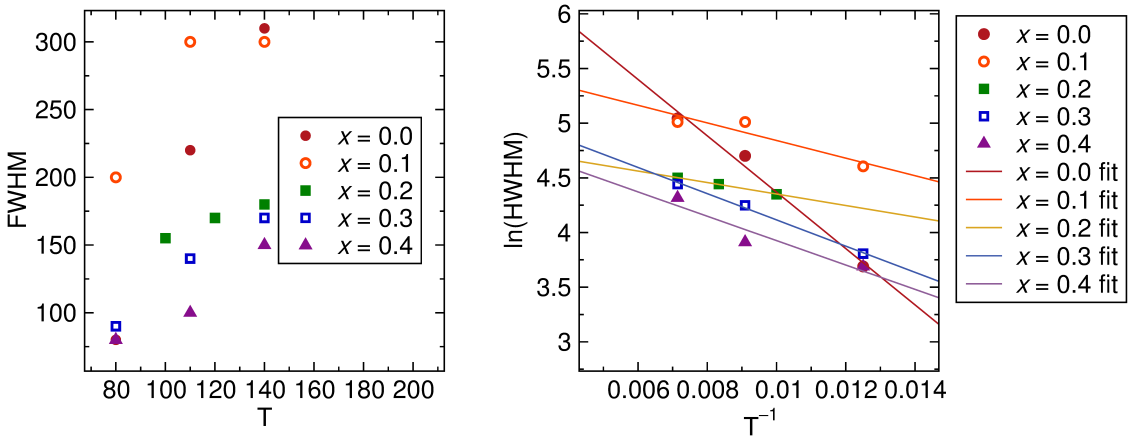

Figure 4.29: (a) The Full-Width-Half-Maximum (FWHM) of the peak in the QENS spectra (Figures 4.24, 4.25) can be used to extract the activation energy of the mode contributing to the quasielastic broadening of the peak. (b) Arrhenius plot where $\ln(HWHM) = \ln(A) - \frac{E_a}{R}\frac{1}{T}$. The activation energies (E_a) extracted from linear regressions are presented in Table 4.1. This analysis can be done if only one dynamic mode is detected; therefore, activation energies cannot be extracted above the freezing temperature of the $C_3 \otimes C_4$ rotation (i.e. after the $\alpha C_3 + (1-\alpha)C_3 \otimes C_4$ model is no longer used).

for $x \leq 0.3$ but is completely frozen for $x = 0.4$ (Figure 4.26c). The $C_3 \otimes C_4$ rotation is frozen out in the low temperature crystal structure for all samples studied. This aligns with the longer residence times in more substituted samples (Figure 4.28) and decrease in activation energies listed in Table 4.1, calculated from the widths of QENS peaks as described in Figure 4.29.

Discussion

The inorganic lattice symmetry and $CH_3NH_3^+$ dynamics described above can be explained by considering these materials as transitioning from a dynamically disordered plastic crystal to an orientational glass with inhibited molecular dynamics as a function both of temperature and of Cs^+ concentration. This paradigm has recently been suggested from the analysis of $ab\ initio$ molecular dynamics simulations of hybrid perovskites.[17] The description of methylammonium lead halide perovskites as plastic crystals at high temperatures is based on the observation that $CH_3NH_3^+$ is dynamic in the cuboctahedral void.[26,175,192] However, the low temperature behavior of many hybrid materials has remained enigmatic, as the organic cation and inorganic framework are not decoupled.

The data presented here show that $(CH_3NH_3)_{1-x}Cs_xPbBr_3$ behaves as an orientational glass at low temperatures and at high x. Both the smearing of the peaks in the heat capacity data (Figure 4.18) during phase transitions and the increased low energy vibrational density of states observed in Figure 4.18c and Figure 4.19 are consistent with a glass forming system.[215,216] The excess localized vibrational modes indicated in Figure 4.18c result from local heterogeneities, further suggested by the increase in residence time calculated

from the peak width in the QENS spectra (Figure 4.28). These slow relaxations are consistent with the increasing persistence of temperature-dependent hysteresis during the phase transitions as a function of x. The inhibition of $CH_3NH_3^+$ molecular reorientations (Figure 4.26), and the heterogeneity of $CH_3NH_3^+$ environments (Figure 4.19) observable in the neutron scattering data provide more evidence for orientational glass behavior. Furthermore, the lack of preferred orientation of $CH_3NH_3^+$ observed in Rietveld refinements demonstrates orientational disorder at low temperatures (Figures 4.17). The glassiness is not isolated to the organic sublattice and influences the inorganic framework. The Pb–Br framework and organic sublattice in hybrid perovskites are known to be coupled,[191,195,217] and the peak broadening in the INS spectra (Figure 4.19) demonstrate the presence of disorder in the inorganic framework as $CH_3NH_3^+$ is diluted with Cs^+. Furthermore, as the concentration of Cs^+ increases, the octahedral tilt patterns change to more closely resemble those of $CsPbBr_3$, even though the majority of A-site cations are still $CH_3NH_3^+$. These results together illustrate that the glassy $CH_3NH_3^+$ dynamics directly relate to the nature of the crystallographic transitions.

A simple description of the slow molecular dynamics of $CH_3NH_3^+$ and its influence on the inorganic crystallographic transitions can be provided by considering the frustration caused by local strain, attributed to differences in size and shape of the Cs^+ and $CH_3NH_3^+$ cations. According to the Goldschmidt tolerance factor, smaller cations prefer a smaller, more distorted cuboctahedral void, which improves coordination of the A-site cation by the surrounding X-site anions.[77,177] In the mixed cation solid solution series $(CH_3NH_3)_{1-x}Cs_xPbBr_3$, the framework of corner-sharing lead bromide octahedra

must sufficiently coordinate both the small, spherical cesium cation as well as the larger, oblate methylammonium cation. The attempt to satisfy the bonding requirements for both cations leads to strain in the cuboctahedral A-site void. This geometric strain manifests in the behavior of the organic cation, where the collapse of the cuboctahedral void increases steric barriers to molecular reorientation (Figures 4.23, 4.26). As discussed above, the inhibition of $CH_3NH_3^+$ dynamics correlates with the disorder of the inorganic framework, leading to the glassiness of the phase transitions.

The change in tilting preferences in the tetragonal phase – from $a^0a^0c^-$ in $I4/mcm$ when $x \leq 0.2$ to resemble $CH_3NH_3PbBr_3$ to $a^0a^0c^+$ in $P4/mbm$ when $0.2 < x \leq 0.4$ to resemble $CsPbBr_3$ – highlights the nature of coupling between the organic and inorganic components and rationalizes compositional solubility. If the phase behavior was dictated solely based on cation size, we would expect solid-solution behavior across the entire series between $x = 0$ and $x = 1$, given that the lattice parameters for all x values follow Vegard's Law (Figure 4.2). We can instead explain this transition by considering previous descriptions of inorganic perovskite halides, which showed that in-phase tilting of $CsPbBr_3$ ($a^0a^0c^+$) permits increased Cs-Br covalency.[77] Therefore, this in-phase tilting preference of Cs helps us to understand the limited solubility of $CH_3NH_3^+$ in $CsPbBr_3$ ($x > 0.4$), as our results suggest static in-phase tilts are not compatible with a dynamic $CH_3NH_3^+$ cation and provides guidelines for compositional engineering.[59]

Previous studies of the series $K(CN)_{1-x}Br_x$ have shown that increasingly glassy behavior of the lattice and the phase transitions as a function of CN^- dilution by Br^- can be attributed to fluctuations in the local potential around substituted sites.[215,218–221] While it

is tempting to assume the local field changes can be attributed solely to the dilution of the electric field of CN^- or $CH_3NH_3^+$, dielectric susceptibility studies show that the geometric strain from the size and shape differences between CN^- and Br^- is competitive with, if not greater than, dipole field effects.[219,220] In either case, the reorientation of the substituted ion is limited by the local potential of the surrounding ions.[220,222] For any given $CH_3NH_3^+$ cation to reorient the cation must overcome an energy barrier from the Born-Landé potential of the inorganic framework. As the lattice deforms and changes tilt patterns to accommodate the mixed occupancy of $(CH_3NH_3)_{1-x}Cs_xPbBr_3$, this Born-Landé potential changes and, therefore, so does the ability of $CH_3NH_3^+$ to reorient. Modulation of this potential through ion substitution leads to the formation of the observed orientational glass.

To better understand how Cs^+ substitution in $CH_3NH_3PbBr_3$ leads to suppressed and reentrant phase transitions, we turn to models previously used to describe reentrant phase behavior in Rochelle salt ($NaKC_4H_4O_2 \cdot 4\,H_2O$).[223] A modified Blume-Capel Hamiltonian can be used to mathematically express the competing interactions that lead to this type of reeentrant behavior ($a.k.a.$ inverse melting) by describing strain coupling between pseudospins.[223,224] The Blume-Capel Hamiltonian for $S = 1$ pseudospins is expressed as:

$$H = -J \sum_{<i,j>} S_i S_j + D \sum_{i=1}^{N} S_i^2 + P\delta V \sum_{<i,j>} S_i S_j,$$

where the coefficient J describes the coupling strength between the i and j pseudospins, S; D describes the self-interaction of the pseudospin with the lattice. The third term describes

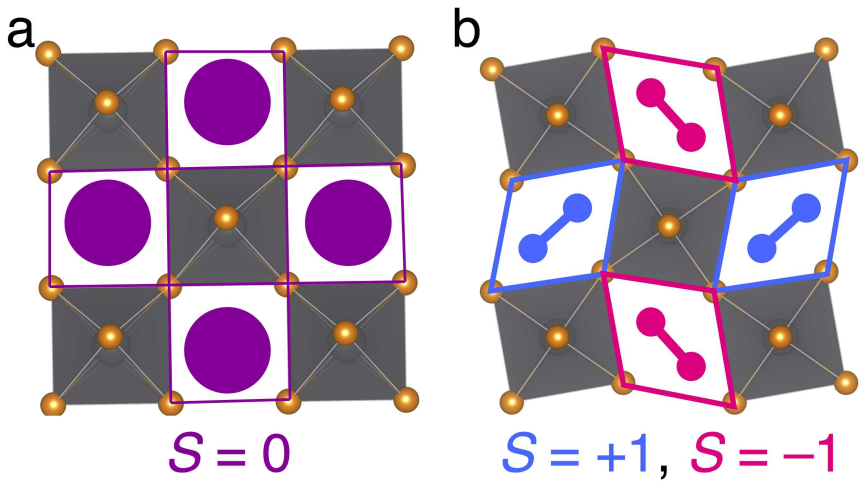

Figure 4.30: Schematic representation of (a) the cubic phase in $(CH_3NH_3)_{0.8}Cs_{0.2}PbBr_3$, where there is no unique orientation of $CH_3NH_3^+$ and (b) the idealized, tilted tetragonal phase in $(CH_3NH_3)_{0.8}Cs_{0.2}PbBr_3$, where there are two preferred orientations of $CH_3NH_3^+$.

a modulation in J that accounts for the energetic cost from the increased strain of two adjacent pseudospins with the same value of S if the material is compressed ($P\delta V > 0$).

According to the Blume-Capel Hamiltonian, reentrant phase transitions can occur when J and D compete between ordered ($J > D, \langle S \rangle = 1$) and disordered ($J < D, \langle S \rangle = 0$) ground states. This model has been mapped onto strained cubic lattices;[225] here we can map the strain pseudospin onto the strain of the cuboctahedral void. This strain directly couples the inorganic lattice via octahedral tilting to the orientational preference of $CH_3NH_3^+$ depicted schematically in Figure 4.30. While the complex energy landscape of hybrid perovskites prohibits explicit modeling, we can consider the forces that cause strain and lead to the observed reentrant phase behavior. Hydrogen bonding between the amine and the halides is known to occur for multiple orientations, with small energy barriers between them.[186,226] Therefore, hydrogen bonds provide a minimal driving force for $CH_3NH_3^+$ cations to align in the same direction and the coupling strength between neighboring $CH_3NH_3^+$ is small relative to interactions between $CH_3NH_3^+$ and Br^- ($J < D$). If we

consider the model used to describe Rochelle salt,[223] we estimate D as approximately 400 K, the energy of a weak hydrogen bond.[227] This strain coupling should supersede dipole-dipole coupling between individual $CH_3NH_3^+$ ions.[2] Conversely, the electrostatic interactions between the cation in the cuboctahedral void and the halide anions that form the void's cage lead to the anisotropy of the cuboctahedral void ($S = +1, -1$).[77] As depicted in Figure 4.30, the geometry of the tilted lattice necessitates that this anisotropy has at least short range order, which suggests a larger coupling strength between the shape of the cuboctahedral void and the organic cation orientation ($J > D$). In $(CH_3NH_3)_{0.8}Cs_{0.2}PbBr_3$ these are appropriately balanced to lead to a reentrant (*i.e.* inverse melting) transition.

Conclusions

In summary, we have prepared the series $(CH_3NH_3)_{1-x}Cs_xPbBr_3$ and characterized the phase behavior and organic cation dynamics as a function of x. Heat capacity and neutron scattering demonstrate glassy behavior at low T and at high x, despite the crystalline nature of the inorganic component; the glassiness principally manifests in orientationally disordered $CH_3NH_3^+$. Temperature-dependent neutron diffraction shows that $(CH_3NH_3)_{0.8}Cs_{0.2}PbBr_3$ undergoes a reentrant phase transition and that the transition from an out-of-phase octahedral tilt pattern to an in-phase octahedral tilt pattern results with increasing amounts of Cs^+. We have examined these two phenomena in terms of a random strain model and a modified Blume-Capel Hamiltonian to demonstrate that the glassiness and reentrance can be explained by considering the effects of a disordered $CH_3NH_3^+$ sublattice coupled to a periodic inorganic framework. This provides experimental validation

for computational methods that describe hybrid perovskites as a combination of an ordered lead-halide octahedral network and a disordered collection of dynamic organic cations.[17] Developing theory to describe the effects of substitution is essential for understanding how substitution in materials such as $Cs_{0.05}(CH_3NH_3)_{0.16}(CH(NH_2)_2)_{0.79}PbI_{2.49}Br_{0.51}$[202] improve device function. Previous work has shown that 5% to 10% Cs^+ doping in $CH_3NH_3PbI_3$ leads to the preservation of stoichiometry and a decrease in the rate of perovskite degradation.[205,206] We have shown that Cs^+ substitution inhibits dipole reorientations and disorders molecular dynamics, which suggests that ionic mobility is also reduced. As migration of halide and organic ions have been implicated in the degradation of hybrid perovskites,[12] the inhibition of organic cation dynamics through Cs^+ substitution could be responsible for the increased stability of doped perovskites. Similar inhibition of lattice dynamics has been observed in halide substituted hybrid perovskites, perhaps indicating a shared mechanism for resistance to decomposition.[210,211] Substitution in hybrid perovskites leads to geometric strain that has a profound influence on the dynamics and structure of hybrid perovskite halides, suggesting that the molecular dynamics and internal strain plays a significant role in the manifesting electronic properties and chemical stability that are essential for use of these materials in semiconducting devices.

Experimental Methods

Preparation: $CH_3NH_3PbBr_3$ and $CsPbBr_3$ perovskites were prepared based on literature reports.[181,185] In short, the precursor CH_3NH_3Br was prepared by dissolving $CH_3NH_2 \cdot HCl$ in HBr and evaporating excess solvent. CH_3NH_3Br was dissolved in dimethylformamide

with equimolar amounts of $PbBr_2$ to produce an orange precipitate. The solid was washed with ethyl ether. To prepare $CsPbBr_3$, CsBr and $PbBr_2$ were sealed in an evacuated silica ampoule (< 10 mTorr) and heated to 600 °C over 11 hours and held at temperature for six hours before furnace cooling to room temperature. Members of the series $(CH_3NH_3)_{1-x}Cs_xPbBr_3$, where $x = 0.1, 0.2, 0.3, 0.4, 0.45, 0.5, 0.6,$ and 0.8 were prepared from the end members. Stoichiometric amounts of $CH_3NH_3PbBr_3$ and $CsPbBr_3$ were ground together and sealed in an evacuated silica ampoule (< 10 mTorr). Solid-state reactions were carried out at 150 °C for five days. After heating, samples were ground together until laboratory X-ray diffraction demonstrated only a single phase was present or appeared biphasic after regrinding. All samples were stored under inert atmosphere as prolonged ($\geq$ 12 hours) air exposure leads to phase separation.

Diffraction: Laboratory powder X-ray diffraction (PXRD) data were collected on a Bruker D8 Discover X-ray diffractometer using a CuK_α radiation source and a Lynxeye XE-T position-sensitive detector to check phase purity. Accurate lattice parameters were obtained using an internal silicon standard intimately mixed with each sample. PXRD data demonstrated that $(CH_3NH_3)_{1-x}Cs_xPbBr_3$, where $x = 0.0,\ 0.1,\ 0.2,\ 0.3,$ and 0.4 were majority single phase, while $x = 0.45,\ 0.5,\ 0.6,$ and 0.8 showed peak splitting indicative of a second phase. High resolution synchrotron powder X-ray diffraction patterns were collected on the diffractometer 11-BM-B at the Advanced Photon Source, Argonne National Laboratory ($\lambda \approx 0.41$ Å) at $T = 300$ K for $(CH_3NH_3)_{1-x}Cs_xPbBr_3$, where $x = 0.0,\ 0.1,\ 0.2,\ 0.3,$ and 0.4 and at $T = 100$ K for $x = 0.2$. Powders were flame sealed in glass capillaries under vacuum. Discrete detectors covering an angular range from -6 to

16° 2θ were scanned over a 34° 2θ range, with data points collected every 0.001° 2θ and scan speed of 0.01° 2θ per second.[89] X-ray diffraction patterns were analyzed using the Rietveld method implemented in TOPAS v4.2 (Bruker AXS). Statistics for relevant datasets are presented in Table 4.2. High resolution time-of-flight neutron powder diffraction (NPD) patterns were collected on the diffractometer POWGEN at the Spallation Neutron Source, Oak Ridge National Laboratory between $T = 10$ K and $T = 300$ K in 10 K increments for $(CH_3NH_3)_{1-x}Cs_xPbBr_3$, where $x = 0.0,\ 0.1,\ 0.2,$ and 0.4. For $x = 0.3$, diffraction data were collected every 20 K between $T = 10$ K and $T = 240$ K. NPD were analyzed using the Pawley method and the Rietveld method implemented in GSAS/EXPGUI.[228] Lattice parameters were extracted using the Pawley method owing to the challenges in accurately modeling the dynamically disordered methylammonium ion positions.[186] Statistics for relevant datasets are presented in Table 4.3.

Residual Nuclear Density Maps: Residual nuclear density maps (Figure 4.17) were generated based on Rietveld refinements implemented in GSAS/EXPGUI of neutron powder diffraction patterns with all atoms with approximate atomic positions and fractional occupancies (Figure 4.6). Space group assignments were taken from Pawley refinements as described in the main text. To gain insight into the shape of the nuclear density in the cuboctahedral void, all free parameters were fixed before erasing Cs, C, N, and H to generate the residual nuclear density map.

Heat Capacity: Heat capacity measurements were performed on pelleted samples using the quasi-adiabatic heat-pulse technique implemented in the Quantum Design, Inc. PPMS at $T = 2 - 298$ K, equilibrating for 4 time constants.

Table 4.2: Statistics from structural refinements from high resolution synchrotron X-ray diffraction.

x	T	R_{wp}
0.0	300 K	11.410
0.1	300 K	7.877
0.2	300 K	8.479
0.2	100 K	10.084
0.3	300K	7.213
0.4	300K	7.615

Inelastic Neutron Scattering (INS): Data were collected using the indirect-geometry spectrometer VISION at the Spallation Neutron Source, Oak Ridge National Laboratory. The instrument measures neutron energy transfer in the range of -2 to 1000 meV, with a resolution of *dE/E* $=1.5\%$. Powders were packed into aluminum canisters. Data were collected at $T = 5$ K, with data collection times up to 1.5 hours. Time-of-flight data were reduced in MANTID.[229] To lend assistance to interpretation of the INS spectra, phonon calculations were performed with phonopy[230] using density functional theory (DFT) calculated forces as implemented in VASP.[231,232] DFT calculations used Projector Augmented Wave (PAW) method[233,234] to describe the effects of core electrons, and Perdew-Burke-Ernzerhof (PBE)[235] implementation of the Generalized Gradient Approximation (GGA) for the exchange-correlation functional. The energy cutoff was set to 800 eV for the plane-wave basis of the valence electrons. The total energy tolerance for the electronic energy minimization was 10^{-8} eV and for structure optimization it was 10^{-7} eV. The maximum interatomic force after relaxation was below 0.001 eV/Å. The optB86b-vdW functional[236] for dispersion corrections was applied. Phonon calculations based on density functional perturbation theory were performed on the $2 \times 1 \times 2$ supercell of the optimized orthorhombic structure[237] with a $1 \times 2 \times 1$ Monkhorst-Pack k-point mesh. The vibrational eigen

Table 4.3: Statistics from structural refinements from high resolution neutron diffraction. R_{wp} values marked with an * are from refinements used to generate residual nuclear density maps (Figure 4.17).

x	T	R_{wp} from Rietveld	R_{wp} from Pawley
0.1	250 K	3.08	2.84
0.1	190 K	3.41	2.50
0.1	80 K	3.96	2.70
0.1	10 K	3.64*	—
0.1	100 K	3.44*	—
0.1	300 K	2.83*	—
0.2	270 K	3.67	3.46
0.2	180 K	3.67	2.69
0.2	130 K	3.93	3.18
0.2	10 K	3.84*	—
0.2	100 K	3.80*	—
0.2	300 K	3.63*	—
0.3	240 K	3.21	2.72
0.3	170 K	4.10	2.46
0.3	80 K	4.68	2.54
0.3	10 K	5.23*	—
0.3	100 K	7.89*	—
0.3	300 K	3.07*	—
0.4	300 K	—	2.05
0.4	150 K	—	2.95
0.4	10 K	—	3.45
0.4	10 K	5.13*	—
0.4	100 K	6.02*	—
0.4	300 K	2.70*	—

frequencies and eigen vectors were then calculated by solving the dynamical matrix using Phonopy.[230] The OClimax software[238] was used to convert the DFT-calculated phonon results to the simulated INS spectra.

Quasielastic Neutron Scattering (QENS): Data were collected using the backscattering spectrometer BASIS at the Spallation Neutron Source, Oak Ridge National Laboratory.[239] The center wavelength of the incident neutron beam was 6.4 Å with 60 Hz operation of the pulsed source using the Si (111) analyzer, which yields a full width half max of the energy resolution at the elastic line of 3.5 μeV over the accessible momentum transfer

range $Q = 0.2$ to 2.0 Å^{-1}. Time-of-flight data were reduced in MANTID.[229] Spectra collected at $T = 20$ K were used as the instrument resolution function. Samples were packed in aluminum foil packets and placed in an annular aluminum cylindrical can sealed with indium wire. Approximately 0.2 g of powder yields approximately 95% transmission of the beam, which minimizes multiple scattering events. Spectra were fit in DAVE,[240] and Elastic Incoherent Structure Factor (EISF) curves were modeled with $ad\ hoc$ python codes. The functions

$$EISF = (1-p) + p\big[\frac{1}{3} + \frac{2}{3}j_0(Qr)\big] \tag{4.1}$$

and

$$EISF = (1-p) + p\frac{1}{36}\sum_{1}^{j} n_j j_0(Qr_j), \tag{4.2}$$

where p is the fraction of quasielastic scattering, j_0 is the zeroth order Bessel function $sin(Qr)/Qr$, r or r_j is the relevant jump distance as previously described,[26] Q is the momentum change of the neutron, and n_j is a whole number coefficient derived from Group Theory, were used to model the C_3 and $C_3 \otimes C_4$ rotations, respectively. Relevant jump distances were calculated based on a geometric evaluation of an idealized $CH_3NH_3^+$. Relevant bond distances were taken from a previous report.[241] A linear combination of the two jump models (Eqns. 4.1,4.2) was constructed to describe a material where a fraction of $CH_3NH_3^+$ undergo only the C_3 rotation and the rest undergo the $C_3 \otimes C_4$ rotation. In the linear combination model, the fractions of quasielastic scattering (p), which can be thought of as the fraction of hydrogen atoms participating in the relevant rotation, were fixed to 1.0 for the $C_3 \otimes C_4$ rotation since all hydrogens on a molecule must move in

a dipole reorientation and to 0.5 for the C_3 rotation as it was assumed the ammonium group forms hydrogen bonds with the inorganic framework and is therefore fixed, while the methyl group is still mobile.

Fitting QENS spectra: The measured QENS spectra were fit with the following expression:

$$S(Q,\omega) = f\Big(A_o\delta(\omega) + 1 - A_o\frac{1}{\pi}\frac{\Delta(Q)}{\omega^2+\Delta^2}\Big) \otimes R(Q,\omega) + B(Q,\omega), \tag{4.3}$$

where Δ is the half width at half maximum (HWHM) of the quasielastic component, and A_o is elastic incoherent structure factor (EISF), defined as the fraction of elastic intensity of the entire spectral intensity. The HWHM of the quasielastic component can reveal information on the characteristic times of the diffusive motion. The Q-dependent EISF provides a measure of the time-averaged spatial distribution of the hydrogen atoms. The delta function represents the elastic component and the Lorentzian function the quasielastic component. They are convoluted (represented by the symbol $\otimes$) with the experimentally determined resolution function $R(Q,\omega)$. $B(Q,\omega)$ is the background term, a straight line that reproduces qualitatively the background arising from the instrument and the sample, and f is a scaling factor.

Extraction of the MSD from QENS spectra: The temperature dependent elastic incoherent neutron scattering (EINS) contribution was extracted from the measured BASIS spectra by integrating over the elastic peak. From the EINS the average mean-square displacement (MSD) can be extracted and estimated using a Gaussian approximation:

$$S_{el}(Q,\omega=0) = Ae^{\frac{-Q^2r^2}{3}}. \tag{4.4}$$

The Gaussian approximation reflects a situation where all the scattering atoms in the material have the same isotropic $\langle r^2 \rangle$, and even if this is not truly the case for the samples measured in this study, it can be used to obtain approximate MSD values. Since the incoherent neutron scattering cross section of hydrogen is an order of magnitude larger than those of the other constituent elements in these samples, the MSD is dominated by the displacements arising from hydrogen motions.

5. Ferroelastic Phase Transitions in the Hybrid Vacancy Ordered Perovskite Formamidinium Tin (IV) Iodide Driven by Organic-Inorganic Coupling

†

Summary

Hybrid perovskites are a technologically relevant family of materials, with potential applications in photovoltaics, solid-state lighting, and radiation detection. Interactions between the inorganic octahedral framework and the organic sublattice have been implicated in the structure and optoelectronic properties, but characterization of these interactions has been challenging because of competition between organic-inorganic coupling and intra-octahedral interactions. Due to their decreased octahedral connectivity, vacancy-ordered double perovskites present an ideal case study to examine organic-inorganic coupling in hybrid perovskites and their derivatives. Here, we describe the low-temperature, hysteretic phase transition of formamidinium tin(IV) iodide from the high symmetry cubic phase to a a lower symmetry monoclinic phase. We propose that the hysteresis stems

†Author Contributions: Eve Mozur collected the powder diffraction data and wrote the manuscript. Annalise Maughan collected and analyzed the powder diffraction data and total scattering data and outlined the manuscript. Andrew Candia prepared the samples. Erica Howard and Brent Melot for collected the X-ray total scattering data. James Neilson edited the manuscript and oversaw the project.

from organic-inorganic coupling mediated by local and spontaneous strain from frustrated orientations of the formamidinium cations, which result in a ferroelastic phase transition.

Introduction

Although hybrid perovskites perform competitively with conventional inorganic semiconductors when incorporated into photovoltaic devices, they are structurally distinct from diamond lattice semiconductors like silicon, cadmium telluride, and gallium arsenide.[242] Compared to these materials, hybrid perovskites are topologically under-constrained, characterized by structural fluctuations of the octahedral framework and liquid-like reorientations of organic cations that reside in the cuboctahedral void.[48,53] These dynamics have been implicated both in the optoelectronic properties of hybrid perovskites through the formation of polarons[41,48] and in the phase transitions of hybrid perovskites, which proceed through softening of these octahedral rotation and titling modes.[17,243]

Coupling between the dynamics of the octahedral framework and the organic sublattice has been implicated in the optoelectronic properties and phase behavior of hybrid perovskites. In methylammonium hybrid perovskites, the dynamic degrees of freedom of the organic sublattice couple strongly to the octahedral tilt pattern.[181,186] Recent spectroscopy studies demonstrate that the octahedral tilting, organic cation dynamics, and optoelectronic properties are all closely correlated.[244] However, in formamidinium perovskites the organic-inorganic coupling manifests quite differently and the nature of these interactions has not been fully elucidated. Some of this complexity is apparent in the phase behavior of formamidinium perovskites; formamidinium lead iodide undergoes a reentrant phase

transition, a transition to a non-perovskite phase, or retains the high temperature structure between room temperature and $T = 8.2$ K based on sample preparation and thermal history.[62,245] The dynamics of formamidinium appear to participate in this unusual phase behavior. The technological relevance of these materials and the importance of organic-inorganic coupling in dictating functional properties motivates a fundamental investigation of how organic cation dynamics and organic-inorganic coupling direct the structure of hybrid perovskites.

Vacancy-ordered double perovskites present an ideal system to probe the role of organic-inorganic coupling in the phase behavior and structure of hybrid perovskites. Hybrid perovskites are characterized by a corner-sharing BX_3 octahedral network with an organic A-site cation occupying the void space between octahedra; any organic-inorganic coupling must compete with the interactions within the octahedral framework. In vacancy-ordered double perovskites every other B-site cation is replaced with a vacancy and have a general formula A_2BX_6.[5] The retention of the closed-packed halide sublattice preserves the optoelectronic properties of three dimensional perovskites, but the lack of octahedral connectivity weakens inter-octahedral interactions and allows for organic-inorganic coupling to manifest more strongly.

Organic-inorganic coupling manifests strongly in vacancy-ordered double perovskites, primarily through the formation of hydrogen bonds. Hydrogen-bonding between the organic A-site cation and the octahedral halide ions directs the structure of A_2PtI_6 compounds, especially at low temperatures.[246] We have previously proposed that similar organic-inorganic coupling in $(CH_3NH_3)_2SnI_6$ and $(CH(NH_2)_2)_2SnI_6$ modifies the room tempera-

ture local coordination environment due to soft, anharmonic lattice dynamics that manifest as random distributions of octahedral tilt angles.[38]

Here we characterize the temperature dependent structural behavior of $(CH(NH_2)_2)_2SnI_6$. The lattice transitions from the cubic vacancy-ordered double perovskite structure (space group: $Fm\bar{3}m$) characterized by high amplitude, anharmonic dynamics to a monoclinic $P2_1/n$ structure characterized by cooperative octahedral tilting and low amplitude, nearly frozen, dynamics. The phase transition exhibits hysteresis, and the changes in particle size, lattice strain, and volume per formula unit depend on the thermal history of the sample. We propose that the phase transition behavior of formamidinium tin(IV) iodide, characterized by domain formation and spontaneous strain from the alignment of formamidinium quadrupoles is indicative of ferroelasticity. These observations demonstrate the importance of organic-inorganic coupling in VODPs and other hybrid perovskite derivatives.

Results

Formamidinium tin(IV) iodide

Formamidinium tin(IV) iodide crystallizes in the cubic vacancy-ordered double perovskite structure at room temperature.[38] Rietveld refinement of the cubic $Fm\bar{3}m$ structure of $(CH(NH_2)_2)_2SnI_6$ against high-resolution synchrotron powder X-ray diffraction (SXRD) data confirms the previously reported room temperature structure,[38] as shown in Figure 5.1a.

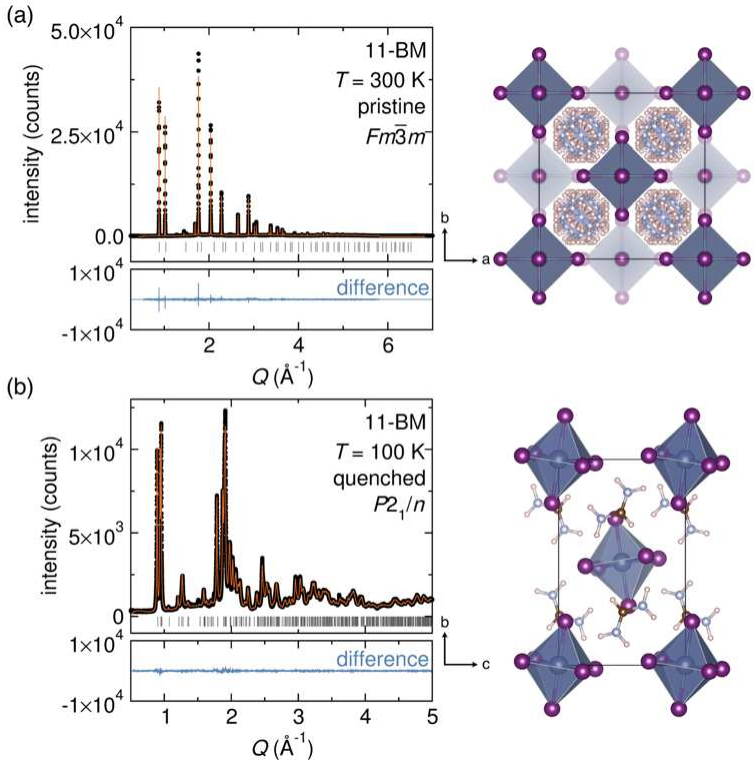

Figure 5.1: High-resolution synchrotron powder X-ray diffraction patterns collected at (a) T = 300 K and (b) T = 100 K (quenched). Data are shown as black circles, the fits to the cubic ($Fm\bar{3}m$) and monoclinic ($P2_1/n$) structures are shown as orange lines, and the difference curves are shown as blue lines in the subplots. The grey tick marks represent the location of predicted Bragg reflections for the structural models shown adjacent.

Upon cooling, formamidinium tin (IV) iodide undergoes a phase transition to a monoclinic structure (space group $P2_1/n$) characterized by cooperative tilting and rotation of the [SnI_6] octahedral units, as shown in Figure 5.1b. The structure is similar to the monoclinic ($P2_1/n$) structure reported for formamidinium platinum(IV) iodide.[246] The positions of the formamidinium ions were determined by simulated annealing of rigid bodies as described in the methods.

The monoclinic structural model also describes the local coordination environment of $(CH(NH_2)_2)_2SnI_6$ at low temperatures. Figure 5.2 shows the X-ray pair distribution function (XPDF) analysis of formamidinium tin(IV) iodide collected at T = 100 K. Below

$r = 5$ Å, the first and second nearest neighbor pair correlations correspond to the Sn–I bond distance and the intra- and interoctahedral I–I bond distances. The correlation between the local coordination environment and average structure of $(CH(NH_2)_2)_2SnI_6$ in the low temperature phase contrasts with the high temperature behavior. In our previous study we found that the local coordination environment in $(CH(NH_2)_2)_2SnI_6$ at $T = 300$ K was poorly described by the cubic structure.[38] Rather, the XPDF was best modeled by anharmonic rotations of $[SnI_6]$ octahedra away from their crystallographic positions, presumably due to high-amplitude octahedral rotations coupled with reorientations of the formamidinium cations. In the low temperature XPDF and SXRD data presented here, however, harmonic atomic displacements capture the peak shape and breadth. The phase transition from cubic to monoclinic correlates with a transition from a regime of high-amplitude anharmonic lattice dynamics to a regime of low-amplitude, nearly frozen octahedral and formamidinium dynamics.

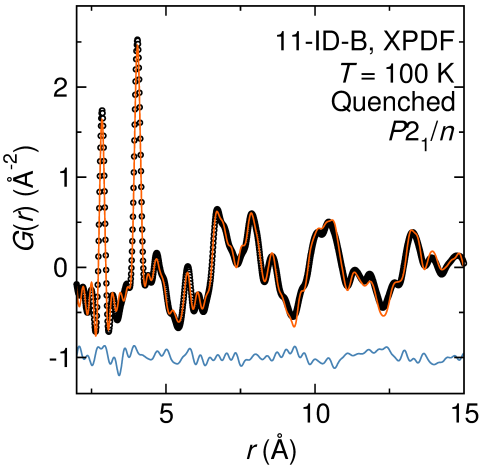

Figure 5.2: X-ray pair distribution function analysis of $(CH(NH_2)_2)_2SnI_6$ collected at $T = 100$ K after quenching. The data are modeled with the monoclinic $P2_1/n$ structure determined from the SXRD data. Black circles are the data, the orange line is the fit, and the blue line is the difference curve.

Formamidinium tin(IV) iodide exhibits path-dependent structural phase behavior. Slow cooling (5 K/min) from $T = 290$ K to $T = 100$ K reveals the onset of new reflections between $0.75 < Q < 1$ Å and $1.75 < Q < 2$ Å beginning at $T = 250$ K, indicative of a first-order crystallographic phase transition (Figure 5.3a). Despite the onset of the phase transition occurring at $T = 250$ K, peaks corresponding to the cubic phase persist to $T = 100$ K, and dwell times up to several hours at $T = 100$ K do not result in full conversion to the low-temperature structure. Upon heating the same sample from $T = 100$ K to $T = 300$ K at 5 K/min (Figure 5.3b), the lattice regains the high temperature cubic structure, though the reflections corresponding to the low temperature phase persist above $T = 250$ K. At $T = 300$ K (Figure 5.3b), the cubic structure is regained fully, but the intensities of the reflections are reduced by a factor of $\sim$5 and we observe significant peak broadening relative to the diffraction pattern collected before thermal cycling. Thermal cycling of $(CH(NH_2)_2)_2SnI_6$ appears to result in irreversible changes to crystallographic strain or particle size within the polycrystalline sample, or a combination therein.

Although slow ramping results in incomplete phase conversion between the high- and low-temperature structures of formamidinium tin(IV) iodide, full phase conversion is achieved with thermal quenching. A new sample of formamidinium tin(IV) iodide was quenched from room temperature to $T = 100$ K, and the resulting diffraction pattern is shown in Figure 5.4. In the quenched sample, the reflections characteristic of the high-temperature cubic structure have disappeared, and the peaks in the resultant diffraction pattern are narrower relative to the slow-cooled sample. This path-dependence is similar to the phase behavior of formamidinium lead iodide.[62] In formamidinium lead iodide, path-dependence

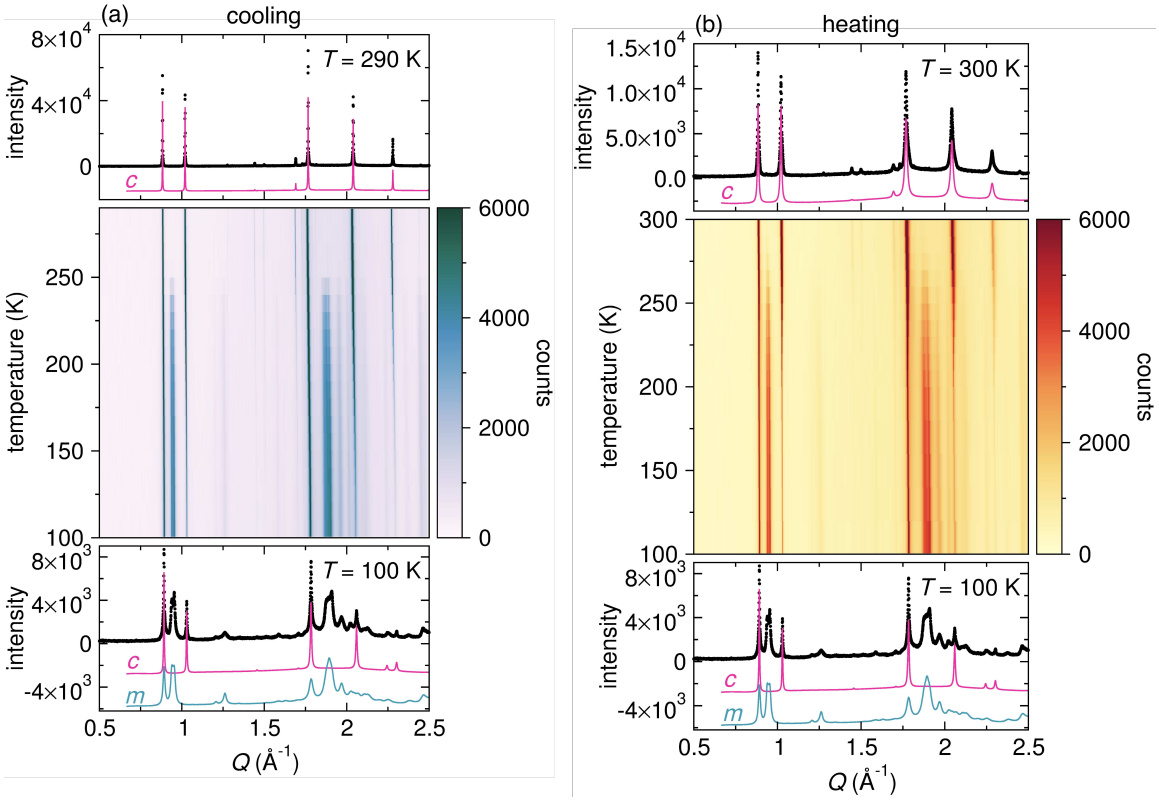

Figure 5.3: False color representation of temperature-dependent high-resolution synchrotron powder X-ray diffraction data of $(CH(NH_2)_2)_2SnI_6$ collected in 10 K increments (a) upon cooling from T = 290 K to T = 100 K and (b) upon warming from T = 100 K to T = 300 K. Measurements were performed upon cooling first in (a), and then again upon heating in (b). The colored lines represent phase-decomposed calculated diffraction patterns for the cubic (*c*, pink) and monoclinic (*m*, teal) phases.

was attributed to a kinetic barrier related to the breaking and reforming of lead-iodide bonds. As the inner octahedral geometry is conserved through the phase transitions of formamidinium tin(IV) iodide, another phenomenon must underly the behavior observed here.

Upon thermally quenching the same sample from $T = 100$ K to $T = 300$ K, the high-temperature structure of formamidinium tin(IV) iodide is almost completely regained. Figure 5.5 compares the high-resolution diffraction data collected before cycling, after thermal quenching to $T = 100$ K and then rapidly heating to $T = 300$ K (*e.g.* inverse thermal quench) to a sample with a slow (5 K/min) cooling and then heating. In the sample

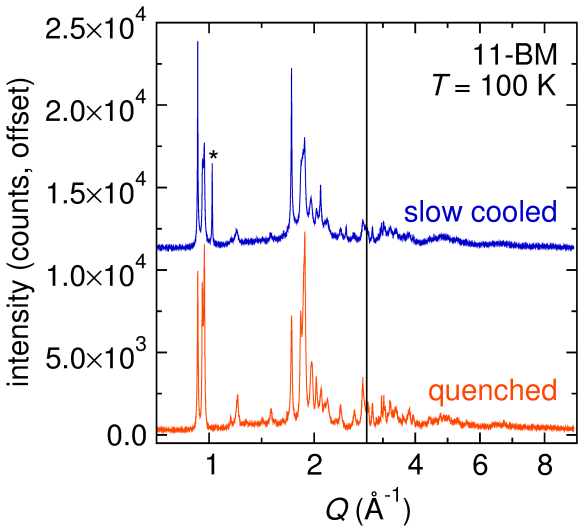

Figure 5.4: Synchrotron powder X-ray diffraction patterns of $(CH(NH_2)_2)_2SnI_6$ collected at $T = 100$ K from a slow-cooled (5 K/min) sample (blue) and a quenched sample (orange). The asterisk denotes the (200) reflection from the high-temperature cubic phase, indicating incomplete phase conversion.

ramped at 5 K/min, the $T = 300$ K structure is regained, but the peaks exhibit a significant loss in intensity and exhibit markedly broadened relative to the pristine sample. In contrast, the diffraction data of the quenched and rapidly heated sample resembles the pristine data, with sharp, narrow reflections and only small losses in intensity. These observations indicate that particle size and crystallographic strain in $(CH(NH_2)_2)_2SnI_6$ depend on the thermal history of the sample.

In order to deconvolute particle size and lattice strain for $(CH(NH_2)_2)_2)SnI_6$ under different temperature cycling conditions, we performed a Williamson-Hall analysis for the data presented in Figure 5.5. In Figure 5.6, the full-width at half-maximum (FWHM) of the seven strongest reflections in the cubic diffraction pattern are shown as a function of Q. The steeper slope of the resultant line for the quenched sample in comparison to the pristine sample indicates a slight increase in microstrain broadening. In contrast, slow thermal cycling results in a drastic increase in the slope and also yields a significant change

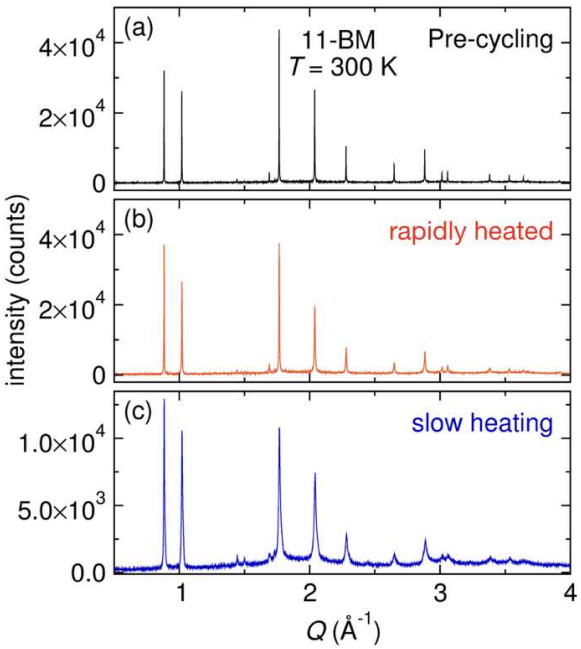

Figure 5.5: Synchrotron powder X-ray diffraction patterns of $(CH(NH_2)_2)_2SnI_6$ collected at $T = 300$ K (a) before thermal cycling, (b) after quenching to $T = 100$ K and then rapid heating to $T = 300$ K, and (c) after slow-cooling to $T = 100$ K and then slow-heating to $T = 300$ K (5 K/min).

in the y-intercept, indicating a larger increase in lattice microstrain as well as a decrease in particle size. Williamson-Hall analysis indicates that thermal cycling of formamidinium tin iodide increases lattice strain relative to pristine samples, and that this effect is particularly pronounced when the sample is cycled slowly. Further, slow temperature cycling affects particle size, which suggests the formation of domains that may contribute to the observed phase transition hysteresis.

Furthermore, differences in temperature ramp rate produce significant differences in the evolution of lattice volumes. As shown in Figure 5.7, the lattice volumes of both the cubic and monoclinic phases decrease smoothly upon slow cooling to $T = 100$ K. However, upon slow warming the lattice volume of the cubic phase increases non-monotonically in the temperature range $T \sim 225$-250 K, which corresponds with growth of the cubic phase as shown in the temperature-dependent diffraction patterns in Figure 5.3b. In contrast,

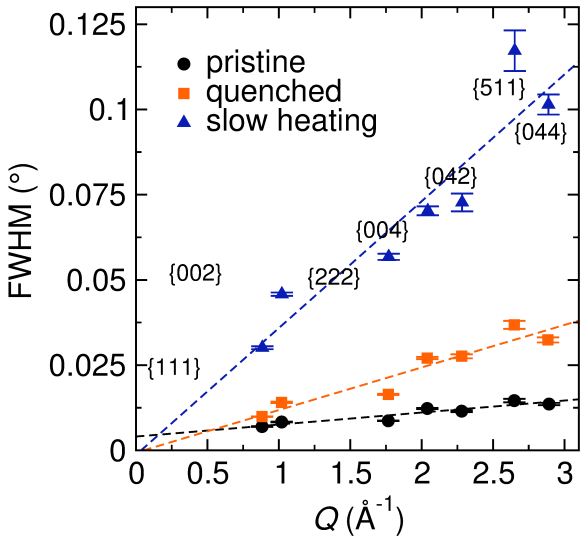

Figure 5.6: Williamson-Hall analysis of the cubic phase of formamidinium tin(IV) iodide for the pristine (black circles), slow cooled and slow heated (orange squares), and quenched (blue triangles) samples. The dashed lines represent linear regressions for each data set. The corresponding diffraction patterns are presented in Figure 5.5.

fast quenching of formamidinium tin(IV) iodide results in significant differences in the lattice volumes. Quenching from the pristine sample to $T = 100$ K results in a monoclinic lattice volume that is significantly reduced relative to that of the slow-cooled sample. Further, after quenching back to $T = 300$ K, the cubic lattice volume is nearly identical to that of the pristine value, indicating that quenching allows the structure to regain the original structure reversibly, while slow-ramping results in irreversible changes to the lattice volume.

Discussion

We propose that the cubic to monoclinic phase transition of formamidinium tin(IV) iodide is ferroelastic in nature. The characterization of the phase transitions of formamidinium tin(IV) iodide presented above are consistent with the two primary characteristics

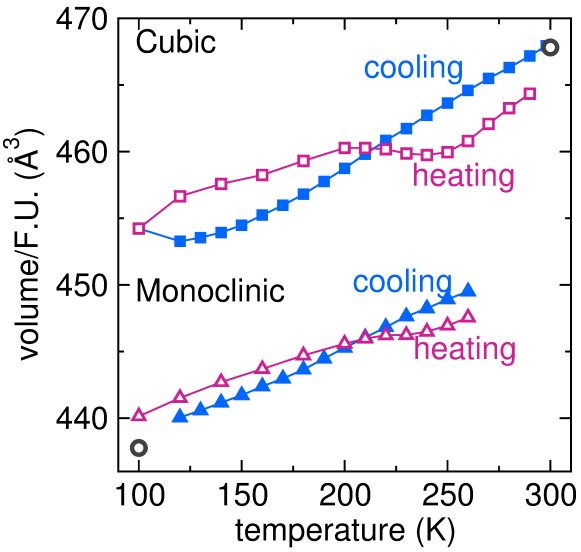

Figure 5.7: Unit cell volume per formula unit for the cubic and monoclinic structures of $(CH(NH_2)_2)_2SnI_6$ determined from temperature-dependent high-resolution synchrotron powder X-ray diffraction data. The data were collected upon cooling first and then again upon heating at a rate of 5 K/min, denoted by the filled and open symbols, respectively. The open grey circles represent the volumes of the cubic and monoclinic structures from quenching. Lattice volume errors bars are smaller than the symbols and are therefore omitted for clarity.

of a ferroelastic phase transition, the presence of spontaneous strain and two or more orientational configurations.

In transitioning from a paraelastic high temperature phase to a ferroelastic low temperature phase, the lattice must occupy two or more orientational states and necessitates the formation of domains.[247] Hysteresis in the crystallography of $(CH(NH_2)_2)_2SnI_6$ is indicative of domain formation (Figure 5.3). The difference in crystallography, lattice microstrain, and particle size between samples that have been quenched or slow cooled suggest a complex domain formation pathway. Similar features to the plateaus and negative thermal expansion in Figure 5.7 have been observed in the lattice parameters and unit cell volume of lead phosphate and were attributed to the formation and coalescence of micro-domains within ferroelastic domains.[248]

The path dependence of the phase transition as a function of temperature ramp rate (Figures 5.4, 5.5, 5.6) is likely a result of temperature dependent domain formation. Ferroelastic domain formation in barium titanate is known to be temperature dependent,[249] which is consistent with the mathematical treatment of ferroelastic domains that suggests that domain formation depends on surface fluctuations, dynamic structural fluctuations, and crystalline defects.[250] Dynamic structural fluctuations in particular will be temperature dependent in hybrid perovskites and their derivatives.[5,128,192,251,252]

The presence of spontaneous strain is consistent with the large change in volume between the cubic and monoclinic phase at the same temperature. For instance, Figure 5.7 shows that at $T = 250$ K for data collected upon cooling, the volume per formula unit in the cubic phase is 463 Å^3 and in the monoclinic phase is 450 Å^3, correlating to a 30% average compressive linear strain ($\sqrt[3]{((463\ \text{Å}^3 - 450\ \text{Å}^3)/463\ \text{Å}^3)}$). Microscopically, there appears to be residual microstrain within the individual crystallites, as indicated by the Williamson-Hall analysis (Figure 5.6)

The strain in $(CH(NH_2)_2)_2SnI_6$ most likely arises from releasing the conformational frustration of dynamic $CH(NH_2)_2^+$ quadrupoles. Unlike other cations commonly incorporated in halide perovskites and perovskite derivatives, such as $CH_3NH_3^+$, $CH(NH_2)_2^+$ has a strong quadrupole moment. Electrostatic quadrupole moments couple strongly to electric field gradients and can then produce directional compressive and expansive strain on the surrounding framework.[86,253] At high temperature, thermally-activated reorientations of formamidinium yield a nearly isotropic local environment around formamidinium that is compatible with the average cubic symmetry, despite significant local and dynamic

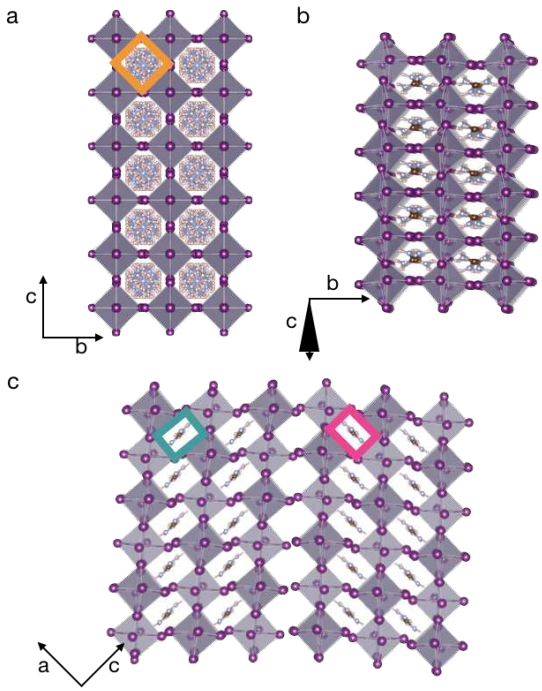

Figure 5.8: (a) Cubic and (b,c) monoclinic structures of $(CH(NH_2)_2)_2SnI_6$ shown at the same scale with the shapes of the A-site void highlighted. The transition between these two phases involves large volume changes and increased anisotropy around the A-site.

disorder (Figure 5.8a).[38] However, on cooling, the organic-organic interactions mediated through the quadrupole moment become more important. Crystallography indicates formamidinium cations orient along the same plane at low temperatures (Figure 5.8c), which has been proposed as a ground state for quadrupole ordering if long-range interactions are strong.[86] This co-planar configuration results in the decrease in symmetry and size of the A-site void between the cubic and monoclinic structures (Figure 5.8) that accompanies the compressive strain produced during the cubic to monoclinic phase transition. In analogy with the ferroic or ferroelastic domains in methylammonium lead iodide,[254] different orientations of formamidinium would distinguish domains (Figure 5.8c).

Conclusions

Organic-inorganic coupling is an important consideration of hybrid perovskites and their structural derivatives, the understanding of which will increase the quality of structure-property relationships. We suggest that changes in the orientation of formamidinium in formamidinium tin (IV) iodide lead to spontaneous strain and domain formation, which manifests in the ferroelastic phase transition from the high temperature cubic phase to the low temperature monoclinic phase. The crystallography data here demonstrate the influence of organic cation orientations and organic-inorganic coupling on the phase behavior of vacancy ordered double perovskites, which can be extrapolated to other perovskite materials.

Methods and Materials

Formamidinium tin(IV) iodide was prepared following the previous literature report.[5] Briefly, stoichiometric amounts of the halide binaries $CH(NH_2)_2I$ and SnI_4 were ground together, sealed in an evacuated silica ampoule ($P < 10$ mTorr), and heated to 150 °C for 48 h.

Characterization

Temperature-dependent high-resolution synchrotron powder X-ray diffraction studies were performed on beamline 11-BM-B at the Advanced Photon Source, Argonnne National Laboratory. Powdered samples of formamidinium tin(IV) iodide were diluted with

amorphous SiO_2 and packed in Kapton capillaries and sealed with modeling clay. The temperature was ramped from $T = 300$ K to $T = 100$ K at 5 K/min. Diffraction patterns ($\sim$30 min scans) were collected in 10 K increments. The temperature was then ramped to $T = 300$ K at 5 K/min, with diffraction patterns collected every 10 K on warming. Quenching studies were performed on a pristine sample of formamidinium tin(IV) iodide. Quenching to $T = 100$ K was achieved by pre-cooling the cryostat to $T = 100$ K and then moving the sample into the cryostat. The sample was allowed to equilibrate at $T = 100$ K for 5 min before data collection. The cryostat was removed and the sample was allowed to come to room temperature for the rapid heating room temperature study.

Diffraction data were modeled using the Rietveld method in TOPAS v6 and the organic molecules were located through simulated annealing of rigid bodies. First, the inorganic [SnI_6] octahedral sublattice and lattice parameters were refined against the $T = 100$ K diffraction data. The positions of the octahedra and the lattice parameters were then fixed and the formamidinium ions were introduced and allowed to rotate and translate as rigid bodies. The bond distances and angles of the formamidinium ions were adopted from prior literature.[255] Once the translational positions of the formamidinium ions were optimized, the simulated annealing procedure was repeated while only allowing the formamidinium ions to rotate as rigid bodies to reach the final structural configuration shown in Figure 5.1. Crystallographic information files for the cubic ($T = 298$ K) and monoclinic ($T = 100$ K) structures of formamidinium tin(IV) iodide are provided as supporting information.

Synchrotron X-ray scattering data suitable for pair distribution function (PDF) analysis were collected at beamline 11-ID-B at the Advanced Photon Source, Argonne National Lab-

oratory, using 86 keV photons and sample-detector distance of 25 cm. A powdered sample of formamidinium tin(IV) iodide was loaded into a polyimide capillary and quenched to T = 100 K. The sample was measured in transmission mode using a Perkin Elmer amorphous silicon image plate detector.[256] GSAS-II was used to calibrate the sample to detector distance and detector alignment with data from a CeO_2 powder standard.[257] Raw scattering data was integrated into one dimensional Q-space, applying a mask and polarization correction during integration. The normalized total scattering patterns, $S(Q)$ were produced in PDFgetX3 by subtracting polyimide container scattering, utilizing the appropriate sample composition, and applying standard corrections for the area detector setup.[256] Experimental PDFs were extracted using PDFgetX3[258] and analyzed using PDFgui.[259] Pair distribution function patterns, $G(r)$, were calculated via Fourier transformation of the total scattering data utilizing a Q maximum of 22 Å^{-1}.

VESTA was used to visualize and render all crystal structures presented in this publication.[260]

6. Directed Local Ordering of Lone Pairs in Tin-Bromide Perovskites

†

Summary

Halide perovskite semiconductors have complex and polarizable structures when compared to conventional inorganic semiconductors. This makes halide perovskites more susceptible to static and dynamic structural deformations. Although many of these deformations, such as cooperative octahedral rotations and tilting, are well understood and synthetically controllable, metal off-centering that occurs in tin and germanium halide perovskites due to stereochemical activation of the valence s^2 lone pair remains relatively under explored. Here, we investigate the different metal off-centering in cesium tin bromide and methylammonium tin bromide. Crystallographic characterization of the solid solution series $(CH_3NH_3)_{1-x}Cs_xSnBr_3$ demonstrates that stereochemical activation can be tuned with substitution by controlling the volume and anisotropy of the A-site void. This study demonstrates that the A-site cation influences the structure of hybrid perovskites through electrostatics and sterics.

†Author Contributions: Eve Mozur prepared the samples, collected and analyzed the diffraction, total scattering, and absorbance data, and wrote the manuscript. Alexandra Koegel and Leighanne Gallington collected the total scattering data. Daniel Olds collected the diffraction data. James Neilson edited the manuscript and oversaw the project.

Introduction

Hybrid halide perovskites are a technologically relevant family of materials, with applications in photovoltaics. Many of their advantageous optoelectronic properties are related to the polarizability of their corner-sharing octahedral framework, composed of a p-block metal coordinated by halide ions, and the organic A-site cation embedded between the octahedra that undergoes stochastic, liquid-like reorientations.[53,83,252] Hybrid perovskites have long electronic excited state lifetimes that have been attributed to polaron formation, in which local structural deformations stabilize excited state charge carriers, and Rashba splitting, in which spin-orbit coupling and the absence of inversion symmetry make electronic relaxations across the band gap spin forbidden.[39] Both of these mechanisms for extending charge carrier lifetimes have been linked to the dynamic distortions of the perovskite structure, including organic cation reorientations, low frequency phonons related to cooperative rotations and tilting of the octahedral framework, and intra-octahedral distortions related to metal off-centering.[41,48,48,53,106,261,262]

The nature of organic cation reorientations and cooperative octahedral modes have been rigorously studied over the past several decades.[15,17,26–28,77,177,181,193,263,264] In comparison, intra-octahedral structural distortions have received less attention and are less well understood. As hybrid perovskites that exhibit metal off-centering and related distortions become more technologically relevant[265–268] understanding these distortions becomes more pressing.

Metal off-centering, characterized by asymmetric octahedra with three long and three short metal-halide bonds, is thought to occur because of stereochemical activation of the valence s^2 lone pair on the metal.[19,21,269] In extended solids, stereochemical activation occurs when fully occupied s states mix with empty p states, leading to isotropic electron density in analogy to sp hybridization of molecules.[270,271] The proximity in energy of s and p states determines whether hybridization will occur. For example, structural distortions related to stereochemical activation can be observed crystallographically in cesium germanium iodide ($CsGeI_3$), but not in cesium tin iodide ($CsSnI_3$) due to the increase in energy level separation between the valence s and p states moving from germanium to tin.[21,272] There is some indication from photoluminescence data that $CsSnI_3$ exhibits stereochemical activation of lone pairs locally or dynamically at high temperatures[272] in a process that has been termed emphanisis, and is consistent with an anharmonic potential well originating from this lone pair.[273,274] In general, germanium perovskites are the most likely to exhibit structural distortions consistent with stereochemical activation of lone pairs, followed by tin, while lead perovskites are unlikely to experience stereochemical activation.[19] Although density functional theory computations on lead and tin chalcogenides suggest that the cation p states contribute more than anion p states,[270] anion identity will also affect the magnitude of the stereochemical activation when the energy of the anion p states approaches the metal s states.[19]

Although the energy levels of the A-site are remote from the relevant s and p states, the identity of the A-site cation appears to impact the behavior of the $5s^2$ tin lone pair in tin bromide perovskites. At room temperature, both methylammonium tin bromide

($CH_3NH_3SnBr_3$) and cesium tin bromide ($CsSnBr_3$) crystallize in the cubic perovskite phase (space group: $Pm\bar{3}m$), which does not allow tin off-centering.[20,275] Local structural characterization in both materials suggest dynamic distortions indicative of stereochemical activation of the metal $5s^2$ lone pair occur on length or time scales too short to be detected in traditional crystallography.[20,269] On cooling, however, $CH_3NH_3SnBr_3$ and $CsSnBr_3$ exhibit markedly different behavior. $CH_3NH_3SnBr_3$ undergoes two phase transitions between room temperature and 100 K; the first to an orthorhombic phase (space group: $Pmc2_1$) characterized by tin off-centering and octahedral distortions indicative of stereochemical activation and the second to an unknown triclinic phase.[275] $CsSnBr_3$ does not exhibit any obvious stereochemical activation in the average structure on cooling; rather, it undergoes two typical perovskite phase transitions to a tetragonal phase (space group: $P4/mbm$) and then to an orthorhombic phase (space group: $Pnam$).[20,276] As summarized in Figure 6.1, the presence of methylammonium in tin bromide perovskites correlates both to local stereochemical activation at high temperatures and to long-range stereochemical activation at low temperatures, while the presence of cesium correlates only to local stereochemical activation at high temperatures.

To investigate how the A-site cation affects stereochemical activation, this chapter characterizes the structure of the solid solution series between $CH_3NH_3SnBr_3$ and $CsSnBr_3$ with synchrotron X-ray diffraction and total scattering data suitable for pair distribution function (PDF) analysis collected between 100 K and 420 K. The series $(CH_3NH_3)_{1-x}Cs_xSnBr_3$ was prepared for $0.0 < x < 1.0$, with a miscibility gap for $0.45 < x < 0.75$. Bragg diffraction data shows that $CH_3NH_3^+$ rich samples have similar average structures to $CH_3NH_3SnBr_3$,

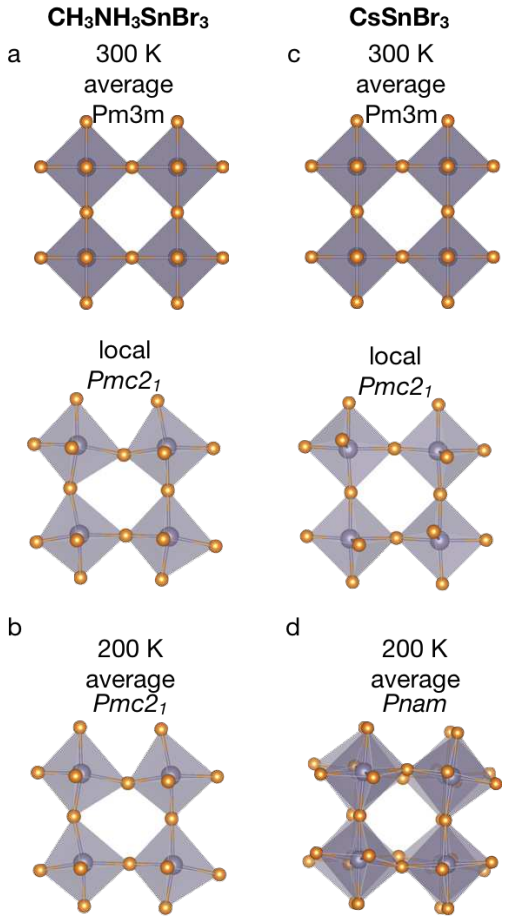

Figure 6.1: Phase behavior of (a,b) $CH_3NH_3SnBr_3$ and (c,d) $CsSnBr_3$ at 300 K and 200 K. At high temperature, both materials crystallize in the high symmetry cubic perovskite phase and undergo local distortions that can be modeled by phases that allow tin off-centering, such as the $Pmc2_1$ phase. On cooling, $CH_3NH_3SnBr_3$ transitions to the $Pmc2_1$ phase on average. $CsSnBr_3$ transitions to the $Pnam$ phase, which does not have tin off-centering.

although the formation of the low temperature triclinic phase is suppressed, and that Cs^+ rich samples have average structures similar to $CsSnBr_3$. Pair distribution function analysis demonstrates that all samples undergo short-range structural distortions indicative of stereochemical activation that can be tuned with substitution.

Results and Discussion

The solid solution series $(CH_3NH_3)_{1-x}Cs_xSnBr_3$ was prepared for $0.0 < x < 1.0$. A miscibility gap occurs for $0.45 < x < 0.75$, in which both a methylammonium rich phase and cesium rich phase are present instead of a single, homogenous phase. This miscibility gap suggests that cesium and methylammonium interact differently with the octahedral framework, either due to their size mismatch or electrostatic interactions, and that competition between these interactions with high levels of substitution cause too much strain to form a stable, single phase material. The multi-phase materials were not investigated further. Compositions were adjusted from the nominal x values for the single phase materials based on from Vegard's Law, which states that the lattice parameters of solid solution should vary linearly with composition. Accurate lattice parameters were obtained from Le Bail refinements of powder diffraction data of the sample intimately mixed with a silicon standard. Differences between the adjusted and nominal x values are a result of additional CH_3NH_3Br that was added to the reaction mixture to account for the volatility of CH_3NH_3Br at reaction temperatures (Figure 6.2, Table 6.1). The adjusted x values are used in the remainder of the manuscript.

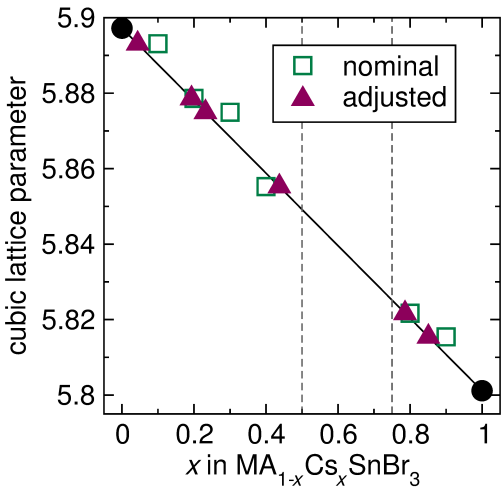

Figure 6.2: Vegard's law plot for $(CH_3NH_3)_{1-x}Cs_xSnBr_3$. Accurate lattice parameters were obtained from Le Bail refinements of the sample intimately mixed with a silicon standard. The solid line is a linear regression between the cubic lattice parameters of the two end members. The pink closed triangles are the compositions adjusted based on Vegard's Law and the green squares are the nominal compositions. Vertical dashed lines show the edges of the miscibility gap. The adjusted lattice parameters are used in the remainder of the manuscript.

Table 6.1: Comparison of the nominal cesium concentration and the cesium concentration adjusted based on Vegard's Law. The adjusted lattice parameters are used in the remainder of the manuscript.

nominal x	adjusted x
0.1	0.04
0.2	0.19
0.3	0.23
0.4	0.43
0.8	0.79
0.9	0.85

Electronic Properties

Diffuse reflectance data collected on $(CH_3NH_3)_{1-x}Cs_xSnBr_3$ were transformed to absorption with the Kubleka-Munk transformation. Linear extrapolation over the linear region in the absorption data allows for calculation of the optical gap (Figure 6.3). The optical band gap energy decreases linearly with x, as expected based on lattice contraction upon increasing concentration of the smaller cesium ion. Lattice contraction in hybrid perovskites leads to a narrowing of the band gap because the top of the valence band is

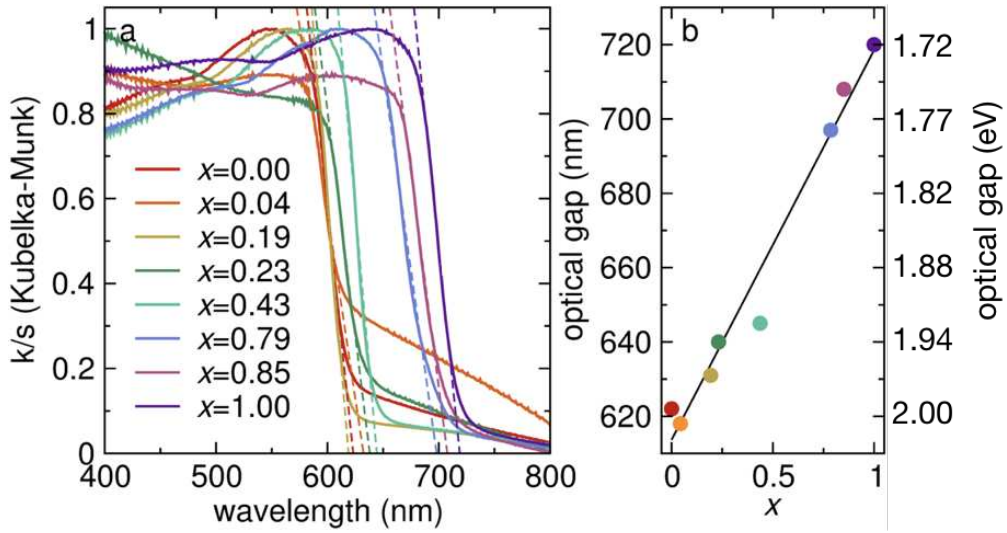

Figure 6.3: (a) Diffuse reflectance data for $(CH_3NH_3)_{1-x}Cs_xSnBr_3$ transformed to absorption with the Kubelka-Munk transformation. The optical gap (b) can be found from linear extrapolation of the linear region (dashed lines) in (a).

composed of anti-bonding states that increase in energy with increased orbital overlap and the bottom of the conduction band is composed of bonding states that decrease in energy with increased orbital overlap.[70] The diffuse reflectance data are roughly consistent with the Vegard's Law change in lattice parameters, indicating the successful preparation of a solid solution.

In several members of the solid solution series, the absorbance data show tailing into the IR (Figure 6.3a). This Moss-Burstein type shift is indicative degenerate doping of the sample, likely though oxidation of tin from tin (II) to tin (IV).[277] The presence of small quantities of nanoscale or amorphous impurities suggestive of this oxidation cannot be ruled out from the diffraction data used to access sample purity. The tailing into the IR is more pronounced for methylammonium rich samples, perhaps because of a similar decrease in the favorability of the oxidation reaction with substitution as observed for bromide substitution in methylammonium lead iodide.[11] The presence of methylammonium

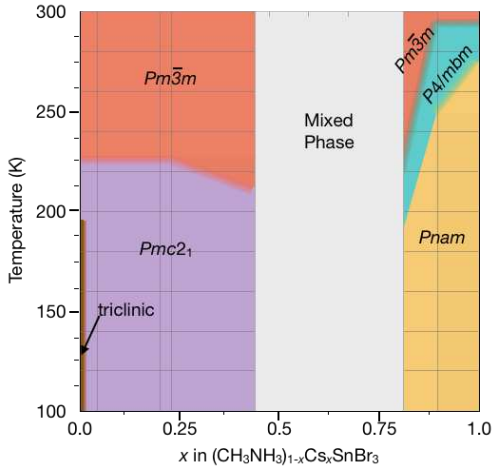

Figure 6.4: Schematic phase diagram of the temperature dependent phase behavior of the solid solution series ($CH_3NH_3)_{1-x}Cs_xSnBr_3$) constructed from diffraction data. The intersections of the gray grid indicate sampled temperatures and compositions.

appears to influence the propensity of tin perovskites to form defect dopants, which have been implicated in their reduced power conversion efficiencies when incorporated into a photovoltaic device.

Crystallography

At room temperature, all members of the solid solution series crystallize in the cubic perovskite structure (space group $Pm\bar{3}m$). On cooling, the methylammonium rich samples behave similarly to methylammonium tin bromide and the cesium rich samples behave similarly to cesium tin bromide. A summary phase diagram is presented in Figure 6.4. Methylammonium tin bromide undergoes two known phase transitions, from the room temperature cubic phase to an orthorhombic phase characterized by tin-off centering and octahedral rotations (space group: $Pmc2_1$) at 230 K and then to an unknown triclinic phase at 190 K.[275] The cubic to orthorhombic phase transition is characterized

by the resolution of two Bragg reflections at Q = 1.6 Å^{-1} and 1.9 Å^{-1} (Figure 6.5). The orthorhombic to triclinic phase transition is characterized by peak splitting of many of the major reflections, perhaps most clearly seen when the peak at Q = 1.9 Å^{-1} splits from two to three reflections (Figure 6.5). The methylammonium rich members of the solid solution series all undergo the higher temperature cubic to orthorhombic phase transition, indicated by the resolution of Bragg reflections from the background (Figure 6.5). However, there is no evidence that the low temperature phase transition occurs in the substituted samples above 100 K – even with only 4% cesium substitution the lattice parameters show an anomaly only at the cubic to orthorhombic phase transition temperature (Figure 6.6). Cesium substitution appears to suppress the orthorhombic to triclinic phase transition in methylammonium tin bromide.

Cesium tin bromide undergoes two known crystallographic phase transitions, from a high-temperature cubic phase (space group: $Pm\bar{3}m$) to a tetragonal phase (space group: $P4/mbm$) at 290 K, and then to an orthorhombic phase (space group: $Pnam$) at 230 K.[20] Tin off-centering is not observed in these phases. The cubic to tetragonal phase transition is indicated by the resolution of a Bragg reflection at Q = 1.7 Å^{-1} and the tetragonal to orthorhombic phase transition is indicated by the resolution of a Bragg reflection at Q = 1.6 Å^{-1} and Q = 1.75 Å^{-1} (Figure 6.5). The resolution of the same Bragg reflections from the background is evident in the cesium rich members of the solid solution series (Figure 6.5). With decreasing amounts of cesium, the phase transition temperatures become lower, which also occurs with cesium substitution in methylammonium lead bromide and formamidinium lead bromide.[253,278]

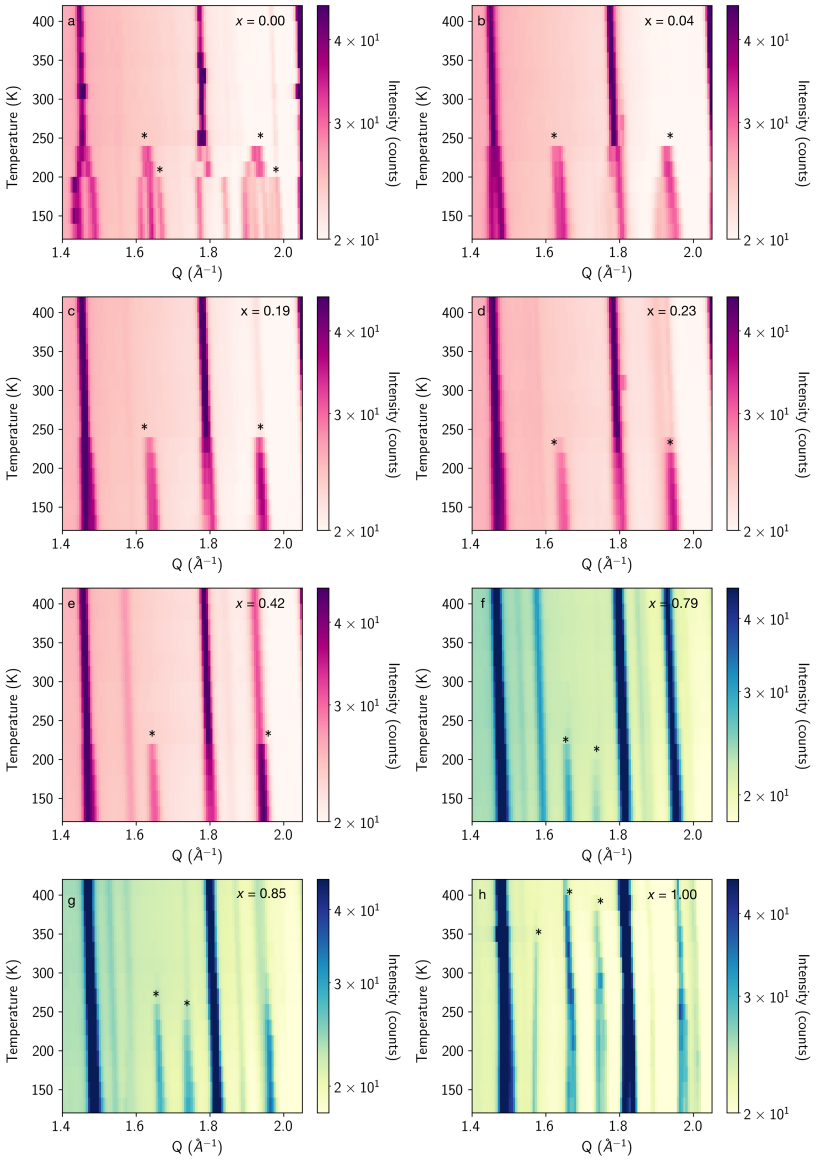

Figure 6.5: False color map of high resolution synchrotron X-ray diffraction patterns for $(CH_3NH_3)_{1-x}Cs_xSnBr_3$ where (a) $x = 0.00$, (b) $x = 0.04$, (c) $x = 0.19$, (d) $x = 0.23$, (e) $x = 0.43$ (f) $x = 1.00$, (g) $x = 0.85$, (h) $x = 0.79$. Asterisks indicate the Bragg reflections characteristic of the phase transitions. Intensity is depicted on a log scale.

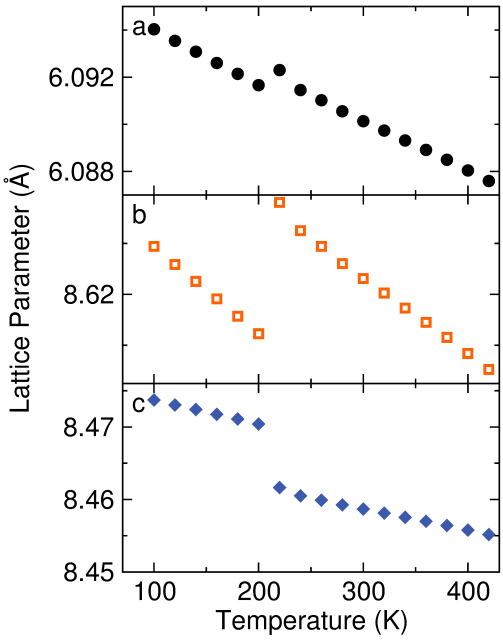

Figure 6.6: The a, b, and c lattice parameters from Le Bail refinements of high resolution synchrotron X-ray diffraction patterns for $(CH_3NH_3)_{0.96}Cs_{0.04}SnBr_3$ as a function of temperature. The discontinuities correspond to the $Pm\bar{3}m$ to $Pmc2_1$ phase transition at 210 K.

Substitution in methylammonium tin bromide and cesium tin bromide does not dramatically affect the phase behavior. For comparison, in methylammonium lead bromide cesium substitution introduces a reentrant phase transition at 20% cesium substitution and changes the intermediate temperature phase from $I4/mcm$ to $P4/mbm$ at 30% and 40% cesium substitution.[278] These changes were attributed to frustrated interactions between the A-site cations and the inorganic octahedra that manifested through long-range changes to the octahedral tilt pattern. The lack of such changes in $(CH_3NH_3)_{1-x}Cs_xSnBr_3$ indicate that the substitution has a small effect on long-range stereochemical lone pair activation, despite the dependence of the tin off-centering on the A-site cation identity.

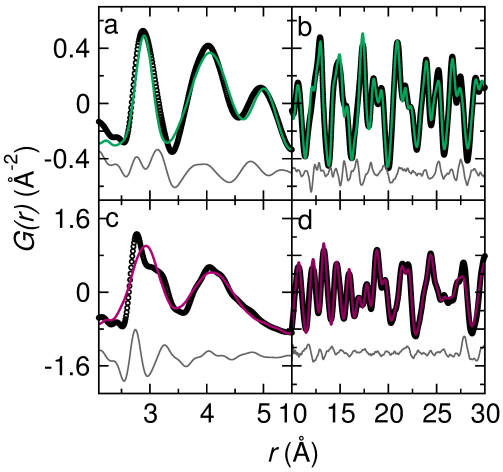

Figure 6.7: Room temperature PDF fit to a cubic perovskite structure over only (a) the short range correlations and (b) long range correlations in $CsSnBr_3$ and (c) the short range correlations and (d) long range correlations in $CH_3NH_3SnBr_3$.

Local Structure

Qualitative comparison of the room temperature PDF across the series $(CH_3NH_3)_{1-x}Cs_xSnBr_3$ mirror the diffraction data, in that the methylammonium rich samples resemble methylammonium tin bromide and the cesium rich samples resemble cesium tin bromide. This is most noticeable in the first correlation at $r = 2.8$ Å, which has a clear shoulder in methylammonium rich samples that is lacking in cesium rich samples (Figure 6.7, 6.8). Based on the bond distances in the cubic perovskites, this first correlation describes both tin-bromide and cesium-bromide interactions, and modeling must be used to distinguish the two.

Comparison of the models required to fit the diffraction data and the PDF confirm that the local structure has additional complexity not captured in the average structure. Attempts to model the PDF with the same $Pm\bar{3}m$ structure determined from Rietveld analysis capture the long-range correlations, but examination of the difference curves indicate

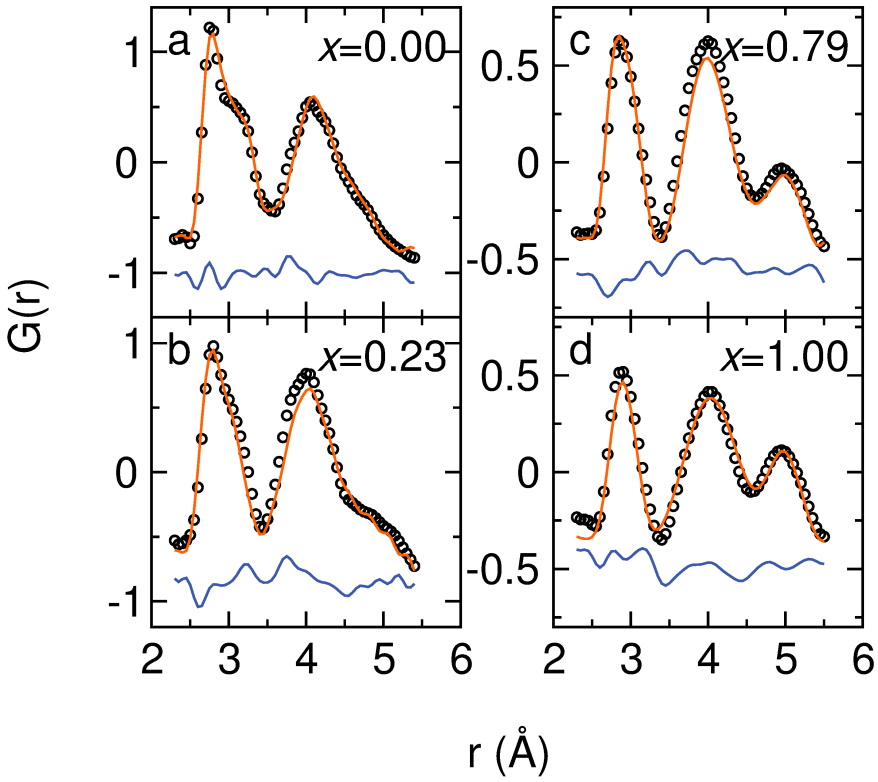

Figure 6.8: Representative low r PDF modeled with the $Pmc2_1$ phase $(CH_3NH_3)SnBr_3$ for $(CH_3NH_3)_{1-x}Cs_xSnBr_3$ where (a) $x = 0.00$, (b) $x = 0.23$, (c) $x = 0.79$, (d) $x = 1.00$. The PDF is represented by black circles, the fit by orange lines, and the difference by blue lines.

Table 6.2: Symmetry descriptors of the displacement modes related to tin and bromine refined during mode refinements of the PDF of $(CH_3NH_3)_{1-x}Cs_xSnBr_3$. All three of the Γ_4^- mode amplitudes were co-refined to avoid parameter correlation. Refinement of the M_3^+ A_{2u} mode amplitude and the M_5^- T_{1u} mode amplitude lead to values within error of zero, and in final refinements were fixed at zero.

Subgroup	Mulliken Symbol	Space Group	Wyckoff Site
Γ_4^-	T_{1u}	$Amm2$	[Sn:a]
	A_{2u}	$Amm2$	[Br:d]
	E_u	$Amm2$	[Br:d]
Γ_5^-	E_u	$Amm2$	[Br:d]
M_2^+	E_u	$P4/mbm$	[Br:d]
M_3^+	A_{2u}	$P4/mbm$	[Br:d]
M_5^-	E_u	$Pmma$	[Br:d]
	T_{1u}	$Pmma$	[Sn:a]

that this structure is insufficient to describe the short-range correlations (shown for the end members in Figure 6.7). The short-range correlations are captured much better with the low-temperature methylammonium tin bromide $Pmc2_1$ structure, which allows for tin off-centering, for all members of the solid solution series (Figure 6.8).

The orthorhombic $Pmc2_1$ phase is related to the cubic $Pm\bar{3}m$ phase through structural distortions that can be described as displacement modes, which are categorized into those that cause in-phase octahedral rotations consistent with $P4/mbm$ space group symmetry, orthorhombic compression of the b axis and expansion of the c axis consistent with $Pmma$ space group symmetry, and stereochemical activation related intra-octahedral deformations as found consistent with $Amm2$ space group symmetry (Table 6.2).[275] The displacement mode amplitudes were refined by grouping together each mode into their symmetry related groups, as described in Table 6.2. Mode refinements of the PDF demonstrate that the magnitude of the octahedral rotation mode labelled as $P4/mbm$ does not depend strongly on x, while the more substituted members of the solid solution series generally have a larger amplitude orthorhombic displacement, labelled as $Pmma$ (Figure

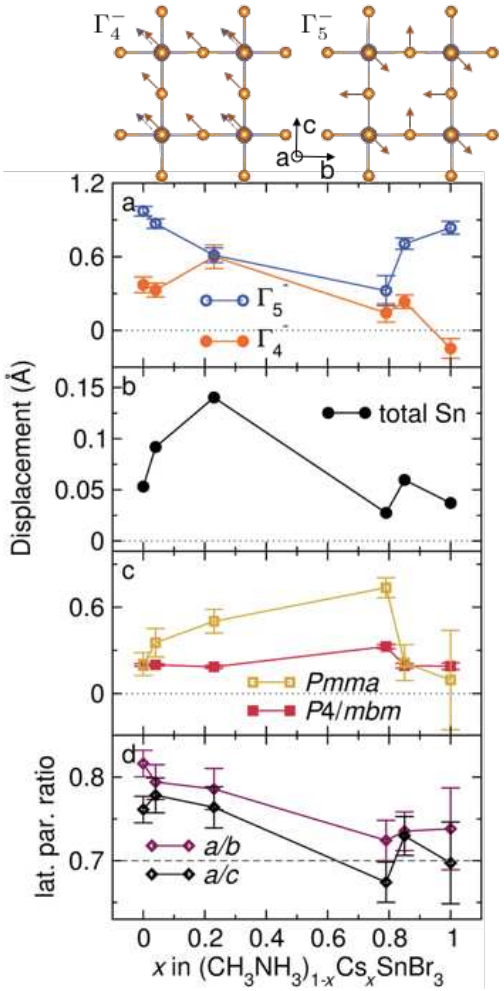

Figure 6.9: Mode refinement parameters from the fits in Figure 6.8 resulting for the series $(CH_3NH_3)_{1-x}Cs_xSnBr_3$. (a) Mode amplitudes related to stereochemical activation in the Γ_4^- subgroup and the Γ_5^- subgroup. The overall displacement directions for each subgroup are shown above the plot. The horizontal grey dotted line shows zero. (b) Calculated total tin displacement based on the representative structures shown in Figure 6.10. (c) Mode amplitudes related to cooperative octahedral distortions leading to $P4/mbm$ symmetry or $Pmma$ symmetry. The horizontal grey dotted line shows zero. (d) Ratio of lattice parameters. The horizontal grey dashed line shows 0.7, where $a = \sqrt{(}2)b$ or $a = \sqrt{(}2)c$.

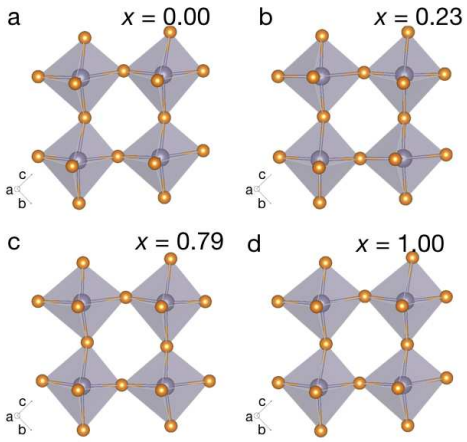

Figure 6.10: Representative structures resulting from the mode refinements of the PDF of the series $(CH_3NH_3)_{1-x}Cs_xSnBr_3$ where (a) $x = 0.00$, (b) $x = 0.23$, (c) $x = 0.79$ and (d) $x = 1.00$.

6.9b). The increase in the orthorhombic distortion magnitude close to the miscibility gap likely indicates anisotropic chemical pressure originating from the different sizes of cesium and methylammonium.

The modes relating to lone pair stereochemical activation belong to either the Γ_4^- or Γ_5^- irreducible representation.[275] The Γ_4^- representation is composed of one mode related to tin displacements (T_{1u} symmetry) and two modes related to bromide displacements (A_{2u}, E_u symmetries). Attempts to refine each mode amplitude individually demonstrated that the variables were highly correlated, so a single amplitude was assigned to all three modes within the Γ_4^- subgroup. The three amplitudes are all positively correlated; anti-correlation between the Γ_4^- mode amplitudes or the other refined mode amplitudes results in statistically and visually worse fits. In general, the amplitude of the Γ_4^- for cesium rich members of the solid solution series have a smaller magnitude than those of the methylammonium rich. This correlates with the tendency of cesium rich members of the solid solution series to have lattice parameters that are locally more cubic, where the ratio

of a/b or a/c is closer to the idealized cubic ratio of 0.7 ($a_{cubic} = \sqrt{2} \times c_{orth}$) (Figure 6.9c). This relationship suggests that with increased chemical pressure exerted on the octahedra to remain regular and consistent with cubic symmetry the tin lone pair will be less likely to stereochemically activate.

The Γ_5^- representation contains only one mode, which relates to bromine scissoring displacements depicted in Figure 6.9. The Γ_5^- mode amplitudes, in contrast to the Γ_4^- mode amplitudes, does not depend monotonically on x and decreases with cation mixing (Figure 6.9a). The trend with x for the Γ_5^- mode amplitude correlates inversely to that of the $Pmma$ symmetry mode amplitude. This relationship demonstrates that anisotropic chemical pressure on the octahedra, in this case from the the compression along b and expansion along c described by the $Pmma$ mode, is in competition with stereochemical activation of the lone pair.

Overall, stereochemical lone pair activation in these materials is a result of the combined amplitudes of the Γ_4^- and Γ_5^- subgroups and can be evaluated by considering tin displacement from the centroid of the octahedron formed by the bromide ions. Tin displacement (Figure 6.9b) does not relate to x monotonically, but it can be tuned between 0.025 and 0.15 Å across the solid solution series $(CH_3NH_3)_{1-x}Cs_xSnBr_3$. Previous characterization[19,20] of similar materials resulted in larger reported displacements for $CsSnBr_3$, most likely resulting from approach for binning the PDF at the Nyquist condition and the pinning of the A-site position in this study. This tunability should have implications for the optoelectronic properties of tin bromide perovskites, as modified or decreased lone pair activation affects polarizability of these materials.[279]

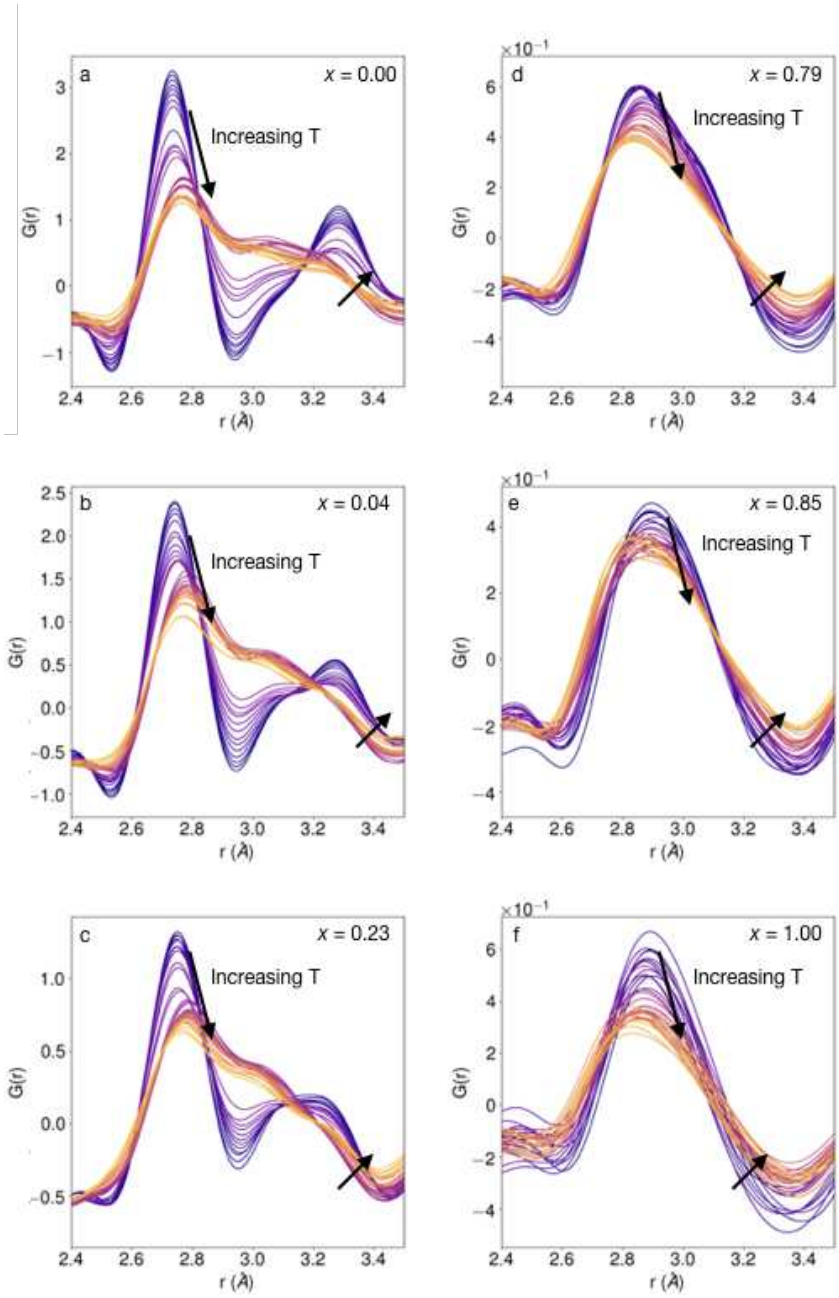

Figure 6.11: Temperature dependence of the PDF for $(CH_3NH_3)_{1-x}Cs_xSnBr_3$ between 100 K and 420 K where (a) $x = 0.00$, (b) $x = 0.04$, (c) $x = 0.23$, (d) $x = 0.79$, (e) $x = 0.85$, and (f) $x = 1.00$. While the peak shape is conserved for cesium rich members of the solid solution, the peak shape abruptly changes at the cubic to orthorhombic phase transition temperature in methylammonium rich members of the solid solution series.

As temperature increases from 100 K to 420 K, the PDF for all samples in $(CH_3NH_3)_{1-x}Cs_xSnBr_3$ exhibit a decrease in peak height and tailing on the high r side of the first correlation (Figure 6.11). In methylammonium rich samples, these trends become more apparent after the $Pmc2_1$ to $Pm\bar{3}m$ phase transition, while in cesium rich samples the trends are monotonic over the entire temperature range. The tailing and decrease in peak height was captured in the room temperature structural refinements by the stereochemical activation modes.[20] In $CsSnBr_3$, the increase in peak tailing with temperature has been attributed to emphanisis, *i.e.* increased structural distortion on heating.[20] Qualitative examination of the temperature-dependent PDF therefore indicates that the local structure in the entire $(CH_3NH_3)_{1-x}Cs_xSnBr_3$ series exhibits local stereochemical activation over a wide temperature range, including in the high temperature cubic phase. The structural distortions actually increase in amplitude with increasing temperature in the cubic phase, despite diffraction data that shows that these distortions are inconsistent with the average crystallographic symmetry.[20] The temperature dependence of lone pair activations in tin bromide perovskites has implications for the temperature dependence of optoelectronic properties that depend on the polarization of the material, such as polaron formation.

Conclusions

Understanding the dynamic landscape and structural distortions of hybrid perovskites is essential to building comprehensive structure-property relationships. In tin bromide perovskites, the nature of average or local and dynamic stereochemical lone pair activation depends on the identity of the A-site cation; on cooling from room temperature methy-

lammonium tin bromide exhibits long-range, static tin off-centering and octahedral asymmetry while the average low temperature phase of cesium tin bromide is characterized by symmetrical octahedra. To investigate the sensitivity of the stereochemical activation to substitution, the local and average structure of the solid solution $(CH_3NH_3)_{1-x}Cs_xSnBr_3$ was characterized. Comparison of the Vegard's Law plot with absorbance data suggest the formation of a homogenous solid solution, where the optical gap is determined by lattice compression. The composition dependent sub-band gap IR tailing in the absorbance data suggests A-site dependent intrinsic defect formation. Substitution leads to changes in the average structure; cesium substitution suppresses the lowest temperature phase transition in methylammonium tin bromide and methylammonium substitution in cesium tin bromide decreases the phase transition temperatures. Comparison of the local structure as a function of x demonstrates that stereochemical activation is in competition with other forms of chemical pressure on the octahedra, and vary over an order of magnitude with x. This tunability of lone pair activation is linked to the polarizability of halide perovskites, and could lead to increased control over many of the advantageous optoelectronic properties.

Experimental Methods

Materials: The precursor methylammonium bromide (CH_3NH_3Br) was prepared by dissolving methylamine hydrochloride in excess hydrobromic acid and evaporating excess solvent.

Methylammonium tin bromide ($CH_3NH_3SnBr_3$) was prepared according to previous literature methods.[275] Briefly, equimolar amounts of methylammonium bromide and tin (II) bromide were dissolved separately into anhydrous ethanol. The tin bromide solution was heated to 80 °C and the methylammonium bromide solution was added dropwise. The resulting red precipitate was filtered and dried. All procedures were carried out under argon.

Cesium tin bromide ($CsSnBr_3$) was prepared from the halide binaries CsBr and $SnBr_2$. Stoichiometric amounts of cesium bromide and tin (II) bromide were ground together, pelleted, and sealed in a quartz ampoule under vacuum. Samples were then heated to 400 °C over 6 h, held at temperature for 6 h, and then furnace cooled. All procedures were carried out under argon.

The solid solution series ($(CH_3NH_3)_{1-x}Cs_xSnBr_3$) was prepared by grinding stoichiometric quantities of the end member perovskites before powders were pelleted, sealed in a quartz ampoule, evacuated, and placed in a convection oven at 150 °C for 5 to 7 d. All procedures were carried out under argon.

The preparation of the solid solution series between $CH_3NH_3SnBr_3$ and $CsSnBr_3$ is complicated by several competing phases with the cubic perovskite structure, such that the preparation of pure materials can require multiple annealing steps and addition of small amounts of the binary reactants. The A^+ poor phase ASn_2Br_5 will react with additional CsBr or CH_3NH_3Br during a 24 h post-synthesis anneal at 150 °C. The A^+ rich phase A_4SnBr_6 will similarly react with additional $SnBr_2$ in a 24 h post-synthesis anneal. The presence of these two impurity phases in solid solution samples will modify the stoi-

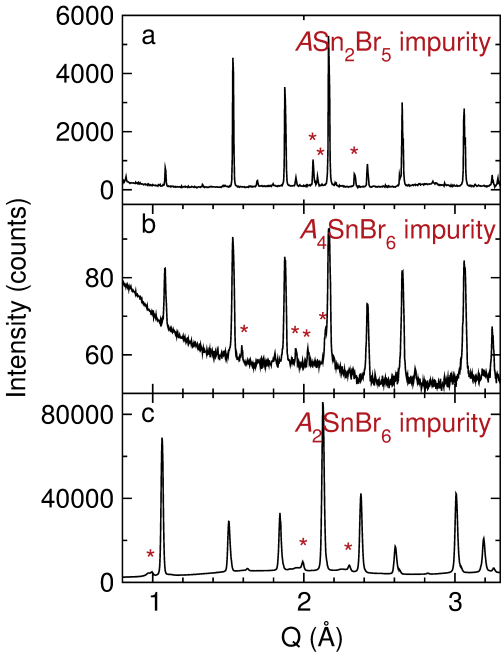

Figure 6.12: (a) High resolution X-ray diffraction pattern of $(CH_3NH_3)_{0.77}Cs_{0.23}SnBr_3$ with a ASn_2Br_5 minor phase indicated with red asterisks. (b) High resolution X-ray diffraction pattern of $(CH_3NH_3)_{0.19}Cs_{0.89}SnBr_3$ with a A_4SnBr_6 minor phase indicated with red asterisks. (c) High resolution X-ray diffraction pattern of $(CH_3NH_3)_{0.77}Cs_{0.23}SnBr_3$ with a A_2SnBr_6 minor phase indicated with red asterisks.

chiometry away from the nominal composition unless the A-site occupancy of the impurity phase is known. For example, if the nominal composition is 70% cesium and 30% methylammonium in a ASn_2Br_5 impurity phase, the addition of CsBr will increase the cesium concentration. The last major competing phase is Cs_2SnBr_6, which requires tin oxidation and mostly likely occurs during air exposure. This reaction appears to be irreversible, and so great care should be taken to limit air exposure. Each phase has characteristic peaks that can be used as a first pass identification, as demonstrated in Figure 6.12, which shows the incomplete synthesis of several members of the solid solution series.

Diffraction: Laboratory powder X-ray diffraction (PXRD) data were collected on a Bruker D8 Discover X-ray diffractometer using a Cu K_α radiation source and a Lynxeye XE-T position-sensitive detector to check phase purity. High-resolution synchrotron pow-

der X-ray diffraction (SXRD) patterns were collected on the diffractometer 28-ID-1 at the National Synchrotron Light Source II, Brookhaven National Laboratory ($\lambda = 0.1668$ Å) between $T = 420$ K and $T = 100$ K in intervals of $\Delta T = 20$ K. Powders were flame sealed in glass capillaries under vacuum.

Total Scattering: Total scattering data suitable for pair distribution function analysis were collected on the diffractometer 11-ID-B at the Advanced Photon Source, Argonne National Laboratory ($\lambda = 0.1423$ Å) between $T = 420$ K and $T = 100$ K in intervals of $\Delta T = 10$ K. Powders were epoxy sealed in glass capillaries under a nitrogen atmosphere. Data reduction was performed with pdfgetx3.[258] Traditional PDF structural refinements were performed in pdfgui[280] and mode refinements in TOPAS v6. To avoid overfitting, the PDF was binned at $dx = 0.05$. The cifs for the mode refinements were distorted from cubic symmetry using ISODISTORT.[281] Including all refineable modes leads to correlation of parameters. Correlated parameters that were smaller than 0.01 were set to 0.0 and not refined. Correlated parameters that were larger than 0.01 were refined together. Electron density for the A-site was approximated in PDF refinements by considering the average number of electrons at the A-site and using the analogous atom. For example, the number of electrons for the average A-site cation in ($(CH_3NH_3)_{0.2}Cs_{0.8}SnBr_3$)$= 0.2 \times 19 + 0.8 \times 55 = 48$, which corresponds to cadmium.

UV-Vis: Absorbance spectra were collected on the diffuse reflectance attachment on the Agilent Cary 5000. Undiluted powders were sealed between two microscope slides under argon.

7. Conclusion

Summary

Characterization of organic cation dynamics and organic-inorganic coupling in hybrid perovskites enables the development of structure-property relationships. In formamidinium perovskites, chemical pressure exerted on the inorganic octahedra by formamidinium electrostatic quadrupoles plays an active role in the phase behavior, whether that is in the orientational phase transitions of formamidinium lead bromide or the hysteretic and ferroelastic phase transition of formamidinium tin (IV) iodide. The formamidinium electrostatic quadrupoles couple strongly to electric field gradient in the inorganic octahedra, amplifying quadrupolar interactions that exert further chemical pressure on the structure. In methylammonium perovskites, hydrogen bonding interactions between methylammonium and the inorganic octahedra lead to unusual octahedral rotations in methylammonium lead bromide, an instability in methylammonium tin (IV) iodide at low temperature, and average tin off-centering in methylammonium tin (II) bromide. The distinction between quadrupolar and dipolar organic-inorganic coupling can determine the stress-strain relationships that give rise to unusual phase behavior. In either case, the orientation and dynamics of the organic cation participate and can direct the phase behavior.

The organic-inorganic couplings that give rise to the phase behavior of hybrid perovskites can be tuned through chemical substitution. Cesium substitution in formamidinium lead bromide suppresses the low temperature orientational phase transitions by

introducing a stronger elastic frustration that overrules the frustration of formamidinium quadrupoles. Cesium substitution also suppresses the low temperature phase transition in methylammonium tin bromide, indicating that cesium interrupts the interactions that lead to that phase transition as well. In other cases, substitution increases lattice microstrain. Cesium substitution in methylammonium lead bromide leads to the formation of an orientational glass and a reentrant phase transition for 20% cesium substituted materials. Both of these phenomena indicate the presence of strongly competing interactions, likely related to the different coordination preferences of cesium and methylammonium in lead halide perovskites. The characterization of substituted materials gives additional insight into the strength and structure directing properties of the organic-inorganic coupling in lead halide perovskites. Furthermore, the top-performing hybrid perovskites incorporated into photovoltaic devices tend to be highly substituted materials, and therefore structure-property relationships for hybrid perovskites must include the impact of substitution.

For conventional inorganic semiconductors like silicon, structure-property relationships tend to be built on the average structure as the covalent and directional lattice has few dynamic degrees of freedom. The polarizable halide perovskite structure, however, has many dynamic degrees of octahedral and molecular dynamic freedom. Only by characterization of the organic cation dynamics, for example, can we explain the changes in the temperature dependent photoconductivity of formamidinium lead bromide or the hysteresis in the phase transitions of methylammonium lead bromide. For hybrid perovskites and other hybrid or polarizable materials, structure-property relationships must include dynamics.

Outlook

Future Experiments

To build comprehensive structure-property relationships, the structural behavior described in this document must be linked to high quality property measurements. Temperature dependent photoluminescence, time resolved photoluminescence, and photoconductivity are powerful probes of the optoelectronic behavior of semiconductors and can be used to investigate the impacts of cesium substitution in methylammonium lead bromide, formamidinium lead bromide, and methylammonium time bromide through the structural changes observed in chapters 3, 4, and 6. The Central Instrument Facility has the capabilities to collect photoluminescence and time resolved photoluminescence on powders at room temperature and at liquid nitrogen temperatures. The sample stage on the photoconductivity instrument developed by Matthew Gorman and Prof. James Neilson can modified to be compatible with bulk powder measurements. Ideally, this sample stage would also be compatible with use in the Physical Properties Measurement System in the Central Instrument Facility or with a cryostat.

Remaining Open Questions

One of the perovskite materials most promising for commercialization in a photovoltaic device is $(CH(NH_2)_2)_{0.79}(CH_3NH_3)_{0.16}Cs_{0.05}Pb(I_{0.84}Br_{0.16})_3$, which has three distinct chemical substitutions.[282] In contrast, this dissertation discusses single substitutions only at the A-site, and only provide a starting point to understanding the impact of substitution. For

example, since cesium substitution relieves strain in formamidinium perovskites, but increases strain in methylammonium perovskites, further studies are necessary to establish how these competing strains manifest in a mixed organic cation material. Halide substitution also affects the organic cation dynamics,[99] and little is known about the structural and dynamic effects of substituting at multiple sites. Substituted hybrid perovskites have a complex potential energy landscape that we have yet to fully map.

Chemically substituting hybrid perovskites slows or suppresses their decomposition under ambient and working conditions. There are several hypotheses in the literature that propose explanations for this relationship. For example, cesium substitution in formamidinium perovskites relieves strain and therefore could stabilize the perovskite structure relative to any competing phases.[179] In methylammonium perovskites, substitution can increase the activation energy of halide migration, which suggests a link between organic cation dynamics, orientational glass formation, and ion mobility that could explain the suppressed decomposition with substitution.[101] Computational and experimental studies focused on cation dynamics during decomposition would fill in several of the gaps in this area and allow for validation of the most relevant hypotheses.

Two dimensional layered perovskites represent an exciting extension of structure property relationships being developed for hybrid perovskites. Layered perovskites are more compositionally diverse then their three dimensional parent compounds,[3] as the decrease in octahedral connectivity lifts the size restrictions on the organic cation. Complex and bulky organics introduce many additional dynamic degrees of freedom and types of organic-inorganic coupling. For example, increasing the alkyl chain length introduces additional

complexity to the organic cation dynamics,[283] which can influence the optoelectronic properties.[56] These initial studies demonstrate the importance of organic cation dynamics in layered perovskite materials, suggest that continuing these investigations will provide valuable insight into the optoelectronic properties of hybrid perovskites.

Bibliography

[1] Stranks, S. D.; Snaith, H. J. Metal-halide perovskites for photovoltaic and light-emitting devices. *Nature Nanotechnology* **2015**, *10*, 391–402.

[2] Walsh, A. Principles of Chemical Bonding and Band Gap Engineering in Hybrid Organic–Inorganic Halide Perovskites. *J. Phys. Chem. C* **2015**, *119*, 5755–5760.

[3] Smith, M. D.; Crace, E. J.; Jaffe, A.; Karunadasa, H. I. The Diversity of Layered Halide Perovskites. *Annual Review of Materials Research* **2018**, *48*, 111–136.

[4] Smith, M. D.; Karunadasa, H. I. White-Light Emission from Layered Halide Perovskites. *Accounts of Chemical Research* **2018**, *51*, 619–627.

[5] Maughan, A. E.; Ganose, A. M.; Scanlon, D. O.; Neilson, J. R. Perspectives and Design Principles of Vacancy-Ordered Double Perovskite Halide Semiconductors. *Chemistry of Materials* **2019**, acs.chemmater.8b05036.

[6] Maughan, A. E.; Ganose, A. M.; Bordelon, M. M.; Miller, E. M.; Scanlon, D. O.; Neilson, J. R. Defect Tolerance to Intolerance in the Vacancy-Ordered Double Perovskite Semiconductors Cs2SnI6 and Cs2TeI6. *Journal of the American Chemical Society* **2016**, *138*, 8453–8464.

[7] Christians, J. A.; Schulz, P.; Tinkham, J. S.; Schloemer, T. H.; Harvey, S. P.; Tremolet de Villers, B. J.; Sellinger, A.; Berry, J. J.; Luther, J. M. Tailored interfaces of

unencapsulated perovskite solar cells for >1,000 hour operational stability. *Nature Energy* **2018**, *3*, 68–74.

[8] Askar, A. M.; Bernard, G. M.; Wiltshire, B.; Shankar, K.; Michaelis, V. K. Multinuclear Magnetic Resonance Tracking of Hydro, Thermal, and Hydrothermal Decomposition of CH3NH3PbI3. *Journal of Physical Chemistry C* **2017**, *121*, 1013–1024.

[9] Nagabhushana, G. P.; Shivaramaiah, R.; Navrotsky, A. Direct calorimetric verification of thermodynamic instability of lead halide hybrid perovskites. *Proceedings of the National Academy of Sciences* **2016**, *113*, 7717–7721.

[10] Dang 1, Z.; Dinh 1, D. A. Interaction of light with lead halide perovskites: A review. *Characterization and Application of Nanomaterials* **2018**, *1*.

[11] Aziz, A.; Aristidou, N.; Bu, X.; Westbrook, R. J. E.; Haque, S. A.; Islam, M. S. Understanding the Enhanced Stability of Bromide Substitution in Lead Iodide Perovskites. *Chemistry of Materials* **2020**, *32*, 400–409.

[12] Wang, Z.; Shi, Z.; Li, T.; Chen, Y.; Huang, W. Stability of Perovskite Solar Cells: A Prospective on the Substitution of the A Cation and X Anion. *Angew. Chemie Int. Ed.* **2017**, *56*, 1190–1212.

[13] Prasanna, R.; Gold-Parker, A.; Leijtens, T.; Conings, B.; Babayigit, A.; Boyen, H.-G.; Toney, M. F.; McGehee, M. D. Band Gap Tuning via Lattice Contraction and Octahedral Tilting in Perovskite Materials for Photovoltaics. *Journal of the American Chemical Society* **2017**, *139*, 11117–11124.

[14] Beal, R. E.; Slotcavage, D. J.; Leijtens, T.; Bowring, A. R.; Belisle, R. A.; Nguyen, W. H.; Burkhard, G. F.; Hoke, E. T.; McGehee, M. D. Cesium Lead Halide Perovskites with Improved Stability for Tandem Solar Cells. *The Journal of Physical Chemistry Letters* **2016**, *7*, 746–751.

[15] Woodward, P. M. Octahedral Tilting in Perovskites. II. Structure Stabilizing Forces. *Acta Crystallographica Section B: Structural Science* **1997**, *53*, 44–66.

[16] Young, J.; Rondinelli, J. M. Octahedral Rotation Preferences in Perovskite Iodides and Bromides. *Journal of Physical Chemistry Letters* **2016**, *7*, 918–922.

[17] Even, J.; Carignano, M.; Katan, C. Molecular disorder and translation/rotation coupling in the plastic crystal phase of hybrid perovskites. *Nanoscale* **2016**, *8*, 6222–36.

[18] Even, J. Pedestrian Guide to Symmetry Properties of the Reference Cubic Structure of 3D All-Inorganic and Hybrid Perovskites. *The Journal of Physical Chemistry Letters* **2015**, *6*, 2238–2242.

[19] Laurita, G.; Fabini, D. H.; Stoumpos, C. C.; Kanatzidis, M. G.; Seshadri, R. Chemical tuning of dynamic cation off-centering in the cubic phases of hybrid tin and lead halide perovskites. *Chem. Sci.* **2017**, *8*, 5628–5635.

[20] Fabini, D. H.; Stoumpos, C. C.; Laurita, G.; Kaltzoglou, A.; Kontos, A. G.; Falaras, P.; Kanatzidis, M. G.; Seshadri, R. Reentrant Structural and Optical Properties and Large Positive Thermal Expansion in Perovskite Formamidinium Lead Iodide. *Angew. Chemie Int. Ed.* **2016**, *55*, 15392–15396.

[21] Stoumpos, C. C.; Frazer, L.; Clark, D. J.; Kim, Y. S.; Rhim, S. H.; Freeman, A. J.; Ketterson, J. B.; Jang, J. I.; Kanatzidis, M. G. Hybrid germanium iodide perovskite semiconductors: Active lone pairs, structural distortions, direct and indirect energy gaps, and strong nonlinear optical properties. *Journal of the American Chemical Society* **2015**, *137*, 6804–6819.

[22] Ibaceta-Jana, J.; Muydinov, R.; Rosado, P.; Mirhosseini, H.; Chugh, M.; Nazarenko, O.; Dirin, D. N.; Heinrich, D.; Wagner, M. R.; Kuhne, T. D.; Szyszka, B.; Kovalenko, M. V.; Hoffmann, A. Vibrational dynamics in lead halide hybrid perovskites investigated by Raman spectroscopy. *Physical chemistry chemical physics : PCCP* **2020**,

[23] Diroll, B. T.; Mannodi-Kanakkithodi, A.; Chan, M. K.; Schaller, R. D. Spectroscopic Comparison of Thermal Transport at Organic-Inorganic and Organic-Hybrid Interfaces Using CsPbBr3 and FAPbBr3 (FA = Formamidinium) Perovskite Nanocrystals. *Nano Letters* **2019**, *19*, 8155–8160.

[24] Pérez-Osorio, M. A.; Lin, Q.; Phillips, R. T.; Milot, R. L.; Herz, L. M.; Johnston, M. B.; Giustino, F. Raman Spectrum of the Organic-Inorganic Halide Perovskite CH3NH3PbI3from First Principles and High-Resolution Low-Temperature Raman Measurements. *Journal of Physical Chemistry C* **2018**, *122*, 21703–21717.

[25] Drużbicki, K.; Pinna, R. S.; Rudic, S.; Jura, M.; Gorini, G.; Fernandez-Alonso, F. Unexpected Cation Dynamics in the Low-temperature Phase of Methylammonium

Lead Iodide: The Need for Improved Models. *J. Phys. Chem. Lett.* **2016**, *7*, 47011–4709.

[26] Chen, T.; Foley, B. J.; Ipek, B.; Tyagi, M.; Copley, J. R. D.; Brown, C. M.; Choi, J. J.; Lee, S. H. Rotational dynamics of organic cations in the $CH_3NH_3PbI_3$ perovskite. *Phys. Chem. Chem. Phys.* **2015**, *17*, 31278–31286.

[27] Carignano, M. A.; Saeed, Y.; Aravindh, S. A.; Roqan, I. S.; Even, J.; Katan, C. A close examination of the structure and dynamics of HC(NH 2) 2 PbI 3 by MD simulations and group theory. *Phys. Chem. Chem. Phys.* **2016**, *18*, 27109–27118.

[28] Fabini, D. H.; Siaw, T. A.; Stoumpos, C. C.; Laurita, G.; Olds, D.; Page, K.; Hu, J. G.; Kanatzidis, M. G.; Han, S.; Seshadri, R. Universal Dynamics of Molecular Reorientation in Hybrid Lead Iodide Perovskites. *Journal of the American Chemical Society* **2017**, *139*, 16875–16884.

[29] Taylor, V. C. A.; Tiwari, D.; Duchi, M.; Donaldson, P. M.; Clark, I. P.; Fermin, D. J.; Oliver, T. A. A. Investigating the Role of the Organic Cation in Formamidinium Lead Iodide Perovskite Using Ultrafast Spectroscopy. *The Journal of Physical Chemistry Letters* **2018**, *9*, 895–901.

[30] Govinda, S.; Kore, B. P.; Swain, D.; Hossain, A.; De, C.; Guru Row, T. N.; Sarma, D. D. Critical Comparison of FAPbX3 and MAPbX3 (X = Br and Cl): How Do They Differ? *Journal of Physical Chemistry C* **2018**, *122*, 13758–13766.

[31] Schueller, E. C.; Laurita, G.; Fabini, D. H.; Stoumpos, C. C.; Kanatzidis, M. G.; Seshadri, R. Crystal Structure Evolution and Notable Thermal Expansion in Hybrid Perovskites Formamidinium Tin Iodide and Formamidinium Lead Bromide. *Inorganic Chemistry* **2018**, *57*, 695–701.

[32] Li, J.; Bouchard, M.; Reiss, P.; Aldakov, D.; Pouget, S.; Demadrille, R.; Aumaitre, C.; Frick, B.; Djurado, D.; Rossi, M.; Rinke, P. Activation Energy of Organic Cation Rotation in CH3NH3PbI3 and CD3NH3PbI3: Quasi-Elastic Neutron Scattering Measurements and First-Principles Analysis Including Nuclear Quantum Effects. *Journal of Physical Chemistry Letters* **2018**, *9*, 3969–3977.

[33] Swainson, I. P.; Stock, C.; Parker, S. F.; Van Eijck, L.; Russina, M.; Taylor, J. W. From soft harmonic phonons to fast relaxational dynamics in CH$_3$NH$_3$PbBr$_3$. *Physical Review B* **2015**, *92*, 100303.

[34] Chen, T.; Chen, W.-L.; Foley, B. J.; Lee, J.; Ruff, J. P. C.; Ko, J. Y. P.; Brown, C. M.; Harriger, L. W.; Zhang, D.; Park, C.; Yoon, M.; Chang, Y.-M.; Choi, J. J.; Lee, S.-H. Origin of long lifetime of band-edge charge carriers in organic-inorganic lead iodide perovskites. *Proceedings of the National Academy of Sciences* **2017**, *114*, 7519–7524.

[35] Ren, Y.; Oswald, I. W. H.; Wang, X.; McCandless, G. T.; Chan, J. Y. Orientation of organic cations in hybrid inorganic-organic perovskite CH3NH3PbI3 from subatomic resolution single crystal neutron diffraction structural studies. *Crystal Growth and Design* **2016**, *16*, 2945–2951.

[36] Lee, J.-H.; Bristowe, N. C.; Bristowe, P. D.; Cheetham, A. K. Role of hydrogen-bonding and its interplay with octahedral tilting in CH 3 NH 3 PbI 3. *Chemical Communications* **2015**, *51*, 6434–6437.

[37] Beecher, A. N.; Semonin, O. E.; Skelton, J. M.; Frost, J. M.; Terban, M. W.; Zhai, H.; Alatas, A.; Owen, J. S.; Walsh, A.; Billinge, S. J. L. Direct Observation of Dynamic Symmetry Breaking above Room Temperature in Methylammonium Lead Iodide Perovskite. *ACS Energy Letters* **2016**, *1*, 880–887.

[38] Maughan, A. E.; Ganose, A. M.; Candia, A. M.; Granger, J. T.; Scanlon, D. O.; Neilson, J. R. Anharmonicity and Octahedral Tilting in Hybrid Vacancy-Ordered Double Perovskites. *Chem. Mater.* **2018**, *30*, 472–483.

[39] Ghosh, D.; Welch, E.; Neukirch, A. J.; Zakhidov, A.; Tretiak, S. Polarons in Halide Perovskites: A Perspective. *The Journal of Physical Chemistry Letters* **2020**, 3271–3286.

[40] Brenner, T. M.; Egger, D. A.; Rappe, A. M.; Kronik, L.; Hodes, G.; Cahen, D. Are Mobilities in Hybrid Organic-Inorganic Halide Perovskites Actually "high"? *Journal of Physical Chemistry Letters* **2015**, *6*, 4754–4757.

[41] Park, M.; Neukirch, A. J.; Reyes-Lillo, S. E.; Lai, M.; Ellis, S. R.; Dietze, D.; Neaton, J. B.; Yang, P.; Tretiak, S.; Mathies, R. A. Excited-state vibrational dynamics toward the polaron in methylammonium lead iodide perovskite. *Nat. Commun.* **2018**, *9*, 2525.

[42] Niesner, D.; Zhu, H.; Miyata, K.; Joshi, P. P.; Evans, T. J. S.; Kudisch, B. J.; Trinh, M. T.; Marks, M.; Zhu, X. Persistent Energetic Electrons in Methylammonium Lead Iodide Perovskite Thin Films. *J. Am. Chem. Soc.* **2016**, *138*, 15717–15126.

[43] Stranks, S. D.; Plochocka, P. The influence of the Rashba effect. *Nature Materials* **2018**, *17*, 381–382.

[44] Berdiyorov, G. R.; Kachmar, A.; El-Mellouhi, F.; Carignano, M. A.; El-Amine Madjet, M. Role of Cations on the Electronic Transport and Optical Properties of Lead-Iodide Perovskites. *The Journal of Physical Chemistry C* **2016**, *120*, 16259–16270.

[45] Motta, C.; El-Mellouhi, F.; Kais, S.; Tabet, N.; Alharbi, F.; Sanvito, S. Revealing the role of organic cations in hybrid halide perovskite CH3NH3PbI3. *Nature Communications* **2015**, *6*, 7026.

[46] Motta, C.; Mandal, P.; Sanvito, S. Effects of molecular dipole orientation on the exciton binding energy of $CH_3NH_3PbI_3$, url = https://link.aps.org/doi/10.1103/PhysRevB.94.045202, volume = 94, year = 2016. *Physical Review B* 045202.

[47] Zhu, H.; Miyata, K.; Fu, Y.; Wang, J.; Joshi, P.; Niesner, D.; Williams, K. W.; Jin, S.; Zhu, X.-Y. Screening in Crystalline Liquids Protects Energetic Carriers in Hybrid Perovskites. *Science (New York, N.Y.)* **2016**, *353*, 1409–1413.

[48] Miyata, K.; Meggiolaro, D.; Tuan Trinh, M.; Joshi, P. P.; Mosconi, E.; Jones, S. C.; De Angelis, F.; Zhu, X. Y. Large polarons in lead halide perovskites. *Sci. Adv.* **2017**, *3*, e1701217.

[49] Davies, C. L.; Borchert, J.; Xia, C. Q.; Milot, R. L.; Kraus, H.; Johnston, M. B.; Herz, L. M. Impact of the Organic Cation on the Optoelectronic Properties of Formamidinium Lead Triiodide. *J. Phys. Chem. Lett.* **2018**, 4502–4511.

[50] Milot, R. L.; Eperon, G. E.; Snaith, H. J.; Johnston, M. B.; Herz, L. M. Temperature-Dependent Charge-Carrier Dynamics in $CH_3NH_3PbI_3$ Perovskite Thin Films. *Adv. Funct. Mater.* **2015**, *25*, 6218–6227.

[51] Snaith, H. J. Present status and future prospects of perovskite photovoltaics. *Nat. Mater.* **2018**, *17*, 372–376.

[52] Lozano, G. The Role of Metal Halide Perovskites in Next-Generation Lighting Devices. *J. Phys. Chem. Lett.* **2018**, *9*, 3987–3997.

[53] Zhu, H.; Miyata, K.; Fu, Y.; Wang, J.; Joshi, P.; Niesner, D.; Williams, K. W.; Jin, S.; Zhu, X.-Y. Screening in Crystalline Liquids Protects Energetic Carriers in Hybrid Perovskites. *Science* **2016**, *353*, 1409–1413.

[54] Katan, C.; Mohite, A. D.; Even, J. Entropy in halide perovskites. *Nat. Mater.* **2018**, *17*, 377–384.

[55] Egger, D. A.; Rappe, A. M.; Kronik, L. Hybrid Organic–Inorganic Perovskites on the Move. *Acc. Chem. Res.* **2016**, *49*, 573–581.

[56] Gong, X.; Voznyy, O.; Jain, A.; Liu, W.; Sabatini, R.; Piontkowski, Z.; Walters, G.; Bappi, G.; Nokhrin, S.; Bushuyev, O.; Yuan, M.; Comin, R.; McCamant, D.; Kelley, S. O.; Sargent, E. H. Electron-phonon interaction in efficient perovskite blue emitters. *Nat. Mater.* **2018**, *17*, 550–556.

[57] Fabini, D. H.; Hogan, T.; Evans, H. A.; Stoumpos, C. C.; Kanatzidis, M. G.; Seshadri, R. Dielectric and Thermodynamic Signatures of Low-Temperature Glassy Dynamics in the Hybrid Perovskites $CH_3NH_3PbI_3$ and $HC(NH_2)_2PbI_3$. *J. Phys. Chem. Lett.* **2016**, *7*, 376–381.

[58] Govinda, S.; Kore, B. P.; Swain, D.; Hossain, A.; De, C.; Guru Row, T. N.; Sarma, D. D. Critical Comparison of $FAPbX_3$ and $MAPbX_3$ (X = Br and Cl): How Do They Differ? *J. Phys. Chem. C.* **2018**, *122*, 13758–13766.

[59] Fabini, D. H.; Siaw, T. A.; Stoumpos, C. C.; Laurita, G.; Olds, D.; Page, K.; Hu, J. G.; Kanatzidis, M. G.; Han, S.; Seshadri, R. Universal Dynamics of Molecular Reorientation in Hybrid Lead Iodide Perovskites. *J. Am. Chem. Soc.* **2017**, *3*, jacs.7b09536.

[60] Gélvez-Rueda, M. C.; Renaud, N.; Grozema, F. C. Temperature Dependent Charge Carrier Dynamics in Formamidinium Lead Iodide Perovskite. *J. Phys. Chem. C.* **2017**, *121*, 23392–23397.

[61] Weber, O. J.; Ghosh, D.; Gaines, S.; Henry, P. F.; Walker, A. B.; Islam, M. S.; Weller, M. T. Phase Behavior and Polymorphism of Formamidinium Lead Iodide. *Chemistry of Materials* **2018**, *30*, 3768–3778.

[62] Chen, T.; Foley, B. J.; Park, C.; Brown, C. M.; Harriger, L. W.; Lee, J.; Ruff, J.; Yoon, M.; Choi, J. J.; Lee, S.-H. Entropy-driven structural transition and kinetic trapping in formamidinium lead iodide perovskite. *Sci. Adv.* **2016**, *2*, e1601650–e1601650.

[63] Prochowicz, D.; Runjhun, R.; Tavakoli, M. M.; Yadav, P.; Saski, M.; Alanazi, A. Q.; Kubicki, D. J.; Kaszkur, Z.; Zakeeruddin, S. M.; Lewiński, J.; Grätzel, M. Engineering of Perovskite Materials Based on Formamidinium and Cesium Hybridization for High-Efficiency Solar Cells. *Chemistry of Materials* **2019**, *31*, 1620–1627.

[64] Bush, K. A. et al. 23.6%-efficient monolithic perovskite/silicon tandem solar cells with improved stability. *Nature Energy* **2017**, *2*, 17009.

[65] Luo, P.; Zhou, S.; Zhou, Y.; Xia, W.; Sun, L.; Cheng, J.; Xu, C.; Lu, Y. Fabrication of CsxFA1-xPbI3 Mixed-Cation Perovskites via Gas-Phase-Assisted Compositional Modulation for Efficient and Stable Photovoltaic Devices. *ACS Applied Materials & Interfaces* **2017**, *9*, 42708–42716.

[66] Diab, H.; Trippé-Allard, G.; Lédée, F.; Jemli, K.; Vilar, C.; Bouchez, G.; Jacques, V. L.; Tejeda, A.; Even, J.; Lauret, J.-S.; Deleporte, E.; Garrot, D. Narrow Linewidth Excitonic Emission in Organic-Inorganic Lead Iodide Perovskite Single Crystals. *The Journal of Physical Chemistry Letters* **2016**, *7*, 5093–5100.

[67] Singh, S.; Li, C.; Panzer, F.; Narasimhan, K. L.; Graeser, A.; Gujar, T. P.; Köhler, A.; Thelakkat, M.; Huettner, S.; Kabra, D. Effect of Thermal and Structural Disorder on

the Electronic Structure of Hybrid Perovskite Semiconductor $CH_3NH_3PbI_3$. *J. Phys. Chem. Lett.* **2016**, *7*, 3014–3021.

[68] Wright, A. D. et al. Electron-phonon coupling in hybrid lead halide perovskites. *Nat. Commun.* **2016**, *7*, 11755.

[69] Varshni, Y. Temperature dependence of the energy gap in semiconductors. *Physica* **1967**, *34*, 149–154.

[70] Tao, S.; Schmidt, I.; Brocks, G.; Jiang, J.; Tranca, I.; Meerholz, K.; Olthof, S. Absolute energy level positions in tin and lead based halide perovskites. *Arxiv preprint* **2019**, 902.06646.

[71] Keshavarz, M.; Ottesen, M.; Wiedmann, S.; Wharmby, M.; Küchler, R.; Yuan, H.; Debroye, E.; Steele, J. A.; Martens, J.; Hussey, N. E.; Bremholm, M.; Roeffaers, M. B. J.; Hofkens, J. Tracking Structural Phase Transitions in Lead Halide Perovskites by Means of Thermal Expansion. *Advanced Materials* **2019**, *1900521*, 1900521.

[72] Schueller, E. C.; Laurita, G.; Fabini, D. H.; Stoumpos, C. C.; Kanatzidis, M. G.; Seshadri, R. Crystal Structure Evolution and Notable Thermal Expansion in Hybrid Perovskites Formamidinium Tin Iodide and Formamidinium Lead Bromide. *Inorg. Chem.* **2017**, 695–701.

[73] Swainson, I. P.; Hammond, R. P.; Soullière, C.; Knop, O.; Massa, W. Phase transitions in the perovskite methylammonium lead bromide, $CH_3ND_3PbBr_3$. *J. Solid State Chem* **2003**, *176*, 97–104.

[74] Rodova, M.; Brozek, J.; Knizek, K.; Nitsch, K. Phase transitions in ternary caesium lead bromide. *J. Therm. Anal. Calorim* **2003**, *71*, 667–673.

[75] Campbell, B. J.; Stokes, H. T.; Tanner, D. E.; Hatch, D. M. ISODISPLACE: A web-based tool for exploring structural distortions. *J. Appl. Cryst.* **2006**, *39*, 607–614.

[76] Kieslich, G.; Sun, S.; Cheetham, T. An Extended Tolerance Factor Approach for Organic-Inorganic Perovskites. *Chem. Sci.* **2015**, *6*, 3430–3433.

[77] Young, J.; Rondinelli, J. M. Octahedral Rotation Preferences in Perovskite Iodides and Bromides. *J. Phys. Chem. Lett.* **2016**, *7*, 918–922.

[78] Liu, Y.; Collins, L.; Belianinov, A.; Neumayer, S. M.; Ievlev, A. V.; Ahmadi, M.; Xiao, K.; Retterer, S. T.; Jesse, S.; Kalinin, S. V.; Hu, B.; Ovchinnikova, O. S. Dynamic behavior of CH 3 NH 3 PbI 3 perovskite twin domains. *Applied Physics Letters* **2018**, *113*, 072102.

[79] Scheie, A. LongHCPulse: Long-Pulse Heat Capacity on a Quantum Design PPMS. *J. Low Temp. Phys.* **2018**, *193*, 60–73.

[80] Dai, J.; Zheng, H.; Zhu, C.; Lu, J.; Xu, C. Comparative investigation on temperature-dependent photoluminescence of $CH_3NH_3PbBr_3$ and $CH(NH_2)_2PbBr_3$ microstructures. *Journal of Materials Chemistry C* **2016**, *4*, 4408–4413.

[81] Yang, B.; Ming, W.; Du, M. H.; Keum, J. K.; Puretzky, A. A.; Rouleau, C. M.; Huang, J.; Geohegan, D. B.; Wang, X.; Xiao, K. Real-Time Observation of Order-

Disorder Transformation of Organic Cations Induced Phase Transition and Anomalous Photoluminescence in Hybrid Perovskites. *Advanced Materials* **2018**, *30*, 1–7.

[82] Ferreira, A. C.; Létoublon, A.; Paofai, S.; Raymond, S.; Ecolivet, C.; Rufflé, B.; Cordier, S.; Katan, C.; Saidaminov, M. I.; Zhumekenov, A. A.; Bakr, O. M.; Even, J.; Bourges, P. Elastic Softness of Hybrid Lead Halide Perovskites. *Physical Review Letters* **2018**, *121*, 085502.

[83] Wilson, J. N.; Frost, J. M.; Wallace, S. K.; Walsh, A. Perspective: Dielectric and Ferroic Properties of Halide Perovskite Solar Cells. *APL Materials* **2019**, *7*, 010901.

[84] Liu, Y.; Collins, L.; Belianinov, A.; Neumayer, S. M.; Ievlev, A. V.; Ahmadi, M.; Xiao, K.; Retterer, S. T.; Jesse, S.; Kalinin, S. V.; Hu, B.; Ovchinnikova, O. S. Dynamic behavior of $CH_3NH_3PbI_3$ perovskite twin domains. *Appl. Phys. Lett.* **2018**, *113*, 072102.

[85] Rothmann, M. U.; Li, W.; Zhu, Y.; Bach, U.; Spiccia, L.; Etheridge, J.; Cheng, Y.-B. Direct observation of intrinsic twin domains in tetragonal $CH_3NH_3PbI_3$. *Nature Communications* **2017**, *8*, 14547.

[86] Grannan, E. R.; Randeria, M.; Sethna, J. P. Low-temperature properties of a model glass. I. Elastic Dipole Model. *Phys. Rev. B.* **1990**, *41*, 7784–7799.

[87] Bretschneider, S. A.; Ivanov, I.; Wang, H. I.; Miyata, K.; Zhu, X.-Y.; Bonn, M. Quantifying Polaron Formation and Charge Carrier Cooling in Lead-Iodide Perovskites. *Adv. Mater.* **2018**, *30*, adma.201707312.

[88] Shi, D. et al. Low trap-state density and long carrier diffusion in organolead trihalide perovskite single crystals. *Science* **2015**, *347*, 519–22.

[89] Wang, J.; Toby, B. H.; Lee, P. L.; Ribaud, L.; Antao, S. M.; Kurtz, C.; Ramanathan, M.; Dreele, R. B. V.; Beno, M. A. A dedicated powder diffraction beamline at the Advanced Photon Source: Commissioning and early operational results. *Review of Scientific Instruments* **2008**, *79*, 085105.

[90] Azuah, R.; Kneller, L.; Qiu, Y.; Tregenna-Piggott, P.; Origin of long lifetime of band edge, C.; Copley, J.; Dimeo, R. DAVE: A comprehensive software suite for the reduction, visualization, and analysis of low energy neutron spectroscopic data. *J. Res. Natl. Inst. Stan. Technol.* **2009**, *114*, 341–358.

[91] Cottingham, P.; Morey, J. R.; Lemire, A.; Lemire, P.; Mcqueen, T. M. Improved Instrumentation for Intensity-, Wavelength, Temperature-, and Magnetic Field-Resolved Photoconductivity Spectroscopy. *J. Solid State Chem.* **2016**, *242*, 199–207.

[92] Deretzis, I.; Smecca, E.; Mannino, G.; La Magna, A.; Miyasaka, T.; Alberti, A. Stability and Degradation in Hybrid Perovskites: Is the Glass Half-Empty or Half-Full? *The Journal of Physical Chemistry Letters* **2018**, acs.jpclett.8b00120.

[93] Schelhas, L. T.; Li, Z.; Christians, J. A.; Goyal, A.; Kairys, P.; Harvey, S. P.; Kim, D. H.; Stone, K. H.; Luther, J. M.; Zhu, K.; Stevanovic, V.; Berry, J. J. Insights into operational stability and processing of halide perovskite active layers. *Energy & Environmental Science* **2019**, *12*, 1341–1348.

[94] Chen, L.; Tan, Y.-Y.; Chen, Z.-X.; Wang, T.; Hu, S.; Nan, Z.-A.; Xie, L.-Q.; Hui, Y.; Huang, J.-X.; Zhan, C.; Wang, S.-H.; Zhou, J.-Z.; Yan, J.-W.; Mao, B.-W.; Tian, Z. Toward Long-Term Stability: Single-Crystal Alloys of Cesium-Containing Mixed Cation and Mixed Halide Perovskite. *Journal of the American Chemical Society* **2019**, jacs.8b11610.

[95] Li, Z.; Yang, M.; Park, J.-S. S.; Wei, S.-H. H.; Berry, J. J.; Zhu, K. Stabilizing Perovskite Structures by Tuning Tolerance Factor: Formation of Formamidinium and Cesium Lead Iodide Solid-State Alloys. *Chemistry of Materials* **2016**, *28*, 284–292.

[96] Lee, J. W.; Kim, D. H.; Kim, H. S.; Seo, S. W.; Cho, S. M.; Park, N. G. Formamidinium and cesium hybridization for photo- and moisture-stable perovskite solar cell. *Advanced Energy Materials* **2015**, *5*.

[97] Poorkazem, K.; Kelly, T. L. Compositional Engineering To Improve the Stability of Lead Halide Perovskites: A Comparative Study of Cationic and Anionic Dopants. *ACS Applied Energy Materials* **2018**, *1*, 181–190.

[98] McMeekin, D. P.; Sadoughi, G.; Rehman, W.; Eperon, G. E.; Saliba, M.; Horantner, M. T.; Haghighirad, A.; Sakai, N.; Korte, L.; Rech, B.; Johnston, M. B.; Herz, L. M.; Snaith, H. J. A mixed-cation lead mixed-halide perovskite absorber for tandem solar cells. *Science* **2016**, *351*, 151–155.

[99] Selig, O.; Sadhanala, A.; Müller, C.; Lovrincic, R.; Chen, Z.; Rezus, Y. L. A.; Frost, J. M.; Jansen, T. L. C.; Bakulin, A. A. Organic Cation Rotation and Immo-

bilisation in Pure and Mixed Methylammonium Lead-Halide Perovskites. *Journal of the American Chemical Society* **2017**, *139*, 4068–4074.

[100] Mozur, E. M.; Maughan, A. E.; Cheng, Y.; Huq, A.; Jalarvo, N.; Daemen, L. L.; Neilson, J. R. Orientational Glass Formation in Substituted Hybrid Perovskites. *Chemistry of Materials* **2017**, *29*, 10168–10177.

[101] Ferdani, D.; Pering, S.; Ghosh, D.; Kubiak, P.; Walker, A.; Lewis, S. E.; Johnson, A. L.; Baker, P. J.; Islam, S.; Cameron, P. J. Partial Cation Substitution Reduces Iodide Ion Transport in Lead Iodide Perovskite Solar Cells. *Energy & Environmental Science* **2019**,

[102] Kulbak, M.; Cahen, D.; Hodes, G. How Important Is the Organic Part of Lead Halide Perovskite Photovoltaic Cells? Efficient CsPbBr 3 Cells. *The Journal of Physical Chemistry Letters* **2015**, *6*, 2452–2456.

[103] Quarti, C.; Mosconi, E.; De Angelis, F. Structural and electronic properties of organo-halide hybrid perovskites from ab initio molecular dynamics. *Physical Chemistry Chemical Physics* **2015**, *17*, 9394–9409.

[104] Miyata, K.; Meggiolaro, D.; Tuan Trinh, M.; Joshi, P. P.; Mosconi, E.; Jones, S. C.; De Angelis, F.; Zhu, X. Y. Large polarons in lead halide perovskites. *Science Advances* **2017**, *3*, e1701217.

[105] Hopper, T. R.; Gorodetsky, A.; Frost, J. M.; Müller, C.; Lovrincic, R.; Bakulin, A. A. Ultrafast Intraband Spectroscopy of Hot-Carrier Cooling in Lead-Halide Perovskites. *ACS Energy Letters* **2018**, *3*, 2199–2205.

[106] McKechnie, S.; Frost, J. M.; Pashov, D.; Azarhoosh, P.; Walsh, A.; van Schilfgaarde, M. Dynamic symmetry breaking and spin splitting in metal halide perovskites. *Physical Review B* **2018**, *98*, 085108.

[107] Etienne, T.; Mosconi, E.; De Angelis, F. Dynamical Origin of the Rashba Effect in Organohalide Lead Perovskites: A Key to Suppressed Carrier Recombination in Perovskite Solar Cells? *The Journal of Physical Chemistry Letters* **2016**, *7*, 1638–1645.

[108] Ghosh, D.; Smith, A. R.; Walker, A. B.; Islam, M. S. Mixed A-Cation Perovskites for Solar Cells: Atomic-Scale Insights into Structural Distortion, Hydrogen Bonding, and Electronic Properties. *Chemistry of Materials* **2018**, *30*, 5194–5204.

[109] Onoda-Yamamuro, N.; Matsuo, T.; Suga, H. Calorimetric and IR spectroscopic studies of phase transitions in methylammonium trihalogenoplumbates (II). *Journal of Physics and Chemistry of Solids* **1990**, *51*, 1383–1395.

[110] Fabini, D. H.; Siaw, T. A.; Stoumpos, C. C.; Laurita, G.; Olds, D.; Page, K.; Hu, J. G.; Kanatzidis, M. G.; Han, S.; Seshadri, R. Universal Dynamics of Molecular Reorientation in Hybrid Lead Iodide Perovskites. *Journal of the American Chemical Society* **2017**, *139*, 16875–16884.

[111] Maheshwari, S.; Fridriksson, M. B.; Seal, S.; Meyer, J.; Grozema, F. C. The Relation between Rotational Dynamics of the Organic Cation and Phase Transitions in Hybrid Halide Perovskites. *The Journal of Physical Chemistry C* **2019**, *123*, 14652–14661.

[112] Chen, T.; Foley, B. J.; Park, C.; Brown, C. M.; Harriger, L. W.; Lee, J.; Ruff, J.; Yoon, M.; Choi, J. J.; Lee, S.-H. Entropy-driven structural transition and kinetic trapping in formamidinium lead iodide perovskite. *Science Advances* **2016**, *2*, e1601650.

[113] Fabini, D. H.; Stoumpos, C. C.; Laurita, G.; Kaltzoglou, A.; Kontos, A. G.; Falaras, P.; Kanatzidis, M. G.; Seshadri, R. Reentrant Structural and Optical Properties and Large Positive Thermal Expansion in Perovskite Formamidinium Lead Iodide. *Angewandte Chemie International Edition* **2016**, *55*, 15392–15396.

[114] Keshavarz, M.; Ottesen, M.; Wiedmann, S.; Wharmby, M.; Küchler, R.; Yuan, H.; Debroye, E.; Steele, J. A.; Martens, J.; Hussey, N. E.; Bremholm, M.; Roeffaers, M. B. J.; Hofkens, J. Tracking Structural Phase Transitions in Lead-Halide Perovskites by Means of Thermal Expansion. *Advanced Materials* **2019**, *1900521*, 1900521.

[115] Mozur, E. M.; Trowbridge, J. C.; Maughan, A. E.; Gorman, M. J.; Brown, C. M.; Prisk, T. R.; Neilson, J. R. Dynamical Phase Transitions and Cation Orientation-Dependent Photoconductivity in CH(NH2)2PbBr3. *ACS Materials Letters* **2019**, *1*, 260–264.

[116] Schueller, E. C.; Laurita, G.; Fabini, D. H.; Stoumpos, C. C.; Kanatzidis, M. G.; Seshadri, R. Crystal Structure Evolution and Notable Thermal Expansion in Hybrid

Perovskites Formamidinium Tin Iodide and Formamidinium Lead Bromide. *Inorganic Chemistry* **2018**, *57*, 695–701.

[117] Rosales, B. A.; Hanrahan, M. P.; Boote, B. W.; Rossini, A. J.; Smith, E. A.; Vela, J. Lead Halide Perovskites: Challenges and Opportunities in Advanced Synthesis and Spectroscopy. *ACS Energy Letters* **2017**, *2*, 906–914.

[118] Franssen, W. M.; Kentgens, A. P. Solid-state NMR of hybrid halide perovskites. *Solid State Nuclear Magnetic Resonance* **2019**, *100*, 36–44.

[119] Roiland, C.; Trippé-Allard, G.; Jemli, K.; Alonso, B.; Ameline, J.-C.; Gautier, R.; Bataille, T.; Le Pollès, L.; Deleporte, E.; Even, J.; Katana, C.; Katan, C. Multinuclear NMR as a tool for studying local order and dynamics in CH3NH3PbX3 (X = Cl, Br, I) hybrid perovskites. *Phys. Chem. Chem. Phys.* **2016**, *18*, 18112–18118.

[120] Wasylishen, R. E.; Knop, O. O.; Macdonald, J. B. Cation Rotation in Methylammonium Lead Halides. *Solid State Communicatios* **1985**, *56*, 581–582.

[121] Kubicki, D.; Prochowicz, D.; Hofstetter, A.; Pechy, P.; Zakeeruddin, S. M.; Grätzel, M.; Emsley, L.; Kubicki, D. J.; Péchy, P. Cation Dynamics in Mixed-Cation (MA)x(FA)1- xPbI3 Hybrid Perovskites from Solid-State NMR. *Journal of the American Chemical Society* **2017**, *139*, 10055–10061.

[122] Xu, Q.; Eguchi, T.; Nakayama, H.; Nakamura, N.; Kishita, M. Molecular Motions and Phase Transitions in Solid CH3NH3PbX3 (X = Cl, Br, I) as Studied by NMR and NQR. *Z. Naturforsch* **1991**, *46a*, 240–246.

[123] Volkov, A. F.; Venevtsev, Y. N.; Semin, G. K. Nuclear quadrupole resonance (NQR) of bromine-79 and bromine-81 [and iodine-127] in perovskite and orthorhombic forms of CsPbBr3 and CsPbI3. *Physica Status Solidi* **1969**, *35*, K167–K169.

[124] Bernard, G. M.; Wasylishen, R. E.; Ratcliffe, C. I.; Terskikh, V.; Wu, Q.; Buriak, J. M.; Hauger, T. Methylammonium Cation Dynamics in Methylammonium Lead Halide Perovskites: A Solid-State NMR Perspective. *Journal of Physical Chemistry A* **2018**, *122*, 1560–1573.

[125] Senocrate, A.; Moudrakovski, I.; Maier, J. Short-range ion dynamics in methylammonium lead iodide by multinuclear solid state NMR and 127I NQR. *Physical Chemistry Chemical Physics* **2018**, *20*, 20043–20055.

[126] Widdifield, C. M.; Chapman, R. P.; Bryce, D. L. *Annual Reports on NMR Spectroscopy*, 1st ed.; Elsevier Ltd., 2009; Vol. 66; pp 195–326.

[127] Szell, P. M.; Bryce, D. L. *Annual Reports on NMR Spectroscopy*, 1st ed.; Elsevier Ltd., 2015; Vol. 84; pp 115–162.

[128] Li, B.; Kawakita, Y.; Liu, Y.; Matsuura, M.; Shibata, K.; Kawamura, S.; Yamada, T.; Nakajima, K.; Shengzhong,; Liu, Rotor-phonon coupling in perovskite CH3NH3PbI3: the origin of exceptional transport properties. **2016**, arxiv:1612.01631.

[129] Swainson, I. P.; Stock, C.; Parker, S. F.; Van Eijck, L.; Russina, M.; Taylor, J. W. From soft harmonic phonons to fast relaxational dynamics in CH$_3$NH$_3$PbBr$_3$. *Physical Review B* **2015**, *92*, 100303.

[130] Bechtel, J. S.; Seshadri, R.; Van der Ven, A. Energy Landscape of Molecular Motion in Cubic Methylammonium Lead Iodide from First-Principles. *The Journal of Physical Chemistry C* **2016**, *120*, 12403–12410.

[131] Bloembergen, N.; Purcell, E. M.; Pound, R. V. Relaxation effects in nuclear magnetic resonance absorption. *Physical Review* **1948**, *73*, 679–712.

[132] Jeffrey, K. R.; Penner, G. H. In *NMR Crystallography*; Harris, R. K., Wasylishen, R. E., Duer, M. J., Eds.; Wiley: Chichester, 2009; pp 387–413.

[133] Page, K.; Siewenie, J. E.; Quadrelli, P.; Malavasi, L. Short-Range Order of Methylammonium and Persistence of Distortion at the Local Scale in MAPbBr 3 Hybrid Perovskite. *Angewandte Chemie International Edition* **2016**, *55*, 14320–14324.

[134] Farid, U.; Khan, H. U.; Avdeev, M.; Injac, S.; Kennedy, B. J. Structural studies of the high temperature phases of AgTaO3. *Journal of Solid State Chemistry* **2018**, *258*, 859–864.

[135] Howard, C. J.; Knight, K. S.; Kennedy, B. J.; Kisi, E. H. Structural phase transitions in strontium zirconate revisited. *Journal of Physics Condensed Matter* **2000**, *12*.

[136] Brivio, F.; Frost, J. M.; Skelton, J. M.; Jackson, A. J.; Weber, O. J.; Weller, M. T.; Goni, A. R.; Leguy, A. M. A.; Barnes, P. R. F.; Walsh, A. Lattice dynamics and vibra-

tional spectra of the orthorhombic, tetragonal, and cubic phases of methylammonium lead iodide. *Physical Review B* **2015**, *92*, 8.

[137] Ivanovska, T.; Quarti, C.; Grancini, G.; Petrozza, A.; De Angelis, F.; Milani, A.; Ruani, G. Vibrational Response of Methylammonium Lead Iodide: From Cation Dynamics to Phonon-Phonon Interactions. *ChemSusChem* **2016**, 1–12.

[138] Leguy, A. M. A.; Goñi, A. R.; Frost, J. M.; Skelton, J.; Brivio, F.; Rodríguez-martínez, X.; Weber, O. J.; Pallipurath, A. Dynamic disorder, phonon lifetimes, and the assignment of modes to the vibrational spectra of methylammonium lead halide perovskites. *Physical Chemistry Chemical Physics* **2016**, *18*, 27051–27066.

[139] Wilkening, M.; Heitjans, P. From Micro to Macro: Access to Long-Range Li+ Diffusion Parameters in Solids via Microscopic 6, 7Li Spin-Alignment Echo NMR Spectroscopy. *ChemPhysChem* **2012**, *13*, 53–65.

[140] Thurber, K. R.; Tycko, R. Measurement of Sample Temperatures under Magic-Angle Spinning from the Chemical Shift and Spin-Lattice Relaxation Rate of 79Br in KBr Powder. *J. Magn. Reson.2* **2009**, *196*, 84–87.

[141] Fabini, D. H.; Hogan, T.; Evans, H. A.; Stoumpos, C. C.; Kanatzidis, M. G.; Seshadri, R. Dielectric and Thermodynamic Signatures of Low-Temperature Glassy Dynamics in the Hybrid Perovskites CH3NH3PbI3 and HC (NH2) 2PbI3. *The journal of physical chemistry letters* **2016**, *7*, 376–381.

[142] Lee, J.-H.; Bristowe, N. C.; Lee, J. H.; Lee, S.-H.; Bristowe, P. D.; Cheetham, A. K.; Jang, H. M. Resolving the physical origin of octahedral tilting in halide perovskites. *Chemistry of Materials* **2016**, *28*, 4259–4266.

[143] Chen, T.; Chen, W.-L.; Foley, B. J.; Lee, J.; Ruff, J. P. C.; Ko, J. Y. P.; Brown, C. M.; Harriger, L. W.; Zhang, D.; Park, C.; Yoon, M.; Chang, Y.-M.; Choi, J. J.; Lee, S.-H. Origin of long lifetime of band-edge charge carriers in organic-inorganic lead iodide perovskites. *Proceedings of the National Academy of Sciences* **2017**, *114*, 7519–7524.

[144] Fredrickson, D. C. DFT-chemical pressure analysis: Visualizing the role of atomic size in shaping the structures of inorganic materials. *Journal of the American Chemical Society* **2012**, *134*, 5991–5999.

[145] Grannan, E. R.; Randeria, M.; Sethna, J. P. Low-temperature properties of a model glass. I. Elastic Dipole Model. *Phys. Rev. B.* **1990**, *41*, 7784–7799.

[146] Ferreira, A. C.; Létoublon, A.; Paofai, S.; Raymond, S.; Ecolivet, C.; Rufflé, B.; Cordier, S.; Katan, C.; Saidaminov, M. I.; Zhumekenov, A. A.; Bakr, O. M.; Even, J.; Bourges, P. Elastic Softness of Hybrid Lead Halide Perovskites. *Physical Review Letters* **2018**, *121*, 085502.

[147] Shannon, R. D.; Prewitt, C. T. Effective ionic radii in oxides and fluorides. *Acta Crystallographica Section B Structural Crystallography and Crystal Chemistry* **1969**, *25*, 925–946.

[148] Kieslich, G.; Sun, S.; Cheetham, T. An Extended Tolerance Factor Approach for Organic-Inorganic Perovskites. *Chem. Sci.* **2015**, *6*, 3430–3433.

[149] Rodova, M.; Brozek, J.; Knizek, K.; Nitsch, K. Phase transitions in ternary caesium lead bromide. *Journal of Thermal Analysis and Calorimetry* **2003**, *71*, 667–673.

[150] Bush, K. A. et al. 23.6%-efficient monolithic perovskite/silicon tandem solar cells with improved stability. *Nature Energy* **2017**, *2*, 17009.

[151] Wang, J.; Toby, B. H.; Lee, P. L.; Ribaud, L.; Antao, S. M.; Kurtz, C.; Ramanathan, M.; Von Dreele, R. B.; Beno, M. A. A dedicated powder diffraction beamline at the Advanced Photon Source: Commissioning and early operational results. *Review of Scientific Instruments* **2008**, *79*, 1–7.

[152] Kupče, Ä.; Freeman, R. Adiabatic Pulses for Wideband Inversion and Broadband Decoupling. *Journal of Magnetic Resonance, Series A* **1995**, 273–276.

[153] Veinberg, S. L.; Lindquist, A. W.; Jaroszewicz, M. J.; Schurko, R. W. Practical Considerations for the Acquisition of Ultra-Wideline 14N NMR Spectra. *Solid State Nucl. Magn. Reson* **2017**, 45–58.

[154] O'Dell, L. A. In *Modern Methods in Solid-state NMR: A Practitioner's Guide*; Hodgkinson, P., Ed.; The Royal Society of Chemistry: London, 2018.

[155] Pecher, O.; Halat, D. M.; Lee, J.; Liu, Z.; Griffith, K. J.; Braun, M.; Grey, C. P. Enhanced efficiency of solid-state NMR investigations of energy materials using an

external automatic tuning/matching (eATM) robot. *J. Magn. Reson* **2017**, *275*, 127–136.

[156] Nazarov, R.; Majevadia, J. S.; Patel, M.; Wenman, M. R.; Balint, D. S.; Neugebauer, J.; Sutton, A. P. First-principles calculation of the elastic dipole tensor of a point defect: Application to hydrogen in α -zirconium. *Physical Review B* **2016**, *94*, 241112.

[157] Profeta, M.; Mauri, F.; Pickard, C. J. Accurate first principles prediction of 17O NMR parameters in SiO2: Assignment of the zeolite ferrierite spectrum. *Journal of the American Chemical Society* **2003**, *125*, 541–548.

[158] Perdew, J. P.; Burke, K.; Ernzerhof, M. Generalized Gradient Approximation Made Simple. *Physical Review Letters* **1996**, *77*, 3865–3868.

[159] McNellis, E. R.; Meyer, J.; Reuter, K. Azobenzene at coinage metal surfaces: Role of dispersive van der Waals interactions. *Physical Review B - Condensed Matter and Materials Physics* **2009**, *80*, 1–10.

[160] Holger Försterling, F. Spin dynamics: Basics of Nuclear Magnetic Resonance, Second Edition. *Medical Physics* **2009**, *37*, 406–407.

[161] Bielecki, A.; Burum, D. P. Temperature Dependence of 207Pb MAS Spectra of Solid Lead Nitrate. An Accurate, Sensitive Thermometer for Variable-Temperature MAS. *J. Magn. Reson. Ser. A.* **1995**, *116*, 215–220.

[162] Arnold, O. et al. Mantid - Data analysis and visualization package for neutron scattering and μ SR experiments. *Nuclear Instruments and Methods in Physics Research, Section A: Accelerators, Spectrometers, Detectors and Associated Equipment* **2014**, *764*, 156–166.

[163] Azuah, R.; Kneller, L.; Qiu, Y.; Tregenna-Piggott, P.; Brown, C.; Copley, J.; Dimeo, R. DAVE: A comprehensive software suite for the reduction, visualization, and analysis of low energy neutron spectroscopic data. *J. Res. Natl. Inst. Stan. Technol.* **2009**, *114*, 341–358.

[164] Clark, S. J.; Segall, M. D.; Pickard, C. J.; Hasnip, P. J.; Probert, M. I. J.; Refson, K.; Payne, M. C. First principles methods using CASTEP. *Zeitschrift für Kristallographie - Crystalline Materials* **2005**, *220*, 567–570.

[165] Meyer, A.; Dimeo, R. M.; Gehring, P. M.; Neumann, D. A. The high-flux backscattering spectrometer at the NIST Center for Neutron Research. *Review of Scientific Instruments* **2003**, *74*, 2759–2777.

[166] Correa-Baena, J.-P.; Abate, A.; Saliba, M.; Tress, W.; Jesper Jacobsson, T.; Grätzel, M.; Hagfeldt, A. The rapid evolution of highly efficient perovskite solar cells. *Energy Environ. Sci.* **2017**, *10*, 710–727.

[167] Cho, H.; Jeong, S.-H.; Park, M.-H.; Kim, Y.-H.; Wolf, C.; Lee, C.-L.; Heo, J. H.; Sadhanala, A.; Myoung, N.; Yoo, S.; Im, S. H.; Friend, R. H.; Lee, T.-W. Overcoming the electroluminescence efficiency limitations of perovskite light-emitting diodes. *Science* **2015**, *350*, 1222–1225.

[168] Saidaminov, M. I.; Adinolfi, V.; Comin, R.; Abdelhady, A. L.; Peng, W.; Dursun, I.; Yuan, M.; Hoogland, S.; Sargent, E. H.; Bakr, O. M. Planar-integrated single-crystalline perovskite photodetectors. *Nat. Commun.* **2015**, *6*, 8724.

[169] Prasanna, R.; Gold-Parker, A.; Leijtens, T.; Conings, B.; Babayigit, A.; Boyen, H.-G.; Toney, M. F.; McGehee, M. D. Band Gap Tuning via Lattice Contraction and Octahedral Tilting in Perovskite Materials for Photovoltaics. *J. Am. Chem. Soc.* **2017**, *139*, 11117–11124.

[170] Zhang, L.; Zeng, Q.; Wang, K. Pressure-Induced Structural and Optical Properties of Inorganic. *J. Phys. Chem. Lett.* **2017**, *8*, 3752–3758.

[171] Filip, M. R.; Eperon, G. E.; Snaith, H. J.; Giustino, F. Steric Engineering of Metal-halide Perovskites with Tunable Optical Band Gaps. *Nat. Commun.* **2014**, *5*, 5757(2014).

[172] Gélvez-Rueda, M. C.; Cao, D. H.; Patwardhan, S.; Renaud, N.; Stoumpos, C. C.; Schatz, G. C.; Hupp, J. T.; Farha, O. K.; Savenije, T. J.; Kanatzidis, M. G.; Grozema, F. C. Effect of cation rotation on charge dynamics in hybrid lead halide perovskites. *J. Phys. Chem. C* **2016**, *120*, 16577–16585.

[173] Bechtel, J. S.; Seshadri, R.; Van Der Ven, A.; der Ven, A. Energy Landscape of Molecular Motion in Cubic Methylammonium Lead Iodide from First Principles. *J. Phys. Chem. C* **2016**, *120*, 12403–12410.

[174] Whitfield, P. S.; Herron, N.; Guise, W. E.; Page, K.; Cheng, Y. Q.; Milas, I.; Crawford, M. K. Structures, Phase Transitions and Tricritical Behavior of the Hybrid Perovskite Methyl Ammonium Lead Iodide. *Scientific Reports* **2016**, *6*, 35685.

[175] Poglitsch, A.; Weber, D. Dynamic disorder in methylammonium trihalogenoplumbates (II) observed by millimeter-wave spectroscopy. *The Journal of Chemical Physics* **1987**, *87*, 6373–6378.

[176] Glazer, A. M. The classification of tilted octahedra in perovskites. *Acta Crystallogr. Sect. B* **1972**, *28*, 3384–3392.

[177] Goldschmidt, V. M. The Laws of Crystal Chemistry. *Natural Sciences* **1926**, *14*, 477–485.

[178] Kieslich, G.; Sun, S.; Cheetham, A. K. Solid-state principles applied to organicc-inorganic perovskites: new tricks for an old dog. *Chem. Sci.* **2014**, *5*, 4712–4715.

[179] Li, Z.; Yang, M.; Park, J.-S. S.; Wei, S.-H. H.; Berry, J. J.; Zhu, K. Stabilizing Perovskite Structures by Tuning Tolerance Factor: Formation of Formamidinium and Cesium Lead Iodide Solid-State Alloys. *Chem. Mater.* **2016**, *28*, 284–292.

[180] Wehrenfennig, C.; Liu, M.; Snaith, H. J.; Johnston, M. B.; Herz, L. M. Charge carrier recombination channels in the low-temperature phase of organic-inorganic lead halide perovskite thin films. *APL Mater.* **2014**, *2*, 081513.

[181] Onoda-Yamamuro, N.; Matsuo, T.; Suga, H. Calorimetric and IR spectroscopic studies of phase transitions in methylammonium trihalogenoplumbates (II). *J. Phys. Chem. Solids* **1990**, *51*, 1383–1395.

[182] Onoda-Yamamuro, N.; Matsuo, T.; Suga, H. Dielectric study of CH3NH3PbX3 (X = Cl, Br, I). *J. Phys. Chem. Solids* **1992**, *53*, 935–939.

[183] Zhang, H.; Qiao, X.; Shen, Y.; Moehl, T.; Zakeeruddin, S. M.; Gratzel, M.; Wang, M. Photovoltaic Behaviour of Lead Methylammonium Triiodide Perovskite Solar Cells Down to 80 K. *J. Mater. Chem. A* **2015**, *22*, 11762–11767.

[184] Comin, R.; Crawford, M. K.; Said, A. H.; Herron, N.; Guise, W. E.; Wang, X.; Whitfield, P. S.; Jain, A.; Gong, X.; McGaughey, A. J. H.; Sargent, E. H. Lattice dynamics and the nature of structural transitions in organolead halide perovskites. *Phys. Rev. B* **2016**, *94*, 094301.

[185] Stoumpos, C. C.; Malliakas, C. D.; Peters, J. A.; Liu, Z.; Sebastian, M.; Im, J.; Chasapis, T. C.; Wibowo, A. C.; Chung, D. Y.; Freeman, A. J.; Wessels, B. W.; Kanatzidis, M. G. Crystal growth of the perovskite semiconductor $CsPbBr_3$: A new material for high-energy radiation detection. *Cryst. Growth Des.* **2013**, *13*, 2722–2727.

[186] Ren, Y.; Oswald, I. W. H.; Wang, X.; McCandless, G. T.; Chan, J. Y. Orientation of organic cations in hybrid inorganic-organic perovskite CH3NH3PbI3 from subatomic resolution single crystal neutron diffraction structural studies. *Cryst. Growth Des.* **2016**, *16*, 2945–2951.

[187] Yin, T.; Fang, Y.; Fan, X.; Zhang, B.; Kuo, J.-L.; White, T. J.; Chow, G. M.; Yan, J.; Shen, Z. X. Hydrogen-Bonding Evolution during the Polymorphic Transformations in CH 3 NH 3 PbBr 3 : Experiment and Theory. *Chemistry of Materials* **2017**, *29*, 5974–5981.

[188] Lee, J.-H.; Bristowe, N. C.; Lee, J. H.; Lee, S.-H.; Bristowe, P. D.; Cheetham, A. K.; Jang, H. M. Resolving the physical origin of octahedral tilting in halide perovskites. *Chem. Mater.* **2016**, *28*, 4259–4266.

[189] Mosconi, E.; Quarti, C.; Ivanovska, T.; Ruani, G.; De Angelis, F. Structural and electronic properties of organo-halide lead perovskites: a combined IR-spectroscopy and ab initio molecular dynamics investigation. *Phys. Chem. Chem. Phys.* **2014**, *16*, 16137–16144.

[190] Amat, A.; Mosconi, E.; Ronca, E.; Quarti, C.; Umari, P.; Nazeeruddin, M. K.; Grätzel, M.; De Angelis, F. Cation-induced band-gap tuning in organohalide perovskites: Interplay of spin-orbit coupling and octahedra tilting. *Nano Lett.* **2014**, *14*, 3608–3616.

[191] Li, B.; Kawakita, Y.; Liu, Y.; Wang, M.; Matsuura, M.; Shibata, K.; Ohira-Kawamura, S.; Yamada, T.; Lin, S.; Nakajima, K.; Liu, S. F. Polar rotor scattering as atomic-level origin of low mobility and thermal conductivity of perovskite $CH_3NH_3PbI_3$. *Nat. Commun.* **2017**, *8*, 16086.

[192] Swainson, I. P.; Stock, C.; Parker, S. F.; Eijck, L. V.; Russina, M.; Taylor, J. W.; Van Eijck, L.; Russina, M.; Taylor, J. W. From soft harmonic phonons to fast relaxational dynamics in $CH_3NH_3PbBr_3$. *Phys. Rev. B* **2015**, *92*, 100303.

[193] Bakulin, A. A.; Selig, O.; Bakker, H. J.; Rezus, Y. L. A.; Muller, C.; Glaser, T.; Lovrincic, R.; Sun, Z. H.; Chen, Z. Y.; Walsh, A.; Frost, J. M.; Jansen, T. L. C. Real-Time Observation of Organic Cation Reorientation in Methylammonium Lead Iodide Perovskites. *J. Phys. Chem. Lett.* **2015**, *6*, 3663–3669.

[194] Quarti, C.; Mosconi, E.; De Angelis, F.; Angelis, F. D. Interplay of Orientational Order and Electronic Structure in Methylammonium Lead Iodide: Implications for Solar Cell Operation. *Chem. Mater.* **2014**, *26*, 6557–6569.

[195] Guo, Y.; Yaffe, O.; Paley, D. W.; Beecher, A. N.; Hull, T. D.; Szpak, G.; Owen, J. S.; Brus, L. E.; Pimenta, M. A. Interplay between organic cations and inorganic framework and incommensurability in hybrid lead-halide perovskite CH3NH3PbBr3. *Physical Review Materials* **2017**, *1*, 042401.

[196] Ivanovska, T.; Dionigi, C.; Mosconi, E.; De Angelis, F.; Liscio, F.; Morandi, V.; Ruani, G. Long-Lived Photoinduced Polarons in Organohalide Perovskites. *J. Phys. Chem. Lett.* **2017**, *8*, 3081–3086.

[197] Kubicki, D. J.; Prochowicz, D.; Hofstetter, A.; Péchy, P.; Zakeeruddin, S. M.; Grätzel, M.; Emsley, L. Cation Dynamics in Mixed-Cation (MA)x(FA)1-xPbI3 Hybrid Perovskites from Solid-State NMR. *J. Am. Chem. Soc.* **2017**, *139*, 10055–10061.

[198] Neukirch, A. J.; Nie, W.; Blancon, J.-C. C.; Appavoo, K.; Tsai, H.; Sfeir, M. Y.; Katan, C.; Pedesseau, L.; Even, J.; Crochet, J. J.; Gupta, G.; Mohite, A. D.; Tretiak, S. Polaron stabilization by cooperative lattice distortion and cation rotations in hybrid perovskite materials. *Nano Lett.* **2016**, *16*, 3809–3816.

[199] Straus, D. B.; Hurtado Parra, S.; Iotov, N.; Gebhardt, J.; Rappe, A. M.; Subotnik, J. E.; Kikkawa, J. M.; Kagan, C. R. Direct Observation of Electron-Phonon Coupling and Slow Vibrational Relaxation in Organic-Inorganic Hybrid Perovskites. *J. Am. Chem. Soc.* **2016**, *138*, 13798–13801.

[200] Motta, C.; El-Mellouhi, F.; Sanvito, S. Exploring the cation dynamics in lead-bromide hybrid perovskites. *Phys. Rev. B* **2016**, *93*, 235412.

[201] Motta, C.; El-Mellouhi, F.; Kais, S.; Tabet, N.; Alharbi, F.; Sanvito, S. Revealing the role of organic cations in hybrid halide perovskite $CH_3NH_3PbI_3$. *Nat. Commun.* **2015**, *6*, 7026.

[202] Mahboubi Soufiani, A. et al. Impact of microstructure on the electron-hole interaction in lead halide perovskites. *Energy Environ. Sci.* **2017**, *10*, 1358–1366.

[203] McMeekin, D. P.; Sadoughi, G.; Rehman, W.; Eperon, G. E.; Saliba, M.; Horantner, M. T.; Haghighirad, A.; Sakai, N.; Korte, L.; Rech, B.; Johnston, M. B.; Herz, L. M.; Snaith, H. J. A mixed-cation lead mixed-halide perovskite absorber for tandem solar cells. *Science* **2016**, *351*, 151–155.

[204] Saladoa, M.; Kokalb, R. K.; Calioa, L.; Kazima, S.; Deepab, M.; Ahmada, S. Identifying the charge generation dynamics in a Cs^+ based triple cation mixed perovskite solar cells. *Phys. Chem. Chem. Phys* **2017**, *19*, 22905–22914.

[205] Deepa, M.; Salado, M.; Calio, L.; Kazim, S.; Shivaprasad, S. M.; Ahmad, S. Cesium Power: Low Cs^+ Levels Impart Stability to Perovskite Solar Cells. *Phys. Chem. Chem. Phys.* **2017**, *19*, 4069–4077.

[206] Niemann, R. G.; Gouda, L.; Hu, J.; Tirosh, S.; Gottesman, R.; Cameron, P. J.; Zaban, A. Cs^+ incorporation into $CH_3NH_3PbI_3$ perovskite: Substitution limit and stability enhancement. *J. Mater. Chem. A* **2016**, *4*, 17819–17827.

[207] Nagabhushana, G. P.; Shivaramaiah, R.; Navrotsky, A. Direct calorimetric verification of thermodynamic instability of lead halide hybrid perovskites. *Proc. Natl. Acad. Sci.* **2016**, *113*, 7717–7721.

[208] Yuan, Y.; Huang, J. Ion Migration in Organometal Trihalide Perovskite and Its Impact on Photovoltaic Efficiency and Stability. *Acc. Chem. Res.* **2016**, *49*, 286–293.

[209] Tong, C.-J.; Geng, W.; Liu, L.; Prezhdo, O. V. The Role of Methylammonium Orientation in Ion Diffusion and Current-Voltage Hysteresis in the $CH_3NH_3PbI_3$ Perovskite. *ACS Energy Lett.* **2017**, *2*, 1997–2004.

[210] Selig, O.; Sadhanala, A.; Müller, C.; Lovrincic, R.; Chen, Z.; Rezus, Y. L. A.; Frost, J. M.; Jansen, T. L. C.; Bakulin, A. A. Organic Cation Rotation and Immobili-

sation in Pure and Mixed Methylammonium Lead-Halide Perovskites. *J. Am. Chem. Soc.* **2017**, *139*, 4068–4074.

[211] Quarti, C.; Mosconi, E.; Umari, P.; De Angelis, F. Chlorine Incorporation in the $CH_3NH_3PbI_3$ Perovskite: Small Concentration, Big Effect. *Inorg. Chem.* **2017**, *56*, 74–83.

[212] Sheng, C.; Zhang, C.; Zhai, Y.; Mielczarek, K.; Wang, W.; Ma, W.; Zakhidov, A.; Vardeny, Z. V. Exciton versus Free Carrier Photogeneration in Organometal Trihalide Perovskites Probed by Broadband Ultrafast Polarization Memory Dynamics. *Phys. Rev. Lett.* **2015**, *114*, 116601.

[213] Liu, X.; Löhneysen, H. V. Specific-heat anomaly of amorphous solids at intermediate temperatures (1 to 30 K). *Europhys. Lett.* **1996**, *33*, 617–622.

[214] Bée, M. In *Quasielastic Neutron Scattering*, 1st ed.; Hilger, A., Ed.; CRC Press: Boca Raton, 1988; pp 176–250.

[215] Mertz, B.; Loidl, A. Specific Heat of $(KBr)_{1-x}(KCN)_x$. *Europhys. Lett.* **1987**, *4*, 583–591.

[216] Pohl, R. O.; Swartz, E. T. Low-lying excitations in amorphous solids. *J. Non. Cryst. Solids* **1985**, *76*, 117–128.

[217] Beecher, A. N.; Semonin, O. E.; Skelton, J. M.; Frost, J. M.; Terban, M. W.; Zhai, H.; Alatas, A.; Owen, J. S.; Walsh, A.; Billinge, S. J. L. Direct Observation of Dynamic

Symmetry Breaking above Room Temperature in Methylammonium Lead Iodide Perovskite. *ACS Energy Lett.* **2016**, *1*, 880–887.

[218] Loidl, A.; Feile, R.; Knorr, K.; Kjems, J. K. Inelastic neutron scattering study of the rotational excitations in $(KBr)_{1-x}(KCN)_x$ in the paraelastic and structural glass state. *Phys. Rev. B* **1984**, *29*, 6052–6062.

[219] Bhattacharya, S.; Nagel, S. R.; Fleishman, L.; Susman, S. Dielectric Susceptibility of $(KBr)_0.5(KCN)_0.5$: Is It a Dipole Glass? *Phys. Rev. Lett.* **1982**, *48*, 1267–1270.

[220] Knorr, K.; A. Loidl, Dielectric Properties of (KBr)$_{1-x}$(KCN)$_x$. *Z. Phys. B.* **1982**, *46*, 219–224.

[221] Michel, K. H.; Courtens, E. Dynamics of translations and rotations in molecular crystals: Macroscopic and microscopic approaches. *Phys. Rev. B* **1981**, *23*, 513–522.

[222] Loidl, A. Orientational glasses. *Annu. Rev. Phys. Chem.* **1989**, *40*, 29–60.

[223] Schupper, N.; Shnerb, N. M. Inverse melting and inverse freezing: A spin model. *Phys. Rev. E* **2005**, *72*, 046107.

[224] Manchon, A.; Koo, H. C.; Nitta, J.; Frolov, S. M.; Duine, R. A. New perspectives for Rashba spin-orbit coupling. *Nat. Mater.* **2015**, *14*, 871–882.

[225] Shankaraiah, N.; Murthy, K. P. N.; Lookman, T.; Shenoy, S. R. Monte Carlo simulations of strain pseudospins: Athermal martensites, incubation times, and entropy barriers. *Phys. Rev. B* **2011**, *84*, 064119.

[226] Kanno, S.; Imamura, Y.; Saeki, A.; Hada, M. Rotational Energy Barriers and Relaxation Times of the Organic Cation in Cubic Methylammonium Lead/Tin Halide Perovskites from First Principles. *J. Phys. Chem. C* **2017**, *121*, 14051–14059.

[227] Steiner, T. The hydrogen bond in the solid state. *Angew. Chem. Int. Ed.* **2002**, *41*, 49–76.

[228] Larson, A.; Von Dreele, V. *General Structure Analysis System (GSAS)*; 1994; Vol. MS-H805.

[229] Arnold, O. et al. Mantid - Data analysis and visualization package for neutron scattering and μ SR experiments. *Nucl. Instruments Methods Phys. Res. Sect. A Accel. Spectrometers, Detect. Assoc. Equip.* **2014**, *764*, 156–166.

[230] Togo, A.; Tanaka, I. First principles phonon calculations in materials science. *Scr. Mater.* **2015**, *108*, 1–5.

[231] Kresse, G.; Hafner, J. Norm-conserving and ultrasoft pseudopotentials for first-row and transition elements. *J. Phys. Condens. Matter* **1994**, *6*, 8245–8257.

[232] Kresse, G.; Furthmüller, J. Efficient iterative schemes for ab initio total-energy calculations using a plane-wave basis set. *Phys. Rev. B* **1996**, *54*, 11169–11186.

[233] Blöchl, P. E. Projector augmented-wave method. *Phys. Rev. B* **1994**, *50*, 17953–17979.

[234] Kresse, G.; Joubert, D. From ultrasoft pseudopotentials to the projector augmented-wave method. *Phys. Rev. B* **1999**, *59*, 1758–1775.

[235] Perdew, J. P.; Burke, K.; Ernzerhof, M. Generalized Gradient Approximation Made Simple. *Phys. Rev. Lett.* **1996**, *77*, 3865–3868.

[236] Klimeš, J. c. v.; Bowler, D. R.; Michaelides, A. Van der Waals density functionals applied to solids. *Phys. Rev. B* **2011**, *83*, 195131.

[237] Leguy, A. M. A.; Goñi, A. R.; Frost, J. M.; Skelton, J.; Brivio, F.; Rodríguez-martínez, X.; Weber, O. J.; Pallipurath, A. Dynamic disorder, phonon lifetimes, and the assignment of modes to the vibrational spectra of methylammonium lead halide perovskites. *Phys. Chem. Chem. Phys.* **2016**, *18*, 27051–27066.

[238] Ramirez-Cuesta, A. J. aCLIMAX 4.0.1, the new version of the software for analyzing and interpreting INS spectra. *Comput. Phys. Commun.* **2004**, *157*, 226–238.

[239] Mamontov, E.; Herwig, K. W. A time-of-flight backscattering spectrometer at the Spallation Neutron Source, BASIS. *Rev. Sci. Instrum.* **2011**, *82*, 085109.

[240] Azuah, R.; Kneller, L.; Qiu, Y.; Tregenna-Piggott, P.; Brown, C.; Copley, J.; Dimeo, R. DAVE: A comprehensive software suite for the reduction, visualization, and analysis of low energy neutron spectroscopic data. *J. Res. Natl. Inst. Stan. Technol.* **2009**, *114*, 341–358.

[241] Page, K.; Siewenie, J. E.; Quadrelli, P.; Malavasi, L. Perovskite Crystal Structure Short-Range Order of Methylammonium and Persistence of Distortion at the Local Scale in $MAPbBr_3$ Hybrid Perovskite. *Angew. Chemie* **2016**, *55*, 14320–14324.

[242] Snaith, H. J. Perovskites: The Emergence of a New Era for Low-Cost, High-Efficiency Solar Cells. *J. Phys. Chem. Lett.* **2013**, *4*, 3623–3630.

[243] Yang, R. X.; Skelton, J. M.; Da Silva, E. L.; Frost, J. M.; Walsh, A. Spontaneous octahedral tilting in the cubic inorganic cesium halide perovskites CsSnX3and CsPbX3(X = F, Cl, Br, I). *J. Phys. Chem. Lett.* **2017**, *8*, 4720–4726.

[244] Munson, K. T.; Doucette, G. S.; Kennehan, E. R.; Swartzfager, J. R.; Asbury, J. B. Vibrational Probe of the Structural Origins of Slow Recombination in Halide Perovskites. *The Journal of Physical Chemistry C* **2019**, acs.jpcc.9b00555.

[245] Fabini, D. H.; Hogan, T.; Evans, H. A.; Stoumpos, C. C.; Kanatzidis, M. G.; Seshadri, R. Dielectric and Thermodynamic Signatures of Low-Temperature Glassy Dynamics in the Hybrid Perovskites CH3NH3PbI3 and HC (NH2) 2PbI3. *J. Phys. Chem. Lett.* **2016**, *7*, 376–381.

[246] Evans, H. A.; Fabini, D. H.; Andrews, J. L.; Koerner, M.; Preefer, M. B.; Wu, G.; Wudl, F.; Cheetham, A. K.; Seshadri, R. Hydrogen Bonding Controls the Structural Evolution in Perovskite-Related Hybrid Platinum (IV) Iodides. *Inorg. Chem.* **2018**,

[247] Salje, E. K. Ferroelastic Materials. *Annu. Rev. Mater. Res.* **2012**, *42*, 265–283.

[248] Salje, E. K. H.; Graeme-Barber, A.; Carpenter, M. A.; Bismayer, U. Lattice parameters, spontaneous strain and phase transitions in Pb 3 (PO 4) 2. *Acta Crystallogr. B.* **1993**, *49*, 387–392.

[249] Merz, W. J. Domain formation and domain wall motions in ferroelectric BaTiO3 single crystals. *Physical Review* **1954**, *95*, 690–698.

[250] Salje, E. K.; Ishibashi, Y. Mesoscopic structures in ferroelastic crystals: Needle twins and right-angled domains. *Journal of Physics Condensed Matter* **1996**, *8*, 8477–8495.

[251] Letoublon, A.; Paofai, S.; Rufflé, B.; Bourges, P.; Hehlen, B.; Michel, T.; Ecolivet, C.; Durand, O.; Cordier, S.; Katan, C.; Even, J. Elastic Constants, Optical Phonons and Molecular Relaxations in the High Temperature Plastic Phase of the $CH_3NH_3PbBr_3$ Hybrid Perovskite. *J. Phys. Chem. Lett.* **2016**, acs.jpclett.6b01709.

[252] Frost, J. M.; Walsh, A. What Is Moving in Hybrid Halide Perovskite Solar Cells? *Accounts of Chemical Research* **2016**, *49*, 528–535.

[253] Mozur, E. M.; Hope, M.; Trowbridge, J. C.; Halat, D. M.; Daemen, L. L.; Grey, C. P.; Neilson, J. R. Cesium Substitution Disrupts Concerted Cation Dynamics in Formamidinium Hybrid Perovskites. *Chemistry of Materials* **2020**, Articles ASAP.

[254] Huang, B.; Kong, G.; Esfahani, E. N.; Chen, S.; Li, Q.; Yu, J.; Xu, N.; Zhang, Y.; Xie, S.; Wen, H.; Gao, P.; Zhao, J.; Li, J. Ferroic domains regulate photocurrent in single-crystalline CH3NH3PbI3 films self-grown on FTO/TiO2 substrate. *npj Quantum Materials* **2018**, *3*, 1–8.

[255] Petrov, A. A.; Goodilin, E. A.; Tarasov, A. B.; Lazarenko, V. A.; Dorovatovskii, P. V.; Khrustalev, V. N. Formamidinium iodide: crystal structure and phase transitions. *Acta. Crystallogr. E* **2017**, *73*, 569–572.

[256] Chupas, P. J.; Qiu, X.; Hanson, J. C.; Lee, P. L.; Grey, C. P.; Billinge, S. J. Rapid-acquisition pair distribution function (RA-PDF) analysis. *J. Appl. Crystallogr.* **2003**, *36*, 1342–1347.

[257] Toby, B. H.; Von Dreele, R. B. GSAS-II: The Genesis of a Modern Open-Source All-Purpose Crystallography Software Package. *J. Appl. Crystallogr.* **2013**, *46*, 544–549.

[258] Juhas, P.; Davis, T.; Farrow, C. L.; Billinge, S. J. PDFgetX3: a rapid and highly automatable program for processing powder diffraction data into total scattering pair distribution functions. *J. Appl. Crystallogr.* **2013**, *46*, 560–566.

[259] Farrow, C.; Juhas, P.; Liu, J.; Bryndin, D.; Božin, E.; Bloch, J.; Proffen, T.; Billinge, S. PDFfit2 and PDFgui: computer programs for studying nanostructure in crystals. *J. Phys.: Condens. Matter* **2007**, *19*, 335219.

[260] Momma, K.; Izumi, F. *VESTA3* for three-dimensional visualization of crystal, volumetric and morphology data. *J. Appl. Crystallogr.* **2011**, *44*, 1272–1276.

[261] Hu, S.; Gao, H.; Qi, Y.; Tao, Y.; Li, Y.; Reimers, J. R.; Bokdam, M.; Franchini, C.; Di Sante, D.; Stroppa, A.; Ren, W. Dipole Order in Halide Perovskites: Polarization and Rashba Band Splittings. *Journal of Physical Chemistry C* **2017**, *121*, 23045–23054.

[262] Leppert, L.; Reyes-Lillo, S. E.; Neaton, J. B. Electric Field- and Strain-Induced Rashba Effect in Hybrid Halide Perovskites. *The Journal of Physical Chemistry Letters* **2016**, 3683–3689.

[263] Mozur, E. M.; Trowbridge, J. C.; Maughan, A. E.; Gorman, M. J.; Brown, C. M.; Prisk, T. R.; Neilson, J. R. Dynamical Phase Transitions and Cation Orientation-Dependent Photoconductivity in CH(NH2)2PbBr3. *ACS Materials Letters* **2019**, *1*, 260–264.

[264] Woodward, P. M. Octahedral Tilting in Perovskites. I. Geometrical Considerations. *Acta Crystallographica Section B: Structural Science* **1997**, *53*, 32–43.

[265] Ke, W.; Stoumpos, C. C.; Kanatzidis, M. G. "Unleaded" Perovskites: Status Quo and Future Prospects of Tin-Based Perovskite Solar Cells. *Advanced Materials* **2018**, *1803230*, 1803230.

[266] Yang, W.; Igbari, F.; Lou, Y.; Wang, Z.; Liao, L. Tin Halide Perovskites: Progress and Challenges. *Advanced Energy Materials* **2020**, *10*, 1902584.

[267] Ganose, A. M.; Savory, C. N.; Scanlon, D. O. Beyond methylammonium lead iodide: prospects for the emergent field of ns 2 containing solar absorbers. *Chemical Communications* **2017**, *53*, 20–44.

[268] Liang, L.; Gao, P. Lead-Free Hybrid Perovskite Absorbers for Viable Application: Can We Eat the Cake and Have It too? *Advanced Science* **2017**, *1700331*, 1700331.

[269] Worhatch, R. J.; Kim, H.; Swainson, I. P.; Yonkeu, A. L.; Billinge, S. J. L. Study of Local Structure in Selected Organic-Inorganic Perovskites in the Pm-3m Phase. *Chemistry of Materials* **2008**, *20*, 1272–1277.

[270] Du, Y.; Ding, H.-C.; Sheng, L.; Savrasov, S. Y.; Wan, X.; Duan, C.-G. Microscopic origin of stereochemically active lone pair formation from orbital selective external potential calculations. *Journal of physics. Condensed matter : an Institute of Physics journal* **2014**, *26*, 025503.

[271] Radha, S. K.; Bhandari, C.; Lambrecht, W. R. L. Distortion modes in halide perovskites: To twist or to stretch, a matter of tolerance and lone pairs. *Physical Review Materials* **2018**, *2*, 063605.

[272] Kontos, A. G.; Kaltzoglou, A.; Arfanis, M. K.; McCall, K. M.; Stoumpos, C. C.; Wessels, B. W.; Falaras, P.; Kanatzidis, M. G. Dynamic Disorder, Band Gap Widening, and Persistent Near-IR Photoluminescence up to At Least 523 K in $ASnI_3$ Perovskites (A = Cs^+,$CH_3NH_3{}^+$ and NH_2-CH=$NH_2{}^+$), url = http://pubs.acs.org/doi/10.1021/acs.jpcc.8b10218, volume = 122, year = 2018. *The Journal of Physical Chemistry C* acs.jpcc.8b10218.

[273] Remsing, R. C.; Klein, M. L. Lone Pair Rotational Dynamics in Solids. *Physical Review Letters* **2020**, *124*, 066001.

[274] Remsing, R. C.; Klein, M. L. A new perspective on lone pair dynamics in halide perovskites. *APL Materials* **2020**, *8*, 050902.

[275] Swainson, I.; Chi, L.; Her, J. H.; Cranswick, L.; Stephens, P.; Winkler, B.; Wilson, D. J.; Milman, V. Orientational ordering, tilting and lone-pair activity in the perovskite methylammonium tin bromide, CH3NH3SnBr3. *Acta Crystallographica Section B: Structural Science* **2010**, *66*, 422–429.

[276] Mori, M.; Saito, H. An x-ray study of successive phase transitions in cssnbr3. *Journal of Physics C: Solid State Physics* **1986**, *19*, 2391–2401.

[277] Gu, S.; Lin, R.; Han, Q.; Gao, Y.; Tan, H.; Zhu, J. Tin and Mixed Lead-Tin Halide Perovskite Solar Cells: Progress and their Application in Tandem Solar Cells. *Advanced Materials* **2020**, *1907392*, 1–16.

[278] Mozur, E. M.; Maughan, A. E.; Cheng, Y.; Huq, A.; Jalarvo, N.; Daemen, L. L.; Neilson, J. R. Orientational Glass Formation in Substituted Hybrid Perovskites. *Chem. Mater.* **2017**, *29*, 10168–10177.

[279] Fabini, D. H.; Seshadri, R.; Kanatzidis, M. G. The underappreciated lone pair in halide perovskites underpins their unusual properties. *MRS Bulletin* **2020**, *45*, 467–477.

[280] Farrow, C. L.; Juhas, P.; Liu, J. W.; Bryndin, D.; Božin, E. S.; Bloch, J.; Proffen, T.; Billinge, S. J. L. PDFfit2 and PDFgui: computer programs for studying nanostructure in crystals. *Journal of Physics: Condensed Matter* **2007**, *19*, 335219.

[281] Campbell, B. J.; Stokes, H. T.; Tanner, D. E.; Hatch, D. M. ISODISPLACE: A web-based tool for exploring structural distortions. *Journal of Applied Crystallography* **2006**, *39*, 607–614.

[282] Christians, J. A.; Schulz, P.; Tinkham, J. S.; Schloemer, T. H.; Harvey, S. P.; Tremolet De Villers, B. J.; Sellinger, A.; Berry, J. J.; Luther, J. M. Tailored interfaces of unen-

capsulated perovskite solar cells for >1,000 hour operational stability. *Nat. Energy* **2018**, *3*, 68–74.

[283] Hu, X.; Zhang, D.; Chen, T.; Chen, A. Z.; Holmgren, E. N.; Zhang, Q.; Pajerowski, D. M.; Yoon, M.; Xu, G.; Choi, J. J.; Lee, S. H. Crystal structures and rotational dynamics of a two-dimensional metal halide perovskite (OA)2PbI4. *Journal of Chemical Physics* **2020**, *152*.